DYNAMICS OF SLIDING MECHANISMS IN NANOSCALE FRICTION

by

Shon W. Yim

B.S. Mechanical Engineering
University of Illinois at Urbana-Champaign, 1995

S.M. Mechanical Engineering
Massachusetts Institute of Technology, 1997

Submitted to the Department of Mechanical Engineering in Partial Fulfillment of the Requirements for the Degree of

DOCTOR OF PHILOSOPHY IN MECHANICAL ENGINEERING

at the

MASSACHUSETTS INSTITUTE OF TECHNOLOGY

June 2002

Signature of Author: _____
Department of Mechanical Engineering
May 3, 2002

Certified by: _____
Nannaji Saka
Principal Research Scientist and Senior Lecturer, Mechanical Engineering
Thesis Supervisor

Accepted by: _____
Ain. A. Sonin
Professor of Mechanical Engineering
Chairman, Department Committee on Graduate Students

DYNAMICS OF SLIDING MECHANISMS IN NANOSCALE FRICTION

by

Shon W. Yim

Submitted to the Department of Mechanical Engineering
on May 3, 2002 in Partial Fulfillment of the
Requirements for the Degree of Doctor of Philosophy in
Mechanical Engineering

ABSTRACT

Nanotribology is the study of friction and wear at the nanoscale, with relevance to such applications as micromechanical systems (MEMS) and thin, hard coatings. For these systems, classical laws of friction are inappropriate due to the small dimensions of the sliding elements and the lack of excessive plastic deformation. This thesis presents a theoretical investigation of friction at the sliding interface by Molecular Dynamics (MD) simulations of ideal Lennard-Jones solids. The effect of the interfacial structure on the frictional behavior is investigated by simulating a variety of interface configurations: commensurate, non-commensurate (or grain boundary), and amorphous. The effect of adhesion on the frictional behavior is also explored through a parametric study. For the commensurate interface, the degree of adhesion determines whether sliding occurs in the frictional or "frictionless" regime; the former is distinguishable by the presence of jump phenomena, the principal mechanism of friction in the MD model. The Sigma-5 [100](310) symmetric tilt grain boundary exhibits three distinct sliding regimes which are, in the order of increasing adhesion, frictionless sliding, frictional sliding, and sliding coupled with grain boundary migration. Twist grain boundaries of the (111) plane exhibit frictionless sliding for all degrees of adhesion. Among the structures simulated, the grain boundary systems have the lowest friction due to the intrinsic misorientation at the sliding interface. In the amorphous system, sliding occurs by a series of random local slips due to the individual atomic motion associated with the disordered structure. Increasing the adhesion leads to the initiation of a shear-induced crystallization process followed by an extremely rapid growth of the crystalline cluster. Friction in the amorphous system increases with adhesion only up to a certain limit due to the onset of bulk deformation. Similar trends have been observed in AFM measurements of the friction of thin, hard coatings.

Thesis Supervisor: Nannaji Saka
Title: Principal Research Scientist and Senior Lecturer

ACKNOWLEDGEMENTS

I would like to express my sincere gratitude to my thesis committee for their support and insightful advice throughout my program. I would like to thank my thesis advisor Dr. Nannaji Saka for his dedication to the integrity of my thesis, as well as the countless hours he devoted to discussions regarding even the finest details of my work. I want to thank Prof. Ali S. Argon for being so approachable despite his standing as a foremost respected figure in his field. He always seemed to have something helpful and timely beneficial to say, and I feel honored that he took interest in my work. I thank Professor Sidney Yip for sharing his world-renowned expertise in computer simulations, as well as his encouragement, especially during the final days. I also thank Prof. Yip for inviting me into his research group, which has been a truly beneficial experience in innumerable ways.

I would like to thank the Korean Institute of Machinery and Materials (KIMM) for sponsoring much of my research and inviting me to visit Korea last year. I especially want to thank Dr. Byung-Sun Kim, the director of the MIT-KIMM collaboration, as well as Dr. Jong-Joo Rha, who made important contributions to this work.

I don't know if I would have made it through without the love of my family, and I hope they know just how important their support has been, particularly during these past two years. My sister Ileen, for her selflessness, and her enduring faith, purity, and hope, which have always been a source of strength for me. I want to thank my father, whose hard work, resilience, and love for us, I will always remember. And to my mother I give my deepest gratitude, for her lifelong sacrifice that I am only now beginning to fully appreciate, and for her courage, which is nothing short of inspiring. And I am happy to welcome our newest family member, my brother-in-law Nam, who became the brother I have never had.

I would like to thank my friends, old and new, just for their friendship, which seems to become a scarce commodity as one grows older. Sol Bahng, Mike Beckett, and Rebecca Chae have all been very important to me in their unique ways, as have Emil Loreto, Guy Salinas, Justin Chung, James Han, John Pahn, Serena Park, and everyone from Evergreen Community Church in Chicago. Also deserving of mention are my "brilliant" friend and officemate Jason Melvin (a.k.a., Melv-o-matic), the incomparable Amir Torkaman, and Jamie Nam, my good friend and my connection for fun in Boston. I would also like to thank my past roommates Peter Liu, Benoit Bellier, and Andre Puong for making life in Ashdown enjoyable. I thank my work friends Dr. Jiun-Yu Lai, Dr. Jeanie Cherng, Wayne Hsiao, Kyung-Yoon Noh, Lisa Falco, Tina Lai, and Dan Acuna. And last but not least, I am greatly indebted to Leslie Regan and the wonderful people in the M.E. graduate office.

TABLE OF CONTENTS

LIST OF FIGURES

LIST OF TABLES

CHAPTER 1

Introduction

1.1 Nanotribology

In the past decade, there has been considerable growth in the area of nanotribology, the study of friction and wear at the atomic scale [1]. The main objective of nanotribology is the understanding of the processes at the sliding interface that lead to friction and wear. The feature that makes nanotribology unique is that the sliding system is perceived at such a small length scale, that it is often appropriate and even necessary to think about the surfaces as atoms and molecules rather than a continuum. Accordingly, friction may be interpreted in terms of the interatomic forces between the surfaces, which is fundamentally different from the classical treatment, where friction is understood only in the context of plastic deformation of the surfaces and their asperities [2,3]. The notion of friction at the nanoscale requires a new mechanism regarding the source of the irreversibility associated with friction, for the concept of plasticity is valid only in conjunction with the laws of continuum. At present, the most widely accepted theory is that of Tomlinson [4], which attributes friction and irreversibility to the occurrence of *jump phenomena* (see also Appendix A). A jump phenomenon (often referred to as *plucking* or *atomic stick-slip*) may be described as the process by which a system of atoms or molecules, upon encountering an unstable configuration during the course of sliding, undergoes a catastrophic transition to a stable configuration. The transition is characterized by the rapid acceleration of atoms toward stable positions, and in the process, much of the stored potential energy becomes converted into kinetic energy of the atoms, such that they arrive at the new positions with increased kinetic energy. The additional kinetic energy, which may be interpreted as thermal energy, is said to be rapidly dissipated away by heat transfer, although it may be noted that Tomlinson's theory does not explicitly treat the dissipation process. An important feature of the Tomlinson model, as well as similar ideas developed later [5,6], is that friction occurs even in the absence of permanent deformation or material removal.

Experimental research of nanotribology has rapidly developed ever since the introduction of the atomic force microscope (AFM) and the friction force microscope (FFM), which are

capable of measuring surface forces as small as a few nanonewtons over a scanning distance comparable to atomic dimensions [7–9]. Such ultra-high resolution instruments have been very successful in revealing the sliding behavior of single asperity contacts. For example, an FFM experiment of a sharp tungsten tip scanning the basal plane of graphite produced a periodic friction-distance curve consisting of sharp peaks and valleys, where the periodicity was commensurate with the repeatability of the graphite lattice [7]. The authors have suggested that the observed periodicity may have been the result of a layer of graphite having adhered to the tungsten tip, resulting in the sliding between layers of graphite. There has been some controversy regarding the claim that the periodicity of the friction measurements truly reflects the atomic topography of the surface, based mainly on the contention that the testing was done in air and the graphite surface must have been contaminated. Still, similar features have been observed on several other surfaces such as mica and diamond [8,9], which suggest that despite surface contamination, the FFM experiments are indeed capable of resolving the friction to the atomic scale. In addition, sharp drops in the friction-displacement curve, which are characteristic of jump phenomena, have been often observed in the FFM experiments, providing support to the theoretical model of Tomlinson. Besides friction testing, the AFM has also been employed to measure the adhesiveness of various surfaces [10–13], a property of great significance in tribology. In addition to the AFM and FFM, the quartz-crystal microbalance has also proven to be a useful tool in the study of nanoscale friction [14].

On the theoretical front, computer simulations using molecular dynamics (MD) [15] have been used extensively to model atomic-scale sliding behavior. These simulations have been helpful in revealing the atomistic processes occurring at the sliding interface, illustrating the mechanisms associated with frictional phenomena, and interpreting results from AFM and FFM experiments. The first MD modeling of friction was reported by Landman et al. [16], who simulated a nano-sized silicon tip sliding on an atomically smooth silicon surface and investigated the interaction of the tip and the surface at the atomic scale. The tip was seen to undergo severe deformation during sliding, which may have been the consequence of edge effects due to the extremely small tip size. Simulations of hydrogen-terminated diamond surfaces using periodic boundary conditions (i.e., infinite contact area) by Harrison et al. [17,18] exhibited friction in conjunction with the plucking of hydrogen atoms, even in the absence of deformation. Such phenomena as nanoindentation [19], boundary lubrication [20–25], elastohydrodynamic lubrication [26], dry sliding friction [27–29], and microcutting [30] have also been simulated by MD. One of the consistent themes from the results of these simulations has been the importance of the interfacial structure and geometry on friction

[27,28]. For example, simulations of incommensurate contacts have yielded a significant reduction in friction compared with a commensurate system consisting of the same materials and surfaces [27,31]. The influence of the interfacial structure on the sliding behavior, which has also been confirmed by experiments [32], is unique to nanotribology.

1.2 Applications of Nanotribology

1.2.1 Tribology of Thin Film Systems

Thin, hard coatings have been used for decades to achieve friction and wear characteristics that are suitable for specific applications. With the exception of such obvious cases as brake and clutch linings, the aim of most coatings is to reduce friction and wear significantly lower than that of the uncoated surface. Ceramic coatings are generally most effective due to their chemical inertness, high temperature tolerance, and most importantly, exceptional hardness (the typical hardness of ceramic coatings is in the range 10–20 GPa [33–37], compared to 600 MPa for copper and 3 GPa for 1095 steel). In addition, the standard physical and chemical vapor deposition (PVD, CVD) processes leave extremely smooth film surfaces (RMS roughness of a few nanometers), thereby significantly reducing the likelihood of indentation, plowing, and asperity deformation. Furthermore, when the film thickness is in the submicron range, there may not be enough dislocations available to initiate plastic flow, which means that there is less of a chance for yielding to take place. In practice, coatings of various nitrides, carbides, and oxides have notably improved performance and life of many machine components and cutting tools [38–41]. In most cases, a friction coefficient of 0.1–0.4 can be expected from ceramic coatings [33–35].

In addition to ceramics, amorphous carbon films have been the subject of extensive research for the past 20 years due to their excellent mechanical and tribological properties [42–44]. Within the amorphous medium, a significant fraction of short-range order can often be found in the form of sp^3 tetrahedral diamond structure as well as sp^2 trigonal graphite structure [45], and for this reason, amorphous carbon is also often called diamond-like carbon (DLC). The hardness of DLC (5–30 GPa) [35,37,46] is comparable to that of ceramic coatings, but one of the many special characteristics of DLC is that its hardness is notoriously sensitive to the sp^2 to sp^3 ratio as well as the hydrogen content [47]. The tribological properties of DLC are also rather unpredictable, exhibiting extraordinary sensitivity to such factors as the hydrogen content, deposition process, and environment. For example, Enke et al. [48] reported that the friction coefficient of a steel ball against DLC increased from 0.01

in dry nitrogen to 0.19 as the relative humidity approached 100%. Memming et al. [49] measured a wide range of friction coefficients (0.02–0.6) for a steel ball sliding against hydrogenated DLC applied by a plasma-activated CVD process, obtaining the lowest friction in inert atmospheres (ultra-high vacuum and dry N_2) and the highest in dry O_2 atmosphere. Hirvonen et al. [50] conducted friction testing using a steel ball on hydrogen-free DLC deposited by an arc-discharge method and found that the friction coefficient ranges between 0.1–0.2 in air with 45% relative humidity. Donnet et al. [43] investigated the influence of hydrogen content on the tribological performance of DLC and found that in high vacuum, the friction coefficient is lower than 0.01 for hydrogen-rich films. Likewise, Erdemir et al. [51] reported "superlow" friction coefficient of 0.003 in inert gas atmospheres for DLC films created in highly hydrogenated plasma. They postulate that the hydrogen-rich plasma has the effect of reducing the number of free σ bonds of carbon at the surface, preventing strong covalent interaction at the interface during sliding. Others have proposed a more mechanical-based explanation that the hydrogen at the surface functions as a lubricant in order to produce the superlow friction [52], or that the hydrogen inside the film diffuses to the surface in vacuum to lubricate the interface [47]. In addition, alternative mechanisms involving graphitization [53] or the transfer of lubricating layers during sliding [54, 55] have also been suggested to account for the low friction behavior of amorphous carbon films. Needless to say, there is a wide range of speculation concerning the tribological properties of DLC coatings.

It had been traditionally believed that the low-friction properties of hard coatings is primarily due to their superb resistance to plastic deformation, this being a purely mechanical interpretation based on the classical understanding of friction. However, the surprising response of DLC films to the hydrogen content as well as the testing environment defies the classical model in a number of ways. For example, it has been established that the hardness of DLC decreases substantially as the hydrogen content increases [37], which implies that hydrogenated DLC should produce higher friction, since softer films are more prone to deformation. Yet, experiments have shown hydrogen to be an excellent friction reducing agent, albeit only in inert and H_2 environments. Another intriguing property of DLC is the sensitivity of friction to the environment, such as the relative humidity of the air [48] or the inertness of the atmosphere [43,51]. Clearly, the environment has a minimal effect on the mechanical properties of the film, and yet the DLC film has been shown to exhibit an order-of-magnitude reduction in friction just from a change in the atmospheric conditions. Such behavior indicates that the friction on hard coatings is governed by local interfacial properties rather than bulk mechanical properties, and it may further be suggested that the interatomic

forces between the sliding surfaces are the principal elements of friction observed at the macroscale. Accordingly, the tribology of hard, thin coatings may be better understood in the context of nanotribology, where the system can be analyzed at the appropriate scale and the decisive factors contributing to friction can be resolved.

1.2.2 Micromechanical Systems

Microsystems, such as micro-electromechanical systems (MEMS) and magnetic recording systems, have extremely low tolerance for friction and wear since even the smallest wear particles could cause seizure and catastrophic failure, but liquid lubrication is not generally a viable option due to problems associated with stiction and contamination. MEMS components, in particular, are typically only a few microns thick and structurally unable to withstand high surface traction, which presents a problem since surface forces become increasingly dominant as the physical dimensions become smaller. Yet many of these devices are subject to severe operating conditions (some micromotors rated at 100,000 rpm [56]), which exacerbates the already challenging task of obtaining low friction solutions.

The characteristic length scales (i.e., component size, contact diameter, and so on) of micromechanical systems are typically of the order of microns. Accordingly, it may be more appropriate to treat the tribological issues in microsystems at the nano- and atomic scale rather than the macroscale. This suggestion is even more pertinent in light of the fact that excessive deformation is undesirable in microsystems for a number of reasons. First, the components are usually made of materials of sufficient hardness (silicon in the case of MEMS, for example) that indentation, wear, and deformation processes are effectively minimized, especially under the light operating loads of most microdevices. Furthermore, the thickness of the sliding components may not be enough to contain a sufficient number of dislocations to allow for plastic flow, in the conventional sense, to take place. Consequently, it may be reasoned that sliding of components in microsystems occurs without much wear and deformation, which means that friction depends mostly on the local interatomic forces at the sliding interface.

A promising solution for low friction in microsystems is the use of thin, hard coatings, especially since standard deposition processes are capable of achieving a coating thickness as small as 1 nm. The benefit of hard coatings is protection against wear and deformation without the use of liquid lubrication, and the coatings typically stay on the substrate exceptionally well, compared to other surface treatments such as self-assembled monolayers and solid lubricants. However, as discussed in the previous part, the problem of finding low-friction coating systems is still in want of a viable solution. Although the recent testing of

DLC coatings, in particular, has yielded very impressive results, the solution is still highly impractical due to the need for strict environmental control. In order to apply the thin film technology to practical systems, the coatings must be designed to deliver low friction in any reasonable environment.

1.3 Problem Statement

At present, the main obstacle to the development of ultra-low friction systems is the lack of fundamental understanding of the mechanisms of friction in the regime of sliding without severe deformation and wear, where friction is determined by the atomic interactions between the clean-shearing surfaces. Despite past efforts, a comprehensive understanding of friction at the atomic level is still lacking, and the fundamental behavior of atoms in the interfacial region has not been characterized well enough to build a useful strategy for the development of low-friction technology. Furthermore, the key system parameters and properties that most influence friction have not been determined.

An obvious strategy for reducing friction is to reduce the strength of interatomic interaction between the surfaces, which can be done by surface treatment with the intention of reducing the free surface energies, for example, or by deliberately choosing weakly adhering materials. This is not unlike the macroscopic strategy of lowering friction by selecting metallurgically incompatible materials [2]. However, there is a logical inconsistency in the belief that low adhesion leads to low friction, since the former is related to the resistance against separation of the surfaces while the latter is related to the resistance against their relative translation. In addition, there is actually no standard which relates adhesion and friction, which means that it is not known how much reduction in friction can be expected per unit reduction of adhesion. Instead of attempting random schemes for low adhesion in the hopes of discovering low friction systems on a trial-and-error basis, the fruitful approach is to first determine the theoretical correlation between adhesion and friction.

1.4 Research Objectives and Tasks

The main objective of this thesis is to conduct a comprehensive investigation of nanoscale friction by Molecular Dynamics simulations. The motivation for this study is to gain deeper theoretical insights concerning the atomic-scale mechanisms involved in frictional sliding, as well as determine the decisive parameters that influence friction in

nanoscale systems. The investigation is primarily focused on the atomic activity at the sliding interface, and a special emphasis is placed on the effect that adhesion between the sliding surfaces has on friction. Experimental research involving the measurement of friction of thin, hard coatings is also conducted in order to supplement the theoretical findings with some practical and tangible results. The following is a list of the key tasks of this thesis.

- Friction at the atomic-scale is investigated using MD simulations of Lennard-Jones systems. The mechanistic features of *jump phenomena* are examined in detail under a number of different conditions in order to better understand the atomistic processes leading to friction and irreversibility. Rather than construct a friction model specific to one material, it is in the interest of this work to reveal *general* trends that apply to a diverse class of materials, for which the Lennard-Jones is the ideal potential function because of its simplicity and adaptability to a vast number of atoms and molecules. Wear and plastic deformation are excluded from the MD models by using defect-free systems, except when structural defects are deliberately introduced to the sliding interface as integral elements of the model.
- The relationship between adhesion and friction is investigated through a parametric MD simulation study. The adhesion between the sliding surfaces is manipulated by adjusting the strength of the interatomic interactions (i.e., by varying the interfacial bond energy). The results of this particular study are useful in the assessment of the reduction of friction which can be theoretically attained, simply from lowering the adhesion by selecting incompatible pairs of materials, for example.
- The effect of the interfacial structure on friction is investigated by modeling the sliding of commensurate crystalline interfaces, bicrystal grain boundaries of the twist and tilt type, and amorphous interfaces. For each structure, the effect of the interfacial adhesion on friction is also examined.
- Experimental research is carried out using standard tribotesters to measure the friction of various sliders on thin, hard films of TiN, Si_3N_4, and DLC, among others. The main goal is to obtain data that properly reflect the sensitivity of friction to the variation of sliding materials. Testing is also done in controlled environments in order to study the effect of the atmosphere on friction. In addition to standard tribotesting, an AFM apparatus is used to measure the adhesiveness of the film surfaces as well as nano-scale friction with a silicon nitride tip.

1.5 Organization of Thesis

The thesis is organized like a compilation of autonomous technical papers, and each chapter is mostly self-contained with its own introduction, main body, conclusion, appendix, and reference sections. For this reason, there is some overlap in content from chapter to chapter, especially in the introduction sections.

Chapter 2 presents the MD simulation of commensurate crystalline interfaces. *Chapter 3* discusses the simulation of incommensurate interfaces, namely symmetric twist and tilt grain boundaries. *Chapter 4* contains the simulation of amorphous interfaces, including the details on the generation of a model amorphous material using a simulated melting-quenching process. *Chapter 5* presents the experimental research, including descriptions of the apparatus and methodology. Finally, *Chapter 6* summarizes all significant conclusions and contribution of the thesis and offers some suggestions for further research. All appendices are attached at the end of the thesis.

1.6 References

1. Bhushan, B., Israelachvili, J.N., and Landman, U., "Nanotribology: Friction, Wear and Lubrication at the Atomic Scale," *Nature*, vol. 374, pp. 607-616, 1995.
2. Rabinowicz, E., **Friction and Wear of Materials**, John Wiley & Sons, Inc., New York, 1995.
3. Suh, N.P., **Tribophysics**, Prentice Hall, New Jersey, 1986.
4. Tomlinson, G.A., "A Molecular Theory of Friction," *Philosophical Magazine*, Ser. 7, Vol. 7, No. 46, pp. 905-939, 1929.
5. Frenkel, Y.I. and Kontorova, "On the Theory of Plastic Deformation and Twinning," *T., Zh. Eksp. teor. Fiz.*, vol. 8, pp. 1340, 1938.
6. McClelland, G.M., "Friction at Weakly Interacting Interfaces," in Adhesion and Friction, Springer Series in Surface Sciences, vol. 17, Eds. Grunze, M. and Kreuzer, H.J., Springer Verlag, pp. 1-16, 1989.
7. Mate, C.M., McClelland, G.M., Erlandsson, R., and Chiang, S., "Atomic-Scale Friction of a Tungsten Tip on a Graphite Surface," *Physical Review Letters*, vol. 59, no. 17, pp. 1942-1945, 1987.
8. Erlandsson, R., Hadziioannou, G., Mate, C.M., McClelland, G.M., and Chiang, S., "Atomic Scale Friction Between the Muscovite Mica Cleavage Plane and a Tungsten Tip," *Journal of Chemical Physics*, vol. 89, no. 8, pp. 5190-5193, 1988.
9. Ruan, J. and Bhushan, B., "Atomic-Scale and Microscale Friction Studies of Graphite and Diamond using Friction Force Microscopy," *Journal of Applied Physics*, Vol. 76, No. 9, pp. 5022-5035, 1994.

10. Burnham, N.A. and Colton, R.J., "Measuring the Nanomechanical Properties and Surface Forces of Materials Using an Atomic Force Microscope," *Journal of Vacuum Science Technology A*, vol. 7, no. 4, pp. 2906-2913, 1989.

11. Argento, C. and French, R.H., "Parametric Tip Model and Force-Distance Relation for Hamaker Constant Determination from Atomic Force Microscopy," *Journal of Applied Physics*, vol. 80, no. 11, pp. 6081-6090, 1996.

12. Cappella, B. and Dietler, G., "Force-Distance Curves by Atomic Force Microscopy," *Surface Science Reports*, vol. 34, pp. 1-104, 1999.

13. Grinevich, O., Mejiritski, A., and Neckers, D.C., "AFM Force-Distance Curve Methods for Measuring the Kinetics of Silicon Chemical Etching and Reactions Between Silylating Agents and a Silicon Surface," *Langmuir*, vol. 15, pp. 2077-2079, 1999.

14. Krim, J., Solina, D.H., and Chiarello, R., "Nanotribology of a Kr Monolayer: A Quartz-Crystal Microbalance Study of Atomic-Scale Friction," *Physical Review Letters*, vol. 66, no. 2, pp.181-184, 1991.

15. Allen, M.P. and Tildesley, D.J., **Computer Simulation of Liquids**, Clarendon Press, Oxford, 1987.

16. Landman, U., Luedtke, W.D., and Ribarsky, M.W., "Structural and Dynamical Consequences of Interactions in Interfacial Systems," *Journal of Vacuum Science Technology A*, vol. 7, no. 4, pp. 2829-2839, 1989.

17. Harrison, J.A., White, C.T., Colton, R.J., and Brenner, D.W., "Molecular-Dynamics Simulations of Atomic-Scale Friction of Diamond Surfaces," *Physical Review B*, Vol. 46, No. 15, pp. 9700-9708, 1992.

18. Perry, M.D. and Harrison, J.A., "Molecular Dynamics Studies of the Frictional Properties of Hydrocarbon Materials," *Langmuir*, vol. 12, pp. 4552-4556, 1996.

19. Landman, U., Luedtke, W.D., Burnham, N.A., and Colton, R.J., "Atomistic Mechanisms and Dynamics of Adhesion, Nanoindentation, and Fracture," *Science*, vol. 248, pp. 454-461, 1990.

20. Thompson, P.A. and Robbins, M.O., "Origin of Stick-Slip Motion in Boundary Lubrication," *Science*, vol. 250, pp.792-794, 1990.

21. Glosli, J.N. and McClelland, G.M., "Molecular Dynamic Study of Sliding Friction of Ordered Organic Monolayers," *Physical Review Letters*, vol. 70, no. 13, pp. 1960-1963, 1993.

22. Cieplak, M., Smith, E.D., and Robbins, M.O., "Molecular Origins of Friction," *Science*, vol. 265, pp. 1209-1212, 1994.

23. Tupper, K.J. and Brenner, D.W., "Molecular Dynamics Simulations of Friction in Self-Assembled Monolayers," *Thin Solid Films*, vol. 253, pp. 185-189, 1994.

24. Koike, A. and Yoneya, M., "Molecular Dynamics Simulations of Sliding Friction of Langmuir-Blodgett Monolayers," *Journal of Chemical Physics*, vol. 105, no. 14, pp. 6060-6067, 1996.

25. Yim. S., Sonwalkar, N., and Saka, N., "Molecular Dynamics Simulation of Boundary Lubricated Interfaces," *Journal of Computer-Aided Materials Design*, vol. 6, pp. 69-80, 1999.

26. Gao, J., Luedtke, W.D., and Landman, U., "Nano-elastohydrodynamics: Structure, Dynamics, and Flow in Nonuniform Lubricated Junctions," *Science*, vol. 270, pp. 605-608, 1995.

27. Sørensen, M.R., Jacobsen, K.W., and Stoltze, P., "Simulations of Atomic-Scale Sliding Friction," *Physical Review B*, Vol. 53, No. 4, pp. 2101-2113, 1996.

28. Buldum, A. and Ciraci, S., "Contact, Nanoindentation, and Sliding Friction," *Physical Review B*, vol. 57, no. 4, pp. 2468-2476, 1998.

29. Hammerberg, J.E., Holian, B.L., Röder, J., Bishop, A.R., and Zhou, S.J., Nonlinear Dynamics and the Problem of Slip at Material Interfaces, *Physica D*, vol. 123, pp. 330-340, 1998.

30. Chandrasekaran, N., Khajavi, A.N., Raff, L.M., and Komanduri, R., "A New Method for Molecular Dynamics Simulation of Nanometric Cutting," *Philosophical Magazine B*, vol. 77, no. 1, pp. 7-26, 1998.

31. Hirano, M. and Shinjo, K., "Atomistic Locking and Friction," *Physical Review B*, vol. 41, no. 17, pp. 11837-11851, 1990.

32. Hirano, M., Shinjo, K., Kaneko, R., and Murata, Y., "Anisotropy of Frictional Forces in Muscovite Mica," *Physical Review Letters*, vol. 67, no. 19, pp. 2642-2645, 1991.

33. Bienk, E.J., Reitz, H., and Mikkelsen, N.J., "Wear and Friction Properties of Hard PVD Coatings," *Surface Coatings and Technology*, vol. 76-77, pp. 475-480, 1995.

34. Wiklund, U., Wänstrand, O., Larsson, M., and Hogmark, S., "Evaluation of New Multilayered Physical Vapour Deposition Coatings in Sliding Contact," *Wear*, vol. 236, pp. 88-95, 1999.

35. Hogmark, S., Jacobson, S., and Larsson, M., "Design and Evaluation of Tribological Coatings," *Wear*, vol. 246, pp. 20-33, 2000.

36. **ASM Engineered Materials Reference Book**, ASM International, Metals Park, OH, 1989.

37. **Handbook of Hard Coatings: Deposition Technologies, Properties, and Applications**, Ed. Bunshah, R.F., Noyes Publications, Park Ridge, N.J., 2001.

38. Su, K.-Y. and Cook, N.H., "Enhancement of High Speed Tool Life by Titanium Nitride Sputter Coating," Proc. Fifth N. Am. Metalworking Research Conference, Univ. of Massachusetts, Amherst, MA, May 23-25, SME, pp. 297-302, 1977.

39. Blair, S., Ramalingam, S., and Winer, W.O., "Tribological Experience with Hard Coats on Soft Metallic Substrates," *Wear*, vol. 60, pp. 413-419, 1980.

40. Ramalingam, S. and Winer, W.O., "Reactively Sputtered TiN Coatings for Tribological Applications," *Thin Solid Films*, vol. 73, pp. 267-274, 1980.

41. Jamal, T., Nimmagadda, R., and Bunshah, R.F., "Friction and Adhesive Wear of Titanium Carbide and Titanium Nitride Overlay Coatings," *Thin Solid Films*, vol. 73, pp. 245-254, 1980.

42. McKenzie, D.R., "Tetrahedral Bonding in Amorphous Carbon," *Reports on Progress in Physics*, vol. 59, pp. 1611-1664, 1996.

43. Donnet, C., Fontaine, J., Grill, A., and LeMogne, T., "The Role of Hydrogen on the Friction Mechanism of Diamond-Like Carbon Films," *Tribology Letters*, vol. 9, no. 3-4, pp. 137-142, 2000.

44. Holmberg, K., Ronkainen, H., and Matthews, A., "Tribology of Thin Coatings," *Ceramics International*, vol. 26, pp. 787-795, 2000.

45. Robertson, J., "Amorphous Carbon," *Advanced Physics*, vol. 35, pp. 317-374, 1986.

46. Habig, K-H., "Fundamentals of the Tribological Behaviour of Diamond, Diamond-like Carbon, and Cubic Boron Nitride Coatings," *Surface Coatings and Technology*, vol. 76-77, pp. 540-547, 1995.

47. Bull, S.J., "Tribology of Carbon Coatings: DLC, Diamond, and Beyond," *Diamond and Related Materials*, vol. 4, pp. 827-836, 1995.

48. Enke, K., Dimigen, H., and Hübsch, H., "Frictional Properties of Diamondlike Carbon Layers," *Applied Physics Letters*, vol. 36, no. 4, pp. 291-292, 1980.

49. Memming, R., Tolle, H.J., and Wierenga, P.E., "Properties of Polymeric Layers of Hydrogenated Amorphous Carbon Produced by a Plasma-Activated Chemical Vapour Deposition Process II: Tribological and Mechanical Properties," *Thin Solid Films*, vol. 143, pp. 31-41, 1986.

50. Hirvonen, J-P, Lappalainen, R., Koskinen, J., Anttila, A., Jervis, T.R., and Trkula, M., "Tribological Characteristics of Diamond-Like Films Deposited with an Arc-Discharge Method," *Journal of Materials Research*, vol. 5, no. 11, pp. 2524-2530, 1990.

51. Erdemir, A., Eryilmaz, O.L., and Fenske, G., "Synthesis of Diamondlike Carbon Films with Superlow Friction and Wear Properties," *Journal of Vacuum Science Technology A*, vol. 18, no. 4, pp. 1987-1992, 2000.

52. LeHuu, T., Zaïdi, H., and Paulmier, D., "Lubricating Properties of Diamond-like Coating," *Wear*, vol. 181-183, pp. 766-770, 1995.

53. Liu, Y., Erdemir, A., and Meletis, E.I., "An Investigation of the Relationship Between Graphitization and Frictional Behavior of DLC Coatings," *Surface and Coatings Technology*, vol. 86-87, pp. 564-568, 1996.

54. Sugimoto, I. and Miyake, S., "Oriented Hydrocarbons Transferred from a High Performance Lubricative Amorphous C:H:Si Film During Sliding in a Vacuum," *Applied Physics Letters*, vol. 56, no, 19, pp. 1868-1870, 1990.

55. Erdemir, A. and Fenske, G.R., "Tribological Performance of Diamond and Diamondlike Carbon Films at Elevated Temperatures," *Tribology Transactions*, vol. 39, no. 4, pp. 787-794, 1996.

56. Tai, Y.C., Fan, L.S., and Muller, R.S., "IC-processed Micro-motors: Design, Technology, and Testing," *Proceedings of IEEE Micro Electro Mechanical Systems*, 1-6, 1989.

CHAPTER 2

Molecular Dynamics Simulation of Friction Between Commensurate Crystalline Surfaces

2.1 Introduction

The rapidly developing field of nanotribology [1] has provided much insight into the micro-and nano-scale mechanisms of friction. Such high-resolution instruments as the friction force microscope (FFM) and the quartz microbalance have been used to measure friction at the atomic scale, where minimal-wear sliding was observed with a relatively low friction coefficients of the order of 0.01 [2–5]. Such experimental observations have motivated atomistic modeling of friction by Molecular Dynamics (MD) simulations to gain a better understanding of the underlying physics. The earliest of such simulations was conducted by Landman and his colleagues [6], who simulated the scanning of a silicon surface by a nano-sized silicon tip and observed *jump phenomena*, also called *atomic stick-slip* or *plucking*, which is the atomic-scale mechanism of friction proposed by Tomlinson and others long ago [7–9]. The occurrence of jump phenomena was also reported by Harrison et al., who simulated the sliding of hydrogen-terminated diamond surfaces [10] as well as the behavior of a mobile molecule trapped at the sliding interface [11]. In addition to these, several simulations have been conducted for tip/substrate interactions [12–14], boundary lubrication [15–18], nanoscale wear [19,20], and deformation of sliding asperities [21,22].

Whereas atomic-scale friction has traditionally been a topic bearing only philosophical significance, it has recently attained technological relevance from the advance of such micro-technologies as micro-electro mechanical systems (MEMS) [23,24], where surface forces, such as friction and adhesion, dominate body forces due to the miniature component sizes. The reduction of friction in sliding components without the aid of lubrication is a critical design issue, and an effective methodology for low friction through intelligent manipulation of design parameters would serve as an impetus for future development of microtechnology. The design of low friction surfaces invariably requires knowledge of the dominant modes of friction, but such continuum models as plowing and asperity deformation [25] are inapplicable because the characteristic size of MEMS components is only of the order of

microns. In order to better comprehend friction in microsystems, a modeling of friction must be conducted at the atomic scale.

A promising possibility for reducing friction is to engineer weakly adhering surfaces by such techniques as surface treatment or the use of thin, hard coatings, for example, in keeping with the widely held belief that weak adhesion produces low friction [26]. This correlation between adhesion and friction is mostly intuitive, as there exists no formal theory to substantiate the relationship. Adhesion, after all, relates to the force required to separate, not slide, two surfaces. Strictly speaking, the relationship between adhesion and friction cannot be properly interpreted at the macroscopic level, but it may be resolved at the atomic scale, where both adhesion and friction come from the same source, that is the interatomic forces at the interface. An atomic-scale investigation of the adhesion-friction relationship is an appealing endeavor, particularly with the mindset of determining the theoretical reduction of friction which is possible per unit reduction of adhesion. Such information may lead to promising strategies for designing ultra-low friction systems through the proper selection of coating materials.

In the present work, MD simulations of dry-sliding surfaces at the atomic scale are performed. One of the objectives of this work is to gain a better understanding of the friction mechanism and jump phenomena. Another important objective is to investigate the adhesion-friction relationship for ideal systems via a parametric study. Furthermore, many central issues involved in atomic-scale friction modeling, such as the very definition of friction and irreversibility, are discussed the following presentation.

2.2 Molecular Dynamics Simulation Methodology

2.2.1 System Description

The simulation cell, illustrated in Figure 2–1, contains materials A and B, each initially arranged into 9 (111) FCC layers in the vertical (z) loading direction. The layers are numbered from bottom to top, as shown in the figure, such that 9 and 10 are the "interfacial layers". The layer numbers are assigned to facilitate the interpretation and discussion of the various results, many of which are examined on a layer-by-layer basis. The cell is bounded in the z direction by the upper and lower finite borders, each consisting of 3 (111) layers of fixed atoms. The simulation cell contains only the dynamic atoms, and the fixed border atoms are positioned outside of the cell. In the horizontal directions (x and y), periodic boundary conditions are enforced, effectively turning the system into an infinitely repeating interface. Sliding occurs in the x direction, which coincides with the $[\bar{1}10]$ slip direction.

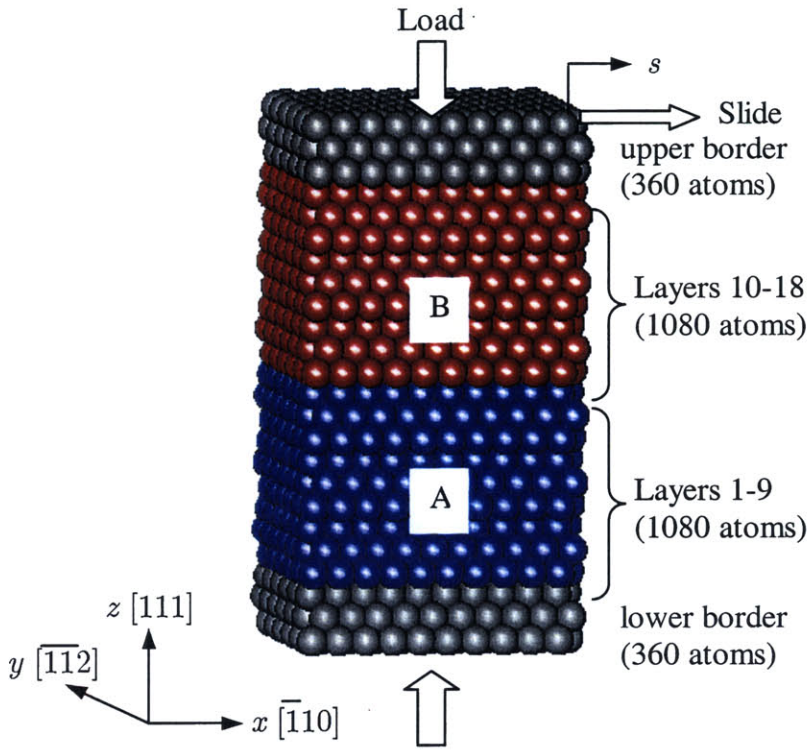

Figure 2–1: MD simulation system. Periodic boundary conditions are applied in the x–y directions only. Graphics are produced by VMD [34].

The distribution of the number of atoms is given in Table 2–1, along with the dimensions of the simulation cell and other relevant details. The listed cell dimensions reflect only the initial conditions. As explained shortly, the cell dimensions are allowed to change throughout the simulation to maintain a desired state of stress. It may be noted that the interface is commensurate (i.e., lattices A and B match perfectly at the interface), which is an important detail considering that several have reported that commensurate sliding interfaces produce significantly higher friction than incommensurate interfaces [6,12,13]. That being said, the present study only examines commensurate systems, as incommensurate systems are the topic of Chapter 3.

Table 2–1: Parameters for sliding simulation.

Number of atoms	1080 in material A 1080 in material B 360 in upper border 360 in lower border
Simulation cell dimensions ($x \times y \times z$)	$2.558 \times 2.658 \times 3.760$ nm
Mass of atom (A or B)	1.06×10^{-22} g (copper)
Mass of dynamic cell walls	1.06×10^{-21} g
Time step	10^{-15} s
Sliding increment of moving border	0.00256 nm
Number of steps following each sliding increment	5000 time steps
Normal load during sliding	300 MPa (compressive)
Temperature (by velocity rescaling)	291 K

2.2.2 Potential Function

All systems in this work are modeled using the Lennard-Jones (L–J) 12–6 pair potential,

$$\phi\left(r_{ij}\right) = 4\varepsilon\left[\left(\frac{\sigma}{r_{ij}}\right)^{12} - \left(\frac{\sigma}{r_{ij}}\right)^{6}\right], \tag{2.1}$$

which describes the potential energy between the pair of atoms i and j separated by a distance of r_{ij} . The L–J parameters ε and σ are related to the bond energy and the distance of nearest approach, respectively, and a unique pair of these parameters defines the material being modeled. At present, three sets of ε and σ are needed to fully define the system, one set for each bulk (A–A and B–B) interaction, and one set for the interfacial (A–B) interaction. Table 2–2 lists the values of all L–J parameters, with the subscript notation denoting the specific interaction. No subscript is used on the parameter σ because it is assumed to be the same for all interactions. This is a reasonable simplification given that σ primarily affects the lattice parameter, which is expected to have a minimal effect on the sliding behavior. Another simplification is $\varepsilon_{AA} = \varepsilon_{BB}$, which essentially means that the bulk properties of A and B are identical. This assumption should also have little effect on the outcome because the bulk interaction is far less important than the interfacial interaction as far as the sliding behavior is concerned.

Table 2–2: Lennard-Jones parameters.

A–A	$\varepsilon_{AA}/k_b = 4733.5$ K	$\sigma = 0.23127$ nm
B–B	$\varepsilon_{BB}/k_b = 4733.5$ K	$\sigma = 0.23127$ nm
A–B	$\varepsilon_{AB}/\varepsilon_{AA}$ = variable ($\varepsilon_{AB}/\varepsilon_{AA} < 1$)	$\sigma = 0.23127$ nm

$k_b = 1.38 \times 10^{-23}$ J/K (Boltzmann's constant)

The key parameter is ε_{AB} because it determines the strength of the interfacial bonds, and the ratio $\varepsilon_{AB}/\varepsilon_{AA}$ is a convenient dimensionless parameter relating the interfacial adhesion to the bulk cohesion. The limiting case of $\varepsilon_{AB}/\varepsilon_{AA} = 1$ is equivalent to the shearing of a bulk material without an interface, whereas a reduced value ($\varepsilon_{AB}/\varepsilon_{AA} < 1$) introduces an interface which is weak relative to the rest of the system, which would be reflective of contaminated surfaces, for example. With ε_{AB} lower than ε_{AA}, the interface can also be considered as a

generic planar defect, where the "strength" of the defect is determined by the ratio $\varepsilon_{AB}/\varepsilon_{AA}$. As this ratio approaches unity, the defect becomes less severe and the system approaches homogeneity. Alternatively, a low value of the ratio gives the system a graphite-like disposition, making it much more prone to shearing in the basal plane. This property is particularly appealing for tribological systems because the material is able to support large normal loads while offering very low sliding resistance. As the ratio approaches zero, the simulated system would reflect a pair of weakly adhering surfaces, an ideal tribological system whose friction coefficient should approach zero.

The bulk L–J parameters (i.e., A–A and B–B) in Table 2–2 are fitted to the specific volume and vaporization enthalpy of copper [27], which is chosen simply as a representative material so that the simulations may reflect the typical behavior of common metals. It is emphasized, however, that the intention of the present work is not to predict the frictional properties of any one specific material. In contrast, the objective is to reveal general trends in the sliding behavior of atomic-scale systems through a parametric study, and the present system should accordingly be viewed as generic L–J surfaces in sliding. The use of the L–J potential raises some concern about the validity of the simulation, given the well known drawbacks of this potential in modeling solids. Indeed, the embedded atom method (EAM) [28] is the preferred potential function for modeling the mechanical properties of such metals as copper, but the EAM is also computationally expensive. For a parametric study, the L–J is actually the ideal potential because of its simplicity and universal applicability to a wide class of materials. Furthermore, the most important interaction in the present system is the interfacial (A–B) interaction, for which a proven potential function does not yet exist. Therefore, it seems impractical to implement a powerful potential function for the bulk interaction when an equally accurate interfacial potential is unavailable.

2.2.3 Boundary Conditions

The *finite border boundary conditions* described in Appendix C are employed. The method is briefly outlined here. Referring back to Figure 2–1, periodic boundary conditions are disabled in the in the z direction and replaced by the finite borders, which are essentially blocks of fixed atoms that lie *outside* of the simulation cell. It may be noted that the finite border are necessary elements of a sliding simulation involving a bimaterial interface. An atom of material A interacts with a fixed atom of the lower border as it would with another A atom, and likewise for a B atom interacting with an upper border atom. Similar to the

Parrinello–Rahman method [29], a constant stress state is maintained by allowing the cell walls to move during the simulation. The stress of a system with finite borders is given by:

$$\tau = -\frac{1}{V}\left[\sum_i m_i \mathbf{v}_i \mathbf{v}_i' + \sum_i \sum_{j>i} \mathbf{r}_{ij}\mathbf{f}_{ij}' + \sum_i \sum_k \tilde{\mathbf{r}}_{ik}\mathbf{f}_{ik}'\right], \tag{2.2}$$

where V is the volume of the simulation cell, m_i is the mass of atom i, $\mathbf{v}_i$ is its velocity vector, $\mathbf{r}_{ij} = \mathbf{r}_i - \mathbf{r}_j$, and $\mathbf{r}_i$ and $\mathbf{r}_j$ are the coordinate vectors of atoms i and j. The primes denote the transpose of the column vectors. Indices i and j loop over only the dynamic atoms inside the cell, while k represents only the fixed atoms of the borders. The tilde, as in $\tilde{\mathbf{r}}_{ik}$, denotes that only the interior portion of the spatial vector is to be used, and this applies only when atom i (always inside the cell) interacts with fixed atom k (always outside the cell). The force exerted on atom i by j, denoted by $\mathbf{f}_{ij}$ (or $\mathbf{f}_{ik}$, when a fixed atom is involved), is related to the derivative of the potential function,

$$\mathbf{f}_{ij} = -\frac{d\phi}{dr_{ij}}\frac{\mathbf{r}_{ij}}{r_{ij}}. \tag{2.3}$$

The constant-stress simulation method described in Appendix C is conceptually similar to the P–R method, except that the P–R method is valid only for fully periodic simulation cells (i.e., periodic in all three directions), whereas the present scheme is adaptable to cells with finite borders. As the cell changes size and shape, the finite borders also undergo a deformation consistent with the deformation of the cell, which means that the fixed atoms go through displacements associated with the strain of the borders. For the sake of eliminating free body rotation and undesirable distortions of the cell, all shear deformations are suppressed in this work, so that the cell is constrained to maintain a tetragonal shape.

2.2.4 Loading and Sliding Methodology

After the positions of all dynamic and fixed atoms have been are arranged according to the ordered structure (see Figure 2–1), and the velocities of the dynamic atoms have been assigned randomly and scaled to the proper temperature, the simulation of sliding follows a three-step procedure: relaxation, loading, and sliding. During relaxation, the system is simulated under zero stress and constant temperature for at least 50000 time steps, which is approximately equivalent to 200 atomic oscillations. This is done to allow the system to find the zero-stress equilibrium. The normal load is then applied by taking the output dump file (i.e., atomic positions and velocities) from the relaxation simulation and using it as the input

to a new simulation where a normal compression in the z direction is applied, while the normal stresses in the x and y directions are kept at zero. Since the normal load is applied instantaneously, 50000 time steps are given for the system to fully equilibrate to the load. The output at the end of this equilibration is then used as the input to the sliding simulation.

Sliding is imposed by incremental displacements of the upper border in the x direction (see Figure 2–1) while holding the lower border in place. The size of the increment is $0.01b$, where b is the lattice period in the sliding direction, usually about .256 nm. This particular sliding increment is less than 1/10 of the estimated amplitude of atomic vibration at the given temperature (see Appendix B). After each increment, 5000 time steps are allowed for equilibration prior to the execution of the next sliding step. This is done so that the entire system always "feels" the effect of the moving border. The 5000 steps is equivalent to 20 atomic oscillations, and mean-square displacement data confirm that the system generally reaches a new equilibrium state during this span.

2.2.5 Potential Energy and Sliding Resistance

During sliding, relevant properties such as the potential energy and sliding resistance are computed with respect to s, the total displacement of the upper border. The potential energy is calculated by simply summing up all pair potentials,

$$\Phi = \frac{1}{2N}\overline{\sum_i \sum_{j \neq i} \phi\left(r_{ij}\right)}, \tag{2.4}$$

where i loops over only the system atoms while j loops over all system and border atoms. The normalization factor N is the total number of system atoms (A and B combined), and the factor of 1/2 compensates for double counting. The overhead bar denotes averaging over the equilibration period after each sliding displacement. The *sliding resistance* is equal to $\overline{\tau}_{xz}$, the shear component of the internal stress of Eqn. (2.2), also averaged over the equilibration period. The sliding resistance is exactly the shear stress exerted by the rigid border on the upper face of the cell (and vice-versa) in equilibrium.

2.2.6 Additional Simulation Details

The atomic motions are numerically integrated using the 5th-order Gear predictor-corrector method. The atomic velocities are rescaled at every time step in order to maintain the temperature at 291 K. The usual methods such as the potential cutoff at 2.5σ, neighbor

list, and the minimum image criteria are applied to improve computational efficiency. Details of these techniques can be found in other sources [30].

2.3 Parameterization of Adhesion

In order to analyze the effect of adhesion on friction, it is necessary to first express adhesion in terms of a parameter that relates to the MD simulation system. This is accomplished by utilizing the concepts of surface energy (γ_A , γ_B), interface energy (γ_{AB}), and work of adhesion (W_{AB}), and relating these to the L–J parameters. The first task is to define γ_A , γ_{AB} , and W_{AB} . Atoms at the free surface have higher energy than bulk atoms, and the *surface energy* γ_A (for surface A, or γ_B for surface B) is defined as the sum of the excess energy (i.e., the amount which exceeds the bulk value) of all such atoms, divided by the surface area. When two free surfaces A and B form an interface, the *interface energy* γ_{AB} is used to define the total excess energy per unit area of the interface. The work of adhesion W_{AB} is the energy needed to separate a unit area of the A–B interface [26],

$$W_{AB} = \gamma_A + \gamma_B - \gamma_{AB}, \tag{2.5}$$

and this quantity is a direct measure of the adhesion between the surfaces. Out of convenience, W_{AB} is sometimes expressed as

$$W_{AB} = c_m \left(\gamma_A + \gamma_B\right), \tag{2.6}$$

where the compatibility factor c_m ranges from 0 (no adhesion) to 1 (perfect adhesion between identical surfaces). Rabinowicz [26] has compiled a chart of estimations of the compatibility factor for various material pairs (mostly metallic) based on binary phase diagrams. Some examples from this chart are listed in Table 2–3.

2.3.1 Analysis of Unrelaxed Structure

The parameterization of adhesion essentially comes down to the derivation of an expression for the work of adhesion (Eqn. (2.5) and (2.6)) in terms of the L–J parameters ε_{AB}, ε_{AA}, and σ. As a first order analysis, the atomic structure of the (111) surface may be represented by the close-packed hard sphere approximation without considering any effect of surface relaxation. Based on this configuration, expressions for γ_A , γ_{AB} , and W_{AB} can be

obtained by considering up to the second nearest neighbor interactions by the L–J pair potential. The detailed derivation is given in Appendix D, and the results are the following:

$$\frac{\gamma_A}{\varepsilon_{AA}/\sigma^2} = 1.7\,, \tag{2.7}$$

$$\frac{\gamma_{AB}}{\varepsilon_{AA}/\sigma^2} = 3.4\left(1 - \frac{\varepsilon_{AB}}{\varepsilon_{AA}}\right), \tag{2.8}$$

$$\frac{W_{AB}}{\varepsilon_{AA}/\sigma^2} = 3.4\left(\frac{\varepsilon_{AB}}{\varepsilon_{AA}}\right). \tag{2.9}$$

These equations are in accord with the previous assumption that the A–A and B–B interactions are identical, but the A–B interaction is different.

Eqn. (2.7) indicates that the surface energy of an L–J solid is linearly dependent on ε_{AA} and inversely dependent on σ^2. It may be recalled that the two main approximations are the neglect of distant neighbors and structural relaxation. The addition of distant neighbors to the model would result in the increase of the constant of proportionality, but the γ_A–ε_{AA} relationship would remain linear because the L–J is a pairwise additive potential. Allowing for relaxation would lead to a lower prediction of γ_A, and it may also cause a deviation from linearity due to the highly nonlinear nature of the potential function, but for small relaxations near equilibrium the deviation from linearity may only be minor. Eqns. (2.8) and (2.9) suggest that the ratio $\varepsilon_{AB}/\varepsilon_{AA}$ plays an important role in the interface energetics. In fact, combining Eqns. (2.6), (2.7), and (2.9) leads to the very convenient relationship,

$$c_m = \frac{\varepsilon_{AB}}{\varepsilon_{AA}}. \tag{2.10}$$

This equation gives a physical interpretation of the ratio $\varepsilon_{AB}/\varepsilon_{AA}$ and establishes a direct connection between an MD parameter and a macroscopic tribological parameter. Consequently, the ratio $\varepsilon_{AB}/\varepsilon_{AA}$ is the ideal feature parameter in the friction-adhesion parametric study, and the values of c_m reported by Rabinowicz (see Table 2–3) suggest that $0.1 < \varepsilon_{AB}/\varepsilon_{AA} < 0.6$ or so is a reasonable range to simulate.

Table 2–3: Compatibility factors typical material pairs [26].

Materials	c_m	Materials	c_m
C – Ni	.5	Cu – Ti	.32
C – Ti	.32	Cu – Mo	.12
C – Cu	.2	Si – Ti	.32
Cu – Al	.5	Si – Pb	.12
Cu – Si	.32	Ti – Al	.5

2.3.2 Analysis of Relaxed System by MD Simulation

The model described in the previous part is expected to incur some error because it does not account for free surface relaxation and long range interactions, and the extent of the error can be tested by computing γ_A , γ_{AB} , and W_{AB} with MD simulations. The surface energy can be computed by removing the upper half of the system in Figure 2–1, thereby exposing a free surface of material A. The equation for the surface energy is

$$\gamma_A = \frac{1}{A_s}\left[\sum_{i=1}^{N}\sum_{j>i}^{N}\phi(r_{ij}) + \frac{1}{2}\sum_{i=1}^{N}\sum_{k=1}^{K}\phi(r_{ik})\right] - \frac{1}{A_s}N\phi_o, \tag{2.11}$$

where indices i and j only loop over the system atoms, $N = 1080$, and A_s is the horizontal area of the simulation cell. The second term inside the brackets accounts for the interaction of the system atoms with the border atoms (the index k loops over the total of $K = 360$ border atoms), where the factor of 1/2 is present on account of the pairwise assumption. The L–J potential function $\phi(r_{ij}$ or $r_{ik})$ is given by Eqn. (2.1), and ϕ_o denotes the potential energy per atom in a defect-free bulk crystal at the same temperature. A separate simulation of a fully periodic homogeneous crystal gives $\phi_o/\varepsilon_{AA} = -6.56$ at $T = 291$ K. Eqn. (2.11) does not account for the kinetic energy of the system, which is constant under the isothermal conditions imposed on the system and consequently does not affect the surface energy. It is further noted that Eqn. (2.11) is the "instantaneous" surface energy, and the average is computed over 50,000 time steps to obtain the equilibrium value.

The result of the free surface simulation is given in Table 2–4, where it can be seen that the computed energy of the relaxed surface is 8% greater than the prediction of the unrelaxed model given by Eqn. (2.7). Generally, the unrelaxed assumption leads to an overprediction

of γ_A , while the neglect of distant neighbors leads to an underprediction. Thus, it can be concluded that neglecting the distant neighbors is a more costly approximation than ignoring the surface relaxation. Still, the rigid model appears to agree sufficiently well with the MD simulations. Table 2–4 also indicates that the surface energy predictions are significantly higher than the experimental value of copper, which suggests that the present L–J parameters may have too deep of a potential well, although it may also be noted that the source of the experimental data also cites a ±25% error.

Table 2–4: Surface energy of copper. MD simulation conducted at 291 K and zero pressure using the L–J parameters in Table 2–2 (A–A only) for 50,000 time steps. Experimental data is reported to have been obtained in an inert environment at the melting point.

	Surface energy ($\varepsilon_{AA}/\sigma^2$)	Surface energy (J/m^2)
MD simulation	1.83	2.24
Unrelaxed model (Eqn. (2.7))	1.7	2.08
Experimental data [26]	–	1.1

The interfacial energy is calculated next by simulating the full system (A+B) shown in Figure 2–1 and using the following equation:

$$\gamma_{AB} = \frac{1}{A_s}\left[\sum_{i=1}^{N}\sum_{j>i}^{N}\phi(r_{ij}) + \frac{1}{2}\sum_{i=1}^{N}\sum_{k=1}^{K}\phi(r_{ik})\right] - \frac{1}{A_s}N\phi_o, \tag{2.12}$$

which is exactly the same as Eqn. (2.11), except that $N = 2160$ and $K = 720$ border atoms (360 upper + 360 lower). As before, $\phi_o/\varepsilon_{AA} = -6.56$. Simulations are done at 291 K and zero pressure over 50,000 time steps for a range of ε_{AB} values while keeping ε_{AA} constant. The results in Figure 2–2 show that the unrelaxed model tends to underpredict the interface energy, which is again, attributable to the neglect of the distant neighbors. The work of adhesion, computed by Eqn. (2.5), and the compatibility factor, computed by Eqn. (2.6), also compare favorably to the unrelaxed model, as shown in Figures 2–3 and 2–4.

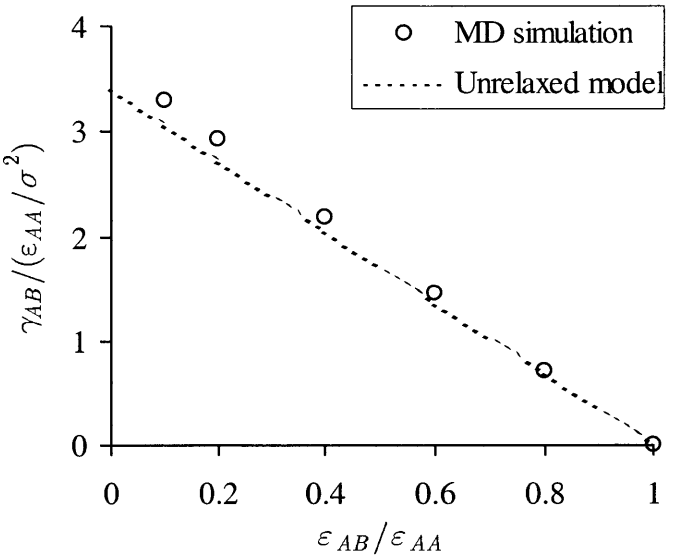

Figure 2–2: Interface energy calculated by unrelaxed model and MD simulations.

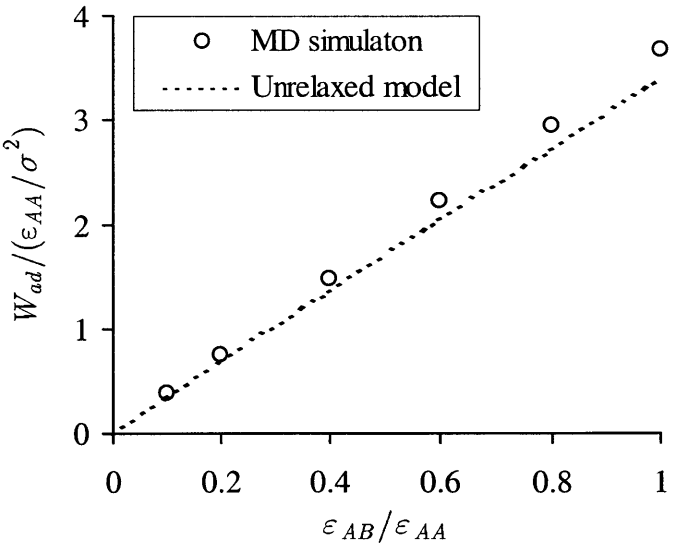

Figure 2–3: Work of adhesion calculated by unrelaxed model and MD simulations.

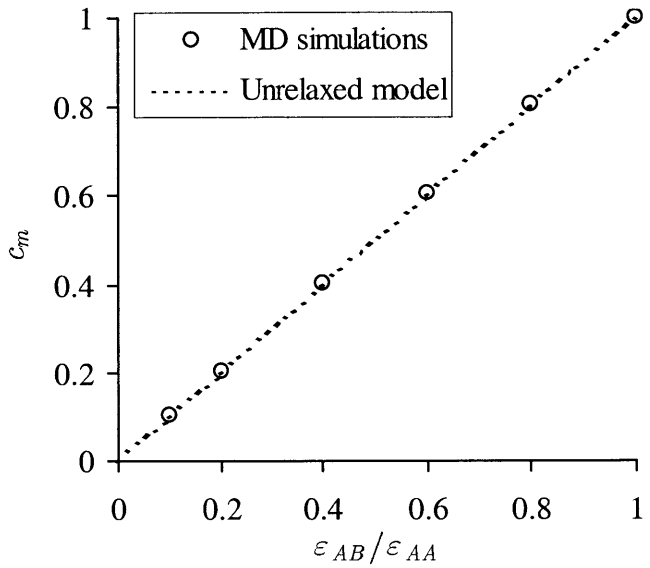

Figure 2–4: Compatibility factor calculated by unrelaxed model and MD simulations.

2.4 Simulation of Sliding in Frictional Regime

2.4.1 Loading and Sliding

This first sliding simulation is done with a moderately strong interface, $\varepsilon_{AB}/\varepsilon_{AA} = 0.4$. The system is first simulated for 20,000 steps under zero stress, then subject to a 300 MPa compressive uniaxial stress in the z direction as described in Section 2.2.4, after which 20,000 more steps are given for equilibration under the load. The simulation cell responds to the load with normal strains of 0.00012, 0.00005, and -0.00058 in the x, y, and z directions, respectively. Note that the horizontal strains are not equal due to the structural anisotropy. The resulting approximation of Young's modulus is 517 GPa, which is almost five times the experimental value of copper. One reason for the discrepancy is that the compression in the simulation is perpendicular to the close packed plane, resulting in a far stiffer elastic response compared to the isotropic behavior captured in experiments. Another cause of the discrepancy is that the potential function used in this study, which was already seen to significantly overpredict the surface energy, may have too deep of a potential well, which has the effect of overestimating the elastic modulus.

Next, sliding is imposed through incremental displacements of the upper border, as explained in Section 2.2.4. Figure 2–5 shows the displacement of each layer, computed by averaging the displacement in the sliding direction of all atoms in each layer. It is evident that the topmost layer (18) moves with the top border while the lowest layer (1) stays in place. Initially, all layers move smoothly in the sliding direction, and it appears that the system as a whole is undergoing a uniform shear strain. Then occurs the first slip, clearly between the interfacial layers (9 and 10), at $s/b = 0.57$ ($b = .256$ nm is the lattice period in x), followed by another slip at $s/b = 0.89$. The slips appear to be very sudden separations between layers 9 and 10 in the x direction. They also involve relative motion in the transverse (y) direction, as shown by Figure 2–6, which means that the sliding follows a zigzag pattern. This is confirmed by the snapshots of the interface in Figure 2–7, where it is evident that the atoms choose the zigzag path in order to jump from one close packed structure to another, namely from the initial FCC structure to a HCP structure (locally at the interface, resulting in a stacking fault), and then back to the FCC structure. Strictly speaking, an *unstressed* stacking fault is never achieved because, by the time the interface slips into the stacking fault formation, the position of the upper border is already at $s/b = 0.57$, whereas the unstressed fault requires that $s/b = 0.5$. Also, y–z shear strains develop in the system while forming the stacking fault because the borders are constrained from moving in the y direction. In the end, layers 1 – 9 return to their original positions while layers 10 – 18 all move by a full lattice spacing. These results demonstrate that the sliding is a sequence of abrupt slip events rather than a smooth, continuous process.

Figure 2–8 illustrates how the dimensions of the simulation cell vary during sliding in order to maintain the normal stresses at $\tau_{xx} = \tau_{yy} = 0$ and $\tau_{zz} = -300$ MPa. The cell expands in x abruptly at the instant of the first slip and contracts just as rapidly at the second slip. The opposite occurs in the y direction, with the contraction first and then the expansion. The cell distortion overlaps with the formation of the stacking fault, which is an odd coincidence since the stacking fault should not result in a cell distortion. The distortion may be a consequence of the y–z shear strain that the system sustains in achieving the stacking fault. In the z-direction, the simulation cell expands initially and suddenly comes down whenever the slips occur, which is intuitive since, at the time of the slips, the interfacial atoms are collapsing into a close-packed configuration. All of the dimensional variations in Figure 2–8 are less than 0.3% of the initial values.

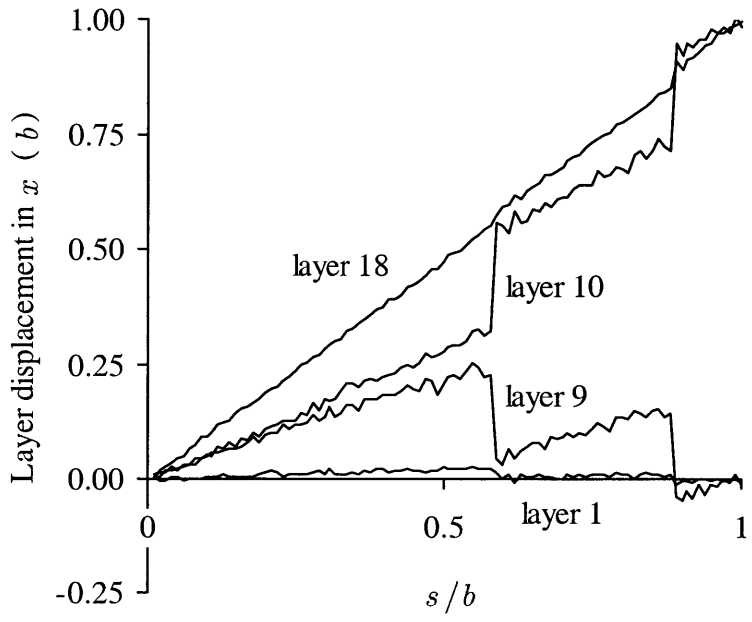

Figure 2–5: Layer-by-layer sliding displacement for $\varepsilon_{AB}/\varepsilon_{AA} = 0.4$ system.

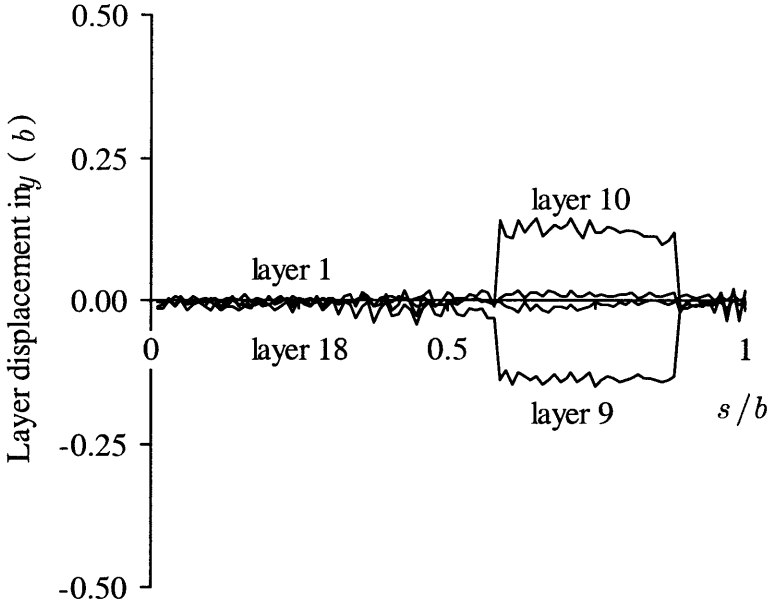

Figure 2–6: Layer-by-layer transverse displacement for $\varepsilon_{AB}/\varepsilon_{AA} = 0.4$ system.

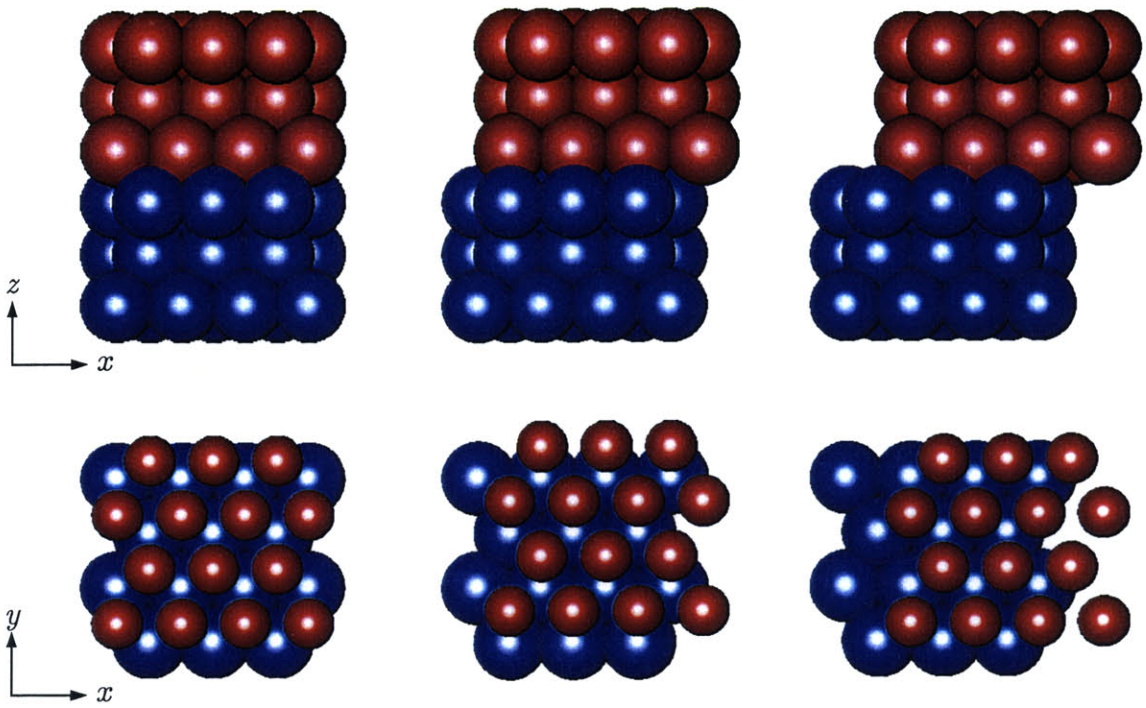

(a) $s/b = 0$ (b) $s/b = 0.6$ (c) $s/b = 1$

Figure 2–7: Snapshots of interface region during sliding of $\varepsilon_{AB}/\varepsilon_{AA} = 0.4$ system. Blue spheres are A atoms and red spheres are B atoms. In the bottom row, the red atoms are drawn smaller only to clearly show the underlying lattice structure of surface A. This figure only shows a sample portion of the interface, but the remainder of the interface behaves uniformly. Graphics are produced by VMD [34].

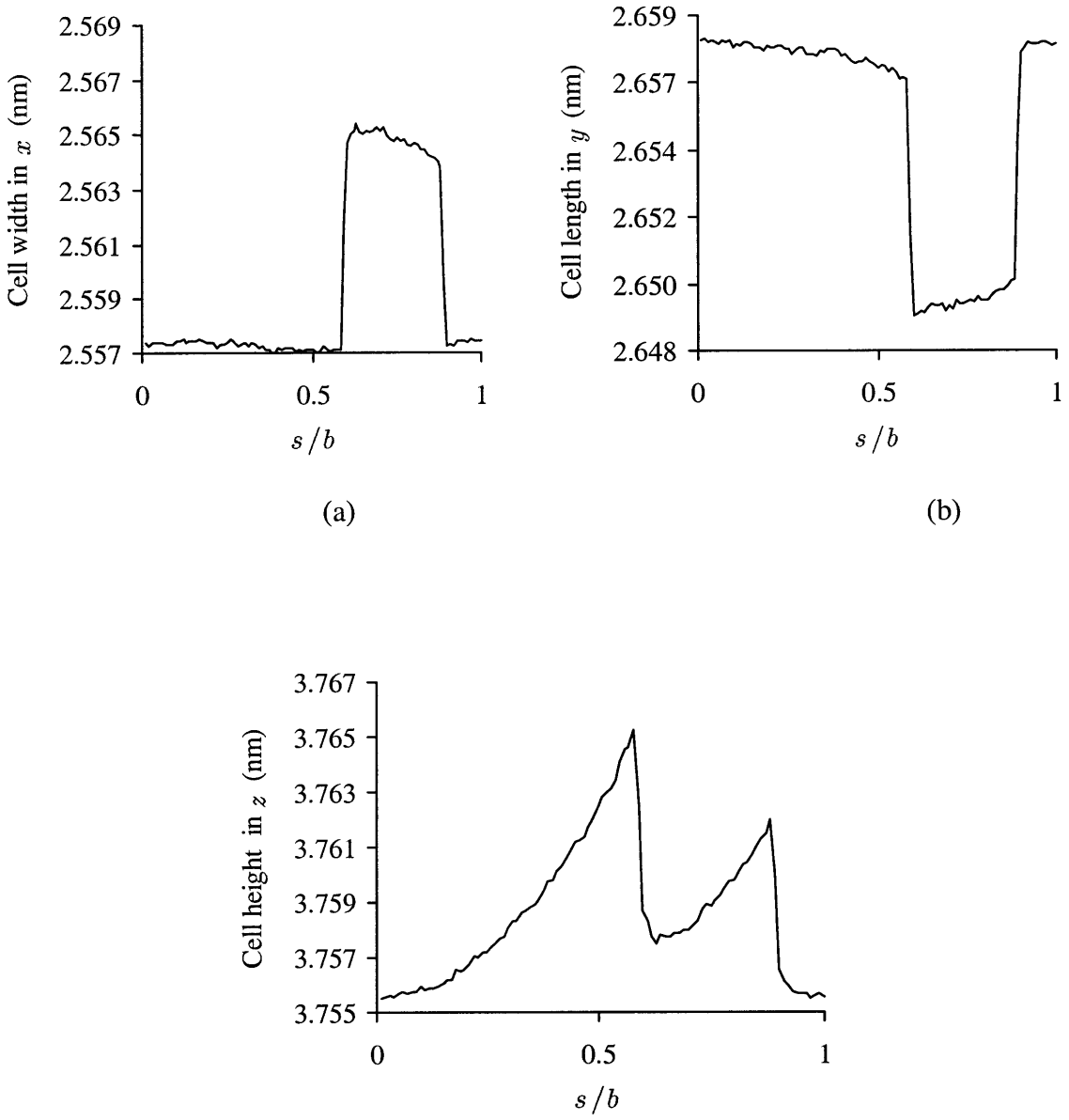

Figure 2–8: Variation of cell dimensions during sliding of $\varepsilon_{AB}/\varepsilon_{AA} = 0.4$ system. (a) cell width (x dimension) (b) cell length (y dimension) (c) cell height (z dimension).

2.4.2 Jump Phenomena

In all past atomistic models with conservative interatomic potential functions, only the jump phenomena have been identified as a legitimate mechanism of friction. A jump phenomenon is the process by which a system in an unstable configuration undergoes a catastrophic transition to a stable configuration [7–9]. Prior to the jump, the system is said to have some stored potential energy, which may be interpreted as strain energy from work done to the system while moving the boundary. During the jump, the atoms "fly" to the new equilibrium positions with heightened velocity, which is the manifestation of the conversion of the stored potential energy into kinetic energy. Thus, a jump phenomenon is essentially an atomic-scale mechanism by which potential energy is converted into kinetic energy, or heat. A number of elements are necessary for a model to exhibit jump phenomena. First, the model must have the capability of storing potential energy, which generally means that it must possess elastic properties. For this reason, a rigid sliding system cannot possibly produce a jump phenomenon. Second, a potential-to-kinetic energy conversion must be possible, which signifies that a system of dynamic particles is the ideal model. Third, an unstable configuration must be encountered sometime during the sliding process, at which point there must also be a stable configuration available for the system to jump to. The instability usually occurs at the slip plane and involves the breaking of bonds between the interfacial atoms. An interfacial bond breaks when the interatomic separation reaches the limit of stability of the potential function. In the L–J potential, for example, this limit is the inflection point which occurs at $r/\sigma = (26/7)^{1/6}$.

A jump phenomenon is identifiable most easily by a sudden drop in the potential energy vs. sliding distance curve, or more formally, where $d\Phi/ds \rightarrow -\infty$ (it never *equals* $-\infty$ for a classic dynamical system). It is easier to detect such a sudden change in the potential energy if Φ does not contain fluctuations from thermal effects. For this reason, the potential energy curve shown in Figure 2–9, represents the average over the 5000 equilibration steps following each sliding increment, effectively averaging out the fluctuations (see Section 2.2.5 and Eqn. (2.4)). Jump phenomena are clearly visible at $s/b = 0.57$ and 0.89, coinciding with the sudden slip events observed in the layer displacement curves. The non-jump portions of the potential energy curve appear to be continuous and concave up, suggestive of elastic shear loading. It is during this shearing process that the work done in moving the upper border accumulates in the system in the form of potential energy. The stored potential energy is released as kinetic energy with each jump phenomenon, whereupon this newly acquired kinetic energy is immediately extracted from the system by the velocity rescaling scheme. By the end of a full sliding period, the potential energy comes back to the initial

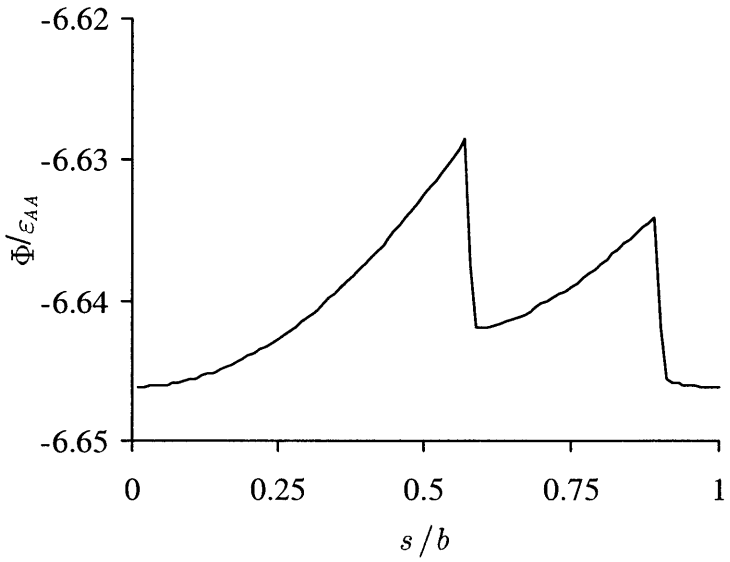

Figure 2–9: Potential energy during sliding of $\varepsilon_{AB}/\varepsilon_{AA} = 0.4$ system.

state. Meanwhile, the kinetic energy is kept constant (except for the two instances just after the occurrence of jumps), so that the total energy (potential+kinetic), which can be viewed as the internal energy in the thermodynamic sense, also returns to the initial state. Therefore, the sliding can be viewed as a cycle, but not an irreversible cycle because the kinetic energy taken out after each jump phenomenon is equivalent to heat dissipated out of the system, meaning that energy is consumed during the cycle. The amount of heat taken out, which is equal to the work done to the system through the moving boundary, can be interpreted as the frictional work. In the next part, some key issues concerning the computation of friction are discussed.

2.4.3 Sliding Resistance and Friction

The sliding resistance, calculated by the method described in Section 2.2.5, is shown in Figure 2–10. The sliding resistance exhibits sharp drops at exactly the same locations as the sudden drops in the potential energy curve (Figure 2–9), demonstrating that the release of potential energy during a jump phenomenon is accompanied by a release of shear stress (it may be recalled that the sliding resistance is nothing more than the average of the internal shear stress τ_{xz}). During the earlier examination of the potential energy curve, it was suggested that the non-jump portions of sliding may be interpreted as elastic loading

processes. These portions appear as linear segments in the resistance curve, indicating that the loading is, in fact, *linearly* elastic to a good approximation. The Hookean behavior exhibited by this material is attributable to the fact that the L–J potential near its valley is well-represented by a harmonic potential. Based on the evidence presented so far, the sliding resistance curve may be interpreted as a sequence of shear loading curves interrupted by jump phenomena. After a jump phenomenon, loading resumes along the "new" loading curve until another jump is encountered. The work done to the system through the upper border is equal to the net area under the loading curves. Figure 2–11 shows the normal component of the internal stress throughout sliding, confirming that the present boundary conditions are indeed successful at maintaining a constant normal stress of 300 MPa.

It may be recalled that sliding occurs by FCC–HCP–FCC transitions of the local interfacial structure. Each elastic loading curve in Figure 2–10 has a unique "reference", or zero-stress state, and each reference may be identified with one of the stable interfacial structures. The first loading curve (segment 'a–b') is referenced at $s = 0$, which corresponds to the initial FCC interfacial structure, such that it may be referred to as an "FCC loading curve", for convenience. Likewise, the last loading curve (segment 'e–f') is another FCC loading curve, different from the initial one by a full sliding period. The middle loading curve (segment 'c–d') starts at a non-zero stress, but the extrapolation to zero stress is at $s/b = 0.5$, indicating that the reference of this particular loading curve corresponds to the HCP interfacial configuration. It may be noted that the peak resistance of the HCP loading curve is 33% lower than the FCC loading curve, mostly due to the fact that the HCP structure is never fully achieved because the finite borders are constrained from moving in the y direction.

Despite the vast literature on MD modeling of atomic friction, there is not an agreed definition of friction or the friction coefficient at the atomic scale. In most of these simulations, the sliding resistance typically exhibits periodic behavior with peaks and valleys, as in Figure 2–10, for example. The mean value of the resistance has been taken to be the friction by some [10–12,16–18], while others have opted to use the peak resistance [6]. Still, others have chosen to consider the average of only the positive portions of the resistance [31]. The difference in value from one approach to another can be quite considerable, and an order-of-magnitude discrepancy is not uncommon due to the fact that the valleys of the resistance curve are often comparable to the hills. It is important, therefore, to adopt a proper definition for friction for the present study, which is done through the following observations and interpretations.

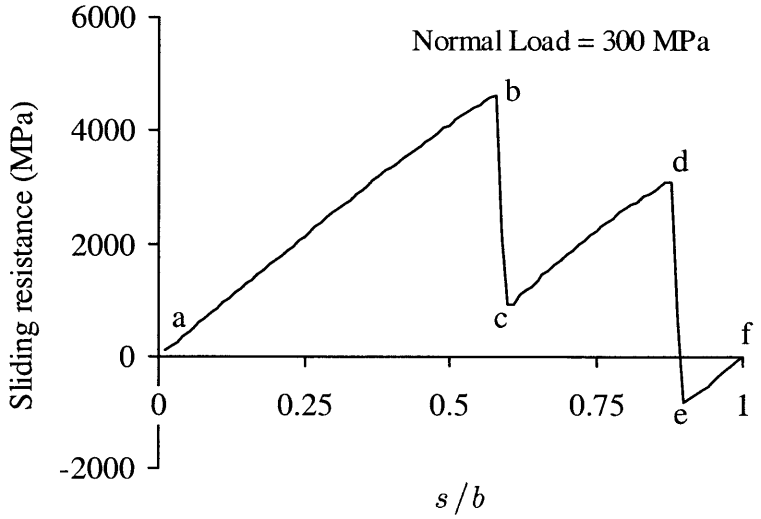

Figure 2–10: Sliding resistance of $\varepsilon_{AB}/\varepsilon_{AA} = 0.4$ system.

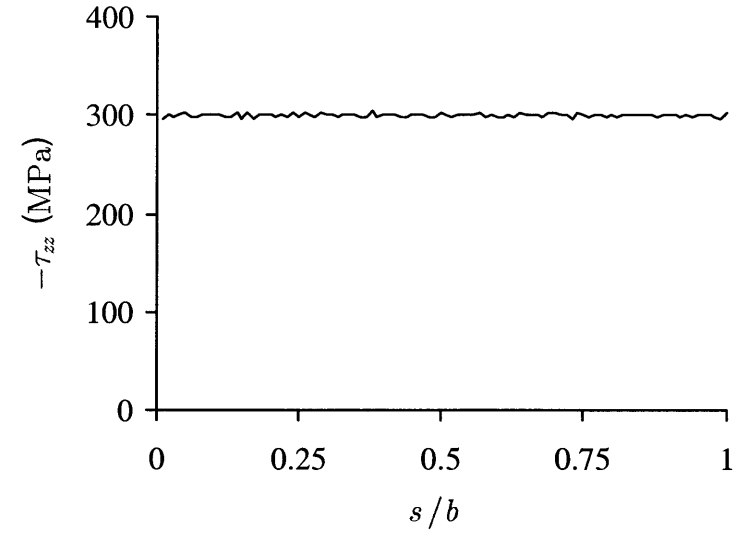

Figure 2–11: Normal stress during sliding of $\varepsilon_{AB}/\varepsilon_{AA} = 0.4$ system.

1. The resistance curve may be understood as a series of shear loading curves separated by jump transitions. Therefore, it is inappropriate to regard the resistance curve as an "instantaneous" friction curve, since most segments of the resistance curve are best interpreted as elastic stress-strain curves, and friction and elastic loading are fundamentally incompatible processes based on thermodynamic reversibility considerations. The concept of instantaneous friction is valid at the macroscale, but at the atomic scale, friction cannot be defined in the instantaneous sense. This point should be noted especially as a warning against referring to some parts of the resistance curve as "negative friction".

2. Sliding is periodic in this system, meaning that all state properties of the system such as the configuration, energy, stress return to the initial values after a unit distance of sliding, b, as a consequence of the repeatability of the interfacial structure, which comes from having used a symmetric and commensurate sliding plane. In such cases, the integral of the resistance-distance curve over a period is equal to the net work done (per unit area), which can be considered as the "frictional work". The frictional work divided by the distance of sliding (which is equivalent to the mean resistance), can then be interpreted as the *average* kinetic friction over that sliding span, or it may just as well be considered as kinetic friction, without the "average" prefix. It may also be noted that in this work, "friction" generally refers to kinetic friction.

3. The peak value of the sliding resistance is often regarded as the static friction. This is consistent with the macroscopic definition of the static friction as the force required to initiate motion. Analogously, the peak resistance is the stress required to activate the slip. However, the macroscopic version of static friction is more closely tied to the shear strength of the asperities because friction is classically understood only in the context of deformation. Therefore, even if the peak resistance is a reasonable analog of the static friction, the connection between the atomic scale and macroscale should be made with some discretion.

4. The concept of the *friction coefficient* (μ = friction/load) is somewhat ambiguous in the MD environment. At the macroscale, μ is independent of most extrinsic parameters such as the *apparent* contact area and applied normal load, mainly because the *real* contact area is said to be independent of the apparent area and grows proportionately with the normal load [26]. The growth of the real area in response to the normal load is a consequence of the plastic flow of the asperities in contact. In contrast, the MD material, free of such structural defects as dislocations, is not prone to yielding and consequently, does not respond to a normal load with an increase in the contact area. Rather, the

contact area is independent of the load, aside from a minor expansion associated with the Poisson effect. Therefore, μ is a function of the load and does not reflect only the intrinsic frictional properties of the sliding system. Still, the friction coefficient is presented in this work in order to make first-order comparisons to experimental values. It may be noted that the normal load used in this work has been deliberately chosen to be the yield strength of copper, in order to achieve consistency between the simulation and experiments.

Based on the above definitions, the friction in the present simulation is 2009 MPa, and the friction coefficient is 6.7. The static friction coefficient is 15.3. A friction coefficient of 6.7 is much bigger than the typical experimental value of 0.5–1.8 for copper-on-copper sliding [32], but experiments are often affected by surface contamination, which has a tendency to lower friction. In experiments conducted in controlled environments, a friction coefficient as high as 4.8 was measured between clean surfaces of copper, and similar figures were also obtained for other metals such as nickel, tungsten, and gold, including non-matching pairs (for example, $\mu = 6.0$ for nickel on tungsten) [33]. Another reason that the simulated friction coefficient is high is that the model interface is defect-free and commensurate, which offers the ideal resistance to shear.

2.5 Simulation of Sliding in Frictionless Regime

For the next simulation, the interface is weakened to $\varepsilon_{AB}/\varepsilon_{AA} = 0.1$. Loading and sliding is done in the same manner as in the previous simulation. The layer displacements shown in Figure 2–12 show that rapid slips associated with the jump phenomena no longer occur. The transverse displacements in Figure 2–13 show that the interface still slides via the zigzag path, which indicates that the stacking fault is achieved in the middle of sliding. This is also confirmed by interface snapshots, which are not shown here. The potential energy curve in Figure 2–14 has three local minima at the start, middle, and end of sliding, which obviously correspond to the FCC, HCP, and FCC interfacial structures. The potential energy at the midpoint ($s/b = 0.5$) has a higher energy than the end states as a consequence of the stacking fault in addition to the elastic energy from the y–z shear strain. At some portions of the resistance curve where $d\Phi/ds < 0$, the upper border is in an unstable position, and the only reason that it does not move to a more stable location is that its motion is constrained. Had the sliding been invoked by a *force* boundary condition instead of the *displacement* boundary

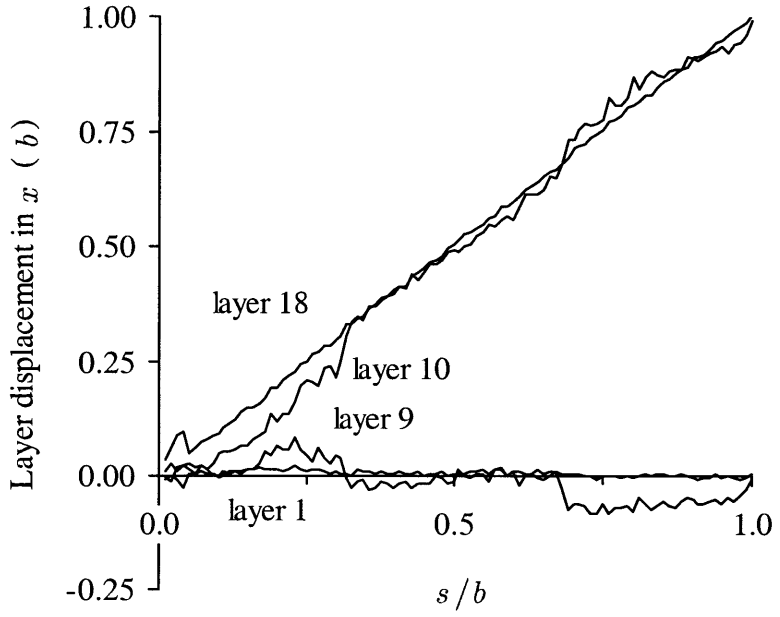

Figure 2–12: Layer-by-layer sliding displacement for $\varepsilon_{AB}/\varepsilon_{AA} = 0.1$ system.

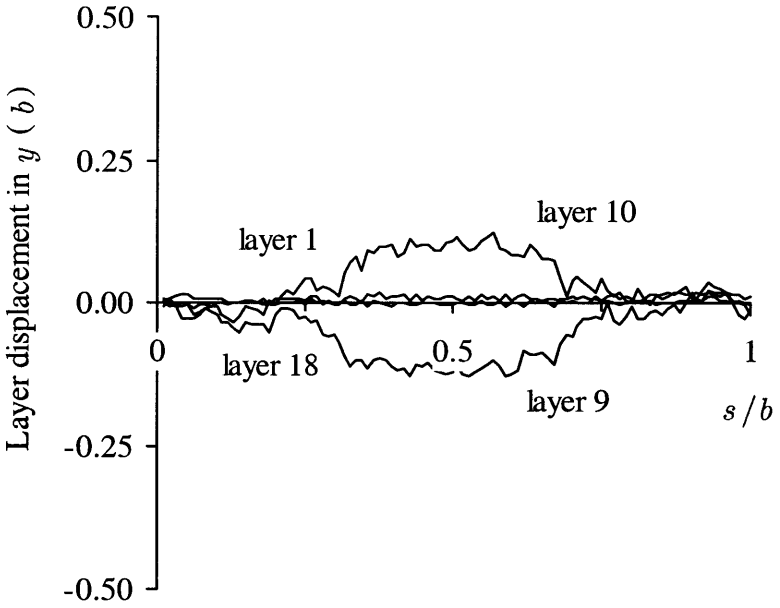

Figure 2–13: Layer-by-layer transverse displacement for $\varepsilon_{AB}/\varepsilon_{AA} = 0.1$ system.

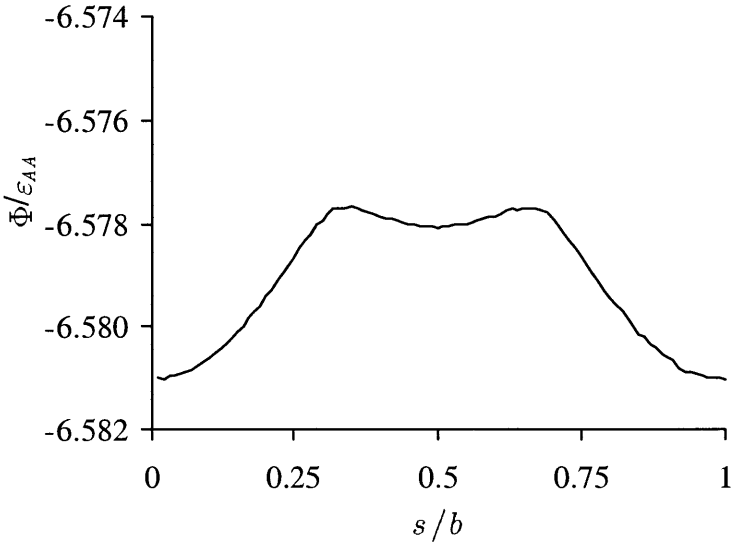

Figure 2–14: Potential energy during sliding of $\varepsilon_{AB}/\varepsilon_{AA} = 0.1$ system.

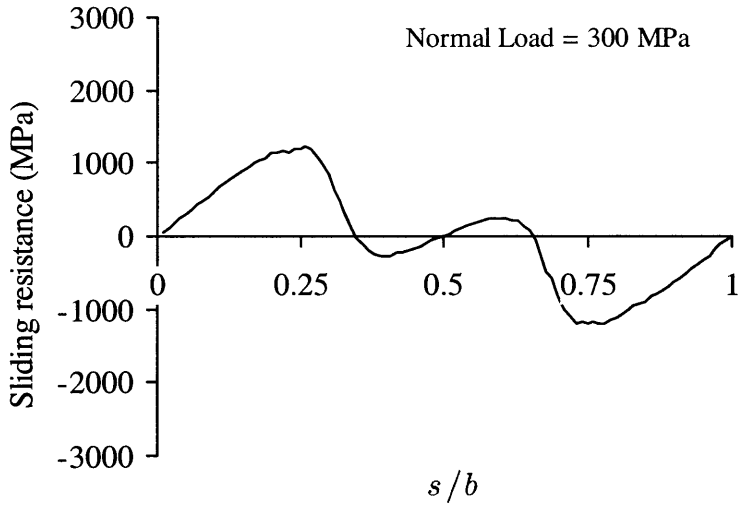

Figure 2–15: Sliding resistance of $\varepsilon_{AB}/\varepsilon_{AA} = 0.1$ system.

condition, the border would not stay in an unstable location for such prolonged periods, and the time history of the sliding process would be markedly different.

The potential energy curve appears to be continuous without any sudden drops, indicating that this sliding simulation is free of jump phenomena, and leading to the conclusion that the present case is one of frictionless sliding. This is confirmed by the sliding resistance in Figure 2–15, where the friction (i.e., average resistance) is 2.7 MPa, which is small enough to be attributable to "statistical noise" from a lack of averaging. It may be recalled that the resistance is computed by averaging τ_{xz} (see Eqn. (2.2)) over the 5000 steps equilibration period following each sliding increment. The averaging effectively removes most, but not all, of the thermal fluctuations, and the stress calculations may be interpreted with about a ± 10 MPa accuracy. The confidence in asserting zero friction in this simulation comes from the fact that jump phenomena are not observed, and the friction calculation supports this conclusion within acceptable limits.

Significant portions of the sliding resistance is negative-valued in Figure 2–15. As stated in Section 2.4.3, this should not be considered as negative friction, which would constitute a clear violation of the second law of thermodynamics. On the contrary, the negative resistance has a valid physical explanation. Sliding may be imagined as a sequence of the interfacial atoms going through hills and valleys of the potential energy landscape, with the valleys corresponding to the stable structures (namely, FCC, HCP) and the hills being associated with the saddle configurations. A negative resistance occurs when the atoms are in the process of sliding down a hill (i.e., $d\Phi/ds < 0$), analogous to pulling back on a roller coaster in order to keep it from accelerating downhill. The resistance curve is antisymmetric about the midpoint ($s/b = 0.5$), which is typical for periodic sliding without any jump phenomena. Finally, it may be noted that even though the average resistance is zero, the peak value is significant at 1214 MPa, which presents a rather peculiar situation where the kinetic friction is zero but the static friction is considerable.

2.6 Friction Summary

In addition to the cases $\varepsilon_{AB}/\varepsilon_{AA} = 0.1$ and 0.4 presented in the preceding sections, several additional sliding simulations have been conducted at various values of $\varepsilon_{AB}/\varepsilon_{AA}$. The sliding resistance curves from these simulations are collectively displayed in Figure 2–16, where the familiar sawtooth pattern is prominent. It may be pointed out that the sawtooth pattern has also been observed in many friction force microscope experiments [2,3,5]. In Figure 2–17, the peak resistance $\hat{\tau}$, which is related to the static friction, appears

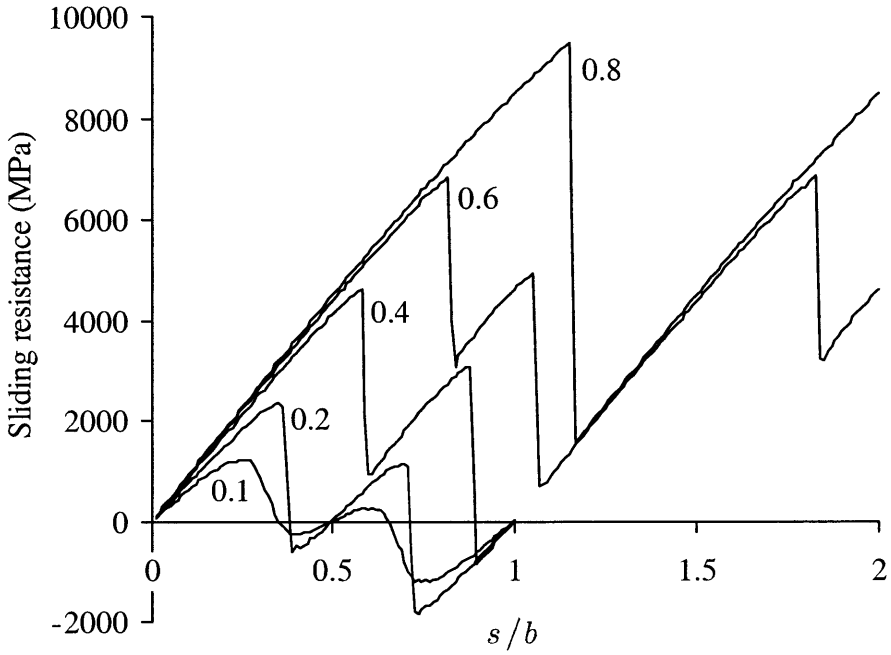

Figure 2–16: Sliding resistance curves. The number next to each curve refers to the value of $\varepsilon_{AB}/\varepsilon_{AA}$.

to be proportional to $\varepsilon_{AB}/\varepsilon_{AA}$. (Strictly speaking, the better interpretation is that $\hat{\tau}$ increases proportionately with only ε_{AB}, since ε_{AA} is kept constant.) A linear relationship between $\hat{\tau}$ and ε_{AB} is intuitive since the peak resistance is related to the "breaking" force of the A–B bonds, and the breaking force of a L–J bond is given by $-d\phi/dr$ at $r=(26/7)^{1/6}\sigma$ (the inflection point), which equals $2.4(\varepsilon_{AB}/\sigma)$. This is for a single bond only, but the addition of multiple bonds only changes the scaling factor since the forces are additive, and the result is that the breaking force of the entire collection of interfacial bonds still scales linearly with ε_{AB}. In the next section, this relationship proves useful in the construction of a general scaling model for friction.

Figure 2–18 shows the relationship between friction and $\varepsilon_{AB}/\varepsilon_{AA}$, which may be best understood in terms of two distinct sliding regimes. The *frictional regime* is observed at relatively high $\varepsilon_{AB}/\varepsilon_{AA}$, and it is characterized by the occurrence of jump phenomena. The frictionless regime occurs at low values of $\varepsilon_{AB}/\varepsilon_{AA}$ and is marked by the absence of jump

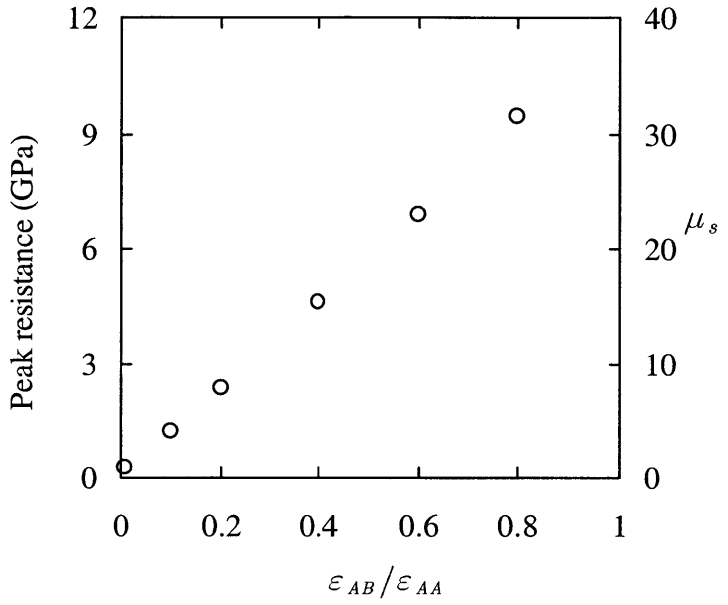

Figure 2–17: Peak sliding resistance versus $\varepsilon_{AB}/\varepsilon_{AA}$. The right-side ordinate is the static friction coefficient, μ_s.

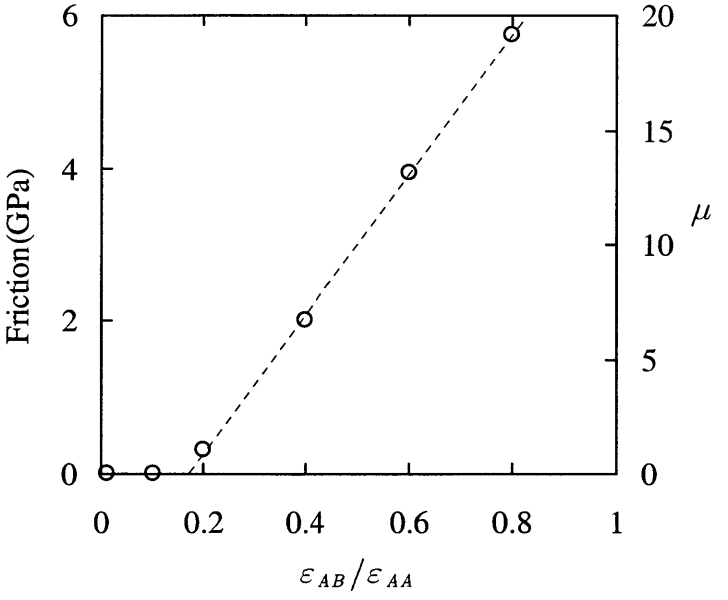

Figure 2–18: Friction (average sliding resistance) versus $\varepsilon_{AB}/\varepsilon_{AA}$. The dotted line is the linear fit through the frictional (i.e., the last four) data points. The right-side ordinate is the friction coefficient, μ, defined as the friction divided by the normal load of 300 MPa.

phenomena, resulting in an antisymmetric resistance curve and zero friction, at least to within the statistical noise level. By visual inspection, a linear relationship seems to exist between friction and $\varepsilon_{AB}/\varepsilon_{AA}$ in the frictional regime (this is evaluated in more detail by a scaling model in the next section), in which case the transition between frictional and frictionless sliding can be identified by drawing a linear fit through the frictional data points ($\varepsilon_{AB}/\varepsilon_{AA} =$ 0.2 through 0.8). In doing so, it is observed that the transition occurs approximately at $\varepsilon_{AB}/\varepsilon_{AA} = 0.17$, where the trendline crosses the abscissa.

2.7 Scaling Model

With the understanding of the sliding mechanism acquired through the simulations, it is possible to construct a scaling model in terms of the relevant input parameters so that the results can be generalized to any L–J material. It has been established that the mechanism of frictional sliding can be viewed as a sequence of elastic loading processes interrupted by jump phenomena from one loading curve to another. Figure 2–19 illustrates a schematic of a typical sliding resistance curve over one sliding period containing all the critical elements of frictional sliding, with three unique elastic loading curves represented by linear segments of identical slope, and two jump phenomena represented by vertical drops. In constructing the resistance curve in this way, a number of important assumptions have already been made. First, the resistance curve pertains only to sliding on the (111) plane, with the first and final loading curves (segments 'a–b' and 'e–f', respectively) representing FCC loading curves (i.e., the reference, or the zero-stress state, corresponds to the FCC interfacial structure) and the middle loading curve (segment 'c–d') representing the HCP loading curve. Second, the elastic loading has been assumed to be linear. Third, the peak resistance associated with the HCP loading curve is assumed to be the same as the peak resistance of the FCC loading curve, even though Figure 2–10 clearly shows that they are not equal. This assumption is made because it simplifies the model without excessively compromising accuracy nor generality.

Friction F (per unit area) is equal to the shaded area in Figure 2–19 divided by b, and a simple geometric analysis yields

$$F = \hat{\tau} - \frac{1}{4}kb\,, \tag{2.13}$$

where $\hat{\tau}$ is the peak resistance and k is the slope of the loading curve, which is the shear stiffness per unit area. The next task is to relate the parameters that appear in Eqn. (2.13) to

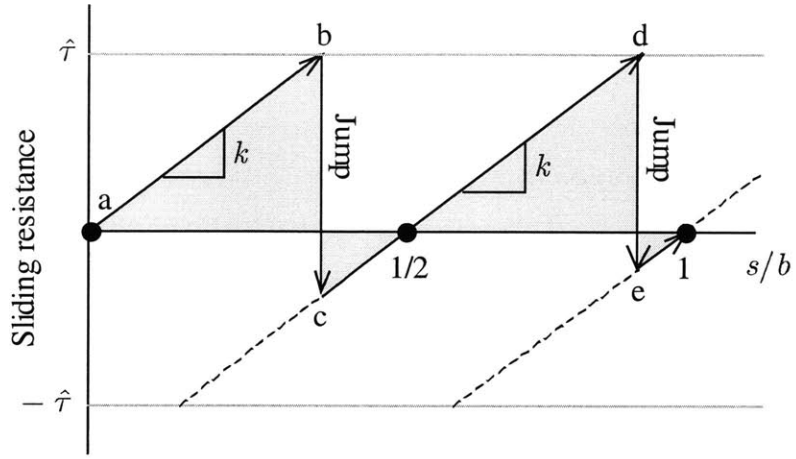

Figure 2–19: Schematic sliding resistance curve.

the L–J parameters ε_{AB} , ε_{AA} , and σ. In Section 2.6, the peak resistance was shown to be proportional to ε_{AB} , so that

$$\hat{\tau} = \alpha \frac{\varepsilon_{AB}}{\sigma^3}, \tag{2.14}$$

where α is a dimensionless geometric factor specific to the structure of the shear plane, and σ^3 is the proper normalization for dimensional consistency. A value for α can be obtained by computing the slope of the linear fit through the data in Figure 2–17, which yields $\alpha = 2.2$.

The analytical expression for k requires more effort to obtain because k is essentially the *composite* stiffness of a multi-layered system. Referring back to Figure 2–1, the system is arranged into 18 atomic layers. In the context of defining the composite stiffness, it is beneficial to view the system as a one-dimensional series of nodes connected by springs, with each node representing a layer. The springs may be assumed to behave linearly, in which case the system may be further simplified as a series of three springs, spring A for material A, spring A–B for the interface, and spring B for material B, connected in that order. The composite stiffness is given by the relation,

$$\frac{1}{k} = \frac{1}{k_A} + \frac{1}{k_B} + \frac{1}{k_{AB}}, \tag{2.15}$$

where it may be noted that the k's actually represent the stiffness per unit area, in recognizing that the MD system has an infinitely repeating interface. The stiffness of A can be expressed as $k_A = G_A/h_A$, where G_A is the shear modulus and h_A is the "height" of material A. Likewise, $k_B = G_B/h_B$ and $k_{AB} = G_{AB}/h_{AB}$. The height of the interface can be approximated as the interlayer distance of adjacent (111) planes in a hard-sphere structure which, given that the hard-sphere diameter is assumed to be equal to $2^{1/6}\sigma$, gives $h_{AB} = \gamma\sigma$, where $\gamma = 2^{2/3}/3^{1/2} = 0.92$. The heights of materials A and B are identical, and each is equal to one-half the total height of the cell minus one-half the interface height, $h_A = h_B = (h-\gamma\sigma)/2$, where h is the total height of the cell. The shear moduli (G_A , G_B , G_{AB}) all apply specifically to shear on the (111) plane in the $[\bar{1}10]$ direction. Note also that the presence of the compressive normal load is completely ignored here, a sacrifice of little significance considering that the shear modulus is generally insensitive to load. The shear modulus is an intrinsic property of the material and is independent of the boundary conditions and the cell dimensions, and for a L–J material, $G_A = G_A(\varepsilon_{AA}, \sigma)$ and $G_{AB} = G_{AB}(\varepsilon_{AB}, \sigma)$. Since $\varepsilon_{BB} = \varepsilon_{AA}$, $G_B = G_A$, which also means that $k_B = k_A$. For L–J materials in general, all elastic moduli scale linearly with ε/σ^3 because the moduli are related to the second derivative of the potential function, which is proportional to ε/σ^3 by a constant dimensionless factor. Consequently, the shear moduli can be expressed as $G_A = \beta(\varepsilon_{AA}/\sigma^3)$ and $G_{AB} = \beta(\varepsilon_{AB}/\sigma^3)$ where β is the dimensionless factor, which has been found to be $\beta = 27.4$ through a separate simulation of a bulk L–J system (i.e., no interface) subject to simple shear on the (111) plane in the $[\bar{1}10]$ direction. The shear stiffness can be expressed in terms of the L–J parameters and h as

$$\begin{aligned} k_A = k_B &= \frac{2\beta}{h-\gamma\sigma}\left(\varepsilon_{AA}/\sigma^3\right) \\ k_{AB} &= \frac{\beta}{\gamma\sigma}\left(\varepsilon_{AB}/\sigma^3\right) \end{aligned}, \tag{2.16}$$

which can be combined with Eqn. (2.15) to give

$$k = k_o\left[\frac{1}{1+\frac{\gamma\sigma}{h}\left(\frac{1}{\varepsilon_{AB}/\varepsilon_{AA}}-1\right)}\right] \tag{2.17}$$

where

$$k_o = \beta \frac{\varepsilon_{AA}}{h\sigma^3} \tag{2.18}$$

is the stiffness of a system without an interface (i.e., $\varepsilon_{AB} = \varepsilon_{AA}$). Figure 2–20 shows that Eqn. (2.17) gives an excellent prediction of the simulated stiffness for a broad range of $\varepsilon_{AB}/\varepsilon_{AA}$ values.

Finally, combining Eqns. (2.13)–(2.17) yields the scaling model:

$$\frac{F}{\left(\varepsilon_{AA}/\sigma^3\right)} = \alpha \frac{\varepsilon_{AB}}{\varepsilon_{AA}} - \beta \frac{b}{4h}\left[\frac{1}{1+\frac{\gamma\sigma}{h}\left(\frac{1}{\varepsilon_{AB}/\varepsilon_{AA}}-1\right)}\right]. \tag{2.19}$$

Eqn. (2.19) demonstrates that the relationship between F and ε_{AB} approaches linearity only as $\varepsilon_{AB}/\varepsilon_{AA} \rightarrow 1$, but even at relatively low $\varepsilon_{AB}/\varepsilon_{AA}$ the relationship is close to linear if $h >> \sigma$, that is, if the simulation cell is sufficiently tall. Solving Eqn. (2.19) with $F = 0$ leads to the following expression for the critical ratio $(\varepsilon_{AB}/\varepsilon_{AA})^*$ corresponding to the transition from frictional to frictionless sliding,

$$\left(\varepsilon_{AB}/\varepsilon_{AA}\right)^* = \frac{b\beta}{4\alpha(h-\gamma\sigma)} - \frac{\gamma\sigma}{h-\gamma\sigma}. \tag{2.20}$$

Inserting $b = .256$ nm, $h = 3.76$ nm, $\alpha = 2.2$, $\beta = 27.4$, and $\gamma = 0.92$ into Eqn. (2.20) gives $(\varepsilon_{AB}/\varepsilon_{AA})^* = 0.165$, which is in excellent agreement with the value of 0.17 obtained from the linear fit through the simulation data in Figure 2–18. The scaling model is very effective overall, as shown by the comparison to simulated results in Figure 2–21.

2.8 Conclusions

Using novel boundary conditions that allow the simulation of sliding under uniaxial loading in a finite-border system, MD simulations are conducted to investigate friction in Lennard-Jones (111) surfaces. The relationship between friction and adhesion is investigated using the parameter $\varepsilon_{AB}/\varepsilon_{AA}$, which is a direct measure of the interfacial bond strength and is equivalent to the so-called compatibility factor, a macroscopic parameter which indicates the adhesiveness of two surfaces. The following are the key results from this work.

- Two regimes of sliding are observable depending on the degree of adhesion. For relatively high adhesion ($\varepsilon_{AB}/\varepsilon_{AA} > 0.17$), the sliding is *frictional* and exhibits *jump phenomena*. Below = 0.17, jump phenomena do not occur, and sliding is consequently

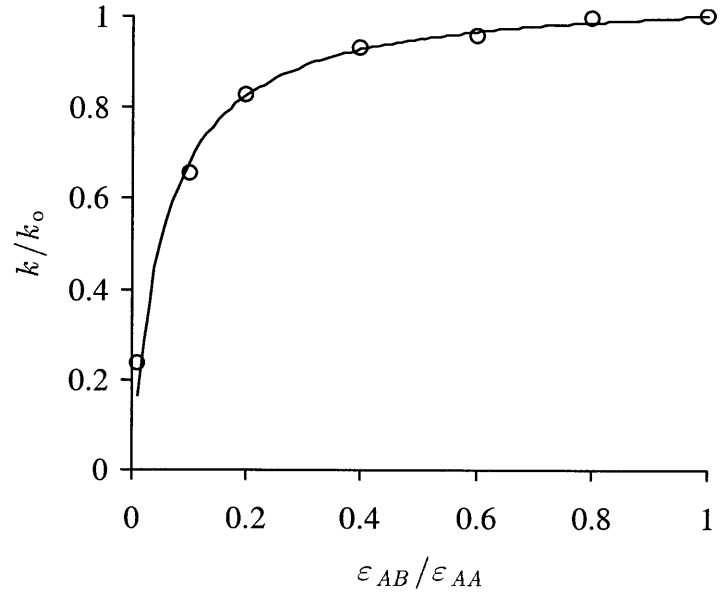

Figure 2–20: Shear stiffness versus $\varepsilon_{AB}/\varepsilon_{AA}$. Open circles are MD simulation results based on the initial slopes of the resistance curves in Figure 2–15. Solid line represents Eqn. (2.17).

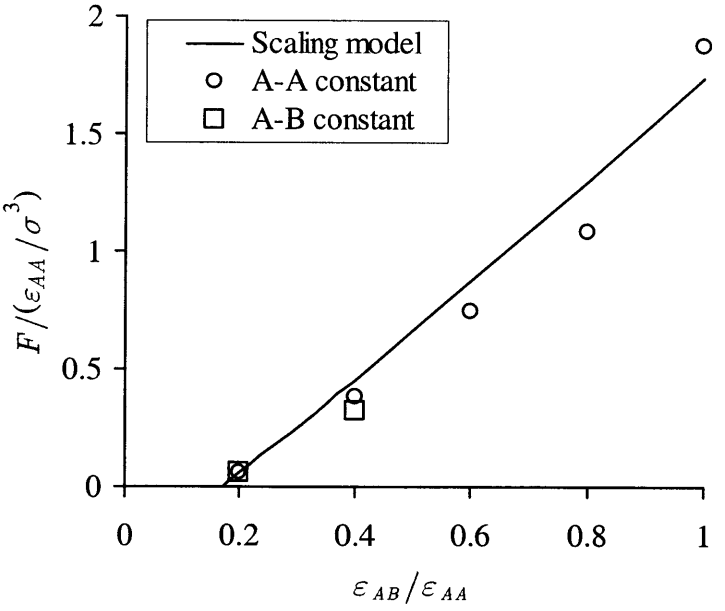

Figure 2–21: Comparison of scaling model and simulation data. "A-A constant" refers to simulations in which ε_{AA}/k_b is held fixed at 4733 K. "A-B" constant" refers to simulations in which ε_{AB}/k_b is held fixed at 473 K.

frictionless. In the frictional regime, the simulation results indicate that the friction-$\varepsilon_{AB}/\varepsilon_{AA}$ relationship is approximately linear, and this has also been confirmed by a scaling model.

- The peak sliding resistance, which is the atomic-scale analog of the static friction, is approximately proportional to ε_{AB}. The frictionless regime is characterized by a rather unusual scenario, in which the static friction is sizable but the kinetic friction is zero. This situation is unique to atomic-scale sliding models and comes from the fact that without jump phenomena, there is no kinetic friction even if static friction exists.
- The structural response of the interface to sliding is a sequence of FCC–HCP–FCC transitions. In the frictional regime, these transitions occur abruptly in conjunction with the jump phenomena, while in the frictionless regime, the transitions occur smoothly.

The results of this work show that friction in MD systems is sensitive to degree of adhesion between the surfaces, which suggests that a promising strategy for reducing friction is to minimize the interfacial interaction by choosing the proper combination of sliding materials with weak adhesion properties. This strategy may also be exploited by engineered surface treatment, with the intention of lowering the free surface energy, thus lowering the interfacial energy and adhesion.

2.9 References

1. Bhushan, B., Israelachvili, J.N., and Landman, U., "Nanotribology: Friction, Wear and Lubrication at the Atomic Scale," *Nature*, vol. 374, pp. 607-616, 1995.
2. Mate, C.M., McClelland, G.M., Erlandsson, R., and Chiang, S., "Atomic-Scale Friction of a Tungsten Tip on a Graphite Surface," *Physical Review Letters*, vol. 59, no. 17, pp. 1942-1945, 1987.
3. Erlandsson, R., Hadziioannou, G., Mate, C.M., McClelland, G.M., and Chiang, S., "Atomic Scale Friction Between the Muscovite Mica Cleavage Plane and a Tungsten Tip," *Journal of Chemical Physics*, vol. 89, no. 8, pp. 5190-5193, 1988.
4. Krim, J., Solina, D.H., and Chiarello, R., "Nanotribology of a Kr Monolayer: A Quartz-Crystal Microbalance Study of Atomic-Scale Friction," *Physical Review Letters*, vol. 66, no. 2, pp.181-184, 1991.
5. Ruan, J. and Bhushan, B., "Atomic-Scale and Microscale Friction Studies of Graphite and Diamond using Friction Force Microscopy," *Journal of Applied Physics*, vol. 76, no. 9, pp. 5022-5035, 1994.

6. Landman, U., Luedtke, W.D., and Ribarsky, M.W., "Structural and Dynamical Consequences of Interactions in Interfacial Systems," *Journal of Vacuum Science Technology A*, vol. 7, no. 4, pp. 2829-2839, 1989.

7. Tomlinson, G.A., "A Molecular Theory of Friction," *Philosophical Magazine*, eer. 7, vol. 7, no. 46, pp. 905-939, 1929.

8. Frenkel, Y.I. and Kontorova, "On the Theory of Plastic Deformation and Twinning," *T., Zh. Eksp. teor. Fiz.*, vol. 8, pp. 1340, 1938.

9. McClelland, G.M., "Friction at Weakly Interacting Interfaces," in Adhesion and Friction, Springer Series in Surface Sciences, vol. 17, Eds. Grunze, M. and Kreuzer, H.J., Springer Verlag, pp. 1-16, 1989.

10. Harrison, J.A., White, C.T., Colton, R.J., and Brenner, D.W., "Molecular-Dynamics Simulations of Atomic-Scale Friction of Diamond Surfaces," *Physical Review B*, vol. 46, no. 15, pp. 9700-9708, 1992.

11. Perry, M.D. and Harrison, J.A., "Friction Between Diamond Surfaces in the Presence of Small Third-Body Molecules," *Journal of Physical Chemistry B*, vol. 101, pp. 1364-1373, 1997.

12. Sørensen, M.R., Jacobsen, K.W., and Stoltze, P., "Simulations of Atomic-Scale Sliding Friction," *Physical Review B*, vol. 53, no. 4, pp. 2101-2113, 1996.

13. Buldum, A. and Ciraci, S., "Contact, Nanoindentation, and Sliding Friction," *Physical Review B*, vol. 57, no. 4, pp. 2468-2476, 1998.

14. Shimizu, J., Eda, H., Yoritsune, M., and Ohmura, E., "Molecular Dynamics Simulation of Friction on the Atomic Scale," *Nanotechnology*, vol. 9, pp. 118-123, 1998.

15. Thompson, P.A. and Robbins, M.O., "Origin of Stick-Slip Motion in Boundary Lubrication," *Science*, vol. 250, pp.792-794, 1990.

16. Glosli, J.N. and McClelland, G.M., "Molecular Dynamic Study of Sliding Friction of Ordered Organic Monolayers," *Physical Review Letters*, vol. 70, no. 13, pp. 1960-1963, 1993.

17. Koike, A. and Yoneya, M., "Molecular Dynamics Simulations of Sliding Friction of Langmuir-Blodgett Monolayers," *Journal of Chemical Physics*, vol. 105, no. 14, pp. 6060-6067, 1996.

18. Yim. S., Sonwalkar, N., and Saka, N., "Molecular Dynamics Simulation of Boundary Lubricated Interfaces," *Journal of Computer-Aided Materials Design*, vol. 6, pp. 69-80, 1999.

19. Zhang, L., Tanaka, H., "Toward a Deeper Understanding of Wear and Friction on the Atomic Scale - A Molecular Dynamics Analysis," *Wear*, vol. 211, 1997, pp. 44-53.

20. Chandrasekaran, N., Khajavi, A.N., Raff, L.M., and Komanduri, R., "A New Method for Molecular Dynamics Simulation of Nanometric Cutting," *Philosophical Magazine B*, vol. 77, no. 1, pp. 7-26, 1998.

21. Hammerberg, J.E., Holian, B.L., Röder, J., Bishop, A.R., and Zhou, S.J., "Nonlinear Dynamics and the Problem of Slip at Material Interfaces," *Physica D*, vol. 123, pp. 330-340, 1998.

22. Holian, B.L., Hammerberg, J.E., and Lomdahl, P.S., "The Birth of Dislocations in Shock Waves and High-Speed Friction," *JCAD*, vol. 5, p. 207, 1998.

23. Deng, K., Ko, W.H., "Static Friction of Diamond-Like Carbon Film in MEMS," *Sensors and Actuators A*, vol. 35, pp. 45-50, 1992.

24. Deng, K., Collins, R.J., Mehregany, M., and Sukenik, C.N., "Performance Impact of Monolayer Coating of Polysilicon Micromotors," *Journal of Electrochemical Society*, vol. 142, no. 4, pp. 1278-1285, 1995.

25. Suh, N.P., **Tribophysics**, Prentice Hall, New Jersey, 1986.

26. Rabinowicz, E., **Friction and Wear of Materials**, John Wiley & Sons, Inc., New York, 1995.

27. Zhen, S. and Davies, G.J., "Calculation of the Lennard-Jones n-m Potential Energy Parameters for Metals," *Physica Status Solidi A*, vol. 78, pp. 595-605, 1983.

28. Daw, M.S., and Baskes, M.I., "Semiempirical, Quantum Mechanical Calculation of Hydrogen Embrittlement in Metals," *Physical Review Letters*, vol. 50, no. 17, pp. 1285-1288, 1983.

29. Parrinello, M. and Rahman, A., "Polymorphic Transitions in Single Crystals: A New Molecular Dynamics Method," *Journal of Applied Physics*, vol. 52, no. 12, pp. 7182-7190, 1981.

30. Allen, M.P. and Tildesley, D.J., **Computer Simulation of Liquids**, Clarendon Press, Oxford, 1987.

31. Zhong, W. and Tomanek, D., "First-Principles Theory of Atomic-Scale Friction," *Physical Review Letters*, vol. 64, no. 25, pp. 3054-3057, 1990.

32. Whitehead, J.R., "Surface Deformation and Friction of Metals at Light Loads," *Proceedings of the Royal Society A*, vol. 201, pp. 109-124, 1950.

33. Bowden, F.P. and Hughes, T.P., "Friction of Clean Metals and Influence of Adsorbed Gases. The Temperature Coefficient of Friction," *Proceedings of the Royal Society A*, vol. 172, pp. 263-279, 1939.

34. Humphrey, W., Dalke, A., and Schulten, K., "VMD - Visual Molecular Dynamics," *Journal of Molecular Graphics*, vol. 14, no. 1, pp. 33-38, 1996.

CHAPTER 3

Molecular Dynamics Simulation of Grain Boundary Sliding

3.1 Introduction

Molecular dynamics (MD) simulations have been used widely to model atomic scale sliding and have proven to be helpful in the interpretation of data acquired by high resolution instruments such as the atomic force microscope (AFM) and the friction force microscope (FFM) [1,2]. Simulations have been carried out for a wide variety of materials, geometries, and processes, including sliding of a silicon tip on a silicon surface [3], nano-indentation of a nickel tip on a gold surface [4], sliding of hydrogen-terminated diamond surfaces [5], and AFM modeling with various tips and substrates [6,7]. The simulations have led to an agreement that at the atomic scale, the interfacial structure plays a very critical role in the frictional behavior, more so than other variables such as the normal load, contact area, and sliding speed [6]. One of the most important structural issues is whether the interface is commensurate or incommensurate, the former having perfectly matching lattices and the latter a mismatch due to misorientations of crystals or dissimilar lattices. The plucking phenomenon [8,9], which many claim to be the dominant source of friction in commensurate contacts [5–10], has been shown by atomic-scale computations to have a much weaker and sometimes even vanishing effect when an interfacial misfit is introduced [6, 10]. In support of this theory, Hirano et al. have also reported experimental evidence of reduced friction in incommensurate interfaces of muscovite mica, even though the experimentally observed reduction is far less than the numerical prediction [11]. Despite the intriguing frictional properties of incommensurate interfaces, most MD studies of sliding have focused on commensurate systems, which are insightful in the fundamental sense but lack practical relevance. At the macroscale, asperities generally are not composed of a single crystal, and a typical asperity contact arguably consists of a random array of incommensurate junctions with an infinite number of possible misfit orientations. A comprehensive MD study of incommensurate interfaces would lead to practically valuable insights as well as a more well-rounded understanding of atomic-scale friction.

Past efforts of MD modeling of incommensurate interfaces mostly fall into one of two categories, the first of which is the simulation of the sliding of a nano-sized tip on an

atomically flat substrate, reflective of AFM and FFM measurement processes. For example, Sørensen et al. conducted simulations of a Cu (111) tip with a flat apex on a Cu (111) surface with a 16° twist misorientation and found that the misfit resulted in a substantial reduction of friction in comparison to the commensurate case [6]. However, they also noted that their system was sensitive to finite contact size effects, such as plucking associated with the pinning of the tip atoms at the edges of the contact area. Buldum et al. simulated the sliding of a Ni (111) tip on a Cu (110) substrate and observed the transfer of low-coordinated Ni atoms from the sharp tip to the Cu surface [7]. During sliding, their simulation showed considerable structural transformation of the tip in conjunction with atom transfer and contact area growth. It seems that in the simulations with a finite contact area, the edge effects often overshadow the intrinsic behavior of the incommensurate interfaces. Since the edge to area ratio is considerable for such small contacts, there are also concerns about the system size dependence.

The second category of MD modeling of incommensurate interfaces is the simulation of systems containing grain boundaries (GB's), including nanophase polycrystalline (or simply nanocrystalline) [12–14] and bicrystalline [15–26] systems. The simulations of nanocrystalline systems have produced some exciting results, particularly in regard to the controversial "reverse Hall-Petch" effect [27] in the context of the grain-size dependence of the material strength, but the deformation involves bulk shearing rather than translational sliding. Furthermore, the systems are grown using randomly oriented crystal seeds and often contain intergranular amorphous layers [13], rendering it impossible to characterize the GB's in the conventional way. For these reasons, simulations of nanocrystalline systems make limited contributions to the fundamental understanding of GB sliding. Bicrystalline systems are more useful because the GB's are well-defined, and an impressive amount of information about the energy and structure of numerous GB's have been compiled through the use of atomistic computations [20,21]. In addition, much modeling effort has been devoted to the migration and sliding of tilt and twist grain boundaries [16,17,22,25]. The observation in MD simulations of spontaneous GB sliding and migration at elevated temperatures, even in the absence of external driving forces, has been explained by very low energy barriers associated with the sliding–migration coupling [16,17]. While these studies are helpful in the general understanding of the atomic mechanisms of GB sliding, the sliding is thermally activated and not very relevant to the friction problem, which is driven by an external mechanical force.

This work is an investigation of the atomistic processes involved in the sliding of GB's using MD simulations. Specifically, the simulations are of bicrystalline GB's without any

extrinsic defects such as GB dislocations and amorphous intergranular layers. In addition, this study looks at heterophase systems where, in addition to the GB's, there exists a phase boundary. The phase boundary is implemented by making the atomic interaction between opposing crystals weaker than the bulk crystal interactions. The purpose of the heterophase grain boundary simulations is to elucidate the atomic mechanisms of sliding at incommensurate interfaces under weak adhesion. Such situations arise when the sliding surfaces consist of materials that are incompatible or weakly interacting, or also if the surfaces are contaminated. A key question to be addressed concerns the relationship between friction and adhesion of bicrystalline interfaces. Another issue which is explored in this work is the role of jump phenomena (also called plucking) in GB sliding. A jump phenomenon is the sudden release of potential energy as kinetic energy of the atoms in the event that an unstable configuration is encountered, and it is the only known source of friction in atomistic models. Two types of boundaries are investigated, a symmetric tilt and symmetric twist boundaries of FCC crystals.

3.2 MD Simulation Methodology

3.2.1 Potential Function

All systems in this work are modeled using the Lennard-Jones (L–J) 12–6 pair potential,

$$\phi\left(r_{ij}\right) = 4\varepsilon\left[\left(\frac{\sigma}{r_{ij}}\right)^{12} - \left(\frac{\sigma}{r_{ij}}\right)^{6}\right], \tag{1.1}$$

which describes the potential energy between the pair of atoms i and j separated by a distance of r_{ij}. Three sets of the L–J parameters ε and σ are required to fully define bicrystal systems, one set for each bulk (A–A and B–B) interaction and one set for the interfacial (A–B) interaction. Table 3–1 contains the values of all L–J parameters. It may be noted that the parameter σ is the same for all interactions. This is a reasonable simplification given that σ mostly affects the lattice parameter, which is expected to have a minimal effect on the sliding behavior. Another simplification is $\varepsilon_{AB} = \varepsilon_{AA}$, which means that the bulk properties of A and B are identical. This assumption should have little effect on the outcome because the interfacial behavior is much more important than the bulk. The essential parameter is ε_{AB} because it determines the strength of the interfacial bonds, and the ratio $\varepsilon_{AB}/\varepsilon_{AA}$ is a convenient dimensionless parameter relating the interfacial adhesion to the bulk cohesion. The limiting case of $\varepsilon_{AB}/\varepsilon_{AA} = 1$ represents a pure GB, whereas a reduced value ($\varepsilon_{AB}/\varepsilon_{AA}$

< 1) represents a heterophase GB. (It is not heterophase, in the strictest sense, because crystals A and B are still identical, but the interaction between A and B is weaker, which introduces an interfacial effect that resembles a phase boundary.) The ratio $\varepsilon_{AB}/\varepsilon_{AA}$ is important in the parametric investigation of the adhesion-friction relationship, in which the friction is computed for various values of ε_{AB} while keeping ε_{AA} constant, such that $0< \varepsilon_{AB}/\varepsilon_{AA} < 1$.

Table 3–1: Parameters for Lennard-Jones potential function.

Interaction	Lennard-Jones Parameters	
A–A	$\varepsilon_{AA} = 65.322 \times 10^{-21}$ J	$\sigma_{AA} = 0.23127$ nm
B–B	$\varepsilon_{BB} = 65.322 \times 10^{-21}$ J	$\sigma_{BB} = 0.23127$ nm
A–B	ε_{AB} = variable, $\varepsilon_{AB}/\varepsilon_{AA} < 1$	$\sigma_{AB} = 0.23127$ nm

The bulk L–J parameters (ε_{AA} , ε_{BB} , σ) are fitted to the specific volume and vaporization enthalpy of copper [28]. It is emphasized, however, that the intention of the present work is not to predict the properties of any one specific material. In contrast, the objective is to reveal universal trends in the sliding behavior of generic bicrystalline systems, and the L–J potential function is well suited for such parametric studies. Copper is chosen simply as a representative material, so that the simulations may reflect the typical behavior of common metals.

3.2.2 System Description and Border Conditions

The MD simulation cell has a tetragonal shape with the edges aligned with the x–y–z coordinate system, as shown in the schematic of Figure 3–1. In the x and y directions, periodic border conditions are applied. (The term *border condition* is used here instead of the more commonly used *boundary condition* in order to avoid confusion in terminology with the grain boundary.) In the z direction, the periodic border conditions are replaced by finite borders consisting of rows of fixed atoms. The fixed atoms are static and lie *outside*

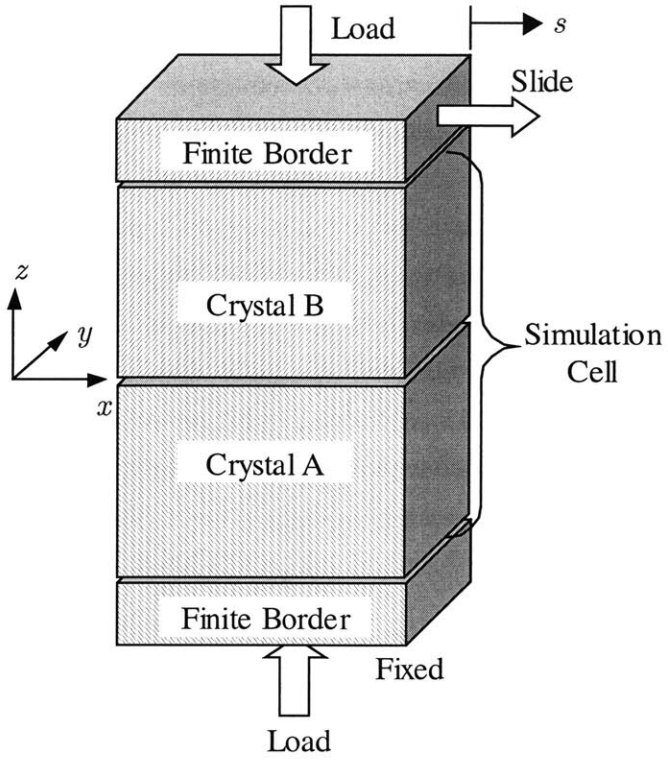

Figure 3–1: Schematic of MD cell for GB simulation. Periodic border conditions are applied in the x–y plane.

the simulation cell. They are arranged to match the lattice of the nearby atoms in the cell, thus creating a semi-infinite effect. The interface of the two crystals, A and B, is a horizontal (x–y) plane located in the middle of the cell.

The system maintains constant stress, rather than constant volume. This means that the cell walls are allowed to move so that the internal stress of the system is equal to the desired setting. The cell walls usually move in a oscillatory manner, such that the cell dimensions are always fluctuating about an equilibrium size and shape corresponding to the desired stress. The internal stress is given by:

$$\boldsymbol{\tau} = -\frac{1}{V}\left[\sum_i m_i \mathbf{v}_i \mathbf{v}_i' + \sum_i \sum_{j>i} \mathbf{r}_{ij} \mathbf{f}_{ij}' + \sum_i \sum_k \tilde{\mathbf{r}}_{ik} \mathbf{f}_{ik}'\right], \tag{1.2}$$

where V is the volume of the simulation cell, m_i is the mass of atom i, $\mathbf{v}_i$ is its velocity vector, $\mathbf{r}_{ij} = \mathbf{r}_i - \mathbf{r}_j$, and $\mathbf{r}_i$ and $\mathbf{r}_j$ are the coordinate vectors of atoms i and j. The primes denote the transpose of the column vectors. Indices i and j loop over only the dynamic atoms inside the cell, while k represents only the fixed atoms of the borders. The tilde, as in $\tilde{\mathbf{r}}_{ik}$, denotes that only the interior portion of the spatial vector is to be used, and this applies only when atom i (always inside the cell) interacts with fixed atom k (always outside the cell). The force exerted on atom i by j, denoted by $\mathbf{f}_{ij}$ (or $\mathbf{f}_{ik}$, when a fixed atom is involved), is related to the derivative of the potential function,

$$\mathbf{f}_{ij} = -\frac{d\phi}{dr_{ij}}\frac{\mathbf{r}_{ij}}{r_{ij}}. \tag{1.3}$$

The unique advantage of this border condition is that a constant stress simulation can be conducted, which is not possible when the dimensions of the cell are fixed. The constant-stress technique is conceptually similar to the Parrinello-Rahman method [29], except that the Parrinello-Rahman method is valid only for fully periodic simulation cells, whereas the present scheme is adaptable to cells with finite borders. In this work, only the normal motions of the cell walls are allowed, meaning that shear deformations of the cell are suppressed. The derivation of Eqn. (1.2) is discussed in full detail in Appendix C. Table 3–2 lists some information about the system, including the initial simulation cell dimensions. The cell dimensions vary throughout, but the variation is usually less than 1% of the initial value. Note that the simulation cell dimensions for the tilt and twist boundaries are different.

3.2.3 Loading and Sliding

After the initial positions of the atoms are assigned, and their velocities are determined randomly and scaled to the desired temperature, the system is simulated under zero stress and 291K for at least 50000 time steps, which is approximately equivalent to 200 atomic oscillations. This is done to allow the system to find the reference equilibrium state. The normal load is then applied by taking the output dump file (atomic positions and velocities) from the relaxation simulation and using it as the input to a new simulation where the stress is set to the desired value. Only a compressive normal stress in the z direction is applied, and the normal stresses in the x and y directions are kept at zero. The shear stresses cannot be controlled because the shear deformations of the cell are constrained. Since the entire normal load is applied instantaneously rather than stepping up the load gradually, 50000 more time steps are given so that the system has plenty of time to fully equilibrate to the

Table 3–2: Parameters for GB Simulation.

Number of atoms (tilt GB)	720 in crystal A
	720 in crystal B
	240 in upper border
	240 in lower border
Number of atoms (twist GB)	1404 in crystal A
	1404 in crystal B
	468 in upper border
	468 in lower border
Simulation cell dimensions ($x \times y \times z$) (tilt GB)	$2.29 \times 2.17 \times 3.52$ nm
Simulation cell dimensions ($x \times y \times z$) (twist GB)	$3.19 \times 2.76 \times 3.77$ nm
Mass of atom (A or B)	1.06×10^{-22} g (copper)
Mass of dynamic cell walls	1.06×10^{-21} g
Time step	10^{-15} s
Number of steps prior to sliding	50000 time steps
Sliding increment of moving border (tilt GB)	0.0023 nm
Sliding increment of moving border (twist GB)	0.0012 nm
Number of steps following each sliding increment	5000 time steps
Normal load during sliding	300 MPa (compressive)
Temperature (by velocity rescaling)	291 K

load. The output from the loaded simulation is then used as the input to the sliding simulation.

Sliding is imposed by incremental displacements of the upper border in the x direction (see Figure 3–1) while holding the lower border in place. The size of the increment, listed in Table 3–2, is never greater than 1/10 of the average amplitude of atomic vibration at the given temperature (see Appendix B). After each increment, 5000 time steps are allowed for equilibration prior to the execution of the next sliding step. This is done so that the entire

system can always "feel" the effect of the moving border. The 5000 steps is equivalent to 20 atomic oscillations, and mean-square displacement data confirm that the system consistently attains equilibrium during this span.

3.2.4 Potential Energy and Sliding Resistance

During sliding, relevant properties such as the potential energy and sliding resistance are computed with respect to s, the total displacement of the upper border. The potential energy is calculated by simply summing up all pair potentials,

$$\Phi = \frac{1}{N}\overline{\sum_i \sum_{j \neq i} \phi\left(r_{ij}\right)}, \tag{1.4}$$

where i loops over only the dynamic atoms while j loops over all dynamic and fixed atoms. The normalization factor N is the total number of dynamic atoms (A and B combined). The overhead bar denotes averaging over the equilibration period following a sliding displacement. The sliding resistance is equal to $\overline{\tau}_{zx}$, the shear component of the internal stress of Eqn. (1.2), also averaged over the equilibration period. The sliding resistance is exactly the shear stress exerted by the rigid border on the upper face of the cell (and vice-versa) in equilibrium. There must be an external stress acting on the border to balance the stress from the cell if mechanical equilibrium is to be satisfied. The sliding resistance is equivalent to this external stress. At the atomic scale, sliding is often periodic, meaning that all state properties of the system such as the configuration, energy, stress return to the initial values after a unit distance of sliding, which can be the lattice parameter of a crystal, for example. In such cases, the integral of the resistance-distance curve over a period is equal to the net work done per unit area by the external force, or equivalently, the average of the resistance over a period can be interpreted as the friction per unit area per unit distance slid (see Chapter 2 for more discussion on this topic).

3.2.5 Additional Simulation Details

Table 3–2 lists all relevant simulation settings. The atomic motions are numerically integrated using the 5th order Gear predictor-corrector method. All simulations use rescaling of the particle velocities at every time step in order to maintain the temperature at 291 K. The usual methods such as the potential cutoff at 2.5σ, neighbor list, and the minimum image criteria are applied to improve computational efficiency [30].

3.3 Simulation of Symmetric Tilt Grain Boundary

3.3.1 GB Characterization and Structure

The system simulated in this section is a pure GB, meaning that $\varepsilon_{AB} = \varepsilon_{AA}$. It is a symmetric tilt GB with a misfit angle of 36.9° about the [100] FCC crystallographic axis. The grain boundary coincides with the (310) planes of both crystals, making this a Σ5 [100] (310) tilt GB under the coincident site lattice (CSL) convention. It may be noted that only CSL GB's can be simulated under the periodic border conditions in the plane of the GB, on account of the repeatability requirement. Figure 3–2 shows the atomic structure of the unrelaxed GB. The familiar kite structure, which is commonly studied in many simulations of tilt GB's [15–19,25], is outlined in the figure. The relative position of the crystals is such that unit cells of A and B coincide exactly at the atoms located at the tips of the kite structures. These tip atoms have been designated to belong to crystal A simply by preference, and this choice has no bearing on the outcome for a single-phase GB. In the heterophase case where the A–B interactions are different from the A–A (and B–B) interactions, choosing the tip atoms to be B rather than A is equivalent to sliding the upper crystal in the $(-x)$ direction instead of the $(+x)$ direction. While the consequences of this choice are not investigated here, it is noted that it may affect the results due to the anisotropy of GB sliding.

The GB is repeatable by a relative translation of the crystals in the x direction by a distance of λ, which is equal to the length of the kite structure. The simulation must cover a sliding distance no less than λ in order to sample the entire topological response. For this GB, $\lambda = 5.7$ Å, approximately 1.6 times the lattice parameter. To the left of the tip of every kite in Figure 3–2, there is a pair of in-plane atoms which are only 1.1 Å apart. This is equal to 0.49σ, which means that the atoms are in a state of tremendous repulsion. This pair will surely attempt to separate during relaxation, but it is a good idea to manually separate the crystals prior to the start of the MD simulation in order to avoid a catastrophic response as a result of the excessively high energy.

3.3.2 GB Energy

The GB is first relaxed in a fixed simulation cell for 50000 time steps so that the atoms in the system, particularly those in the vicinity of the interface, can settle into equilibrium without the external influence of the moving borders. This is followed by 50000 more steps,

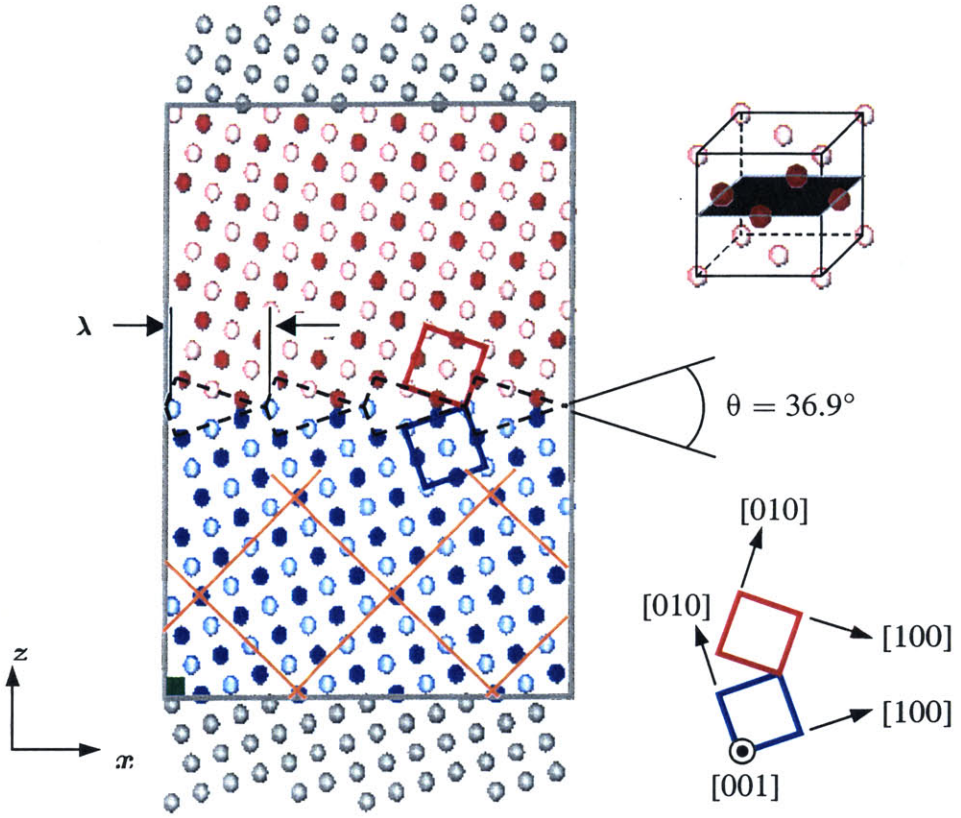

Figure 3–2: Unrelaxed structure of Σ5 [100] (310) symmetric tilt grain boundary. Gray box outlines the simulation cell. Blue and red spheres denote atoms of crystals A and B, respectively, and the light and dark colors represent alternating [001] layers, as illustrated in the upper-right insert. The gray spheres are the fixed atoms forming finite borders in the z direction, and periodic border conditions are applied in the x and y directions. The FCC lattice unit cells are outlined in blue and red while the CSL is outlined in orange. The DSC lattice unit cell is shown by the filled green block in the lower left corner of the simulation cell.

this time with the cell walls relaxed to zero pressure. The fully relaxed configuration is shown in Figure 3–3a, and it can immediately be seen that the pair of atoms that were extremely close together in the unrelaxed state have separated to a comfortable distance. The kite structure is still in place, but the tip now has assumed a more blunt shape following the relaxation.

The GB energy can be calculated by summing up the excess energy of all the atoms in the system. The excess energy of an atom is defined here to be the amount of potential

energy exceeding a reference value ϕ_o, where ϕ_o is the reference potential energy of an atom in a perfect FCC crystal at the same temperature. The excess energy of atom i is given by

$$\phi_i = \frac{1}{2}\left[\sum_{j \neq i} \phi\left(r_{ij}\right)\right] - \phi_o . \tag{1.5}$$

The factor of 1/2 is present because it is assumed that the energy of a bond is shared equally by the two participating atoms in a pairwise system. It is further noted that the summation in Eqn. (1.5) also includes the fixed atoms. The reference energy, obtained from a separate simulation of a bulk crystal at 291 K, has a value of $\phi_o = -6.65\varepsilon$. Figure 3–3b shows the excess energy of every atom in the system plotted against the z coordinate. Note that $z = 0$ at the bicrystalline interface, between rows of A and B atoms. Figure 3–3b shows that the excess energy is concentrated in the .9 nm thick region near the interface, and atoms away from this region do not feel the presence of the GB. The GB thickness can be considered to be equal to the thickness of the high energy region, or 0.9 nm, which is equivalent to about 3.4 atomic diameters if one atomic diameter is approximately equal to 1.12σ. A subtle point to clarify is the exact meaning of the potential energy. In a dynamic system, the instantaneous potential energy is continuously changing because the position of each atom is always changing. The potential energy here refers to the minimum value over an oscillation, which is obtained by computing the energy based on the average position of the atom over several vibrational periods.

The GB energy is calculated by summing up the excess energy of the system and dividing by the area A of the interface:

$$E_{GB} = \frac{1}{A}\sum_{i=1}^{N} \phi_i . \tag{1.6}$$

This summation *does not* include the border atoms. This calculation yields $E_{GB} = 3.4$ J/m^2, or $E_{GB} = 2.8(\varepsilon/\sigma^2)$ in reduced form. This value is high in comparison to Wolf's calculation of $1.74(\varepsilon/\sigma^2)$ for a similar GB [21], and the difference is partly due to the fact this particular GB is very sensitive to the relative translations of the crystals in the x and y directions. It is shown shortly hereafter that the sliding of the upper crystal results in the decrease of the system energy. In addition, there is a possibility that his GB has a slightly different core structure which yields a lower GB energy.

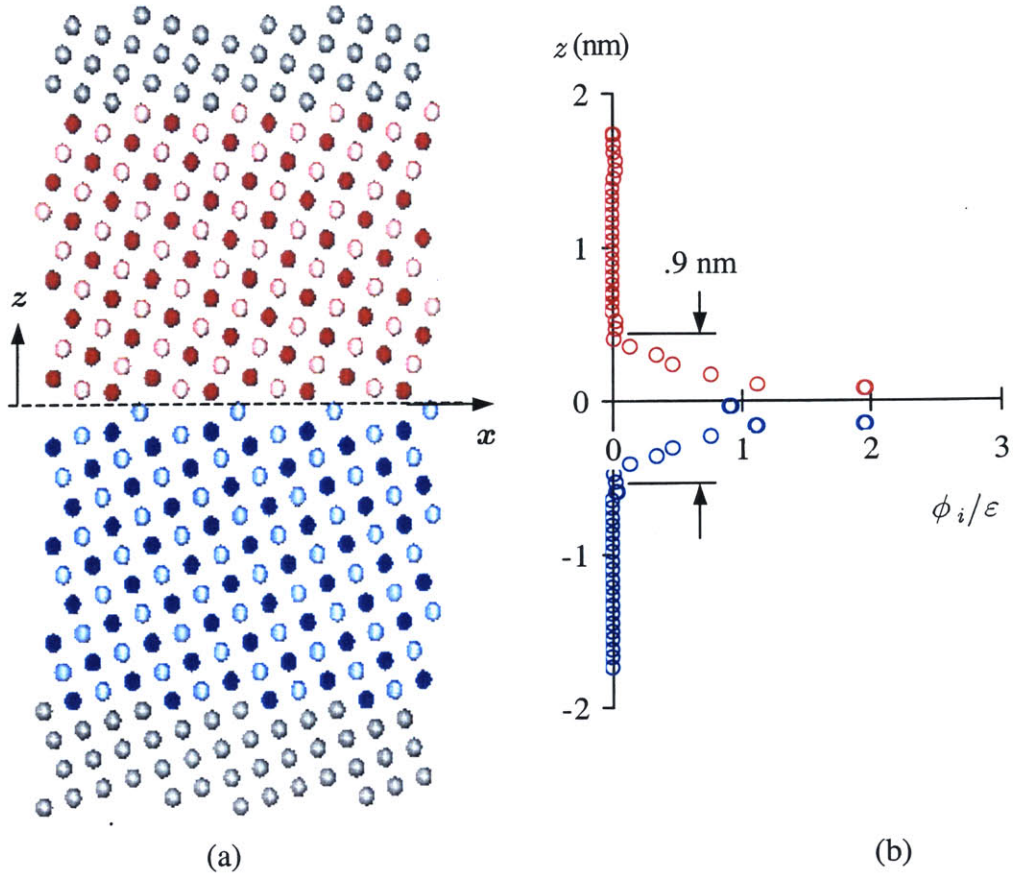

Figure 3–3: Relaxed grain boundary. (a) Side view. Color coding is the same as in Figure 3–2. (b) Excess energy of atoms with respect to their z–coordinates.

3.3.3 GB Sliding

The relaxed system is given a compressive normal load of 300 MPa in the z direction. The simulation cell responds to the stress with an overall normal strain in z of –0.001, 54% of which occurs within the GB region (i.e., the 0.9 nm thick high energy region shown in Figure 3–3). This strain localization is directly linked to the large free volume of the atoms in the grain boundary region. In the x and y directions, the cell undergoes strains of 0.0002 and 0.0005, respectively, and the inequality of the horizontal strains is due to the structural anisotropy. The loaded system is next subject to sliding while maintaining the normal load and temperature at 300 MPa and 291 K. The average configuration, potential energy, and stress are computed following each displacement.

Figure 3–4 shows the snapshots of the GB at various points during sliding. It is apparent from these pictures that the sliding is coupled to an upward migration of the GB. The motion of the GB can be traced by tracking the kite structure. The kite structure is clearly identifiable at the start of sliding (Figure 3–4a) but becomes distorted as sliding commences (Figure 3–4b). It is recovered by $s/\lambda = 0.6$ (Figure 3–4e), except that it has been displaced in the x direction by 0.6λ and in the z direction by 0.05λ. The x displacement of the GB is clearly the sliding, while the z displacement is the migration. It can also be seen that the atomic arrangement within the kite structure has been changed. Initially in Figure 3–4a, blue atoms are at the point of the kites, but by Figure 3–4e, red atoms have taken over the points. The coupled sliding–migration phenomenon has also been observed in past simulations at high temperatures [16,17], and the present results confirm that it also occurs at low temperature under forced sliding. The coupling takes place because the migration–sliding process is energetically favorable to a pure sliding process [25]. The progression shown in Figure 3–4 indicates that a period of the GB sliding–migration process is about 0.6λ. According to a purely geometric analysis, the sliding–migration periodicity should be equal to $(2/3)\cos^2(\theta/2)\lambda$, where θ is the GB tilt angle. For $\theta = 36.9°$, this comes out to exactly 0.6λ, which agrees perfectly with the simulation results.

The potential energy of the system is plotted as a function of the sliding distance in Figure 3–5. Initially, the potential energy is at a maximum, and the curvature of the graph indicates that the upper border is unstable in this position. If not for the fact that the border is constrained, a small perturbation would send it to a stable position of lower energy. The stable, minimum potential energy position is at $s/\lambda = 0.3$ (Figure 3–4c). At this point, the initially sharp, single–atom tip of the kite structure has been replaced by a blunt lip formed by a pair of atoms, one from each crystal. The difference in the potential energy between the initial (maximum) value and the minimum value is 0.02ε per atom, which translates to 0.36 J/m^2 for the interface, which is about 10% of the GB energy calculated in the previous section. It is clear that the GB energy is rather sensitive to the relative translation of the crystals. An important feature of the potential energy curve is the absence of sharp drops which are associated with jump phenomena. The absence of jumps suggests that the sliding-migration process is frictionless, as discussed in Chapter 2.

The sliding resistance is plotted in Figure 3–6. Initially, the resistance is negative, which means that a stress has to be applied to hold the border from slipping forward, analogous to having to hold a roller coaster car from accelerating downhill. This driving force comes from the interface, where the atoms prefer to move out of the kite structure (Figure 3–4a) and into the lower energy structure (Figure 3–4c). The minimum value of the resistance is –3421

MPa and occurs at $s/\lambda = 0.05$ (see configuration in Figure 3–4b) while the maximum of 3412 MPa occurs at $s/\lambda = 0.55$ (Figure 3–4d). The maximum and minimum are about equal in magnitude and occur anti-symmetrically about the halfway point of sliding. The anti-symmetry is a typical feature of sliding without any jump phenomena. The average resistance of 1.7 MPa, which is the friction for this sliding case (see discussion in Chapter 2), is small enough that it can be considered to be an error from an insufficient equilibration following each sliding displacement. (The sliding resistance may be understood to be about ±10 MPa accurate under the present equilibration period.) Given a much longer equilibration period, the resistance curve would arguably approach perfect anti-symmetry, resulting in a zero average resistance, or zero friction. Thus, it can be concluded that this sliding system is frictionless, a conclusion which is consistent with the observation that jump phenomena do not occur. Although the average resistance is negligible, the peak resistance of 3412 MPa is a sizable 27% of the ideal shear strength. With such a high peak resistance, it is somewhat surprising that jump phenomena do not take place, particularly in light of the previous study of commensurate systems, where jump phenomena are observed when the peak resistance is only 17% of the ideal shear strength (see Chapter 2). Evidently, the coupling of the migration to the sliding provides a configurational path which not only lowers the system energy compared to the alternative of pure sliding, but also suppresses the jump phenomena by avoiding unstable configurations.

3.4 Sliding Simulation of Heterophase Symmetric Tilt Grain Boundary

To the tilt GB described in the previous section, an additional planar defect is now introduced to the bicrystalline interface by setting $\varepsilon_{AB} < \varepsilon_{AA}$. No other L–J parameters are changed. The result is that the interface is a phase boundary in addition to being a grain boundary. Although A and B are still identical in terms of the sameness of the L–J parameters $\varepsilon_{AA} = \varepsilon_{BB}$, the fact that the A–B interaction is different creates the heterogeneity. This setup more closely resembles a tribological system in that the interface is more reflective of a general asperity junction where the surfaces are different materials. The heterophase GB system is subject to the same treatment of loading and sliding used in the previous section, and the same 300 MPa normal load is used. The only difference in the simulation setup involves the relative starting position of the crystals. In the previous simulation of the pure GB, the starting position was such that the kite structure was evident at the interface, but that particular structure turned out to be the maximum energy configuration. Therefore, in order to start the sliding at the minimum energy state, the upper crystal is given a 0.3λ head start. This is not by any means an essential adjustment because

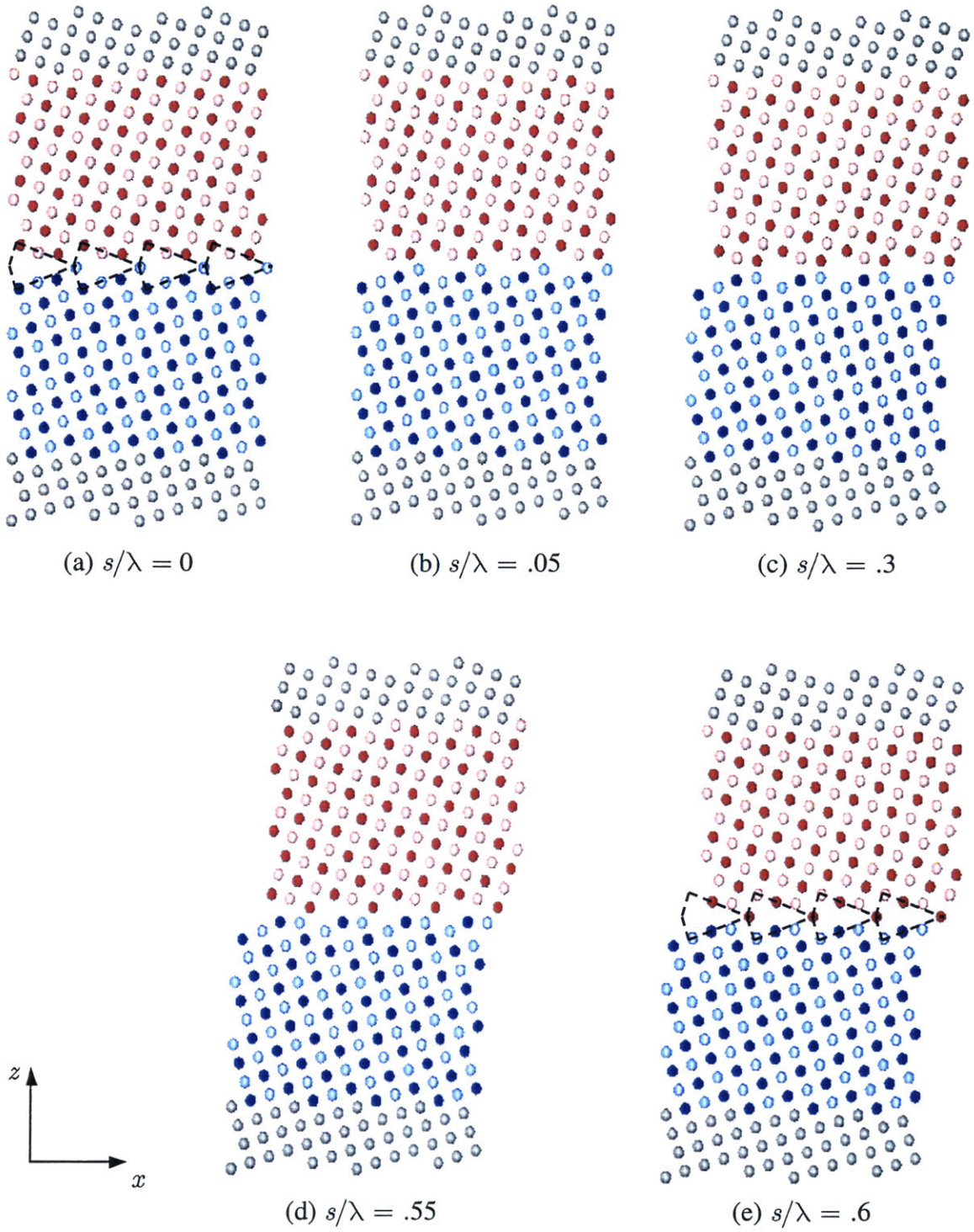

(a) $s/\lambda = 0$ (b) $s/\lambda = .05$ (c) $s/\lambda = .3$

(d) $s/\lambda = .55$ (e) $s/\lambda = .6$

Figure 3–4: Snapshots of tilt GB sliding.

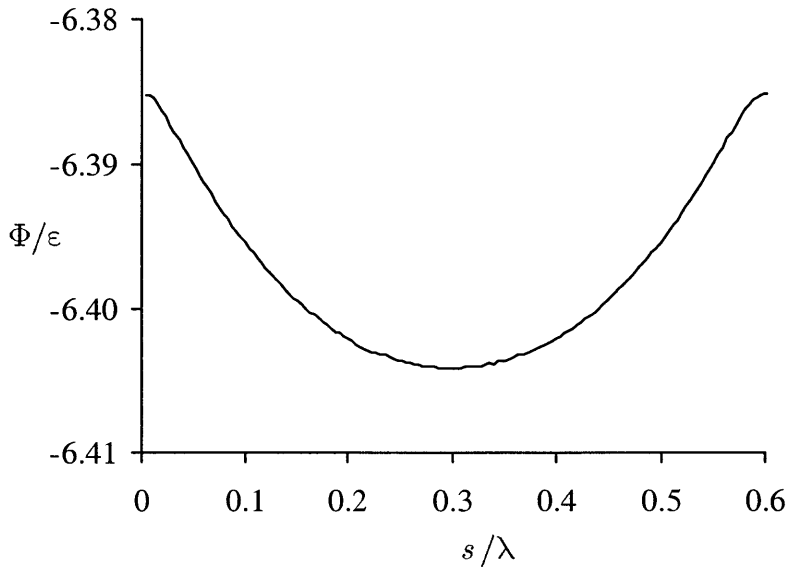

Figure 3–5: Potential energy per atom of tilt GB sliding system.

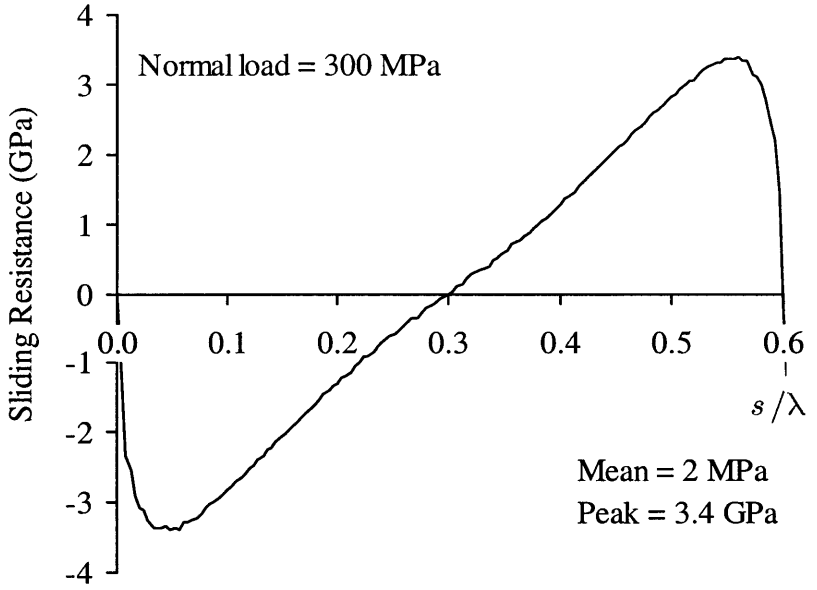

Figure 3–6: Sliding resistance tilt GB sliding system.

the sliding is expected to be periodic and the starting point should be inconsequential. The adjustment is made mostly to facilitate the interpretation of the data. The ratio $\varepsilon_{AB}/\varepsilon_{AA}$ is the critical parameter in this investigation, after it was found to play an important role in the sliding behavior of commensurate interfaces in Chapter 2. In the commensurate system, $\varepsilon_{AB}/\varepsilon_{AA}$ was seen to be the decisive factor between two distinct sliding regimes, the frictional and frictionless. The present results indicate that these two regimes also exist in heterophase GB sliding, and this will be illustrated through the following presentation of three cases: $\varepsilon_{AB}/\varepsilon_{AA} = 0.7$, 0.5, and 0.2.

3.4.1 Frictional Sliding: $\varepsilon_{AB}/\varepsilon_{AA} = 0.7$

Figure 3–7 shows the snapshots during various points of sliding for the relatively strong interface. The figure shows two views side-by-side. The pictures provide conclusive proof that the sliding is not accompanied by GB migration. The phase boundary evidently has the effect of suppressing the sliding-migration coupling, and pure sliding is now the preferred mechanism. Substantial action occurs between $s/\lambda = 0.31$ (Figure 3–7b) and $s/\lambda = 0.32$ (Figure 3–7c). Even though the border only moves slightly, there is significant slip at the interface in both the x and y directions. The transverse slip in the y–direction is particularly interesting because it leads to noticeable z–y shear strains in both crystals. Between $s/\lambda = 0.73$ (Figure 3–7e) and $s/\lambda = 0.74$ (Figure 3–7f), a reversal of the transverse slip relieves the crystals of these strains.

The potential energy, shown in Figure 3–8, initially starts at a minimum and increases continuously until it reaches a maximum at $s/\lambda = 0.31$, at which point the energy abruptly falls. Such a discontinuous drop in potential energy is a clear indication of a jump phenomenon. The occurrence of a jump is always the result of a structural instability. In this case, the unstable structure can be determined by visual inspection of the atomic configuration snapshots. Just prior to the jump at $s/\lambda = 0.31$, Figure 3–7b shows that the GB is very close to achieving the kite structure. Right after the jump at $s/\lambda = 0.32$, Figure 3–7c illustrates that the system has already passed beyond the kite structure, which implicates the kite as the unstable structure. The system spends only fleeting moments in the kite formation because the instability does not allow an extended stay. The transverse slip also takes place during this jump. This means that the jump causes the interfacial atoms to slip at an angle rather than straight along the sliding direction. This is also observed in the sliding of the (111) commensurate interface, where the atoms slip in a zigzag fashion, leading to FCC-HCP-HCC transitions (see Chapter 2). There is a local minimum of the potential

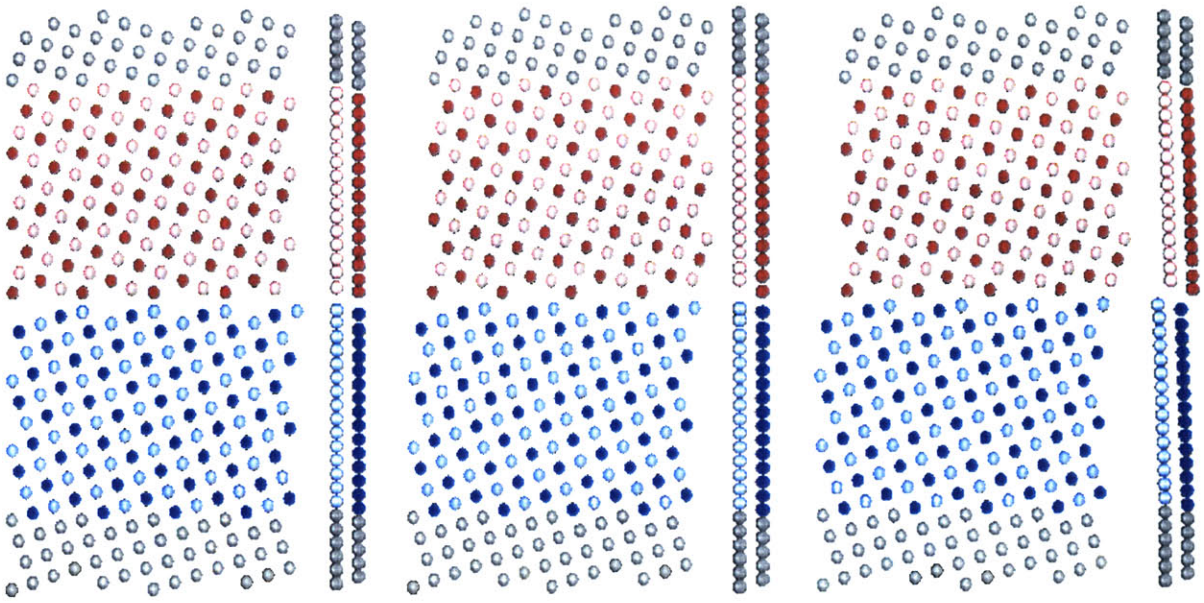

(a) Start (b) $s/\lambda = 0.31$ (c) $s/\lambda = 0.32$

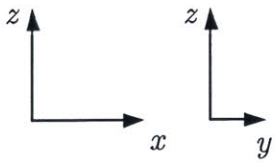

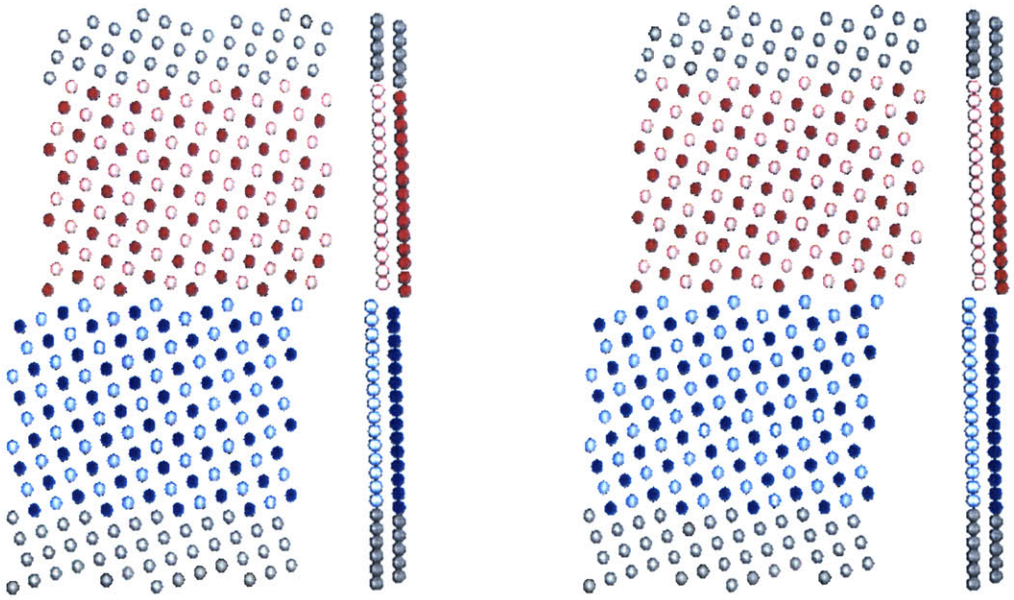

(d) $s/\lambda = .50$ (e) $s/\lambda = .73$

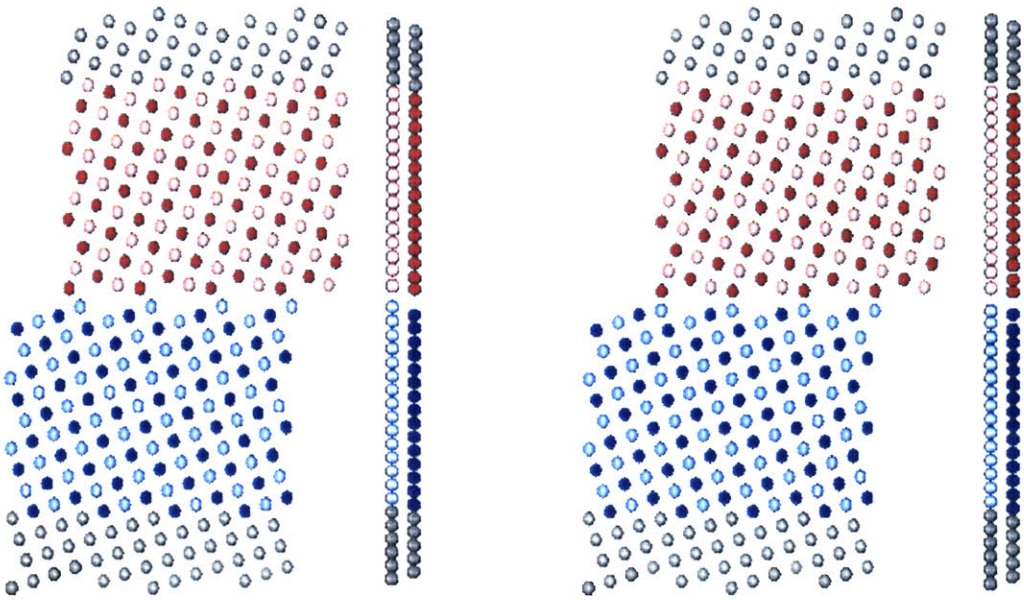

(f) $s/\lambda = 0.74$ (g) $s/\lambda = 1.0$

Figure 3–7: Snapshots of GB sliding. The left side of each subfigure is the view of the $x-z$ plane and the right side is the view of the $y-z$ plane. On the latter view, only two columns out of the total of 12 are shown.

energy curve at $s/\lambda = 0.5$ (Figure 3–7d), indicative of a metastable state. Much of the energy at this state is the result of the fact that both crystals are still under elastic shear strains brought on by the transverse slip. At $s/\lambda = 0.73$, there is a second peak in the potential energy followed by another discontinuous drop, a second and final jump phenomenon. The reverse transverse slip in the y–direction also happens at this point. As shown in Figures 3–7e and 3–7f, the system again passes over the kite structure during the jump, confirming again that the kite is the source of the jump phenomenon and friction in the sliding of this GB.

The sliding resistance, shown in Figure 3–9, is no longer antisymmetric, which is always the case when jump phenomena are present. The peak resistance is 3109 MPa, compared to 3412 MPa for the pure GB. It is not surprising that the heterophase GB has a lower peak resistance because the phase boundary is a defect, and it should make the interface weaker than the pure GB. The average resistance of 278 MPa is the friction for the heterophase GB. It is somewhat unexpected that the heterophase GB slides with so much friction while the pure GB, which has more adhesion at the interface and a higher peak resistance, slides without any friction. The answer lies in the coupled sliding–migration process, which is

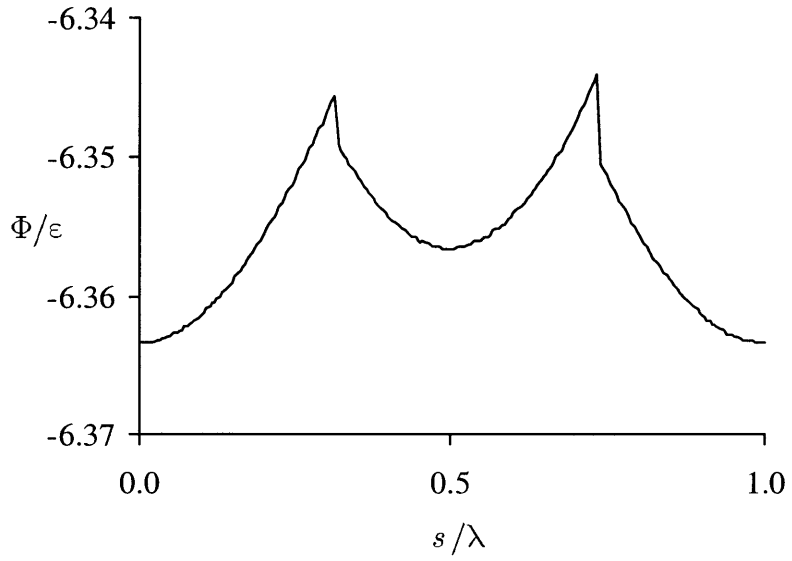

Figure 3–8: Potential energy per atom of GB sliding system with $\varepsilon_{AB}/\varepsilon_{AA}$= 0.7.

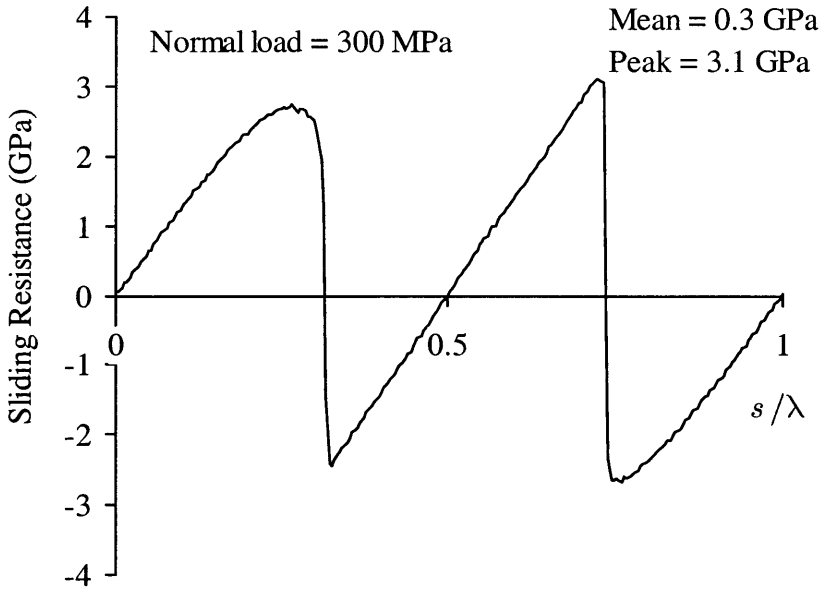

Figure 3–9: Sliding resistance of GB sliding system with $\varepsilon_{AB}/\varepsilon_{AA} = 0.7$.

jump-free and frictionless. The implementation of the phase heterogeneity at the interface essentially turns off the coupled mechanism, instead favoring the pure sliding process. In doing do, the system is exposed to jump phenomena because the pure sliding is susceptible to configurational instabilities. Due to the jump phenomena, the friction in the heterophase is significant, even if the peak resistance is still lower than in the pure GB sliding.

3.4.2 *Transition:* $\varepsilon_{AB}/\varepsilon_{AA} = 0.5$

This weaker interface system also undergoes pure sliding without any migration. The potential energy, plotted in Figure 3–10, exhibits two discontinuous transitions at $s/\lambda = 0.32$ and 0.68, but in each case there does not appear to be any potential energy drop which normally accompanies a jump phenomenon. This unusual circumstance of a discontinuous energy curve without any jump phenomena can only mean that the present case of $\varepsilon_{AB}/\varepsilon_{AA} = 0.5$ is near the transition between the frictional and frictionless regimes. As a comparison, the transition in the commensurate case occurs around $\varepsilon_{AB}/\varepsilon_{AA} = 0.17$. A rational explanation for why the incommensurate system has a higher transition value is that the transition depends on the overall strength of the interface, not just the value of $\varepsilon_{AB}/\varepsilon_{AA}$. Since the presence of the GB alone has a weakening effect on the interface, $\varepsilon_{AB}/\varepsilon_{AA}$ does not need to be lowered as much in the GB system for the transition to occur. Figure 3–11 shows the sliding resistance, which appears to be anti-symmetric about $s/\lambda = 0.5$. However, the average resistance of 16 MPa suggests that this system must actually be slightly on the frictional side. This means that even though a clear evidence of the jump phenomenon is visually undetectable in the potential energy curve, a small jump event must be occurring near the discontinuous transitions. Still, the actual transition is probably not too far below $\varepsilon_{AB}/\varepsilon_{AA} = 0.5$.

3.4.3 *Frictionless Sliding:* $\varepsilon_{AB}/\varepsilon_{AA} = 0.2$

The potential energy and sliding resistance are displayed in Figures 3–12 and 3–13, respectively. The smooth and continuous appearance of the potential energy curve provides sufficient evidence that the sliding is free of jump phenomena. The average resistance is calculated to be 6 MPa, but it can be better interpreted as zero since jumps do not occur and the value is low enough that it can be considered to be an error attributed to the insufficient equilibration. During some portions of sliding, the resistance curve has a negative slope, which indicates an instability. The only reason that the system goes through such extended periods of instability is that the upper border undergoes constrained motion. Under a force

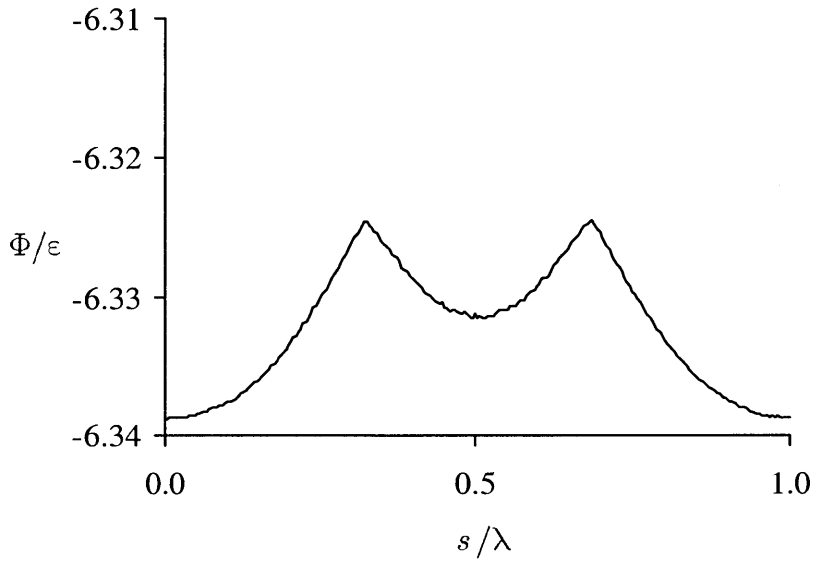

Figure 3–10: Potential energy per atom of GB sliding system with $\varepsilon_{AB}/\varepsilon_{AA} = 0.5$.

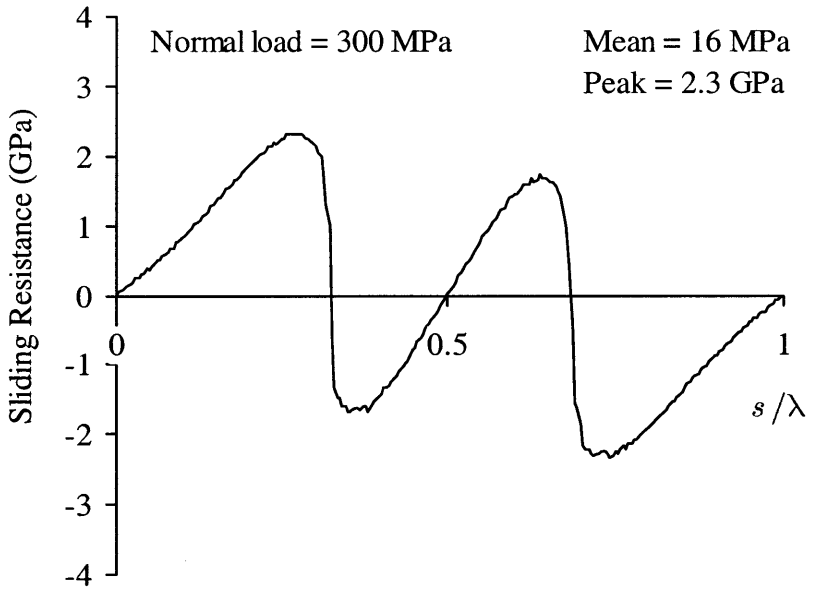

Figure 3–11: Sliding resistance of GB sliding system with $\varepsilon_{AB}/\varepsilon_{AA} = 0.5$.

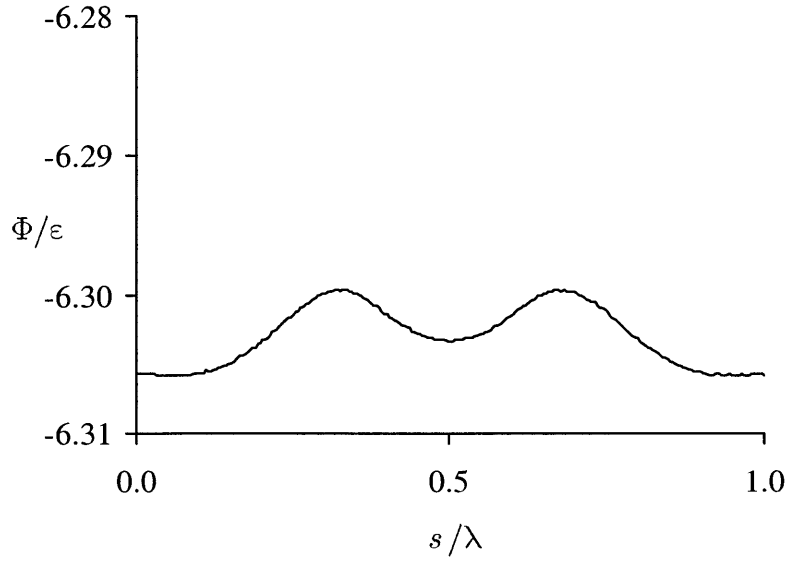

Figure 3–12: Potential energy per atom of GB sliding system with $\varepsilon_{AB}/\varepsilon_{AA} = 0.2$.

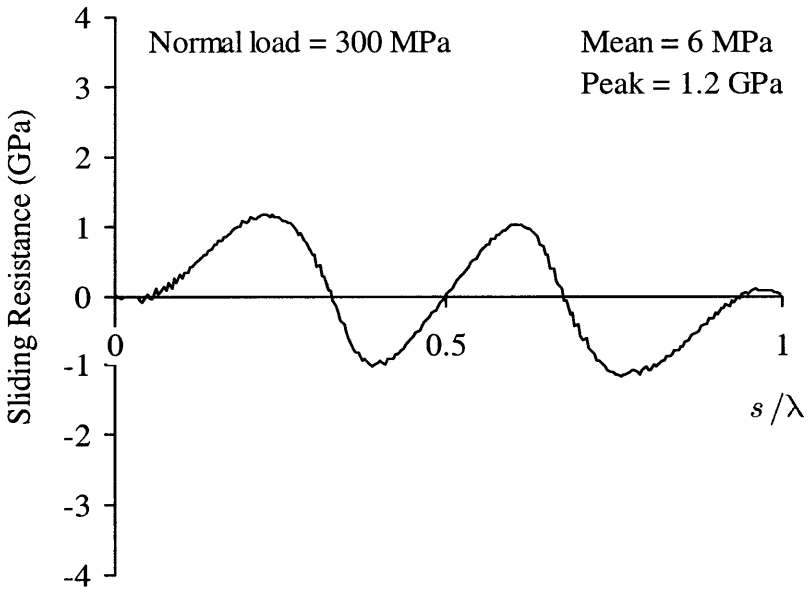

Figure 3–13: Sliding resistance of GB sliding system with $\varepsilon_{AB}/\varepsilon_{AA} = 0.2$.

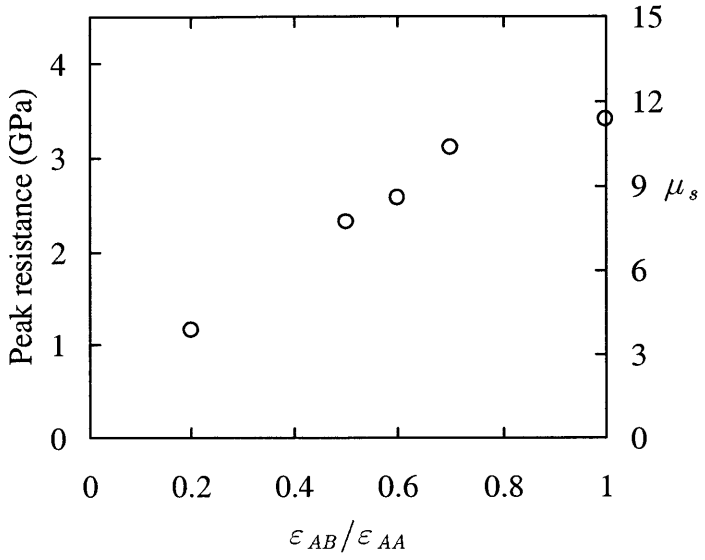

Figure 3–14: Peak resistance in GB sliding simulations. μ_s is the peak resistance divided by the normal load of 300 MPa.

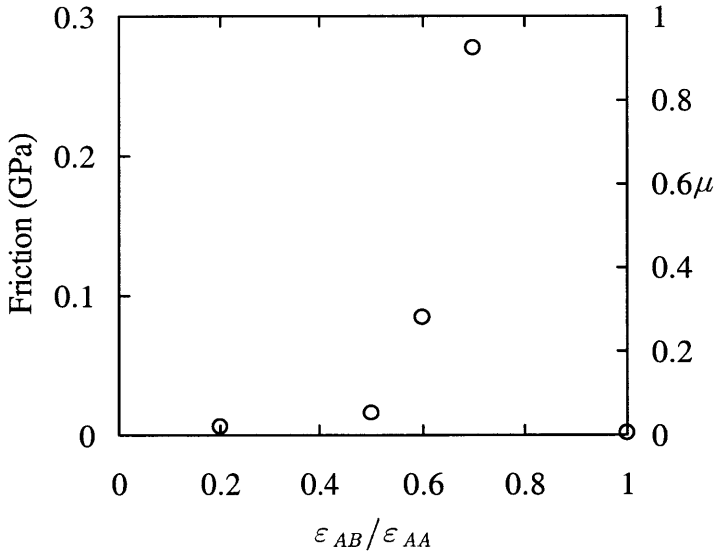

Figure 3–15: Friction (average sliding resistance) in GB sliding simulations. μ is friction divided by the normal load of 300 MPa.

constraint sliding scheme, the upper border would rapidly pass over the unstable regions. By the end of sliding, the configuration and potential energy return to the initial state. No potential energy is converted into kinetic energy by jump phenomena, so zero net thermal energy is extracted by the velocity rescaling scheme. Since the system energy (potential + kinetic) returns to the original value and there is zero net work or heat exchanged with the environment, this sliding process is reversible, as is expected for frictionless sliding.

3.4.4 Summary of Tilt GB Simulations

The peak and average sliding resistance and friction coefficient are plotted in Figures 3–14 and 3–15 to summarize the heterophase GB sliding simulations. In Figure 3–14, it can be seen that the peak resistance does not exactly have a linear relationship with $\varepsilon_{AB}/\varepsilon_{AA}$, unlike in the commensurate system. The linearity seems to apply for $\varepsilon_{AB}/\varepsilon_{AA} < 0.7$, but the $\varepsilon_{AB}/\varepsilon_{AA} = 1$ data point deviates from the linear trend. This may be related to the fact that sliding is coupled to migration for the pure GB. The average sliding resistance in Figure 3–15 demonstrates three regimes of sliding: frictionless sliding for $0 < \varepsilon_{AB}/\varepsilon_{AA} < 0.5$; frictional sliding from $\varepsilon_{AB}/\varepsilon_{AA} = 0.5$ to at least 0.7; and frictionless sliding–migration at the pure GB limit $\varepsilon_{AB}/\varepsilon_{AA} = 1$. The second ordinate in Figure 3–15 displays the friction coefficient, $\mu =$ Friction/Load. The highest friction coefficient of 0.93 is well in the range of typical experimental values of such metals as copper. It is recalled that the commensurate system predicts a much higher friction coefficient of over 30. This shows that by explicitly introducing a structural defect in the form of a GB to the model, much more realistic predictions of the friction coefficients are made possible.

3.5 Simulation of Symmetric Twist Boundary

3.5.1 Twist GB Characterization, Structure, and Energy

The symmetric twist GB is illustrated in the schematic of Figure 3–16. The twist axis is the [111] FCC axis, and the misorientation angle is 32.2°. Figure 3–17 shows the normal view of the unrelaxed boundary with outlines of the CSL, DSC, and unit cell lattices. This is a $\Sigma 13$ [111] symmetric twist GB. The translational period of the GB, $\lambda = 0.12$ nm, is equal to the x dimension of the DSC unit cell.

The GB energy is computed using Eqns. (1.5) and (1.6) over a relaxation of 50000 time steps under zero stress. This is a pure GB, meaning $\varepsilon_{AB} = \varepsilon_{AA}$. The picture of the relaxed interface is not shown because it is practically indistinguishable from the unrelaxed interface

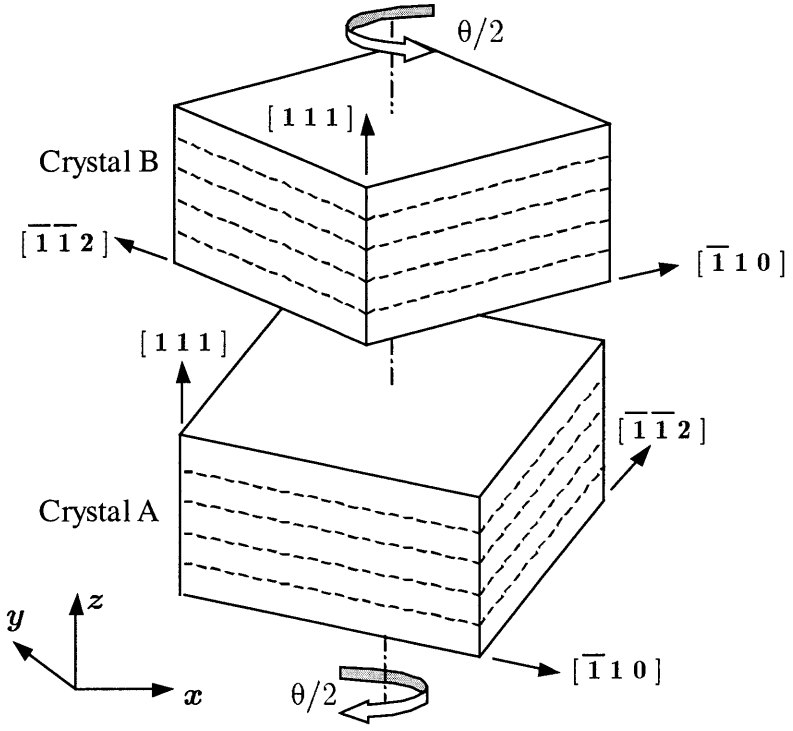

Figure 3–16: Schematic of Σ13 [111] symmetric twist grain boundary with $\theta = 32.2°$.

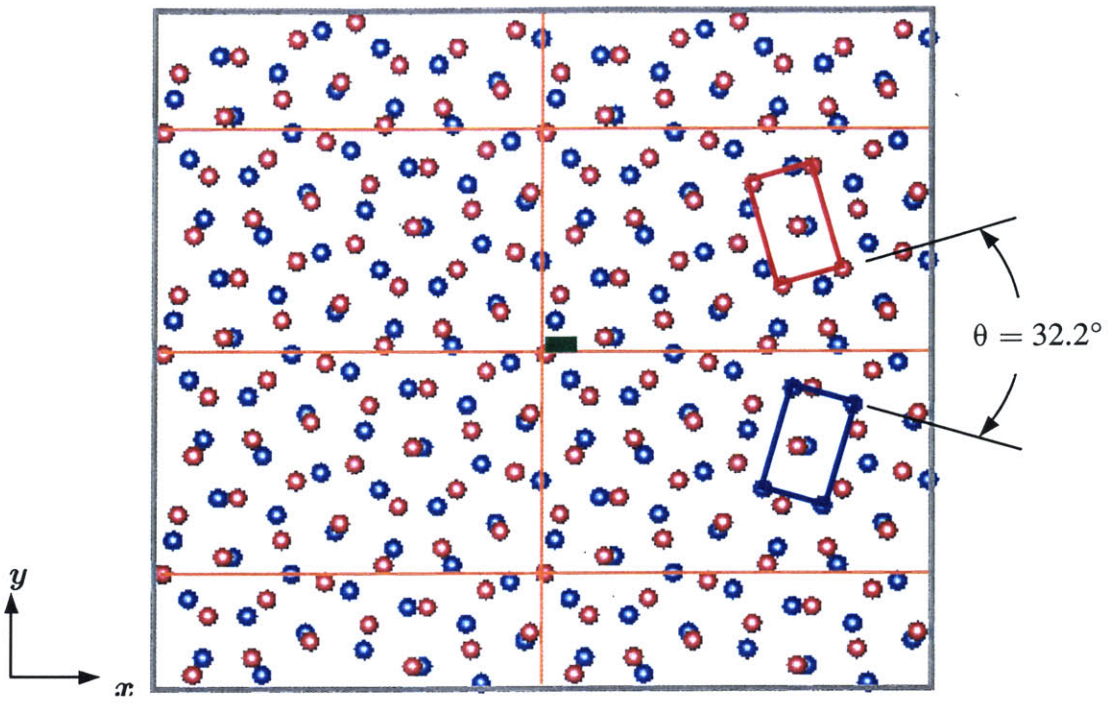

Figure 3–17: Overhead view of the unrelaxed atomic structure of Σ13 [111] symmetric twist GB. Only the two interfacial layers are shown. Blue and red spheres denote atoms of crystals A and B, respectively. The gray box outlines the simulation cell. The FCC lattice unit cells are outlined in blue and red while the CSL is outlined in orange. The DSC lattice unit cell is shown by the filled green block.

shown in Figure 3–17. The side view of the relaxed structure is shown in Figure 3–18 along with the scatter plot of the excess energy, where it can be seen that 99.6% of the excess energy is localized in the four atomic layers closest to the interface (two on each side of the interface). This gives the GB a thickness of 0.64 nm. The GB energy is 0.92 J/m^2, or equivalently $0.75(\varepsilon/\sigma^2)$, which is reasonably close to the value of $0.7(\varepsilon/\sigma^2)$ obtained by Wolf [21]. The twist GB energy is nearly four times less than the tilt GB energy calculated previously, and this is partially due to the fact that this particular twist boundary interface is the close packed plane and has less free volume than the tilt GB.

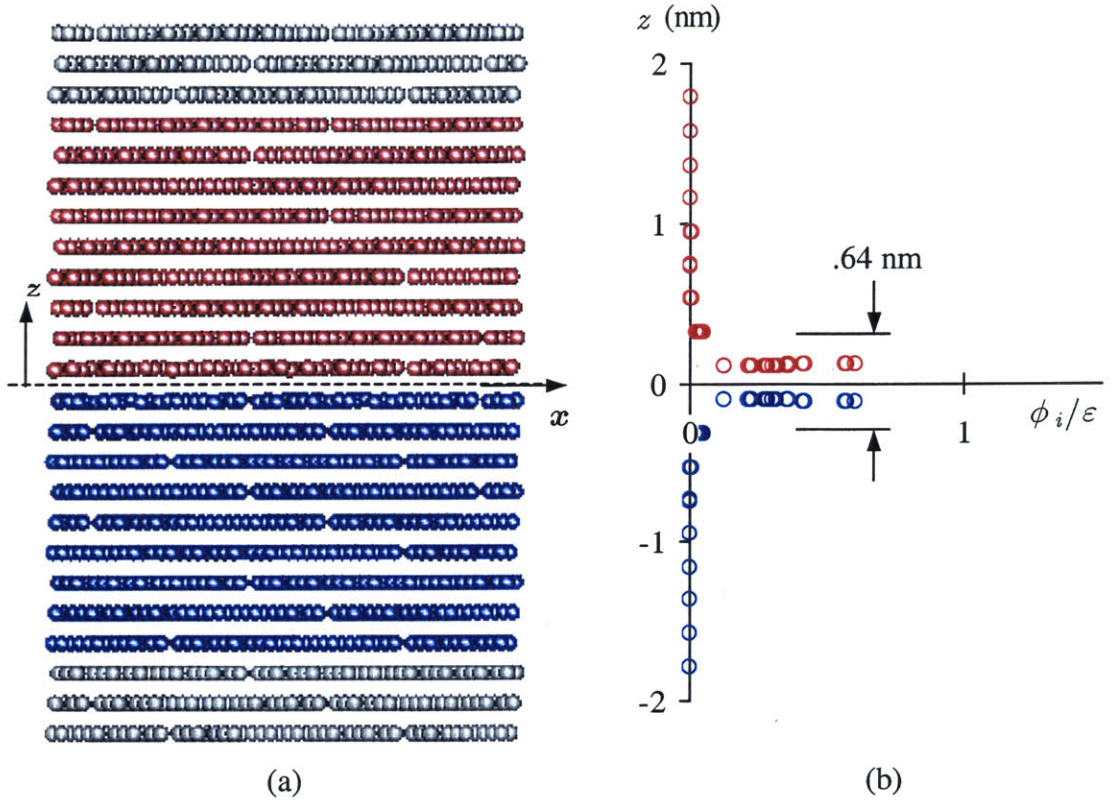

Figure 3–18: Relaxed twist grain boundary. (a) Side view. Blue and red spheres denote atoms of crystals A and B, respectively, and the gray spheres are the fixed atoms forming finite borders in the z direction. Periodic border conditions are applied in the x and y directions. (b) Excess energy of atoms with respect to their z–coordinates.

3.5.2 Twist GB Sliding

The sliding of the twist GB is done by the incremental displacement of the upper border in the x–direction over a full period, λ. Prior to sliding, the system is equilibrated under a 300 MPa normal compressive load, as usual. As a result of the load, the simulation cell undergoes normal strains of –0.0005 in the z–direction and 0.0001 in the x and y directions. The loaded system is then subject to sliding. Figure 3–19 shows overhead snapshots of the interface during various stages of sliding. It is clear that the layers slip past each other without any structural distortion, resembling a rigid body translation. By the end of the sliding (Figure 3–19d), the pattern has been shifted, but the overall GB structure is equivalent to the initial structure due to the effect of the periodic border conditions in the $x-y$ plane.

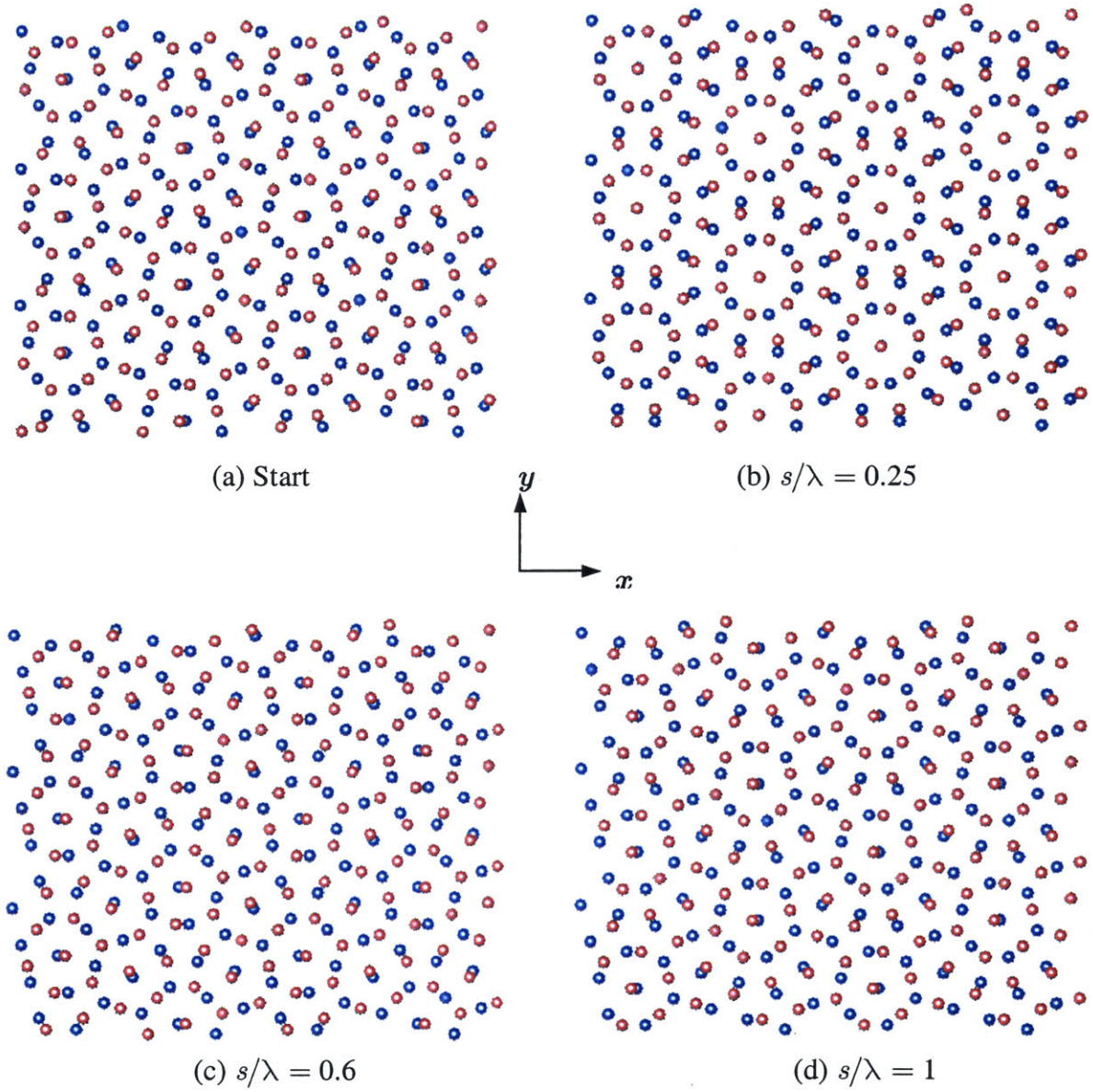

(a) Start (b) $s/\lambda = 0.25$

(c) $s/\lambda = 0.6$ (d) $s/\lambda = 1$

Figure 3–19: Snapshots of twist GB sliding.

The potential energy and sliding resistance are plotted in Figures 3–20 and 3–21, respectively. The absolute height of the energy hill is only 0.0002ε per atom, which is more than two orders of magnitude less than the kinetic energy of 0.092ε at the given temperature of 291 K. The average magnitude of the fluctuations in Figure 3–20 is comparable to the coarse features of the potential energy. The fluctuations are there because the dynamics causes the system configuration to constantly fluctuate, which in turn causes the system potential energy to fluctuate. Although the potential energy is averaged over an equilibration period, some of the fluctuation still remain because the equilibration may not be long enough. The fluctuations are not immediately apparent in the other potential energy curves (for example, Figures 3–5, 3–8, and 3–10) because the scale of those curves are much greater than the amplitude of the fluctuations. The important feature of Figure 3–20 is not so much the fluctuations, but rather the extremely low potential energy barrier. Such small energy variations have been observed for this particular GB by other investigators. For example, Wolf observed that horizontal translations have very little effect on the GB energy, a property he attributes to the fact that this GB involves the densest plane of the FCC lattice [21]. In a different study of (100) twist boundaries of aluminum, Wolf finds that while the Morse potential predicts negligible variations of the GB energy with translation, a pseudopotential predicts very high sensitivity, up to a 50% variation in energy [20]. His results suggest that the sensitivity of the energy to sliding is dependent on the potential function, and the Lennard-Jones potential could be partially responsible for the negligible sensitivity observed in the present case.

Interpreting the coarse features of Figure 3–20 and ignoring the fluctuations, it appears that the energy does return to its initial value by the end of sliding, which confirms that the sliding is periodic, as expected. The peak of the potential energy hill seems to occur around $s/\lambda = 0.25$. Figure 3–19b shows that at this point, the atoms are arranged in a pattern of circles, at the center of which is a direct overlap of atoms (the blue atoms are hidden under the red ones in the figure). Due to the fluctuations in the potential energy curve, it is difficult to determine if jump phenomena occur, although the overall scale of the energy variation is a convincing indication that jump phenomena probably do not occur in this case.

The sliding resistance in Figure 3–21 also contains fluctuations, which can be explained in the same way as the potential energy fluctuations. The peak and average values of the sliding resistance are 101 MPa and .4 MPa, respectively, the latter of which is negligible because it is much smaller than the average magnitude of the fluctuations. The resistance is zero around $s/\lambda = 0.25$, which corresponds to the maximum potential energy configuration. The resistance is also zero at $s/\lambda = 0.6$, and since the potential energy appears to be at a

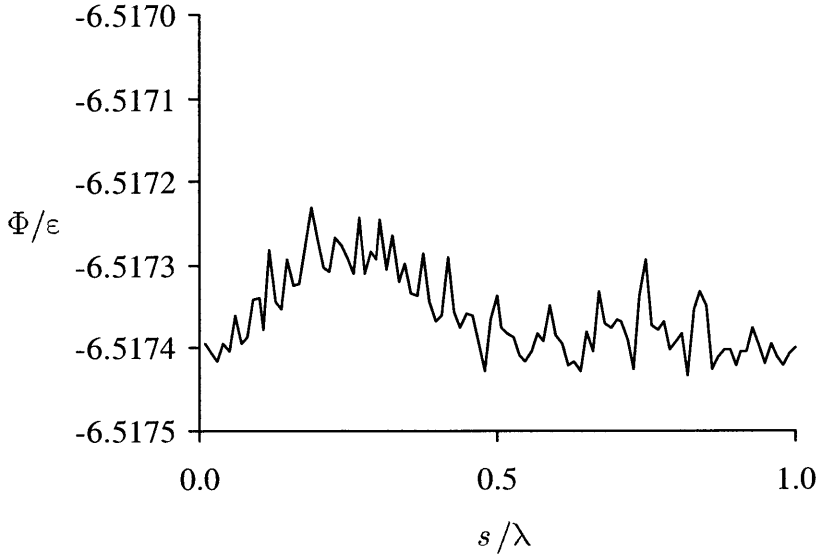

Figure 3–20: Potential energy per atom of twist GB sliding system.

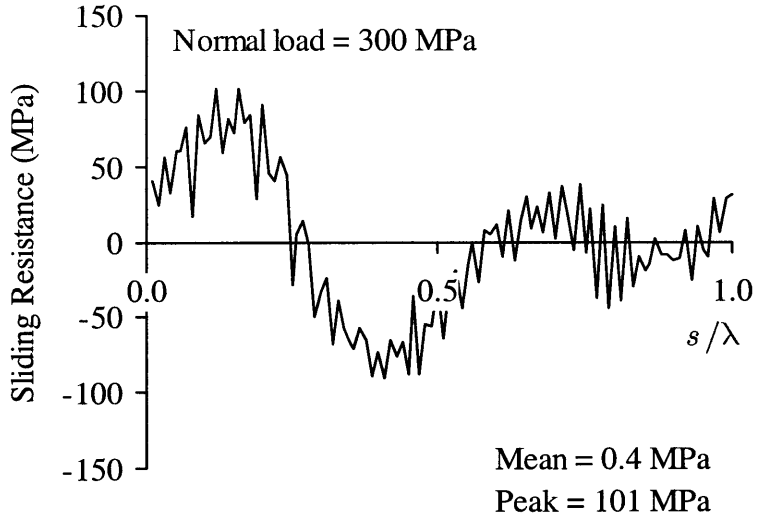

Figure 3–21: Sliding resistance twist GB sliding system.

minimum here, this structure shown in Figure 3–19c, is stable. Overall, this GB offers almost no resistance to sliding. At room temperature, the thermal energy alone would be enough to activate spontaneous slips. Considering that a commensurate interface of the same (111) system has a peak resistance of 12.8 GPa, the interface weakening effect of the twist misfit is rather remarkable.

3.6 Conclusions

The objective of this work was to use molecular dynamics (MD) simulations to study the atomic processes at the interface during grain boundary (GB) sliding. A fundamental issue which needed to be resolved was whether or not jump phenomena occur in GB sliding, as they do in the sliding of commensurate interfaces. Two types of GB's were modeled: the $\Sigma 5$ [100] (310) tilt and $\Sigma 13$ [111] symmetric twist GB's. In addition to the pure GB's, heterophase GB's were also studied by adjusting the interfacial atomic potential parameter, ε_{AB}. The following are the main conclusions from this work.

Tilt Boundary

- The GB energy, which is calculated for a relaxed system under zero pressure, is $2.8(\varepsilon/\sigma^2)$. This is with the interface in the kite structure. It turns out, however, that the kite structure is not the lowest energy configuration for this GB, as a relative sliding of the crystals results in a 10% reduction of the system potential energy. This result leads to the conclusion that this particular GB is highly sensitive to the relative positioning of the crystals.
- The sliding of the pure tilt GB is coupled by a migration mechanism, which is commonly observed for tilt GB's. The coupled motion is free of jump phenomena, or equivalently, the process is frictionless. The peak sliding resistance is 3412 MPa, which is 27% of the simulated ideal shear strength of a perfect crystal. This is a significant peak, particularly in light of the fact that the average resistance is practically zero. The sliding–migration coupling is unique in that it is the energetically favorable path compared to pure sliding, but it also avoids unstable configurations which trigger the jump phenomena.
- The heterophase GB has two regimes of sliding, frictional and frictionless, depending on the value of $\varepsilon_{AB}/\varepsilon_{AA}$, the ratio of the interfacial interaction strength to the bulk interaction strength. The frictional regime, $0.5 < \varepsilon_{AB}/\varepsilon_{AA} < 0.7$, is characterized by pure sliding (without migration) and the presence of jump phenomena. The jump phenomena

are triggered by the unstable nature of the kite structure at the GB. The frictionless regime, $\varepsilon_{AB}/\varepsilon_{AA} < 0.5$, is characterized by pure sliding without any jump phenomena.

- The friction in the heterophase GB system is much lower than the friction in commensurate systems due to the weakening effect of the GB. The highest friction coefficient computed from the present simulations is 0.93 about 17 times lower than that of a comparable commensurate system. The friction coefficient is well within the range typically observed in experiments, suggesting that the introduction of a defect in the form of a GB is a positive step in the direction of modeling realistic systems. The good agreement also helps to validate the MD model.

Twist Boundary

- The GB energy is $0.75(\varepsilon/\sigma^2)$, about 73% lower than the tilt GB energy. In addition, the twist boundary is almost completely insensitive to the relative positioning of the two crystals. The maximum difference in potential energy as a function of sliding is 0.0002ε per atom, which is over two orders of magnitude below the average kinetic energy of an atom at 291 K.
- Sliding occurs without migration. Based the potential energy curve, it appears that jump phenomena do not occur during sliding. The sliding resistance is also very low compared to the tilt boundary, with the peak of 101 MPa being 97% lower than the peak resistance of the tilt GB. The low resistance is related to the low energetic sensitivity to sliding.

3.7 References

1. Mate, C.M., McClelland, G.M., Erlandsson, R., and Chiang, S., "Atomic-Scale Friction of a Tungsten Tip on a Graphite Surface," *Physical Review Letters*, vol. 59, no. 17, pp. 1942-1945, 1987.
2. Ruan, J. and Bhushan, B., "Atomic-Scale and Microscale Friction Studies of Graphite and Diamond using Friction Force Microscopy," *Journal of Applied Physics*, vol. 76, no. 9, pp. 5022-5035, 1994.
3. Landman, U., Luedtke, W.D., and Ribarsky, M.W., "Structural and Dynamical Consequences of Interactions in Interfacial Systems," *Journal of Vacuum Science Technology A*, vol. 7, no. 4, pp. 2829-2839, 1989.
4. Landman, U., Luedtke, W.D., Burnham, N.A., and Colton, R.J., "Atomistic Mechanisms and Dynamics of Adhesion, Nanoindentation, and Fracture," *Science*, vol. 248, pp. 454-461, 1990.

5. Harrison, J.A., White, C.T., Colton, R.J., and Brenner, D.W., "Molecular-Dynamics Simulations of Atomic-Scale Friction of Diamond Surfaces," *Physical Review B*, vol. 46, no. 15, pp. 9700-9708, 1992.

6. Sørensen, M.R., Jacobsen, K.W., and Stoltze, P., "Simulations of Atomic-Scale Sliding Friction," *Physical Review B*, vol. 53, no. 4, pp. 2101-2113, 1996.

7. Buldum, A. and Ciraci, S., "Contact, Nanoindentation, and Sliding Friction," Physical Review B, Vol. 57, No. 4, pp. 2468-2476, 1998.

8. Tomlinson, G.A., "A Molecular Theory of Friction," *Philosophical Magazine*, ser. 7, vol. 7, no. 46, pp. 905-939, 1929.

9. McClelland, G.M., "Friction at Weakly Interacting Interfaces," in Adhesion and Friction, Springer Series in Surface Sciences, vol. 17, Eds. Grunze, M. and Kreuzer, H.J., Springer Verlag, pp. 1-16, 1989.

10. Hirano, M. and Shinjo, K., "Atomistic Locking and Friction," *Physical Review B*, vol. 41, no. 17, pp. 11837-11851, 1990.

11. Hirano, M., Shinjo, K., Kaneko, R., and Murata, Y., "Anisotropy of Frictional Forces in Muscovite Mica," *Physical Review Letters*, vol. 67, no. 19, pp. 2642-2645, 1991.

12. Van Swygenhoven, H. and Caro, A., "Plastic Behavior of Nanophase Ni: A Molecular Dynamics Computer Simulation," *Applied Physics Letters*, vol. 71, no. 12, pp. 1652-1654, 1997.

13. Keblinski, P., Wolf, D., and Gleiter, H., "Molecular-Dynamics Simulation of Grain-Boundary Diffusion Creep," *Interface Science*, vol. 6, pp. 205-212, 1998.

14. Heino, P. and Ristolainen, E., "Strength of Nanoscale Polycrystalline Copper Under Shear," *Philosophical Magazine A*, vol. 81, no. 4, pp. 957-970, 2001.

15. Kwok, T., Ho, P.S., Yip, S., Balluffi, R.W., Bristowe, P.D., and Brokman, A., "Evidence for Vacancy Mechanism in Grain Boundary Diffusion in bcc Iron: A Molecular-Dynamics Study," *Physical Review Letters*, vol. 47, no. 16, pp. 1148-1151, 1981.

16. Bishop, Jr., G.H., Harrison, R.J., Kwok, T., and Yip, S., "Computer Molecular-Dynamics Studies of Grain-Boundary Structures. I. Observations of Coupled Sliding and Migration in a Three-Dimensional Simulation," *Journal of Applied Physics*, vol. 53, no. 8, pp. 5596-5608, 1982.

17. Bishop, Jr., G.H., Harrison, R.J., Kwok, T., and Yip, S., "Computer Molecular-Dynamics Simulation Studies of Grain-Boundary Structures. II. Migration, Sliding, and Annihilation in a Two-Dimensional Solid," *Journal of Applied Physics*, vol. 53, no. 8, pp. 5609-5616, 1982.

18. Kwok, T., Ho, P.S., and Yip, S., "Molecular-Dynamics Studies of Grain Boundary Diffusion. I. Structural Properties and Mobility of Point Defects," *Physical Review B*, vol. 29, no. 10, pp. 5354-5362, 1984.

19. Kwok, T., Ho, P.S., and Yip, S., "Molecular-Dynamics Studies of Grain Boundary Diffusion. II. Vacancy Migration, Diffusion Mechanism, and Kinetics," *Physical Review B*, vol. 29, no. 10, pp. 5363-5371, 1984.

20. Wolf, D., "Effect of Interatomic Potential on the Calculated Energy and Structure of High-Angle Coincident Site Grain Boundaries – I. (100) Twist Boundaries in Aluminum," *Acta Metallurgica*, vol. 32, no. 2, pp. 245-258, 1984.

21. Wolf, D., "A Broken-Bond Model for Grain Boundaries in Face-Centered Cubic Metals," *Journal of Applied Physics*, vol. 68, no. 7, pp. 3221-3236, 1990.

22. Rickman, J.M., Phillpot, S.R., Wolf, D., Woodraska, D.L., and Yip, S., "On the Mechanism of Grain-Bondary Migration in Metals: A Molecular Dynamics Study," *Journal of Materials Research*, vol. 6, no. 11, pp. 2291-2304, 1991.

23. Marinopoulos, A.G., Vitek, V., and Carlsson, A.E., "Significance of Non-Central Forces in Atomistic Studies of Grain Boundaries in BCC Transition Metals," *Philosophical Magazine A*, vol. 72, no. 5, pp. 1311-1330, 1995.

24. Keblinski, P., Phillpot, S.R., Wolf, D., and Gleiter, H., "Thermodynamic Criterion for the Stability of Amorphous Intergranular Films in Covalent Materials," *Physical Review Letters*, vol. 77, no. 14, pp. 2965-2968, 1996.

25. Chandra, N. and Dang, P., "Atomistic Simulation of Grain Boundary Sliding and Migration," *Journal of Materials Science*, vol. 34, pp. 655-666, 1999.

26. Kurtz, R.J., Hoagland, R.G., and Hirth, J.P., "Computer Simulation of Extrinsic Grain-Boundary Defects in the Sigma-11, <101>{131} Symmetric Tilt Boundary," *Philosophical Magazine A*, vol. 79, no. 3, pp. 683-703, 1999.

27. Yip, S., "The Strongest Size," *Nature*, vol. 391, pp. 532-533, 1998.

28. Zhen, S. and Davies, G.J., "Calculation of the Lennard-Jones n-m Potential Energy Parameters for Metals," *Physica Status Solidi A*, vol. 78, pp. 595-605, 1983.

29. Parrinello, M. and Rahman, A., "Polymorphic Transitions in Single Crystals: A New Molecular Dynamics Method," *Journal of Applied Physics*, vol. 52, no. 12, pp. 7182-7190, 1981.

30. Allen, M.P. and Tildesley, D.J., **Computer Simulation of Liquids**, Clarendon Press, Oxford, 1987.

CHAPTER 4

Molecular Dynamics Simulation of Amorphous System

4.1 Introduction

Nanotribology, or the study of friction and wear at the atomic scale, has received considerable attention in the past decade from both the theoretical [1-3] and experimental [4-6] standpoint. In particular, computer simulations have been very helpful in improving the understanding of the tribological processes at the atomic scale. For instance, molecular dynamics (MD) simulations of dry friction [7-11], boundary lubrication [12-14], elastohydrodynamic lubrication [15], nanocutting [16], and nanoindentation [17] have been used to successfully model phenomena directly at the contact region. So far, most simulations of friction have been focused on crystalline systems with commensurate or incommensurate sliding interfaces, which have yielded interesting results regarding atomic-scale frictional mechanisms. Among them, the *jump phenomenon*, also called *plucking* or *atomic stick-slip*, has been repeatedly mentioned to be the principal mechanism of atomic scale friction [1-3,7-9,12]. This is not to say that absolutely no other mechanisms of friction exist, just that none other have been detected by the models, which are predominantly of the MD variety and consist of conservative interatomic potential functions. A jump phenomenon is a catastrophic process by which the interface, having encountered an unstable configuration, suddenly slips to a new, stable configuration. In the process, stored potential energy is converted into kinetic energy of the atoms. The kinetic energy, or equivalently the thermal energy, is subsequently dissipated away. An appealing element of this theory is that it bears close resemblance to the macroscopic understanding of friction, namely the work-to-heat conversion that always accompanies frictional sliding. It may be noted that sliding can take place in the model without any jump phenomena, but if jump phenomena do not occur, the sliding is frictionless, and vice-versa.

There still remains much uncharted territory in the area of atomic-scale friction modeling, especially regarding amorphous sliding interfaces, which is a most relevant topic in light of the recent discovery of the excellent tribological properties of amorphous carbon [18-21], also called diamond-like carbon (DLC). For instance, vapor-deposited DLC films with thickness in the micron range have been reported to deliver a friction coefficient of the order

of 0.001 [20,21], which is at least an order of magnitude lower than the friction in standard ceramic hard coatings [22]. While it has been suggested that the low friction in DLC is primarily the consequence of its high hardness and favorable chemical properties [20, 23-25], the intrinsic effect of the amorphous structure on the sliding behavior has not received much discussion. Yet the fundamental differences between amorphous and crystalline materials in terms of their mechanical properties and behavior, and past revelations that the sliding behavior at the atomic scale is exceptionally sensitive to the interfacial structure [9], prompt the investigation into the characteristic sliding behavior of amorphous systems.

Although the study of amorphous sliding systems is scarce in the literature, there exists a rich history of work in the modeling of amorphous materials in general, dating back to Bernal's famous treatment of liquids as a dense random network of spheres [26], followed by theoretical models of the plastic deformation mechanisms of metallic glasses [27-29]. In addition, soap bubble rafts have proved useful for the visualization and analysis of plastic flow in a 2D amorphous network [30]. Some early computer simulations of the deformation of amorphous metals are also worth mentioning [31-36] for their contributions of many useful simulation techniques, such as the melting–quenching preparation of amorphous systems, for example [33]. In regard to the geometric characterization of the amorphous structure, the Voronoi polyhedron construction [37,38] is the most widely accepted method, having been applied consistently to hard sphere systems [39] and Lennard-Jones systems [40,41], among others. More recent contributions in the area of computer modeling include the simulation of the thermal conductivity of glass [42], fracture in amorphous iron [43], nano-indentation of amorphous carbon films [44], and the deposition and growth of DLC films [45,46], Furthermore, ab-initio and tight binding studies of DLC have also been conducted [47-49].

In light of the evident interest in the mechanical behavior of amorphous materials, and the ongoing need for new information that can lead to developments in low friction technology, the present work investigates the atomic processes associated with dry sliding friction in an amorphous system using MD simulations. This chapter is organized as follows. Section 4.2 presents the MD simulation details as well as the methodology involved in the simulation of sliding. In Section 4.3, the amorphous system is prepared by a melting-quenching simulation, and the structure of the amorphous system is characterized using the Voronoi polyhedron construction, among other methods. Section 4.4 presents the results of the sliding simulation, with an emphasis on the occurrence of local jump phenomena. Section 4.5 discusses a very interesting observation of the sliding-induced crystallization of the amorphous material. The computed friction from sliding simulations is summarized and

compared to result from an analogous crystalline system in Section 4.6, and overall conclusions are given in Section 4.7.

4.2 Molecular Dynamics Simulation Methodology

4.2.1 Potential Function

All systems in this work are modeled using the Lennard-Jones (L–J) 12–6 pair potential,

$$\phi\left(r_{ij}\right) = 4\varepsilon\left[\left(\frac{\sigma}{r_{ij}}\right)^{12} - \left(\frac{\sigma}{r_{ij}}\right)^{6}\right], \tag{4.1}$$

which describes the potential energy between the pair of atoms i and j separated by a distance of r_{ij}. The L–J parameters ε and σ are related to the interatomic bond energy and the atomic diameter, respectively, and a unique pair defines the model material. The L–J parameters used in this work are fitted to the specific volume and vaporization enthalpy of copper [50] (the values of the parameters are given in later sections). Copper is chosen simply as a representative material, so that the simulations may reflect the typical behavior of common metals. It is emphasized that the intention of the present work is not to predict the properties of any one specific material, this being an important point in light of the fact that pure copper is not known to exist in the amorphous state. In contrast, the objective is to reveal general trends in the sliding behavior of amorphous systems through a parametric study, and the present system should be viewed as a generic L–J material rather than a specific material.

4.2.2 Boundary Conditions

Two types of boundary conditions are employed in this work, *periodic boundary conditions* for bulk modeling of the melting-quenching process and *finite border conditions* for the modeling of sliding. The periodic boundary conditions are used in conjunction with the famous Parrinello-Rahman (P–R) method [51] in order to simulate under constant hydrostatic pressure. The P–R method treats the simulation cell walls as dynamics elements capable of translational and rotational motion, to the effect that the cell dimensions fluctuate about an equilibrium size and shape corresponding to the desired state of stress. Any further details about the P–R method can be obtained in the original reference. In this work, the

shear deformations of the cell are suppressed, so that the cell is constrained to always keep a tetragonal shape.

In the presence of a bimaterial interface, fully periodic boundary conditions are not valid for the sliding simulation, and so boundary conditions containing finite borders need to be employed. A schematic of a system with such boundaries is displayed in Figure 4–1. Periodic boundary conditions are disabled in the in the z direction and replaced by the finite borders, which are essentially blocks of fixed atoms. The fixed atoms are static and lie *outside* of the simulation cell. In the x and y directions, periodic boundary conditions are still applied, essentially creating the effect of an infinitely repeating interface. The fixed atoms are arranged into a random structure to be consistent with the rest of the system. The procedure for the determination of the fixed atom positions is discussed later.

Similar to the P–R method, a constant stress state is maintained in the finite border system by allowing the cell walls to move during the simulation. The stress of a system with finite borders is given by:

$$\boldsymbol{\tau} = -\frac{1}{V}\left[\sum_i m_i \mathbf{v}_i \mathbf{v}_i' + \sum_i \sum_{j>i} \mathbf{r}_{ij}\mathbf{f}_{ij}' + \sum_i \sum_k \tilde{\mathbf{r}}_{ik}\mathbf{f}_{ik}'\right], \tag{4.2}$$

where V is the volume of the simulation cell, m_i is the mass of atom i, $\mathbf{v}_i$ is its velocity vector, $\mathbf{r}_{ij} = \mathbf{r}_i - \mathbf{r}_j$, and $\mathbf{r}_i$ and $\mathbf{r}_j$ are the coordinate vectors of atoms i and j. The primes denote the transpose of the column vectors. Indices i and j loop over only the dynamic atoms inside the cell, while k represents only the fixed atoms of the borders. The tilde, as in $\tilde{\mathbf{r}}_{ik}$, denotes that only the interior portion of the spatial vector is to be used, and this applies only when atom i (always inside the cell) interacts with fixed atom k (always outside the cell). The force exerted on atom i by j, denoted by $\mathbf{f}_{ij}$ (or $\mathbf{f}_{ik}$, when a fixed atom is involved), is related to the derivative of the potential function,

$$\mathbf{f}_{ij} = -\frac{d\phi}{dr_{ij}}\frac{\mathbf{r}_{ij}}{r_{ij}}. \tag{4.3}$$

The method of maintaining a constant stress in the finite border system is conceptually similar to the P–R method. As the cell changes size and shape, the finite borders also undergo deformations along with the deforming cell. This means that the fixed atoms undergo displacements associated with the uniform strain of the border, but they do not exhibit individual motion. The shear deformations of the cell are suppressed in this work. The derivation of the finite border conditions are presented in full detail in Appendix C.

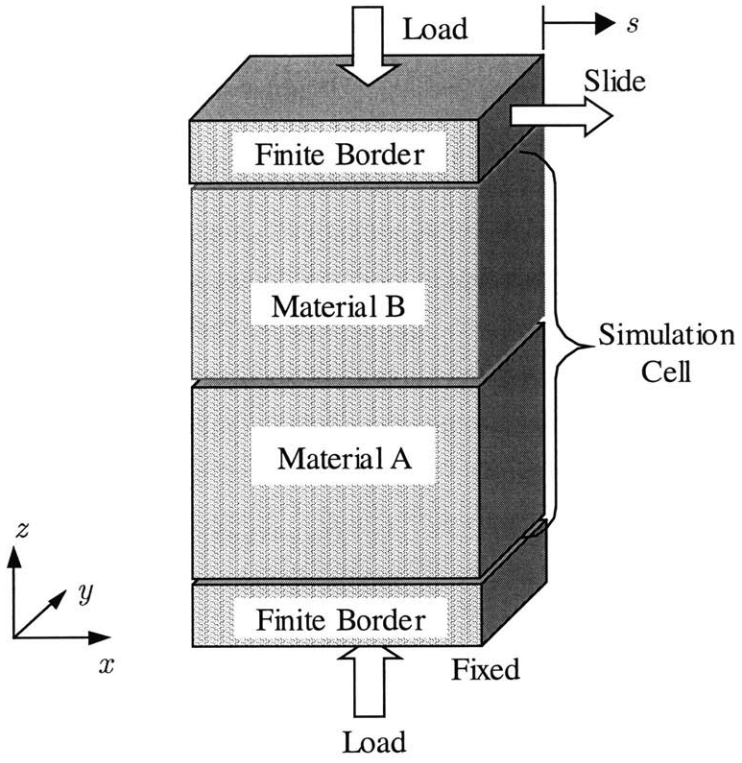

Figure 4–1: Schematic of MD cell for the sliding simulation of amorphous system. Periodic boundary conditions are applied in the x–y plane. Finite borders are used in the z direction.

4.2.3 Loading and Sliding Methodology

The simulation of sliding follows a three-step procedure: relaxation, loading, and sliding. During the first step, the system is simulated under zero stress and constant temperature for at least 50,000 time steps, which is approximately equivalent to 200 atomic oscillations. This is done to allow the system to reach equilibrium. The normal load is then applied by taking the output file (atomic positions and velocities) from the relaxation simulation and using it as the input to a new simulation where the stress is set to the desired value. Only a compressive normal stress in the z direction is applied, and the normal stresses in the x and y directions are kept at zero. Since the entire normal load is applied instantaneously, 50,000 time steps are given for the system to fully equilibrate to the load. The output at the end of this equilibration is then used as the input to the sliding simulation.

Sliding is imposed by incremental displacements of the upper border in the x direction (see Figure 4–1) while holding the lower border in place. The size of the increment is less than 1/10 of the average amplitude of atomic vibration at the given temperature (see Appendix B). After each increment, 5000 time steps are allowed for equilibration prior to the execution of the next sliding step. This is done so that the entire system can feel the effect of the moving border. The 5000 steps is equivalent to 20 atomic oscillations, and mean-square displacement data confirm that the system consistently reaches equilibrium during this span.

4.2.4 Potential Energy and Sliding Resistance

During sliding, relevant properties such as the potential energy and sliding resistance are computed with respect to s, the total displacement of the upper border. The potential energy is calculated by simply summing up all pair potentials,

$$\Phi = \frac{1}{2N}\overline{\sum_i \sum_{j \neq i} \phi\left(r_{ij}\right)}, \tag{4.4}$$

where i loops over only the dynamic atoms while j loops over all dynamic and fixed atoms. The normalization factor N is the total number of dynamic atoms (A and B combined), and the factor of 1/2 compensates for double counting. The overhead bar denotes averaging over the equilibration period after each sliding displacement. The *sliding resistance* is equal to $\overline{\tau}_{zx}$, the shear component of the internal stress of Eqn. (4.2), also averaged over the equilibration period. The sliding resistance is exactly the shear stress exerted by the rigid border on the upper face of the cell (and vice-versa) in equilibrium. There must be an external stress acting on the border to balance the stress from the cell if mechanical equilibrium is to be satisfied. The sliding resistance is equivalent to this external stress. At the atomic scale, sliding is often periodic, meaning that all state properties of the system such as the configuration, energy, stress return to the initial values after a unit distance of sliding, which can be the lattice parameter of a crystal, for example. In such cases, the integral of the resistance-distance curve over a period is equal to the net work done per unit area by the external force, or equivalently, the average of the resistance over a period can be interpreted as the friction per unit area per unit distance slid.

4.2.5 Additional Simulation Details

The atomic motions are numerically integrated using the 5th order Gear predictor-corrector method. All simulations use rescaling of the particle velocities at every time step in order to maintain the temperature at 291 K. The usual methods such as the potential cutoff at 2.5σ, neighbor list, and the minimum image criteria are applied to improve computational efficiency.

4.3 Preparation of the Amorphous System

4.3.1 System Description

Before any sliding simulations can be conducted, the amorphous medium must be prepared, meaning that the positions and velocities of the atoms in the MD cell must be defined. The velocities can simply be assigned randomly, as usual, but the assignment of the atomic positions requires a little more effort. The preferred method of generating the atomic coordinates is the simulated melting-quenching technique, which begins with the atoms arranged into the well-behaved FCC lattice. The atoms are initially assigned velocities according to a random distribution corresponding to a solid-state temperature. The temperature is then raised sequentially by scaling up the atomic velocities until the system melts, after which the temperature is rapidly dropped. Performed properly, the quenching traps the system in a metastable state with a random configuration lacking long-range order. There are a number of advantages to the melting-quenching method over a random position assignment scheme. First, there is no risk of creating an unphysical configuration, a problem common to random coordinate generation. Second, the melting-quenching process is more intuitive and realistic than using random numbers.

Table 4–1 lists all of the physical details of the system that apply to the melting-quenching simulation. During this portion, periodic boundary conditions are applied in all directions, and the system is treated as a bulk material. Parameters for the L–J potential function are given in Table 4–2, and as stated earlier, these values represent copper. The atoms are initially arranged into with 24 FCC (111) layers stacked in the vertical (z) direction. Parrinello-Rahman boundary conditions are used in order to conduct the entire melting-quenching simulation under zero hydrostatic stress, although shear stresses are prone to develop because the shear deformations of the simulation cell are suppressed. There are a number of reasons for using the fully periodic border conditions rather than the finite border conditions. For melting to occur, the atoms must be able to move around diffusively, but the presence of finite borders takes away a degree of freedom from the atoms near the borders.

The finite borders may also exhibit the no-slip condition associated with the fluid mechanics of channel flow, leading to the development of viscous effects which hinder the melting process by limiting the mobility of the atoms in the entire system. Finally, the lattice structure of the finite borders may be imparted onto the atoms near the border, resulting in solid boundary layers which resist melting even at excessively high temperatures.

Table 4–1: Parameters for melting-quenching simulation.

Number of atoms	2880
Simulation cell dimensions ($x \times y \times z$)	$2.656 \times 2.556 \times 5.009$ nm
Mass of atom	1.06×10^{-22} g (copper)
Mass of dynamic cell walls (for P–R method)	1.06×10^{-21} g
Time step	10^{-15} s
Temperature (by velocity rescaling)	291 K

Table 4–2: Lennard-Jones parameters for melting-quenching simulation.

$\varepsilon/k_b = 4733.5$ K	$\sigma = 0.23127$ nm

$k_b = 1.38 \times 10^{-23}$ J/K (Boltzmann's constant)

4.3.2 Melting

The crystal is relaxed at 291 K and zero pressure for 20,000 time steps. The temperature is then raised instantaneously to 500 K by scaling up the particle velocities, and the system is again relaxed for 20,000 time steps at the new temperature and zero pressure. It will be shown shortly that the isobaric elevation of the temperature results in a volume increase, thus satisfying the expected thermodynamic relations. The temperature is next increased

systematically to 1000, 1500, 2000, 2500, 3000, 3100, 3200, 3210, 3220, 3230, 3250, and 3300 K, with each increase executed instantaneously and followed by a 20,000 time step relaxation under zero pressure. At every temperature, the system volume is averaged over the relaxation period. Figure 4–2 shows the resulting temperature-volume diagram of the melting process, where a nonlinear thermal expansion of the system volume is observed up to 3230 K. The thermal expansion is a product of the anharmonic nature of the L–J potential. As a consequence of the nonlinear expansion, the thermal expansion coefficient varies with temperature. The volumetric thermal expansion coefficient at 291 K, computed from the initial slope of the curve, is equal to 35.4×10^{-6} K^{-1}, which is correct to an order of magnitude to the experimental value of 51×10^{-6} K^{-1} for copper at room temperature. The agreement is satisfactory, particularly in light of the fact that the thermal expansion properties were not considered in the fitting of the present L–J parameters.

The sudden increase in the volume at 3230 K ($k_B T/\varepsilon = 0.682$ in reduced units) in Figure 4–2 is clear evidence of a solid-liquid phase change. This melting temperature is significantly higher than the experimental value of 1357 K for copper. The reason for the discrepancy is that the model solid is defect-free and does have free surfaces, leaving no nucleation sites for melting to begin. Consequently, melting does not occur until the system thermally expands to the point that the structure becomes mechanically unstable, at which time a homogeneous collapse of the lattice takes place. This mechanism of melting, often called mechanical melting, requires a much higher temperature than the more familiar thermodynamic melting, which is a nucleation-assisted process. In a clever MD study of silicon with free surfaces, Phillpot et al. [52] observed the surface nucleation of melting and the ensuing propagation of the melt front into the bulk crystal. Their prediction of the melting point agreed very well to the experimental value. The implication for the present study is that a better prediction of the melting point can be obtained by implementing a free surface in the system, but this would be a diversion from the main focus of the investigation.

The system is then simulated at 3300 K for 100,000 more time steps, followed by 100,000 steps at 3400 K. This extensive simulation in the liquid state is done to ensure full melting, in order to avoid any residual crystalline clusters which may be potential nucleation sites for crystallization during the ensuing quenching stage. The monotonic increase in the mean square displacement of Figure 4–3a is an indication of the diffusive behavior of the atoms, confirming that the system is indeed, in the liquid state. Furthermore, the radial distribution function in Figure 4–3b illustrates that the FCC second neighbor peak has vanished, which provides further evidence that the system is a liquid.

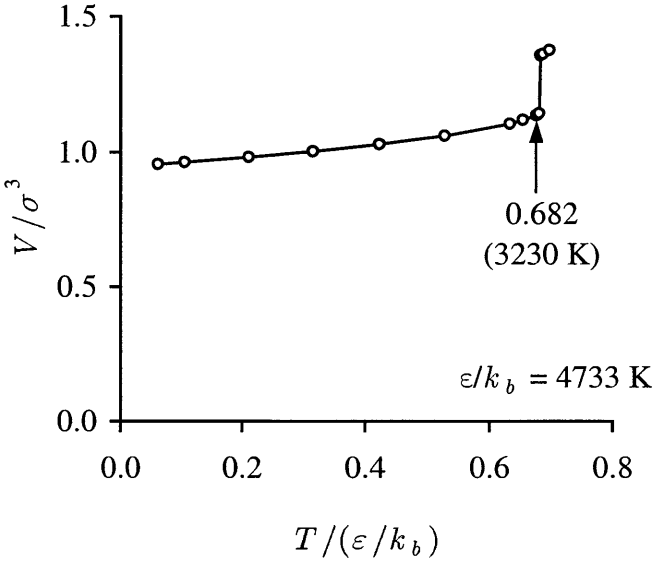

Figure 4–2: Temperature-volume (T–V) diagram of the melting process. V is the volume per atom normalized by the L–J parameter σ^3. The temperature is normalized ε/k_B = 4733 K, where ε is the L–J parameter and k_B is Boltzmann's constant.

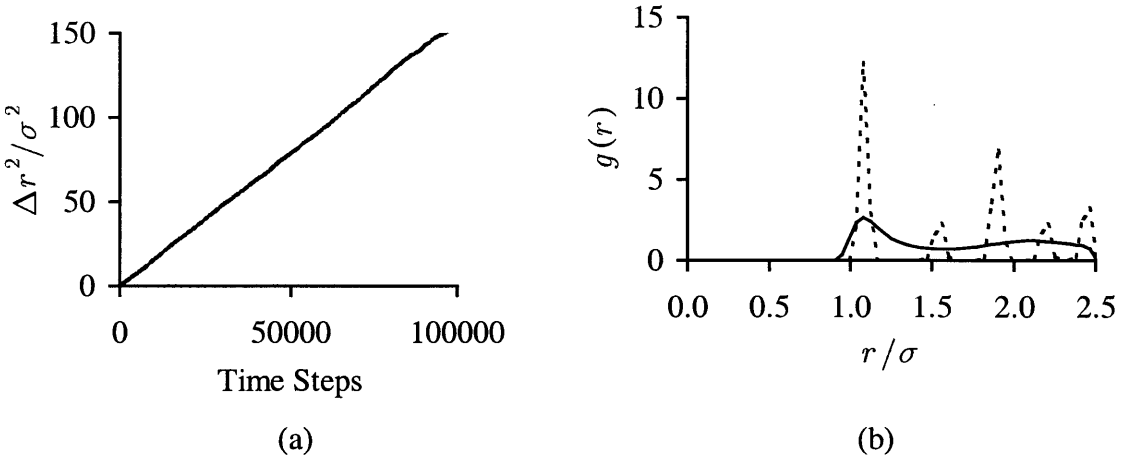

Figure 4–3: Melted system at 3400 K. (a) Mean squared displacement, Δr^2, normalized by σ^2. (b) Radial distribution function, $g(r)$. The dotted curve represents the radial distribution function of an FCC crystal at 291 K and zero pressure.

4.3.3 Quenching

The melted system is quenched by instantaneously dropping the temperature back to 291 K, and afterward the system is simulated at zero pressure for 100,000 time steps. The quenched system, shown in Figure 4–4a, certainly appears to have lost structural order, based on a visual inspection, alone. The mean square displacement (MSD) in Figure 4–4b flattens out after an initial climb, which is an indication that the atoms do not behave diffusively as in the liquid state, but rather oscillate about equilibrium positions, which implies that the system is in the solid state. Figure 4–4b also indicates that even in the flat region, the MSD still increases very slowly over time, suggesting that there is a slow time-scale relaxation taking place in the quenched system. Upon closer examination, the increase in the MSD appears mainly to be the result of a series of isolated events rather than a continuous increase. Such behavior may be linked to random relaxations occurring locally throughout the medium. The quenching process invariably results in the development of a number of local regions of high energy and stress concentration, and the thermal energy, given a long enough time, is able to activate structural transformations of some of the local regions in the direction of lower energy and stress. Such relaxation events would show up as sudden increases in the MSD curve. The radial distribution function (RDF) in Figure 4–4c does not have the FCC second-neighbor peak, which indicates that the structure lacks long range order, similar to the liquid. Also, the split peak near $r/\sigma = 2.0$ is a well-known characteristic feature of random close packing associated with amorphous materials.

The volume per atom of this amorphous system is $1.011\sigma^3$, an excess of 5.9% relative to a crystal at the same temperature. Kristensen [53] found a similar excess volume of 6% in an MD simulation of a Lennard-Jones amorphous system at zero pressure. In contrast, Finney obtained a value of 16.3 % for a model of random packed hard spheres [39]. Some of this discrepancy can be attributed to the fact that the hard sphere model does not account for any attractive forces between the spheres, whereas the L–J potential features a short-range attraction which tends to pack atoms closer, and this effect may be especially influential in the amorphous structure where the atoms are not in the densest packing structure. However, based on Bernal's proposition that the structure of amorphous solids is determined mostly by the repulsive forces [26], it is not rational to claim that the attraction alone accounts for the entire discrepancy between the L–J system and the hard sphere system. Another possible explanation may be that the structure of the present amorphous system, as a consequence of the well-known tendency of pair potentials to form the close-packed structure, may be far from the limit of maximum randomness. The hard sphere model is only driven by the one-dimensional force of gravity, which may enable it to better resist close packing and achieve

near-maximum randomness. In concluding the present discussion regarding the excess volume, it may be noted that a typical crystal-glass expansion for many metal and alloys is only about 1.5 % [54], which implies that the both L–J and the hard-sphere models overpredict the volume increase of real amorphous materials.

4.3.4 Structural Analysis of Amorphous System

The system volume and the RDF analyses in the previous section yield information only at the volumetric level and are often insufficient to completely characterize the amorphous structure. Since structural heterogeneity is a unique feature of amorphous systems, it is worthwhile to devote some effort into a more thorough investigation of its topological features. This section characterizes the amorphous system at the local level using the neighbor distribution and Voronoi polyhedron statistics.

The coordination number, which is defined as the number of its nearest neighbors, is an important parameter concerning the mechanical behavior of amorphous materials. Given that r_{ij} is the distance separating atoms i and j, atom j is a nearest neighbor of atom i (and vice-versa) if $r_{ij} < 1.319\sigma$. The value of 1.319 is simply the average of the distances of the first and second peaks in the RDF of the crystal at 291 K (see Figure 4–4c, dotted curve). Likewise, j is a second nearest neighbor of i if $1.319\sigma < r_{ij} < 1.708\sigma$. In a close-packed structure like the FCC lattice, every atom is 12-coordinated, but in the present amorphous system, the average coordination number is calculated to be 11.6 (see Table 4–3). There is a broad scatter of values, as indicated by the 6.8% standard deviation. Figure 4–5 shows the histogram of coordination numbers in the system, where it is shown that most of the atoms (45%) are 12-coordinated, with 11-coordinated atoms being the next most populous. The implication is that close packing may still exist at many local sites, even if the structure lacks long range order.

Table 4–3: Computed coordination number of amorphous and crystalline systems. Averaged over all 2880 atoms. The standard deviation (STD) is given in parentheses.

	Amorphous	FCC crystal
Coordination number	11.6 (0.8)	12 (0)

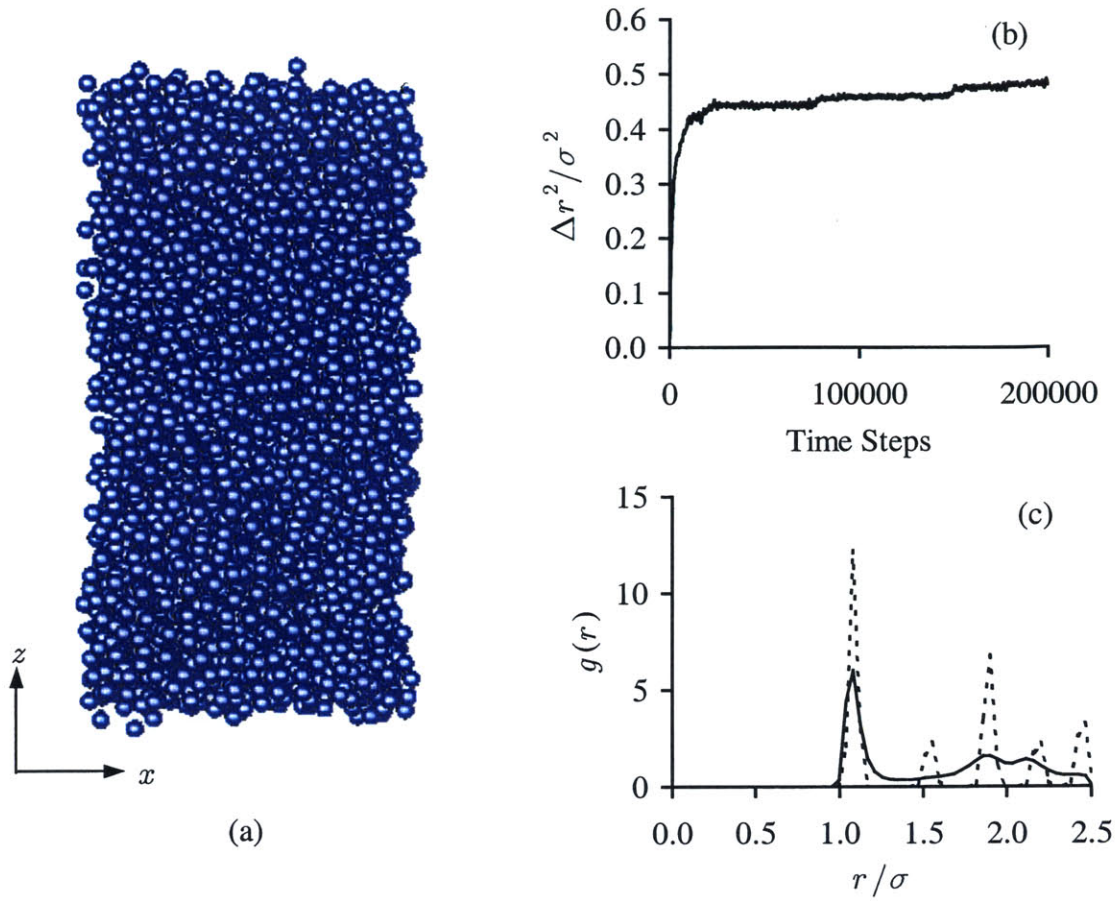

Figure 4–4: (a) Quenched amorphous system at 291 K. Graphics provided by reference [61]. (b) Mean square displacement. (c) Radial distribution function. In (c), the dotted curve represents the radial distribution function of an FCC crystal at the same temperature and pressure.

Voronoi polyhedra are helpful in the elucidation of the local structure and free volume at the site of a single atom. The method of constructing the polyhedra is described in detail elsewhere [37,38], so just a brief overview is presented here. The underlying concept behind the Voronoi construction is the following. Given a volume filled by N atoms (the position of the atom is treated as a point in space), it is possible to assign any point inside the volume to the nearest atom. If every point in the volume is allocated in this manner, the result is the segmentation of the volume into N domains (not generally equal in size and shape), with each domain assigned to an atom, so that every atom is surrounded by its own *local volume*. It can be proven by geometry that the local volumes are always in the shape of polyhedra of

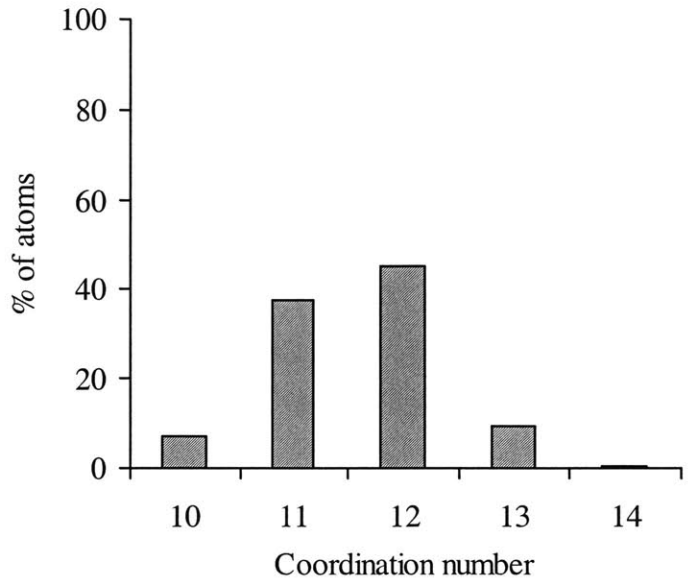

Figure 4–5: Distribution of the coordination number in the amorphous system.

various shapes and sizes. Every face of a polyhedron coincides with a plane perpendicularly bisecting the central atom (i.e., the atom associated with that particular polyhedron) and a neighboring atom, and every edge is the intersection of such planes. Under this construction, all of the polyhedra fill up the entire volume. In a perfect FCC lattice, every atom has an identical polyhedron with 12 faces and four edges per face. In a real crystal, however, thermal fluctuations can lead to a slight distortion of the regular polyhedron, sometimes resulting in the appearance of one or two additional faces and edges. This effect can be diminished by implementing the following techniques in the Voronoi computation. First, the polyhedra may be constructed based on the average configuration over a sufficient number of steps (but not too many steps, since a relaxation can happen given a long enough time) rather than the instantaneous configuration, such that the thermal fluctuations are effectively averaged out. This is sensible to do because the Voronoi polyhedra should reflect the metastable equilibrium structure of the amorphous system, rather than the instantaneous structure. In this work, all Voronoi polyhedron constructions are based on atom positions averaged over 5000 steps, which is about 20 atomic oscillations. Second, in sorting the faces of the polyhedra, an edge is only counted if it is longer than 0.01Å. This condition removes the possibility of counting edges or faces which are only artifacts of the floating point error of numerical computations. Without this condition, for instance, even a perfect FCC lattice

yields more than 12 faces and 4 edges due to the degeneracy of FCC polyhedra, which is the condition where more than three edges share a common vertex.

Table 4–4 lists the results of the Voronoi analysis data for the amorphous system. For comparison, data for an FCC crystal at 291 K are also presented, along with relevant results from past references. The present results agree well with the amorphous argon simulations of Tanaka [41], except that his system has a much lower average polyhedron volume. This discrepancy could be due to the fact that Tanaka used a fixed cell in his simulations, whereas the present study allows cell expansion through the use of the Parrinello-Rahman method. The slight differences in the number of faces and edges between Tanaka and the present work may be attributed to the discrepancy in the specific volume, as well as the fact that the polyhedron construction in the present work is based on average atomic coordinates. In addition, the face and edge results are sensitive to variations in structure caused by thermal fluctuations or different preparation methods, and Tanaka uses a finite quench rate (as opposed to the instantaneous quenching used in this study) and a lower final quench temperature. The polyhedra characteristics of the L–J systems are substantially different from the hard-sphere model, and this may be attributed to elementary structural differences between the L–J hard sphere models.

Table 4–4: Voronoi polyhedron summary. Data under amorphous and crystal systems are from present study using the L–J potential for copper at 291 K ($.061\varepsilon/k_b$) and zero pressure. Amorphous argon data is from MD simulation with L–J potential at 4.22 K ($.035\varepsilon/k_b$). Standard deviations are given in parentheses. Polyhedron volumes are normalized by the L–J parameter σ^3 (or $D^3/\sqrt{2}$ for the hard sphere model, based on the approximation $2^{1/6}\sigma = D$, where D is the hard sphere diameter).

	Volume per polyhedron	Faces per polyhedron	Edges per face
Crystal system	0.954 (0.001)	12.003 (0.059)	4.000 (0.005)
Amorphous system	1.012 (0.039)	14.026 (1.024)	5.132 (0.071)
Amorphous argon [41]	0.960	14.086	5.148
Hard sphere [39]	1.163	14.251	5.158

Figure 4–6 displays a histogram of the number of faces per polyhedron in the amorphous system. Also shown in the same chart is the histogram of the crystal, in which almost all polyhedra are 12-faced, characteristic of the FCC lattice (0.3% have 13 faces, due to thermally-induced lattice distortions, in spite of the effort to minimize thermal effects). The distribution is much broader in the amorphous system, which is reflective of the wide diversity of local structure in the amorphous medium. Most of the polyhedra have 14 faces (38.7%), followed by 15 faces (24.6%) and 13 faces (23.8%). The histogram of the number of edges per face is given in Figure 4–7. Once again, the crystal distribution is concentrated while the amorphous distribution has more spread, with 5 faced-edges being the most numerous at 45.5%. In Finney's hard sphere model [39] and Tanaka's L–J argon [41], the 14-faced and 5-edged arrangements were also found to be the most abundant.

The distribution of the polyhedron volume in the amorphous and crystalline systems is shown in Figure 4–8. The spread in the amorphous data is in direct contrast to the crystalline data, which shows up as a singular peak. The peak of the amorphous distribution is situated to the right of the crystalline peak, illustrating the overall increase in volume of the amorphous system. The distribution of the polyhedron volume, or equivalently the local volume per atom, is believed to be an important parameter in the deformation of amorphous materials, where plastic deformation is believed to be the outcome of local shear transformations, which occur with more probability in regions of relatively high local volume [27,28]. Due to the fundamental similarities that exist between the mechanistic behavior of plastic deformation and frictional sliding, the concept of local volume may also be relevant to sliding simulations, and the local volume statistics are accordingly monitored in order to reveal any insightful correlations in the upcoming sliding simulations.

Figure 4–9 displays the correlation between the local volume and the coordination number. These data points are obtained by averaging the polyhedron volume of all atoms with a common coordination number. The plot shows that the relationship between the coordination and the local volume is not monotonic. The 12-coordinated atoms have the lowest local volume, which is intuitive since this particular coordination corresponds to the close-packed structure. Having less than 12 nearest neighbors results in an increase in the local volume, and this can be attributed to the fact that the central atom has fewer neighbors with whom to share the local space. However, having more than 12 nearest neighbors also results in a volume increase, and this may be attributed to the fact that the nearest neighbor cage must be expanded in order to accommodate more than the preferred 12 closest neighbors.

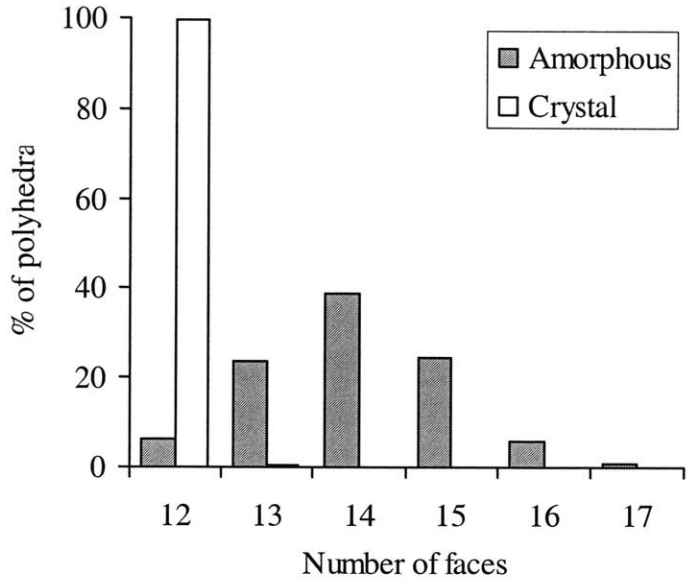

Figure 4–6: Distribution of the number of n–faced Voronoi polyhedra in the amorphous system and a crystalline system at 291 K.

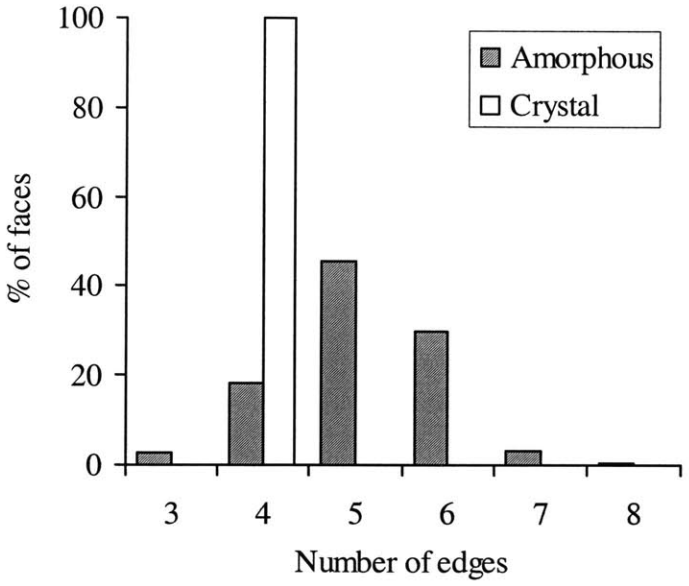

Figure 4–7: Distribution of the number of n–edged faces in the Voronoi polyhedra in the amorphous system and a crystalline system at 291 K.

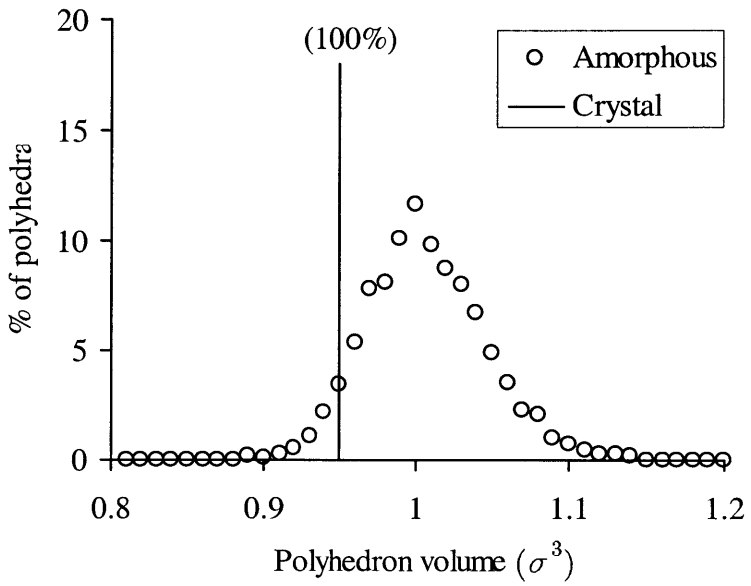

Figure 4–8: Distribution of the Voronoi polyhedron volume in the amorphous system and a crystalline system at 291 K.

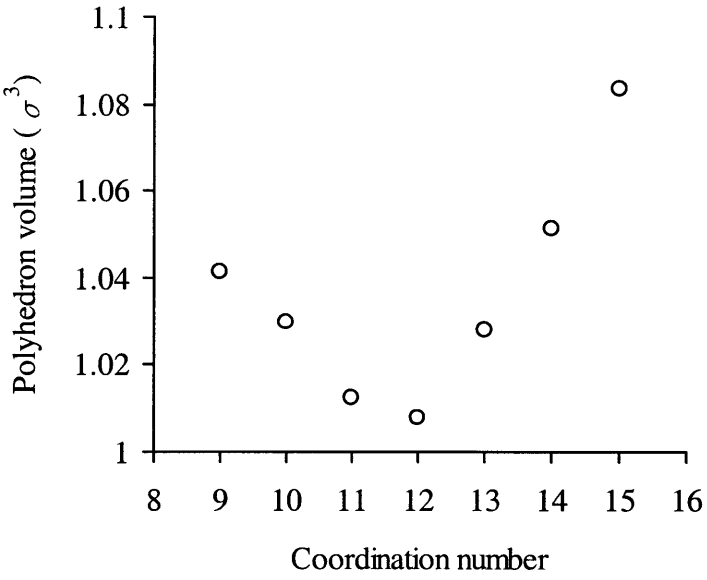

Figure 4–9: Average Voronoi polyhedron volume vs. the coordination number in the amorphous system at 291 K.

4.4 Sliding of the Amorphous System

4.4.1 Interface Creation

The interfacial system is constructed by taking the bulk amorphous system prepared by the melting-quenching process in the previous section and dividing the simulation cell into four zones in the vertical direction. Starting from the bottom, these zones are the lower border, material A, material B, and the upper border (see Figure 4–10). The interface between A and B is such that it divides the simulation cell exactly in half. Materials A and B are inside a new simulation cell, shorter than the original cell, and bounded in the z direction by the upper and lower borders. These borders serve as the finite borders as described in Section 4.2.2. Periodic boundary conditions are applied only in the horizontal (x–y) directions. The advantage of converting portions of the original bulk amorphous system into the finite borders is that the borders now have amorphous structures which were created in a physical process, rather than by random assignment. The breakdown of the number of atoms in each zone is given in Table 4–5, along with the dimensions of the simulation cell and other details. Returning to Figure 4–10, the lower and upper halves of the simulation cell (i.e., materials A and B) are considered to be divided each into 9 equal "layers" in the z direction. This is only a labeling scheme and does not mean that there are now 18 more interfaces. The layers are assigned simply for interpretation and discussion purposes, so that various results can be examined on a layer-by-layer basis. Each layer is approximately one atomic diameter thick.

The sliding simulation features an interface between materials A and B and thus needs three sets of ε and σ to fully define the system, one set for each bulk (A–A and B–B) interaction and one set for the interfacial (A–B) interaction. Table 4–6 contains the values of all L–J parameters, with the subscript notation denoting the specific interaction. No subscript is used on the parameter σ because it is the same for all interactions. This is a reasonable simplification given that σ mostly affects the lattice parameter, which is expected to have a minimal effect on the sliding behavior. Another simplification is $\varepsilon_{AA} = \varepsilon_{BB}$, which essentially means that the bulk properties of A and B are identical. This assumption should have little effect on the outcome, because the bulk interaction is far less important than the interfacial interaction as far as the sliding behavior is concerned. The vital parameter is ε_{AB} because it determines the strength of the interfacial bonds, and the ratio $\varepsilon_{AB}/\varepsilon_{AA}$ is a convenient dimensionless parameter relating the interfacial adhesion to the bulk cohesion. The limiting case of $\varepsilon_{AB}/\varepsilon_{AA} = 1$ represents the shearing of a bulk system without an interface, whereas a reduced value ($\varepsilon_{AB}/\varepsilon_{AA} < 1$) introduces an interface which is weak relative to the rest of the system. This ratio plays a key role in distinguishing various regimes

of sliding in amorphous systems. The value of ε_{AB} used here is $0.1\varepsilon_{AA}$, resulting in an interface with a relatively low adhesion. Having such weak adhesion helps to localize the sliding to the interfacial plane, which makes it convenient to analyze the sliding behavior.

Table 4–5: Parameters for sliding simulation.

Number of atoms	1082 in material A 1083 in material B 354 in upper border 361 in lower border
Simulation cell dimensions ($x \times y \times z$) (sliding)	$2.887 \times 2.110 \times 4.478$ nm
Mass of atom (A or B)	1.06×10^{-22} g (copper)
Mass of dynamic cell walls	1.06×10^{-21} g
Time step	10^{-15} s
Sliding increment of moving border	0.0023127 nm
Number of steps following each sliding increment	5000 time steps
Normal load during sliding	300 MPa (compressive)
Temperature (by velocity rescaling)	291 K

Table 4–6: Lennard-Jones parameters for sliding simulation.

	Sliding Simulation	
A–A	$\varepsilon_{AA}/k_b = 4733.5$ K	$\sigma = 0.23127$ nm
B–B	$\varepsilon_{BB}/k_b = 4733.5$ K	$\sigma = 0.23127$ nm
A–B	$\varepsilon_{AB}/\varepsilon_{AA} = 0.1$	$\sigma = 0.23127$ nm

$k_b = 1.38 \times 10^{-23}$ J/K (Boltzmann's constant)

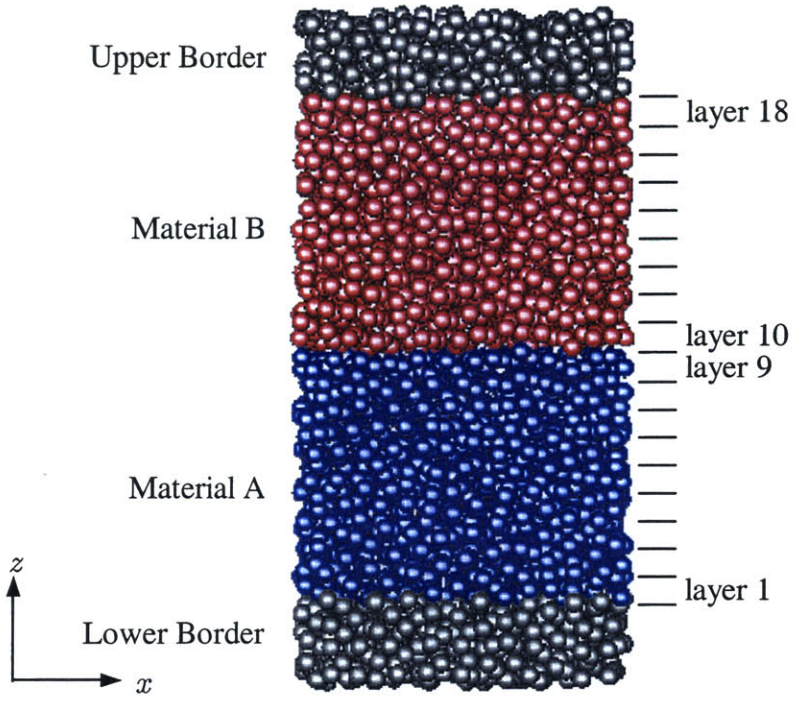

Figure 4–10: Amorphous sliding system with $\varepsilon_{AB}/\varepsilon_{AA} = 0.1$ interface. Periodic boundary conditions are applied in the x and y directions only, and the sliding occurs in the x direction with the normal load is placed along the z direction. Graphics provided by reference [61].

4.4.2 Interface Relaxation

Having instantaneously changed the physical attributes of the simulation cell by introducing finite borders and creating an interface by changing the L–J parameters, it is important to allow the system many steps to relax to equilibrium prior to sliding. This relaxation is done at 291 K under zero pressure over 100,000 time steps, and the mean-square displacement confirms that equilibrium is reached within this period. The final structure of the relaxed system is then analyzed using the Voronoi polyhedron method. The average number of faces and edges are respectively 14.026 and 5.130, which are hardly different from the bulk values listed in Table 4–4. The volume per atom, $1.019\sigma^3$, is a 0.7% increase from the system without the interface, this being a direct consequence of the weaker attraction between A and B atoms, which lessens the driving force for dense packing. The average local volume for each layer in the system is shown in Figure 4–11, where it is clearly revealed that the atoms in layers 9 and 10 (the A–B interfacial layers) have noticeably higher

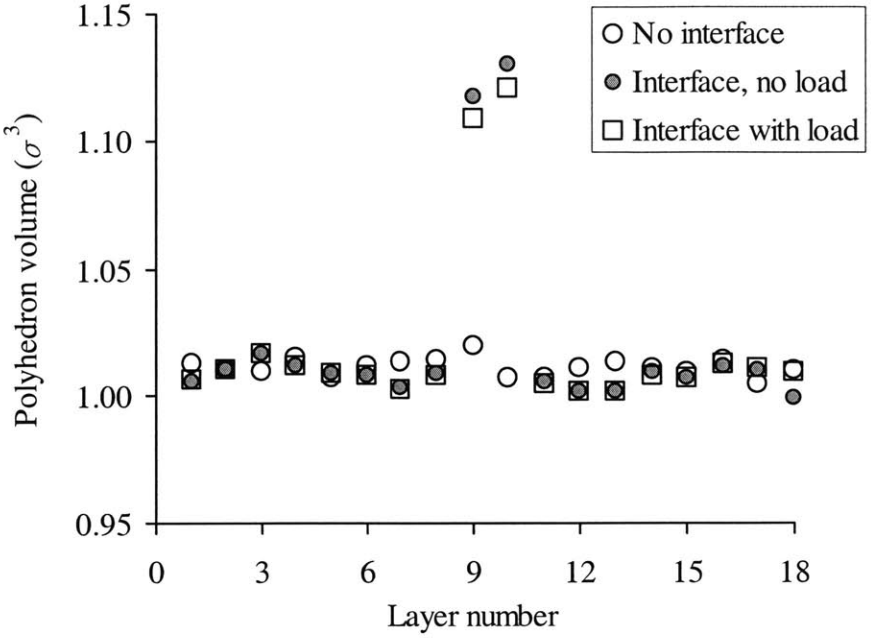

Figure 4–11: Average Voronoi polyhedron for each layer in the amorphous system. Results are given for system before the creation of interface, with the $\varepsilon_{AB}/\varepsilon_{AA} = 0.1$ interface relaxed to zero pressure, and with the interface under 300 MPa compressive uniaxial load.

local volume than the rest of the system. On average, the local volume of layers 9 and 10 are 11.5% higher than elsewhere.

4.4.3 Loading

After the relaxation, a 300 MPa compressive uniaxial load is placed in the z direction by the technique described in Section 4.2.3. The system is equilibrated for 50,000 time steps under load, during which time the simulation cell undergoes x–y–z strains of 0.0007, 0.0006, and –0.0023, resulting in a 0.1% volumetric contraction. The layer distribution of the local volume plotted in Figure 4–11 indicates that the majority of the volume decrease takes place in the interfacial layers, which is the intuitive outcome, considering that the interfacial region has the least dense packing prior to the load. In fact, the local strain at the interface, computed by comparing the 9–10 interlayer distance before and after the load, is –0.0119, which is a factor of 4 greater than the overall strain. As Table 4–7 indicates, the local modulus of elasticity at the interface is less than everywhere else in the system. The reason for the lower modulus at the interface is twofold. First, the interatomic potential well depth

is only 10% of the rest of the system (i.e., $\varepsilon_{AB} = 0.1\varepsilon_{AA}$) and second, the average interatomic spacing at the interface is larger, and the stiffness coefficient of the Lennard-Jones potential function decreases as the atoms are moved apart beyond the minimum energy separation. Table 4–7 also lists the modulus of a crystalline system for comparison. The lower elastic modulus of amorphous materials compared to their crystalline counterparts is also a well known property observed in many metallic glasses [54]. As for the Voronoi polyhedra, the average number of faces and edges are 14.018 and 5.132, so the load results in a 0.06% decrease in the number of faces and a 0.04% decrease in the number of edges.

Table 4–7: Modulus of elasticity (in GPa) of amorphous system with interface.

Interface (only layers 9 and 10)	25.3
Bulk (layers 1–8 and 11–18)	179.1
Overall (layers 1–18)	130.4
Crystal (with interface)*	210.0
Crystal (bulk)**	258.0

* obtained in simulation of FCC system under 300 MPa uniaxial compression in the [001] direction at 291 K using the same L–J parameters for copper, including an interface with $\varepsilon_{AB} = 0.1\varepsilon_{AA}$.

** same as (*), but without the interface (i.e., $\varepsilon_{AB} = \varepsilon_{AA}$).

4.4.4 Sliding

Sliding is simulated by the method described in Section 4.2.3 for a total distance of 3σ while maintaining a 300 MPa load and a temperature of 291 K. The average displacement in the x direction of the atoms are computed on a layer-by-layer basis. Figure 4–12 shows the results for the boundary layers (1 and 18) and the interfacial layers (9 and 10). The boundary layers mostly stick close to their respective borders, with layer 1 exhibiting no motion and layer 18 following the moving border almost perfectly. The clear separation between layers 9 and 10 confirms that the slip takes place mostly the bimaterial interface. However, some

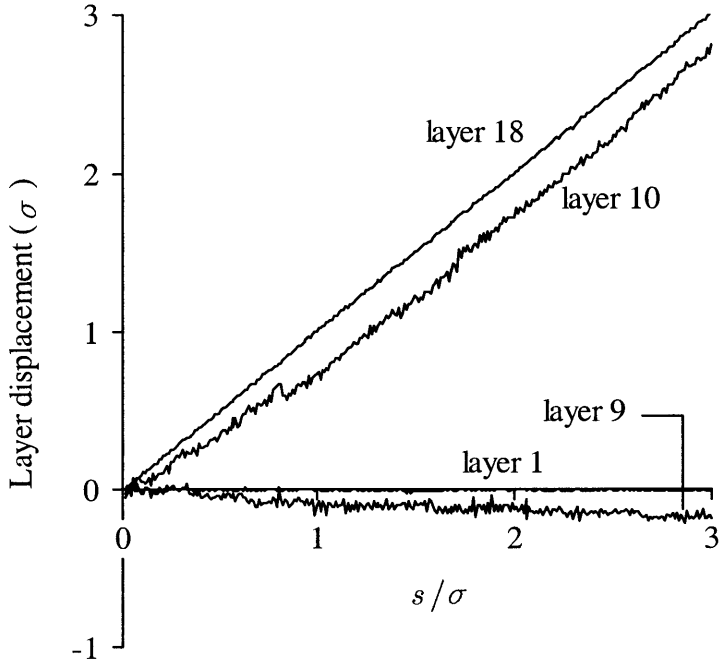

Figure 4–12: Layer displacement for $\varepsilon_{AB}/\varepsilon_{AA} = 0.1$ system, computed by averaging the displacement of all atoms in the layer. The abscissa is the displacement of the upper border. The layer 1 curve is difficult to see because coincides almost perfectly with the horizontal axis.

deformation also occurs within the bulk region of material B, as indicated by the 0.2σ separation between layers 10 and 18 by the end of sliding, which translates to a shear strain of 0.02. In material A, there appears to be a *reverse* deformation leading to a –0.02 shear strain, as evident by the negative total displacement of layer 9. This phenomenon may be attributed to the fact that the moving border may cause the activation of relaxations in the bulk region, which would very likely have been trapped in an unrelaxed state from the quenching simulation. The quenched material, in a metastable state prior to sliding, is induced to a more stable, lower energy state with the help of the shear stresses that develop during sliding.

The potential energy and the sliding resistance are computed as a function of s, the sliding distance of the upper border, as described in Section 4.2.4. The potential energy curve in Figure 4–13 exhibits an overall decrease over the course of sliding, and the "bulk" curve, which is the total potential energy minus the A–B contribution, has a nearly identical decreasing trend, which means that the decrease in the overall potential energy can be

attributed to the relaxations of only the bulk regions. The decrease of the potential energy curve is not smooth, but rather discrete, which is consistent with the representation of the deformation as a sequence of local relaxations, each of which contributes a potential energy drop. It may be noted that the potential energy released during each relaxation event is converted into the kinetic energy of the atoms involved in the relaxation, but the isothermal conditions imparted by the velocity rescaling method immediately extracts the extra kinetic energy.

Figure 4–14 is the sliding resistance. The initial resistance of 302 MPa, which is a residual stress from the melting-quenching process, explains the motivation for the reverse deformation of material A observed in the layer displacements of Figure 4–12. The average resistance over the entire sliding simulation is 152 MPa. In Chapter 2, it was determined that the average sliding resistance may be considered to be equal to the kinetic friction, provided that the average is computed over a proper sliding distance. If the sliding is periodic, as is often the case with crystalline systems, one period is the minimum distance required for averaging, as anything less can yield highly erroneous results due to insufficient sampling. The present amorphous system exhibits no clear periodicity, so it cannot be not known with certainty that 3σ is the proper distance averaging. However, it is safe to assume that the sliding is not periodic about some distance much longer than 3σ, because the topology of an amorphous interface does not possess long-range order. As a result, averaging over 3σ is not expected to incur significant error, so the 152 MPa can be considered to be the friction, which yields a friction coefficient of 0.5.

4.4.5 Kinematics of Sliding at the Interface

The normal view of the sliding interface is shown in Figure 4–15. Only the atoms of layers 9 and 10 are shown, with the brightness coordinated with the potential energy of the atom. The random scatter of the potential energy is immediately evident, and this is one of the features that is very different from the commensurate sliding interface (Chapter 2), where the potential energy distribution is homogeneous. The scatter of the energy is, of course, directly related to the random structure of the interface, which is also apparent in Figure 4–15. The energetic and structural heterogeneity results in a sliding behavior which is unlike that of the commensurate system, in which the atoms of the interfacial layer move in unison, such that the sliding may justifiably be described as the relative slip of rigid atomic layers. In contrast, the interfacial atoms of the present amorphous system exhibit a significant degree of individual mobility, because they are not structurally linked to the rest of the layer by a

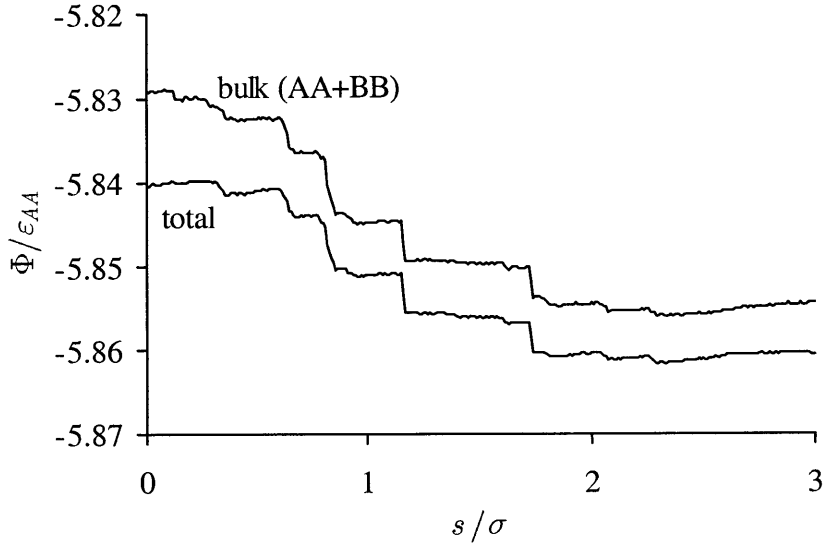

Figure 4–13: Potential energy for $\varepsilon_{AB}/\varepsilon_{AA} = 0.1$ system.

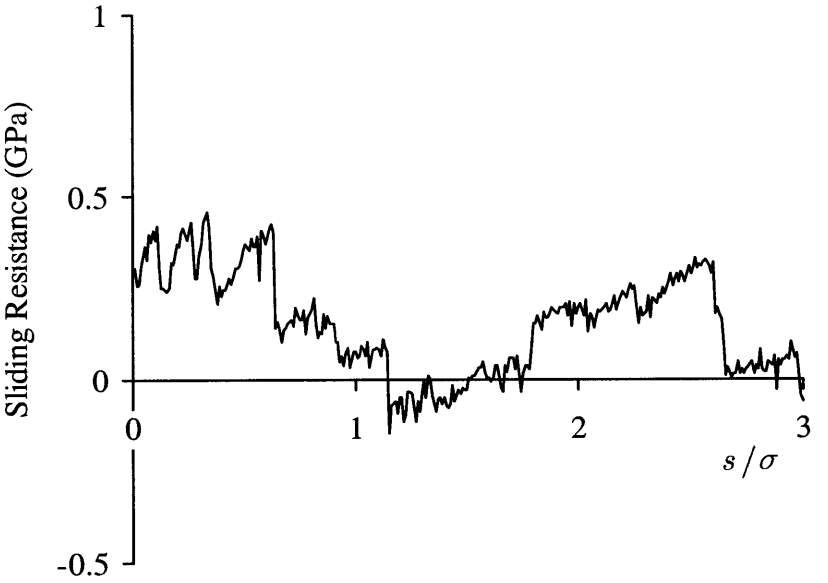

Figure 4–14: Sliding resistance for $\varepsilon_{AB}/\varepsilon_{AA} = 0.1$ system.

lattice. Consequently, there is a wide variety of kinematic responses among the atoms within the sliding layer, as is evident in Figure 4–16, where the trajectories of a select sample of atoms in layer 10 are traced. It can readily be seen that in many instances, the trajectory is not straight along the sliding direction, but rather consists of several detours in the y (and z, not shown) directions. This is understandable, since the straight path may not always be the lowest energy path, and a roundabout path is sometimes energetically preferable for not just the atom, but also the atoms in the surrounding region of influence. Figure 4–17 shows the displacements in x of the sample atoms as a function of s. The atoms obviously do not move synchronously, but each according to its own schedule. Figures 4–16 and 417 also illustrate that often, the atoms move backwards (follow, for example, atoms 'c', 'd', and 'e'), a phenomenon which was not observed in the crystalline system. Overall, sliding of the amorphous system is essentially the sum of a random assortment of atomic motions. Although each atomic trajectory may be characterized as independent, a cluster of 2 to 10 atoms can, at times, be seen moving in unison.

The energetic response of the interfacial atoms during the motion are shown in Figure 4–18, in which is plotted the potential energy ϕ_i of each sample atom denoted in Figure 4–15. The expression for the potential energy of atom i is given by

$$\phi_i = \frac{1}{2}\overline{\sum_j \phi(r_{ij})}, \tag{4.5}$$

where j indexes all of the neighbors of atom i within the cutoff radius, and the overhead bar denotes equilibrium averaging over the 5000 step period after each sliding increment. Since all of the sample atoms belong to the interfacial layer, roughly 1/4 of the interactions are of the A–B variety, which involves the L–J parameter ε_{AB}. The potential energy curves of the sample atoms are as unpredictable as their trajectories, and many are marked by very sudden drops, which are characteristic of jump phenomena. Some discretion needs to be applied when interpreting a drop in the potential energy as a jump phenomenon, because the curves in Figure 4–18 seem to be affected by thermal noise. It may be suggested that a rough criterion for a jump phenomenon is a potential energy decrease exceeding the average kinetic energy of an atom, which is equal to $0.09\varepsilon_{AA}$ at 291 K (see Appendix B), with the drop occurring within one sliding increment, 0.01σ. Under this convention, all of the sample atoms undergo at least one jump, and the particularly intense jumps (if the intensity may be measured by the amount of energy drop) are clearly evident in Figure 4–18 for atoms 'a', 'd', 'e', 'g', 'h', 'i', 'j', and 'l' at various times during sliding. There is no correlation in the jump behavior among the atoms, which is to say that the jump phenomena occur at incoherent

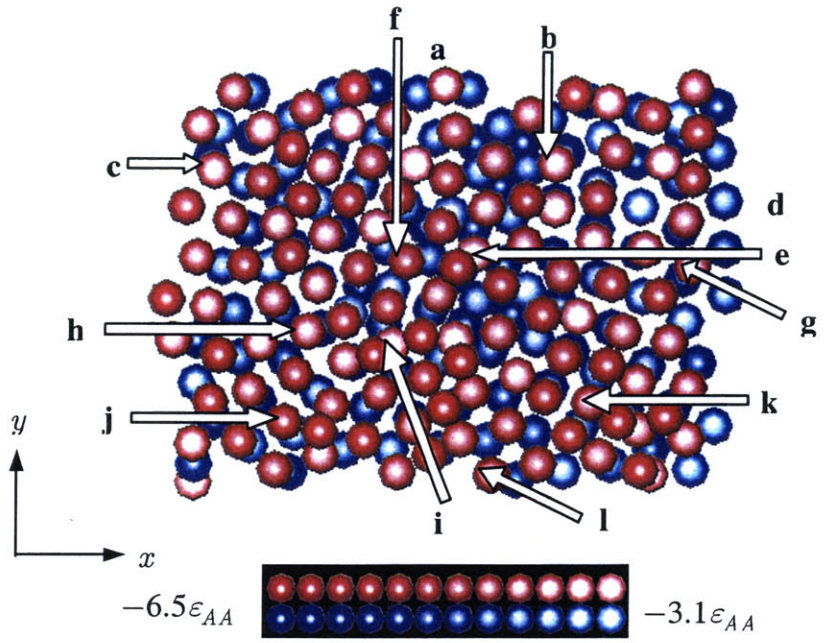

Figure 4–15: Interfacial atoms of $\varepsilon_{AB}/\varepsilon_{AA} = 0.1$ system. Only layers 9 (blue) and 10 (red) are shown. The brightness indicates the potential energy of the atom. This is the configuration prior to sliding. 12 sample atoms are marked ('a-l')for future reference.

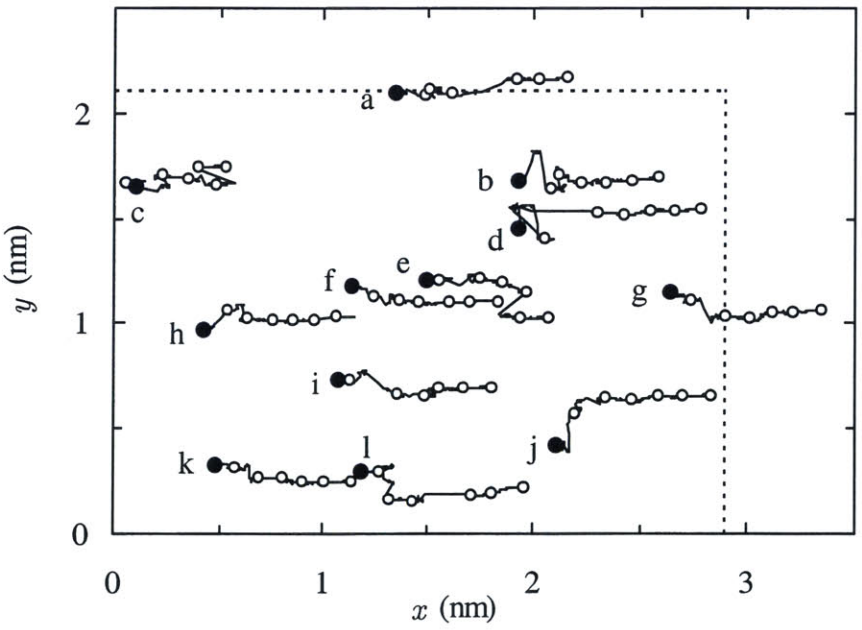

Figure 4–16: Trajectories of sample interfacial atoms on $x-y$ plane during sliding of $\varepsilon_{AB}/\varepsilon_{AA} = 0.1$ system. Sample atoms shown in Figure 4–15. Closed circles mark the initial position. Open circles denote position at every 50 sliding increments (0.5σ).

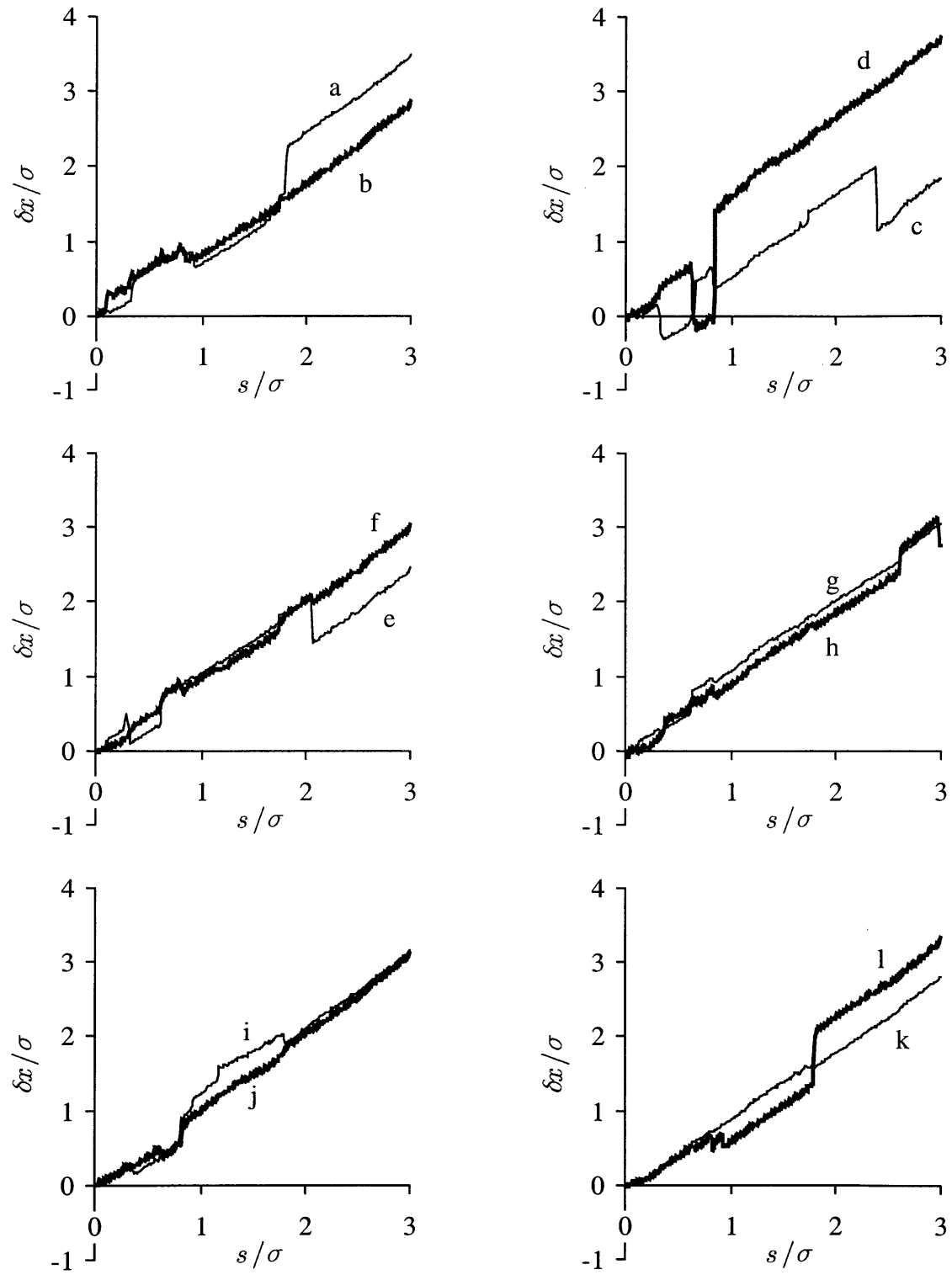

Figure 4–17: Displacement in x of sample atoms. δx is the displacement in reference to the initial position of each atom.

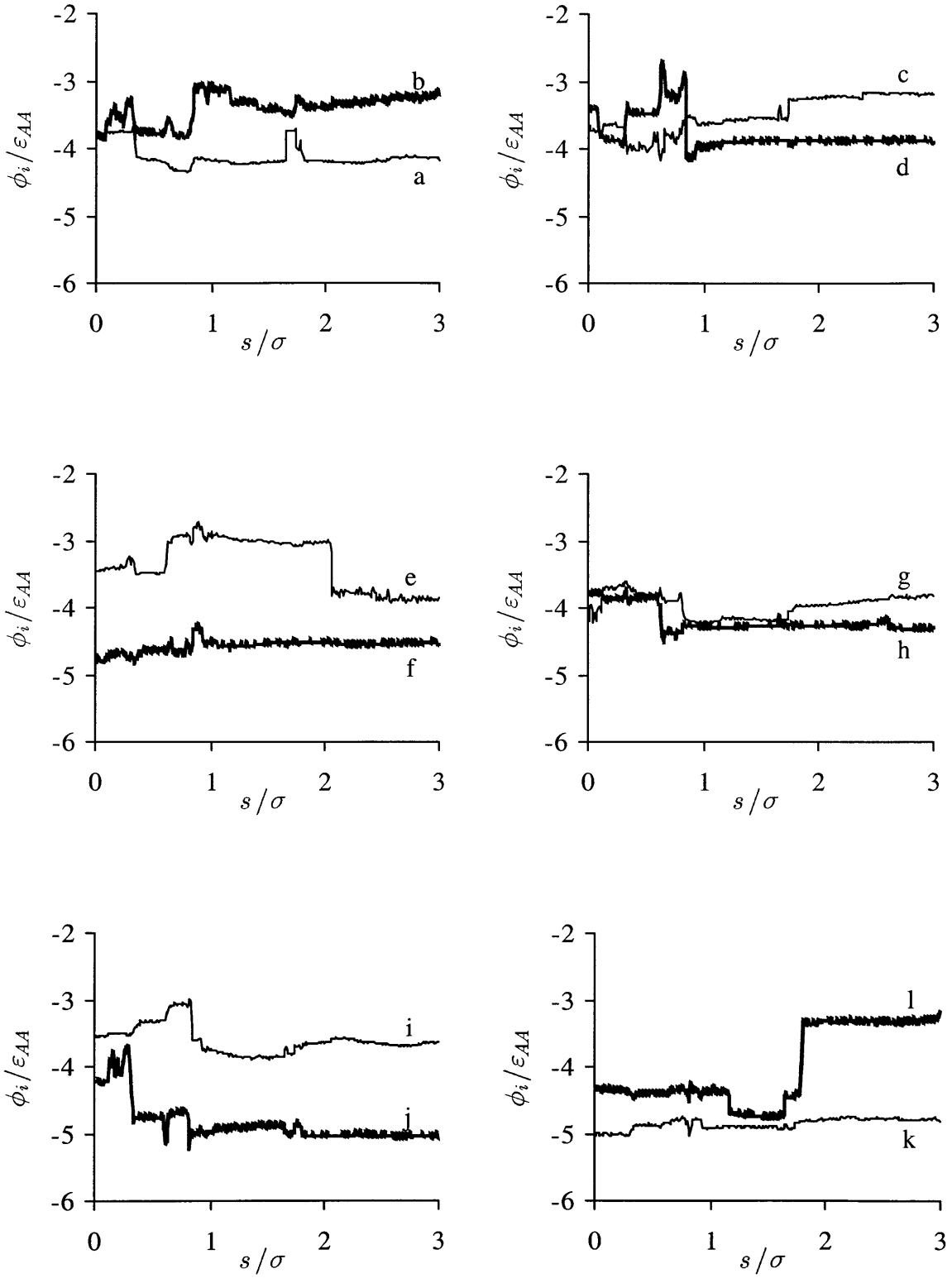

Figure 4–18: Potential energy of sample atoms.

times and locations, and no two jumps are exactly alike. This is in direct contrast to the sliding of the crystalline system in Chapter 2, where jump phenomena involve slips of a layer as a whole, where all atoms of the layer move coherently. In the amorphous system, the independence of the atoms allows local jump phenomena to take place, and the friction for this system, calculated previously to be 152 MPa, comes from the accumulation of the series of local jumps.

Table 4–8: Statistics of jump phenomena at sliding interface. Data reflect only the atoms in layer 10, of which there are 115. The total distance of sliding is 3σ.

	Forward Normal	Forward Inverse	Backward Normal	Backward Inverse
Number of jumps	509	408	329	289
Avg. displacement in x (σ)	0.07	0.05	–0.09	–0.06
Avg. energy change (ε_{AA})	–1.01	0.18	–0.39	0.19

The jump behavior varies from atom to atom, and while some atoms undergo relatively intense jump events (atoms 'd', 'e', and 'j', for example), some experience only mild jumps (atom 'k'). It may also be noted that a number of "inverse" jumps occur, which refer to the peculiar phenomenon where the atom undergoes a jump transition to a higher potential energy state, evident in the curve of atom 'l' and, to a lesser extent, atoms 'a' and 'c'. (To clarify the terminology, "normal" and "inverse" jumps refer only to the energetic response, with the former being a drop in potential energy and the latter an increase. "Forward" and "backward" jumps refer to the direction of the jump, with the former associated with a jump transition in the $+x$ direction, and the latter in the $-x$ direction. Incidentally, both normal and inverse jumps can coincide with either forward or backward jumps.) Inverse jump transitions do not occur in crystalline sliding systems, yet they occur frequently in the amorphous system, because an atom may be forced to a higher energy configuration by surrounding atoms attempting to attain lower energy configurations of their own. Using the criterion of a jump phenomenon proposed earlier, all of the atoms in layer 10 have been tested for jump events throughout the sliding, and Table 4–8 lists the frequency of the forward and backward

jumps, along with their energetic characteristics. Forward normal jumps occur most frequently and with the greatest change in the potential energy, while backward inverse jumps occur least frequently. The average energy drop of the normal jumps is considerably greater than the average energy increase of the inverse jumps. Overall, forward jumps occur just about 1.5 times as often as backward jumps, which may be attributed to the forward bias created by the shear stress that develops during sliding. Although they occur less frequently as the forward type, the average distance of the backward jumps is slightly bigger.

4.5 Interfacial Sliding with Bulk Deformation

The next simulation is done with $\varepsilon_{AB}/\varepsilon_{AA} = 0.4$. The process of interface relaxation and loading follows the same procedure described in Sections 4.4.1–4.4.3, using the same initial bulk quenched amorphous system. The details of the interface creation, relaxation, and loading are not very different from the previous case, so the results of these procedures are not discussed here. Instead, the sliding results are presented in detail in this section.

Figure 4–19 shows the layer displacement plots, where it is clear that while the majority of the slip still occurs between the interfacial layers 9 and 10, the bulk regions undergo much more deformation than in the $\varepsilon_{AB}/\varepsilon_{AA} = 0.1$ system. By the end of sliding, total shear strains of 0.075 and 0.086 have taken place in materials A and B, respectively. The potential energy during sliding is given in Figure 4–20, and the similarity of the features of the total (AA+BB+AB) and the bulk (AA+BB) potential energy curves indicate that the energetic response is largely governed by the bulk behavior, rather than the interfacial behavior. The increase in the strength of the A–B interactions makes the interface more sticky, which results in the development of higher shear stress in the system. Higher stress leads to more deformation through the structural transformation regions which could not be activated under low stress. The behavior of this system is clearly characterized by a mixture of sliding and deformation, and the sliding resistance, shown in Figure 4–21, reflects both the sliding resistance at the A–B interface, as well as the deformation resistance of the bulk regions. The average resistance of 1.4 GPa may tentatively be called friction, with the understanding that friction partly comes from bulk deformation in addition to pure sliding.

4.6 Deformation and Crystallization of Amorphous System Under Shear

This section describes the simulation of the amorphous system with $\varepsilon_{AB}/\varepsilon_{AA} = 1$, where the A–B interface no longer exists, and the sliding of the upper border effectively simulates

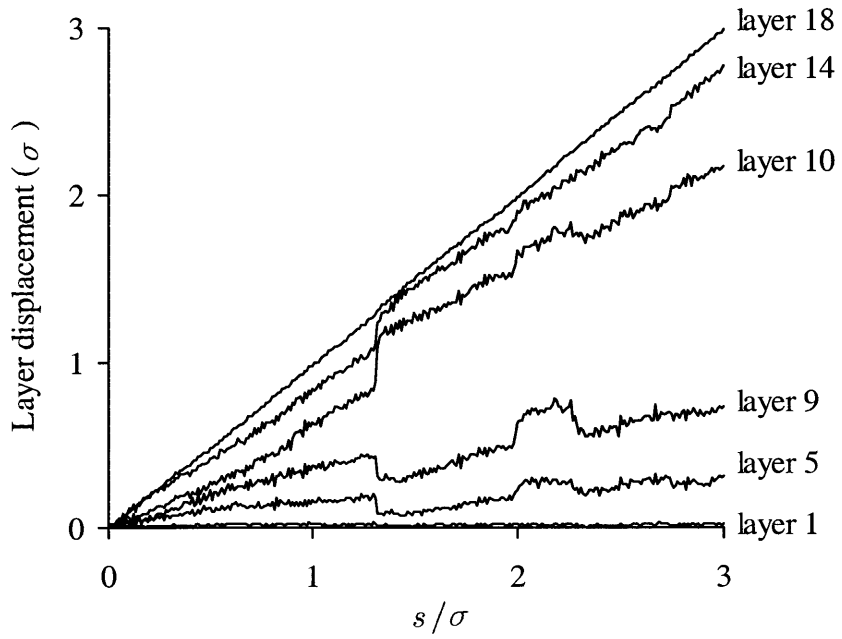

Figure 4–19: Layer displacement for $\varepsilon_{AB}/\varepsilon_{AA} = 0.4$ system.

the shearing of bulk amorphous material. The system is prepared in the usual way, by starting from the quenched system prepared in Section 4.3, implementing the finite borders, relaxing at zero stress for 20,000 time steps, and applying the 300 MPa normal load in the z direction, followed by 20,000 time steps of equilibration. Upon the placement of the normal load, the simulation cell undergoes average x–y–z normal strains 0.0008, 0.0005, and –0.0016, resulting in a Poisson's ratio of 0.4 and Young's modulus of 188 GPa, the latter of which is 27% lower than the Young's modulus of a bulk crystal. The purpose this simulation is to complete the parametric study of the friction in amorphous systems, and for this reason, such parameters as the normal load, temperature, and sliding increment are the same as the values used in Sections 4.4 and 4.5. The shearing is seen to result in the crystallization of the amorphous material after a substantial amount of deformation. The next part, Section 4.6.1, discusses mostly the results of the shearing simulation prior to the onset of crystallization, and Section 4.6.2 is devoted to the discussion of the crystallization phenomenon.

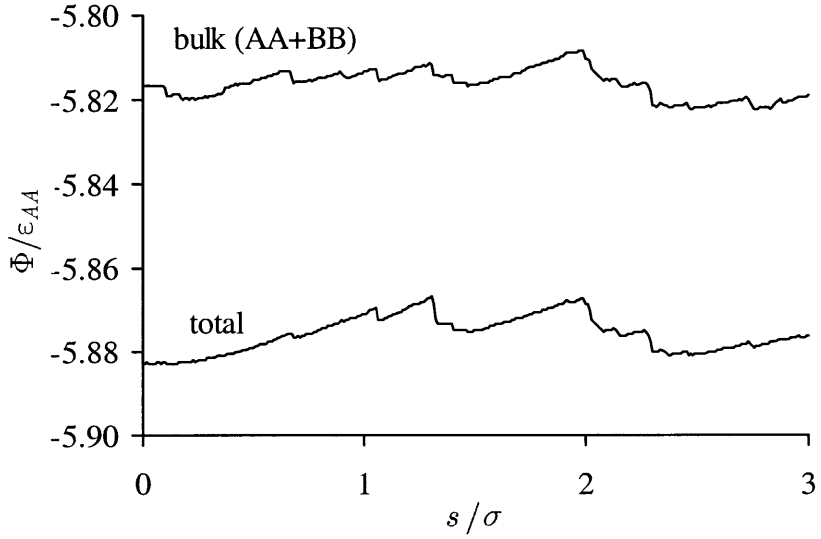

Figure 4–20: Potential energy for $\varepsilon_{AB}/\varepsilon_{AA} = 0.4$ system.

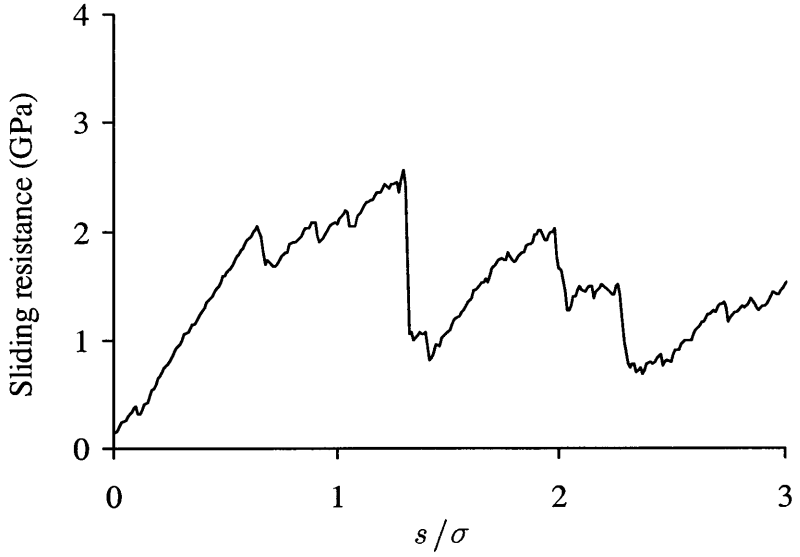

Figure 4–21: Sliding resistance for $\varepsilon_{AB}/\varepsilon_{AA} = 0.4$ system.

4.6.1 Shear Deformation of Bulk Amorphous System

Shearing is done by moving the upper border in the x direction, as usual, in increments of 0.01σ, with 5000 equilibration steps following each increment. (An exception is made near the crystallization event, but this is discussed in more detail in the next part.) In the previous simulations with $\varepsilon_{AB}/\varepsilon_{AA} < 1$ (Sections 4.3 and 4.4), the slip was seen to occur mostly between the interface layers, even when the sliding was accompanied by significant deformation of the bulk region, as in the case of the $\varepsilon_{AB}/\varepsilon_{AA} = 0.4$ system (Section 4.4). In the present case, where a weakened interface does not exist, sliding is no longer concentrated in one particular plane. This is clearly shown by the layer displacement curves in Figure 4–22, where the interlayer sliding is distributed rather evenly among all layers. The indication is that the shear deformation is homogeneous, and this is an important response to consider because the low-temperature deformation behavior of metallic glasses is known to be heterogeneous, as demonstrated by the observation of distinct shear bands in deformed samples [27,55-57]. The reason that the present system does not exhibit such localized deformation may be that the simulation cell is much too small to capture the shear band formation. The measured distance between shear bands of deformed amorphous metals is typically of the order of 0.1 μm [55-57], which is 20 times bigger than the height of the present simulation cell. Furthermore, the thickness of a shear band is usually only 10 nm or so, which is over twice the height of the simulation cell. It seems, based on the experimental evidence, that the shear band formation involves some long-range phenomena, which is impossible to simulate with such a small system. Instead, it may be suggested that the present simulation cell represents a deforming volume of material within an active shear band.

The potential energy of the system, shown in Figure 4–23, is steady up to $s/\sigma = 3.4$ or so, at which point the curve drops suddenly due to the onset of crystallization. The energy drops because the crystallization is essentially a phase transition from the metastable amorphous state to the ground crystalline state. Prior to the crystallization, the amorphous material undergoes a significant total deformation of 0.18 shear strain. The sliding resistance, shown in Figure 4–24 (or shear resistance, since sliding does not occur here), exhibits a series of discontinuous drops, which should not be interpreted as atomic stick-slip or plucking, even if the sawtooth shape is consistent with such phenomena. Stick-slip is not possible when sliding does not occur, and so the discontinuous features of the resistance curve can be better attributed to discrete local relaxations, which are believed to be the unit events of the plastic deformation of amorphous materials [R]. Friction is computed by averaging the shear resistance of only the portion prior to the crystallization, so that only the

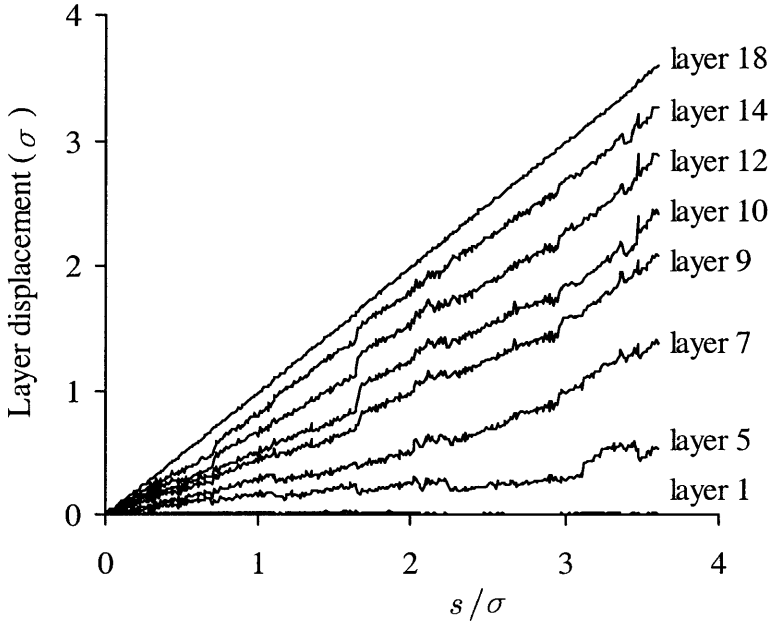

Figure 4–22: Layer displacement for $\varepsilon_{AB}/\varepsilon_{AA} = 1$ system.

amorphous sliding (or shearing) regime is considered. Friction is then equal to 1.7 GPa, which yield a friction coefficient of 5.7.

4.6.2 Deformation-Induced Crystallization

The formation of nanocrystallites during low-temperature deformation of amorphous metals has been experimentally verified for a number of alloys through transmission electron microscope (TEM) images of the shear band [55-57]. The nanocrystallites have been measured to be 7-20 nm in diameter, and they are usually embedded in highly deformed amorphous regions after extreme bending or ball-milling of glass ribbons [55,56], or nano-indentation of amorphous metal samples [57]. In addition, an MD simulation of a 2-dimensional nickel using a Morse-type pair potential has also been reported to produce crystallization [58]. It is not clear whether the mechanistic aspects of deformation-induced crystallization is fundamentally similar to thermally-induced crystallization of metallic glasses, which takes place only at elevated temperatures, where high atomic mobility aids in the nucleation and growth of a crystallite even in the absence of deformation. The suggestion that the deformation-induced nucleation is actually the consequence of the local heat-up

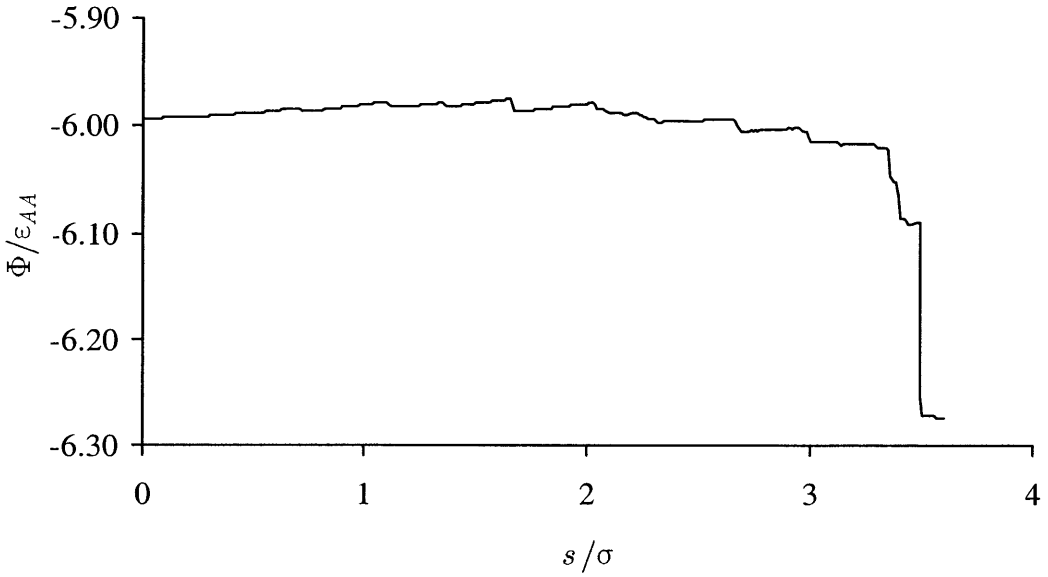

Figure 4–23: Potential energy for $\varepsilon_{AB}/\varepsilon_{AA} = 1$ system.

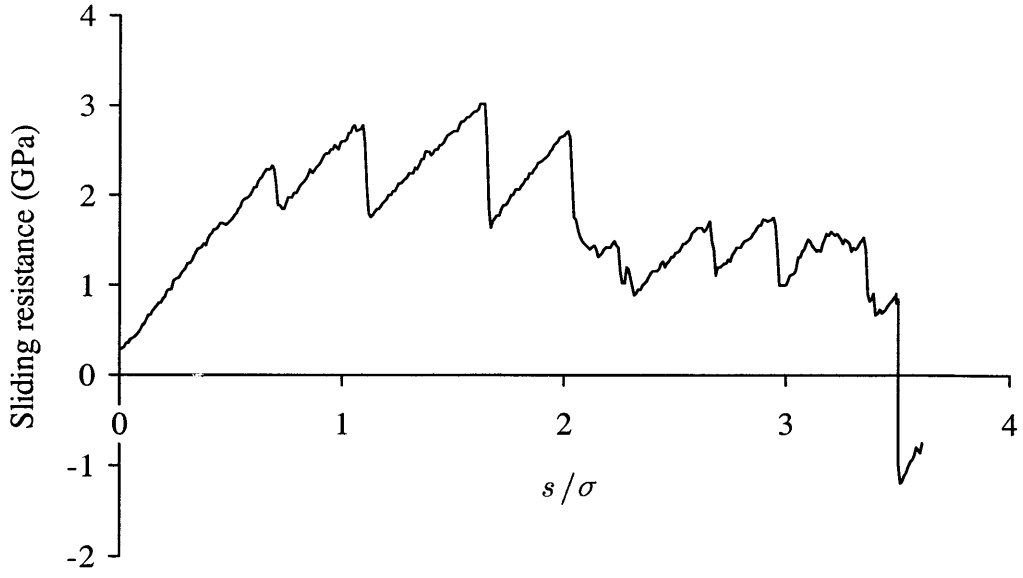

Figure 4–24: Sliding resistance for $\varepsilon_{AB}/\varepsilon_{AA} = 1$ system.

associated with excessive strain rates has been dismissed on the basis that the temperature rise is negligible if the deformation process is executed near-quasistatically [57], or if the heat dissipation is dominant, as in the case of thin ribbons [55]. Based on the observation that the crystallites appear to be similar to ones formed by thermal annealing, the suggestion has been made that the deformation-induced nucleation is a diffusion-driven phenomenon [57], with the diffusivity of deforming volumes being comparable to the diffusivity near the glass-transition temperature due to the well-known local flow dilatation associated with the shear deformation of amorphous materials [27,28]. This explanation is especially convincing in situations where the structure of the formed crystallite is composition-sensitive. However, as the present simulation results show, deformation-induced crystallization of a single-component substance is possible even without the involvement of diffusion.

In order to clearly demonstrate the evolution of the crystallization during the simulation of shear deformation, "crystalline" atoms are distinguished in the snapshots in the next few figures. In the present discussion, an atom is considered to be crystalline if, based on the average system configuration over the equilibration period following each sliding increment, the following conditions are satisfied:

- The atom has exactly 12 nearest neighbors. An atom is considered to be another's nearest neighbor if the distance separating the two is less than 1.32σ.
- Given a central atom with 12 nearest neighbors and a set of 12 vectors, with each vector going from the central atom to a nearest neighbor, there are 66 unique vector pairs, and each pair forms a certain angle. The distribution of the 66 angles must conform to one of the following sets:

  FCC: 180° – 6 120° – 24 90° – 12 60° – 24

  HCP: 180° – 3 146.4° – 6 120° – 18 109° – 3 90° – 12 60° – 24

  An atom must be either FCC or HCP in order to be classified as a crystalline atom. (A 12-coordinated atom which does not have one of the above angle distributions is still not considered to be crystalline.) In the assessment of the angles, a deviation of ± 4° is allowed, so for example, any angle between 176°–184° is counted as a 180° angle. The value of 4° for the deviation angle is chosen arbitrarily, and it may be noted that the quantitative aspects of some of the results to follow are somewhat sensitive to this value. However, the qualitative content of the results is independent of the choice of the deviation angle.

It was discovered in the course of the simulation study that the 5000 steps of equilibration following a sliding increment is insufficient if, after the increment, the system undergoes any crystallization. The full equilibration of the system following each sliding step is an important factor in these simulations, because the strain rate is 5 orders of magnitude higher than experimental values. The only way to neutralize any artifacts associated with the extremely high strain rate is to assure that the system fully relaxes following each incremental shear, which is to say that the simulation should ideally follow the quasistatic behavior as much as possible. For this reason, the mean-square displacement is constantly monitored, and the appropriate number of equilibration steps are always allowed after each sliding increment. The standard 5000 step equilibration is usually sufficient, but 40,000 steps are needed when a crystallization process occurs. Furthermore, the sliding increment of the border is reduced at times in order to elucidate the development of the crystallization process in finer detail. The specifications of the new sliding schedule are given in Table 4–9.

Table 4–9: Sliding schedule for $\varepsilon_{AB}/\varepsilon_{AA} = 1$ system. Sliding increment of the upper border and the equilibration period following each sliding increment are given.

	Sliding increment (σ)	Equilibration (time steps)
$0 < s/\sigma < 3.35$	0.01	5000
$3.35 < s/\sigma < 3.49$	0.01	40,000
$3.49 < s/\sigma < 3.495$	0.001	40,000
$3.495 < s/\sigma < 3.4953$	0.0001	40,000
$3.4953 < s/\sigma < 3.6$	0.01	5000

Crystallization does not take place in the early stages of deformation, and the first cluster of crystalline atoms appears at $s/\sigma = 3.13$ (0.1741 shear strain) in the form of 16 atoms, shown in Figure 4–25a. The cluster grows slowly over the next few increments, reaching the size of 29 atoms By $s/\sigma = 3.35$ (0.1741), as shown in Figure 4–25c. With the next increment, the cluster grows suddenly to 95 atoms (Figure 4–25c). Afterward, there is a period of gradual growth, and by $s/\sigma = 3.4951$ (0.1816, Figure 4–25d), 170 out of the 2165

total atoms are crystalline. After the very next increment (note that an increment is now only 0.0001σ, equivalent to a strain increment of 10^{-5}), the cluster rapidly precipitates to a size of 411 atoms (Figure 4–25e), and then to 830 atoms after yet another increment (Figure 4–25f). From this point on, the cluster grows steadily to reach a final size of 1071 atoms by the end of the shearing at $s/\sigma = 3.6$. Throughout the entire simulation, the material near the borders remains amorphous. This is because the borders themselves are rigidly amorphous, essentially acting as barriers to the propagation of crystallization.

Figure 4–26 shows the same sequence as Figure 4–25 except with a rotated view, and from this perspective, close-packed crystalline layers can be identified. Furthermore, there are several non-crystalline atoms that appear to have ordered structure, especially in the later stages of development in Figures 4–26e and 4–26f. While these atoms fail to strictly meet the crystalline criteria established earlier, the order of their structure is evident even from just a visual inspection. This suggests a flaw in the above classification of a crystalline atom, and a more relaxed set of criteria might have identified these borderline atoms to be crystalline. At the same time, criteria that are too loose would not be proper because there is not so much difference between the local structure of crystalline and amorphous systems. For example, the majority of atoms in the amorphous state are 12-coordinated, and the angle distributions among the nearest neighbors are not too far from the crystalline structure. The point is that even though the present classification of crystalline atoms may be too strict, it serves the purpose of elucidating the qualitative aspects of the evolution of the crystallization process. Still, the available data has been examined from several perspectives in order to fully comprehend the phenomenon.

Figures 4–27 and 4–28 are similar to 4–25 and 4–26, except that only the crystalline atoms are displayed in order to provide clearer images of the cluster development. Furthermore, FCC and HCP atoms are distinguished by color. The front views of Figure 4–27 show that the cluster growth resembles a nucleation-propagation process, and the rotated view of Figure 4–28a reveals that the cluster starts as three or four stacks of close-packed layers of both FCC and HCP atoms. The cluster grows in the direction normal to the close-packed planes by adding more layers, in addition to expanding outward by adding more atoms to the periphery of the existing layers. It is interesting that the atoms seem to arrange themselves into exclusive layers consisting of only FCC or HCP atoms. This behavior may be energetically driven, given that the mixing of FCC and HCP atoms in the same plane would require the presence of such defects as vacancies and possibly dislocations, which places the system in a higher state of energy. The unit normal vector of the close packed planes is calculated to be (–0.23, 0.50, 0.84), which is not correlated to the planes of

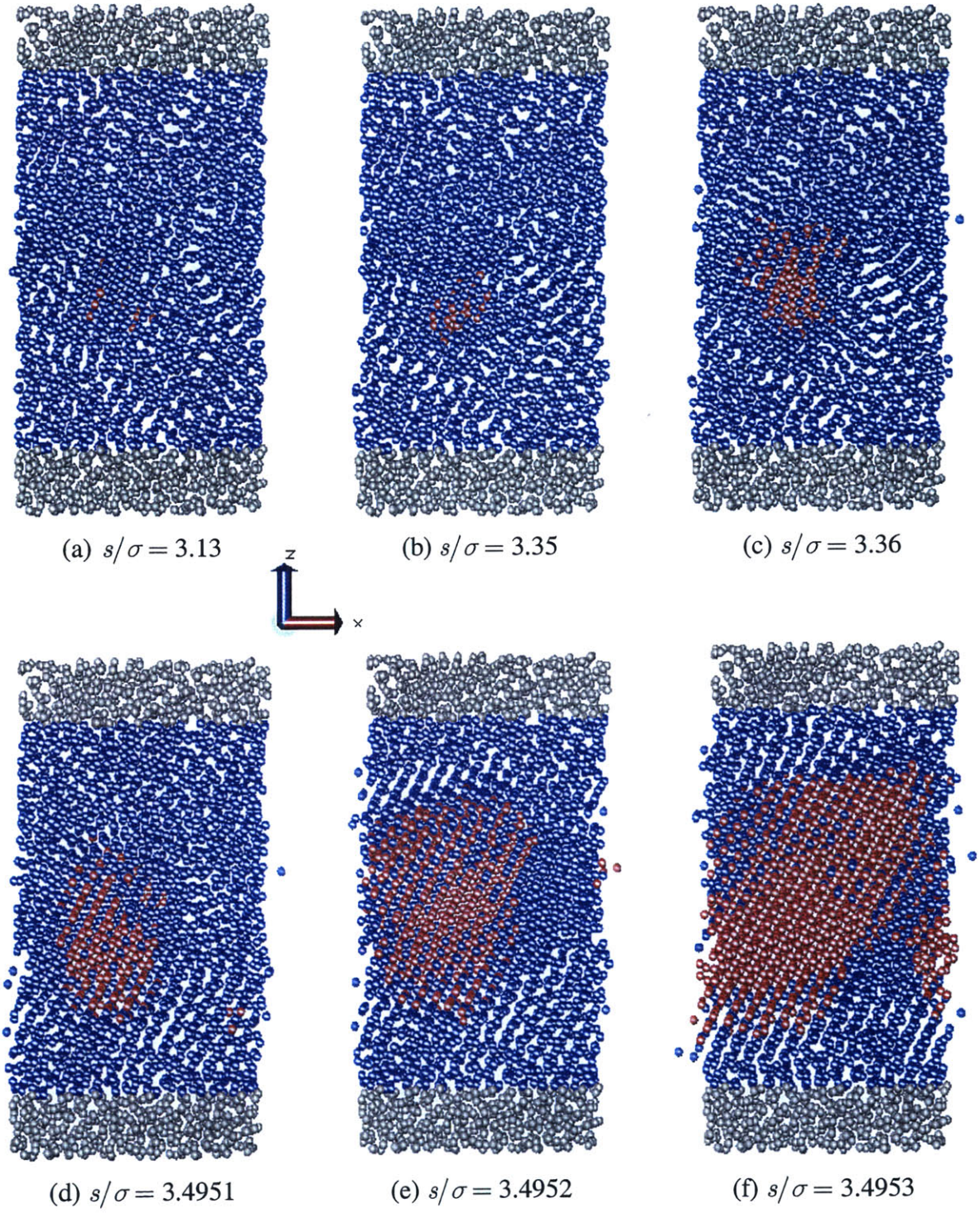

Figure 4–25: Snapshots of crystallization process. Crystalline atoms are shown in red, non-crystalline atoms in blue. All boundary atoms are shown in gray. Graphics by ref. [61].

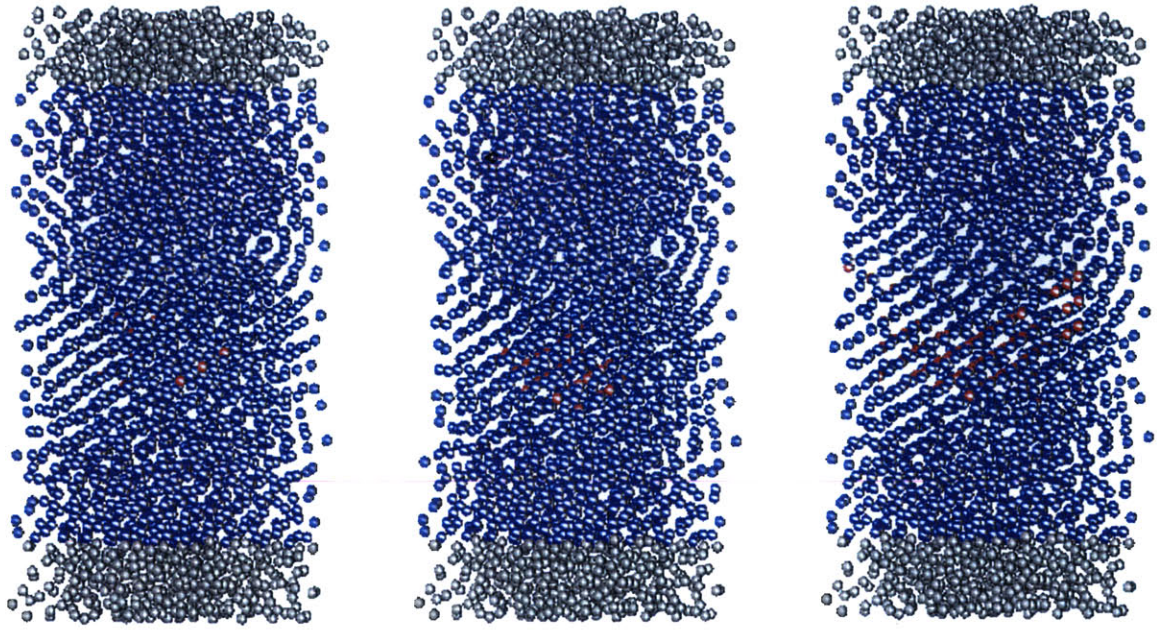

(a) $s/\sigma = 3.13$ (b) $s/\sigma = 3.35$ (c) $s/\sigma = 3.36$

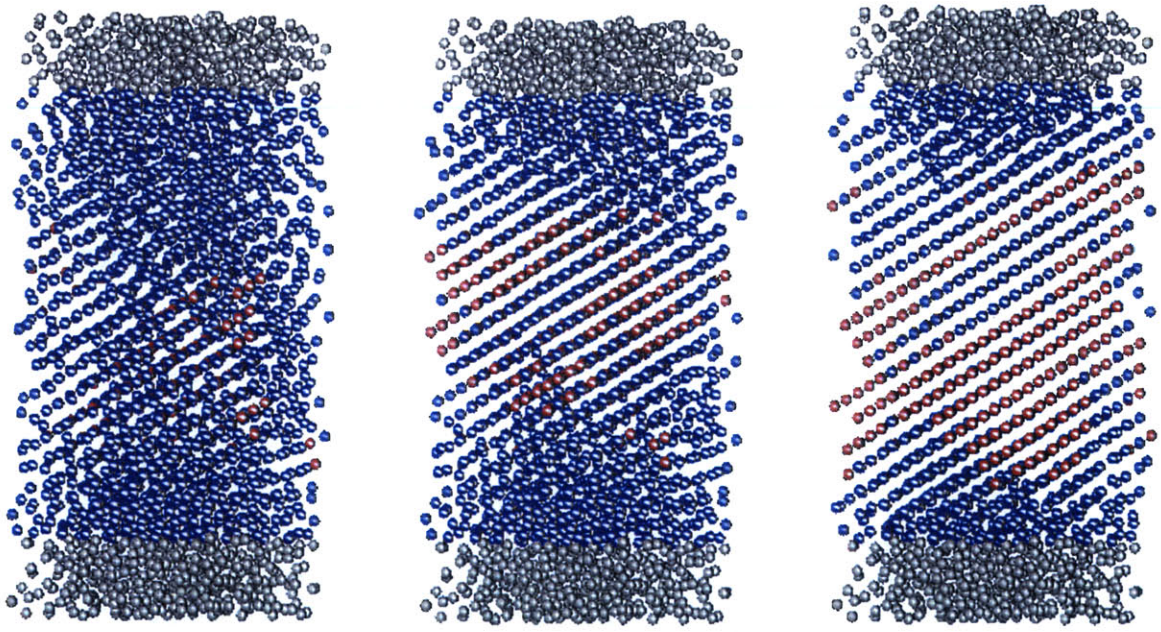

(d) $s/\sigma = 3.4951$ (e) $s/\sigma = 3.4952$ (f) $s/\sigma = 3.4953$

Figure 4–26: Snapshots of crystallization process, rotated view. Rotation angle is 67° about the z axis relative to the view in Figure 4–24. Graphics by reference [61].

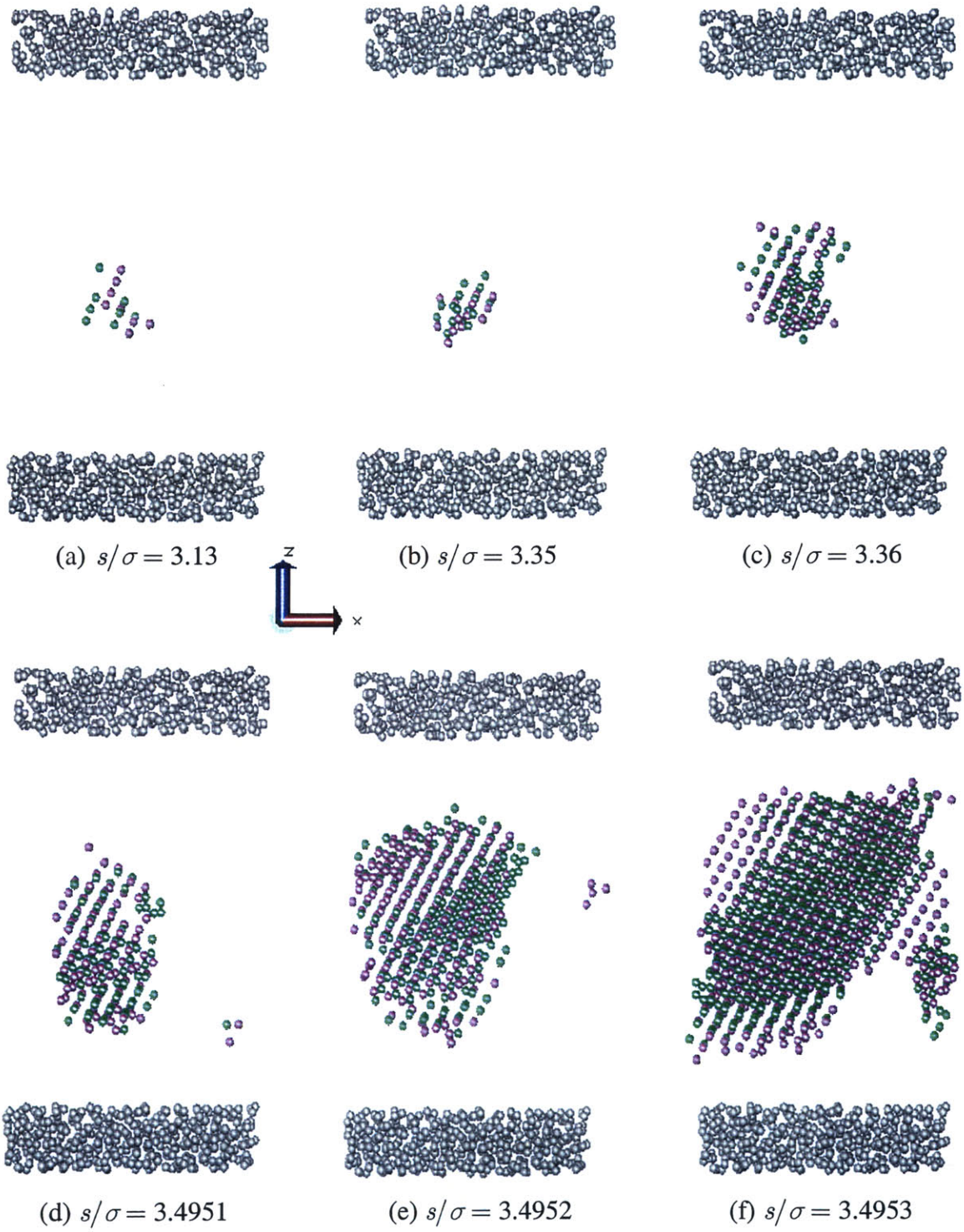

Figure 4–27: Same as Figure 4–24, except only crystalline atoms are shown. FCC atoms are in green, HCP in purple. Graphics by reference [61].

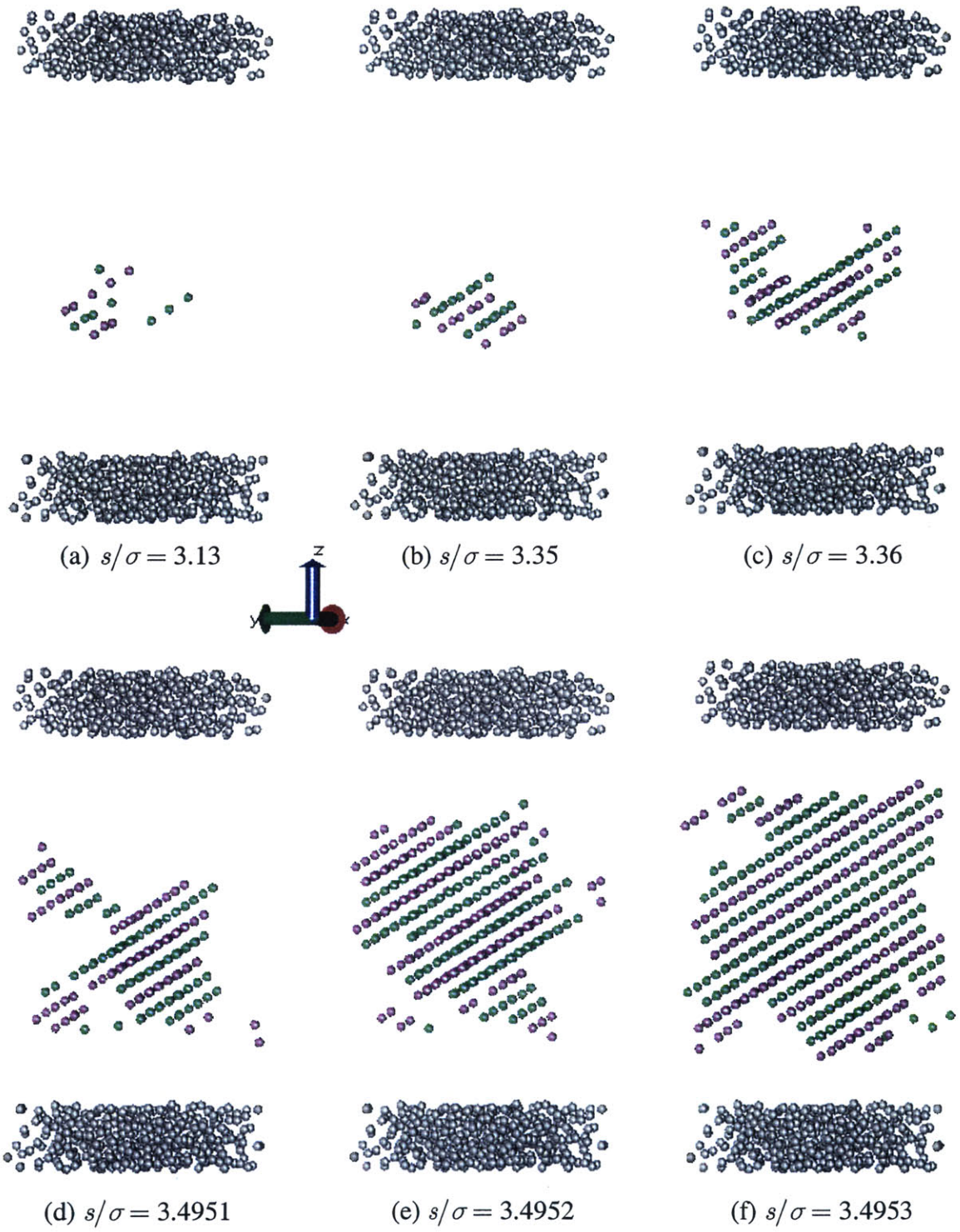

Figure 4–28: Same as Figure 4–25, except only crystalline atoms are shown. FCC atoms are in green, HCP in purple. Graphics by reference [61].

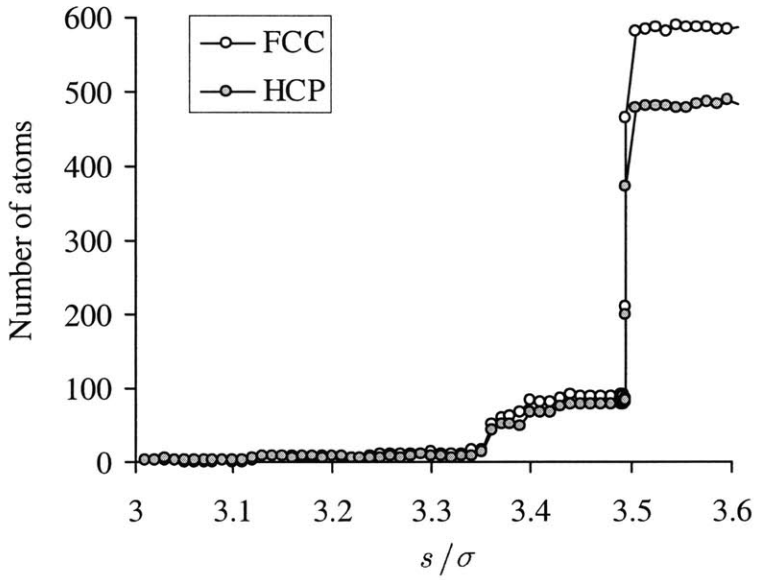

Figure 4–29: Number of FCC and HCP atoms formed during sliding.

principal stress. This is somewhat surprising, as it would have been logical if the close-packed layers were coplanar to the maximum compressive stress plane, for example. However, the cluster displays no such orientational preference, which suggests that the nucleation occurs with a random orientation. Figure 4–29 shows the plots of the number of FCC and HCP atoms over the period leading up to and including crystallization. By the end of shearing, the FCC atoms outnumber the HCP by 100, but there is not any particular reason for there to be more FCC atoms on a consistent basis, because the L–J potential function makes a very weak distinction between the FCC and HCP structure.

4.6.3 Discussion of Crystallization

The fundamental driving force for the crystallization in this simulation is the well-known tendency of pair potentials to form the close-packed structure. Due to this intrinsic property, quenched liquids described by pair potentials commonly exhibit spontaneous nucleation of crystallites even in the absence of shear, provided that the temperature is sufficiently high and enough time is allowed for thermal effects to take over [59,60]. The temperature is far too low for thermal effects to be of any consequence in the present simulations, but the lack of thermal assistance is perhaps compensated by the work done to the system by the shearing

action, meaning that the nucleation is mechanically assisted. When the system is subject to a sufficiently high shear stress for an extended period, some "fertile" regions may be given enough of a push over the energy barrier for a local transformation. Many of these regions will be inclined to relax in the direction of the minimum-energy crystalline structure. While some sites may successfully undergo such transitions, others may be prevented from doing so by uncooperative surroundings.

In discussing the nucleation of the crystallite, some discretion must be exercised regarding the definition of nucleation. For example, the images in Figure 4–25 and 4–26 imply that nucleation is signified by the first sign of a cluster of red atoms, but this definition depends too much on the criteria for crystalline atoms suggested in Section 4.6.2. If the criteria were to be altered by increasing the allowed angle deviation, for example, red atoms would appear much earlier. It is difficult to discern exactly when the nucleation takes place, and even more challenging to determine its exact mechanism. However, viewing the system from a different perspective may be of some help in revealing the true progression of the crystallization phenomenon. In Figure 4–30, the system is shown from a rotated view at progressive stages of sliding leading up to the appearance of the first crystalline cluster. At $s/\sigma = 1.69$ (Figure 4–30b), the atoms inside the highlighted oval show the first signs of layering. By $s/\sigma = 3.0$, the emergence of structural order is clearly evident, even if none of the atoms meet the criteria for crystallinity, and the ordered region has also grown larger. By the time the first crystalline cluster appears at $s/\sigma = 3.13$, it is surrounded by material that has already achieved a considerable degree of order. The sequence of events which is communicated by these figures is that crystalline nucleation does not just happen spontaneously in the midst of an amorphous background. Instead, the amorphous material is first worked into some state of quasi-order, where the structure is not exactly crystalline, but a clear semblance of order is evident. It is in such a "fertile" region that the a crystallite is able to nucleate. The nucleite then precipitates rapidly because the surrounding region is already relatively well-ordered.

Based on these findings, it may be more appropriate to consider the cluster outlined in Figure 4–30b as the nucleite, and at this point, that is left as a matter of choice. The mechanism of crystallization requires that the amorphous material must undergo substantial work in order to gradually become more suitable for the formation of a nucleite, which is consistent with the fact that nucleation does not occur in the simulation until after a significant amount of deformation, which is, in turn, consistent with the experimental observation that nanocrystallites are always found in highly deformed shear bands. The results of these simulations suggest that the nanocrystallites found in deformed amorphous

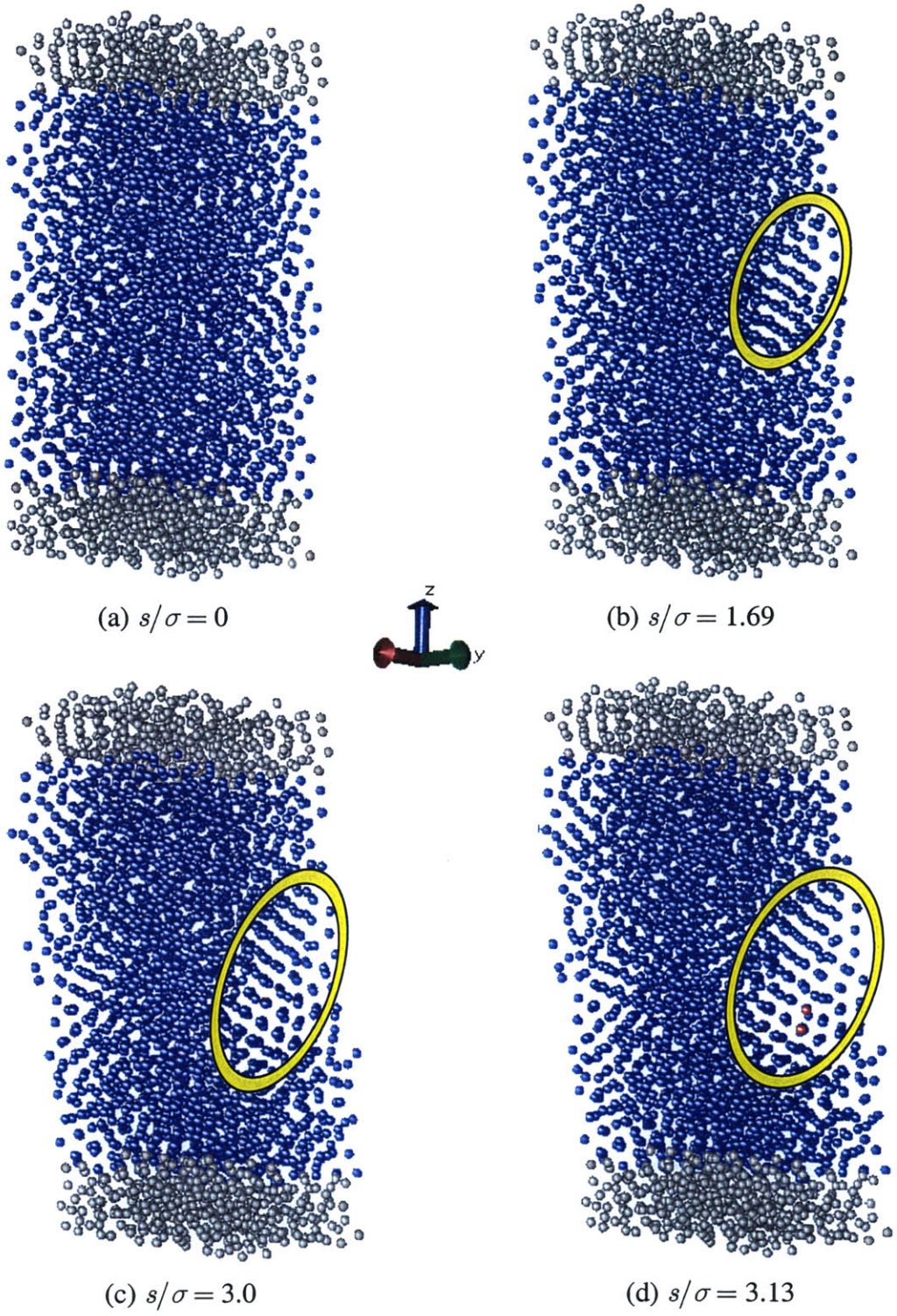

(a) $s/\sigma = 0$ (b) $s/\sigma = 1.69$

(c) $s/\sigma = 3.0$ (d) $s/\sigma = 3.13$

Figure 4–30: Snapshots leading up to crystallization, rotated view. Crystalline atoms are shown in red, non-crystalline atoms in blue. All boundary atoms are shown in gray. Graphics by ref. [61].

metals may, indeed, be the products of a mechanically-driven phenomenon. Still, the comparisons between simulations and experiment must be made with discretion, given the many fundamental differences that exist between the model and the real system. For example, the simulation model consists of a pure material, whereas most amorphous metals contain more than one component. The presence of second-phase elements may play a critical role in stabilizing the amorphous structure [33], thus affecting the crystallization behavior significantly. Nevertheless, the simulations provide theoretical evidence that deformation of amorphous materials, without the assistance of thermal effects or diffusion, does lead to the nucleation and growth of crystalline clusters.

4.7 Sliding Simulation Summary

4.7.1 Friction vs. $\varepsilon_{AB}/\varepsilon_{AA}$

The friction (i.e., average of the sliding resistance) for each of the cases simulated in this work are plotted against $\varepsilon_{AB}/\varepsilon_{AA}$ in Figure 4–31. In addition to the $\varepsilon_{AB}/\varepsilon_{AA} = 0.1$, 0.4, and 1.0 systems presented in Sections 4.4–4.6, simulations were also conducted for $\varepsilon_{AB}/\varepsilon_{AA} =$ 0.2 under similar conditions. The sliding behavior of the $\varepsilon_{AB}/\varepsilon_{AA} = 0.2$ system may be described to be somewhere between the 0.1 and 0.4 systems, which is to say that most of the sliding is confined at the A–B interface, but there also occurs more bulk deformation than in the $\varepsilon_{AB}/\varepsilon_{AA} = 0.1$ system. The asymptotic trend of the curve in Figure 4–31 can be explained in the following way. At low $\varepsilon_{AB}/\varepsilon_{AA}$, there is minimal adhesion between materials A and B, and sliding is consequently localized mostly to the bimaterial interface, which is the weakest plane in terms of sliding resistance due the low A–B attraction. As $\varepsilon_{AB}/\varepsilon_{AA}$ is increased, the sliding resistance likewise increases because the A–B bonds become stronger, but the sliding also starts to become accompanied by significant deformation of the bulk regions. This effect becomes noticeable at $\varepsilon_{AB}/\varepsilon_{AA} = 0.2$, and becomes more dominant as $\varepsilon_{AB}/\varepsilon_{AA}$ increases. At some point after $\varepsilon_{AB}/\varepsilon_{AA} = 0.4$, sliding at the A–B interface becomes practically negligible, and the response is dominated by the deformation of the bulk regions. Consequently, any further increase of $\varepsilon_{AB}/\varepsilon_{AA}$ has almost no effect on the sliding response and friction.

4.7.2 Comparison to Crystalline System

This section compares the results from the amorphous sliding simulations to some key findings from a previous simulation study of the sliding of a crystalline system (ref. Chapter

2). The crystalline system is set up similar to the present amorphous system in most aspects, except that materials A and B are both ordered in the FCC structure with a (111) sliding plane. Otherwise, parameters related to the potential functions, temperature, normal load, and sliding speed are all identical to the present amorphous system. There are two distinct sliding regimes for the crystalline data in Figure 4–31, namely the frictionless ($\varepsilon_{AB}/\varepsilon_{AA} < 0.17$) and the frictional ($0.17 < \varepsilon_{AB}/\varepsilon_{AA} < 1$). In the latter regime, the friction increases proportionately with $\varepsilon_{AB}/\varepsilon_{AA}$. In the frictionless regime, sliding occurs without any jump phenomena, which is the reason why the friction is zero even though the interfacial adhesion is non-zero.

The amorphous-crystalline comparison for the $\varepsilon_{AB}/\varepsilon_{AA} = 0.1$ case shows that the friction is higher in the amorphous system, which is somewhat counter-intuitive. This paradox can be resolved by recalling that in these atomic scale models, friction is the measure of the intensity of jump phenomena, where intensity refers to the amount of potential-to-kinetic energy conversion. In the crystalline case for $\varepsilon_{AB}/\varepsilon_{AA} = 0.1$, the sliding is frictionless because no jump phenomena occur, but in the amorphous system, jump phenomena do occur locally. The reason that jump phenomena occur in the amorphous system but not in the crystalline system is that the amorphous interface allows its atoms significant individual mobility, but the atoms in the crystalline interface are constrained to behave homogeneously within the layer. Therefore, jump phenomena can not be activated unless the entire layer is involved, and that requires a stronger interface. In contrast, local jump activation of a jump does not require as strong an interface, which is why the amorphous system is able to experience jump phenomena and consequently, friction.

In the $\varepsilon_{AB}/\varepsilon_{AA} = 0.2$ case, the crystalline system does experience jump phenomena, but the amorphous system still produces higher friction. The intensity of the jumps in the crystalline case is relatively weak, because the interface is only now strong enough to produce minor jumps. Meanwhile, the local jump phenomena at the sliding interface of the amorphous system is accompanied by inelastic deformation of the bulk regions, elevating the friction even more. As the interface is made stronger, the friction in the crystalline system eventually exceeds that of the amorphous system at $\varepsilon_{AB}/\varepsilon_{AA} = 0.4$, where friction in the amorphous system has started to level off due to the dominance of bulk deformation over interfacial sliding. Beyond $\varepsilon_{AB}/\varepsilon_{AA} = 0.4$, friction continues to increase for the crystalline case but plateaus for the amorphous system.

A comparison of the peak sliding resistances, shown in Figure 4–32, leads to the intuitive conclusion that the crystalline system consistently has a higher peak resistance than the

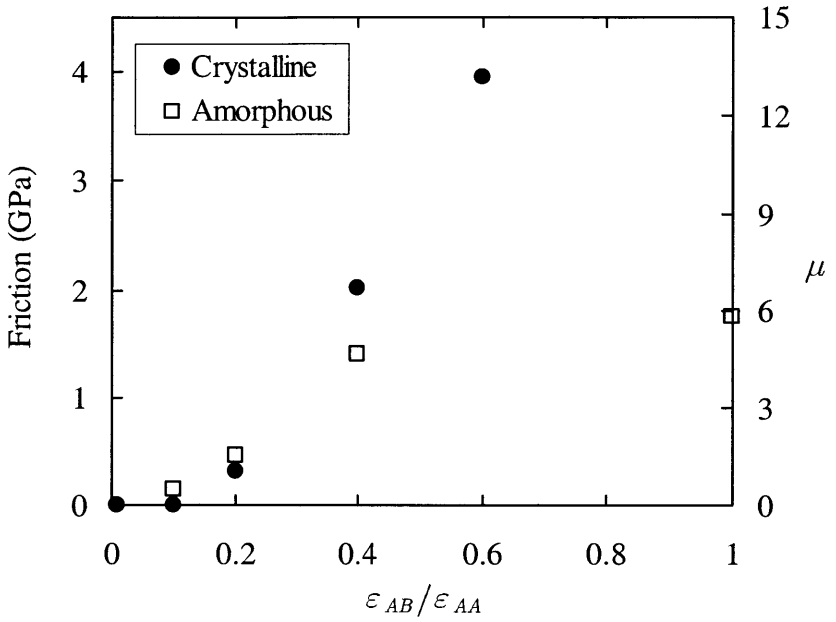

Figure 4–31: Comparison of friction of crystalline (filled circles – Chapter 2) and amorphous (open squares – present work) sliding systems. The friction coefficient (μ) is the friction divided by the normal load of 300 MPa.

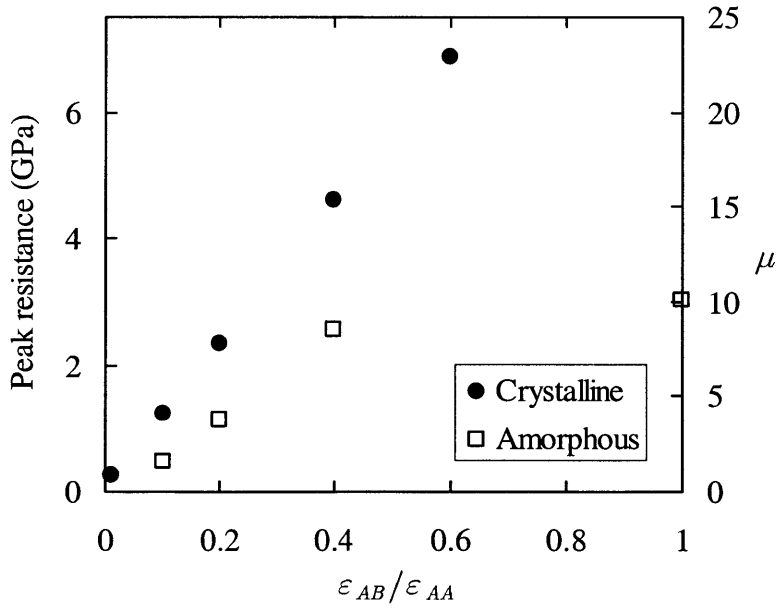

Figure 4–32: Comparison of peak resistance of crystalline (filled circles – Chapter 2) and amorphous (open squares – present work) sliding systems.

amorphous systems. The peak resistance is related to the strength of the interface against shear, and the crystalline interface is the ideal structure for the maximum shear strength. In both systems, the peak resistances have proportional relationships with the interfacial potential parameter $\varepsilon_{AB}/\varepsilon_{AA}$, due to the linear relationship between the breaking force of an interatomic bond and the L–J parameter ε.

4.8 Conclusions

The atomistic mechanisms of friction in amorphous sliding systems was investigated through Molecular Dynamics simulations of Lennard-Jones (L–J) materials. The amorphous materials were prepared by fully melting an FCC crystal and instantaneously quenching the melt. The amorphous solid was then divided into two semi-infinite bodies A and B. The system was subject to sliding under various degrees of interfacial adhesion by adjusting the L–J parameter ratio $\varepsilon_{AB}/\varepsilon_{AA}$. The overall sliding behavior was analyzed using potential energy and sliding resistance calculations. The following are some of the key results of this study.

- Under a weak interface, ($\varepsilon_{AB}/\varepsilon_{AA} = 0.1$), the kinematics of sliding is best described as an assortment of individual motions of the interfacial atoms, or sometimes a small cluster of atoms. Each atom follows independent routes according to independent schedules, but all motion is generally in the direction of sliding. Friction is caused by jump phenomena, which occur locally in amorphous systems. A uniqueness about the amorphous system is that the jump phenomena occur both in the forward and backward directions, although the forward type occur more frequently.
- At a moderate interface ($\varepsilon_{AB}/\varepsilon_{AA} = 0.4$), the system begins experiences noticeable bulk deformation, but the majority of the sliding still takes place at the A–B interface. As a result of the sliding-deformation coupling, the computed friction reflects the sliding resistance of the interface and the deformation resistance of the bulk region.
- The shearing of a bulk system without an interface ($\varepsilon_{AB}/\varepsilon_{AA} = 1$) leads to a deformation-induced crystallization process which nucleates after a significant amount of strain (0.16). Atoms of both FCC and HCP structure make up the crystallized cluster. The fact that the FCC and HCP atoms arrange themselves into close-packed layers containing only their own kind can be justified on an energetic basis. Long before the appearance of the first crystalline cluster, the atoms in the region undergo extensive rearrangement into a quasi-

ordered structure, which is not exactly crystalline according to strictly geometric criteria, but definitely appears to possess a good degree of order. Such an ordered region may be necessary for a nucleite to form. The fact that a substantial amount of deformation is needed to produce crystallization is consistent with the fact that experimentally observed nanocrystallites have all been found inside shear bands.

- The friction in the amorphous system initially increases with $\varepsilon_{AB}/\varepsilon_{AA}$ when the A–B adhesion is weak and sliding is localized to the interface. As the interface becomes stronger, the sliding starts to become accompanied by bulk deformation, and past $\varepsilon_{AB}/\varepsilon_{AA} = 0.4$, bulk deformation is the dominant response. As a result, the friction becomes more or less insensitive to $\varepsilon_{AB}/\varepsilon_{AA}$ beyond 0.4.

4.9 References

1. Tomlinson, G.A., "A Molecular Theory of Friction," *Philosophical Magazine*, ser. 7, vol. 7, no. 46, pp. 905-939, 1929.
2. Frenkel, Y.I. and Kontorova, T., *Zh. Eksp. teor. Fiz.*, vol. 8, pp. 1340, 1938.
3. McClelland, G.M., "Friction at Weakly Interacting Interfaces," in Adhesion and Friction, Springer Series in Surface Sciences, vol. 17, Eds. Grunze, M. and Kreuzer, H.J., Springer Verlag, pp. 1-16, 1989.
4. Mate, C.M., McClelland, G.M., Erlandsson, R., and Chiang, S., "Atomic-Scale Friction of a Tungsten Tip on a Graphite Surface," *Physical Review Letters*, vol. 59, no. 17, pp. 1942-1945, 1987.
5. Ruan, J. and Bhushan, B., "Atomic-Scale and Microscale Friction Studies of Graphite and Diamond using Friction Force Microscopy," *Journal of Applied Physics*, vol. 76, no. 9, pp. 5022-5035, 1994.
6. Krim, J., Solina, D.H., and Chiarello, R., "Nanotribology of a Kr Monolayer: A Quartz-Crystal Microbalance Study of Atomic-Scale Friction," *Physical Review Letters*, vol. 66, no. 2, pp.181-184, 1991.
7. Landman, U., Luedtke, W.D., and Ribarsky, M.W., "Structural and Dynamical Consequences of Interactions in Interfacial Systems," *Journal of Vacuum Science Technology A*, vol. 7, no. 4, pp. 2829-2839, 1989.
8. Harrison, J.A., White, C.T., Colton, R.J., and Brenner, D.W., "Molecular-Dynamics Simulations of Atomic-Scale Friction of Diamond Surfaces," *Physical Review B*, vol. 46, No. 15, pp. 9700-9708, 1992.
9. Sørensen, M.R., Jacobsen, K.W., and Stoltze, P., "Simulations of Atomic-Scale Sliding Friction," *Physical Review B*, vol. 53, no. 4, pp. 2101-2113, 1996.
10. Buldum, A. and Ciraci, S., "Contact, Nanoindentation, and Sliding Friction," *Physical Review B*, vol. 57, no. 4, pp. 2468-2476, 1998.

11. Hammerberg, J.E., Holian, B.L., Röder, J., Bishop, A.R., and Zhou, S.J., Nonlinear Dynamics and the Problem of Slip at Material Interfaces, *Physica D*, vol. 123, pp. 330-340, 1998.

12. Thompson, P.A. and Robbins, M.O., "Origin of Stick-Slip Motion in Boundary Lubrication," *Science*, vol. 250, pp.792-794, 1990.

13. Glosli, J.N. and McClelland, G.M., "Molecular Dynamic Study of Sliding Friction of Ordered Organic Monolayers," *Physical Review Letters*, vol. 70, no. 13, pp. 1960-1963, 1993.

14. Yim. S., Sonwalkar, N., and Saka, N., "Molecular Dynamics Simulation of Boundary Lubricated Interfaces," *Journal of Computer-Aided Materials Design*, vol. 6, pp. 69-80, 1999.

15. Landman, U., Luedtke, W.D., and Gao, J., "Atomic-Scale Issues in Tribology: Interfacial Junctions and Nano-elastohydrodynamics," *Langmuir*, vol. 12, pp. 4514-4528, 1996.

16. Chandrasekaran, N., Khajavi, A.N., Raff, L.M., and Komanduri, R., "A New Method for Molecular Dynamics Simulation of Nanometric Cutting," *Philosophical Magazine B*, vol. 77, no. 1, pp. 7-26, 1998.

17. Landman, U., Luedtke, W.D., Burnham, N.A., and Colton, R.J., "Atomistic Mechanisms and Dynamics of Adhesion, Nanoindentation, and Fracture," *Science*, vol. 248, pp. 454-461, 1990.

18. Enke, K., Dimigen, H., and Hübsch, H., "Frictional Properties of Diamondlike Carbon Layers," *Applied Physics Letters*, vol. 36, no. 4, pp. 291-292, 1980.

19. Erdemir, A. Bindal, C., Fenske, G.R., and Wilbur, P., "Tribological Properties of Hard Carbon Films on Zirconia Ceramics," *Tribology Transactions*, vol. 39, no. 3, pp. 735-744, 1996.

20. Erdemir, A., Eryilmaz, O.L., and Fenske, G., "Synthesis of Diamondlike Carbon Films with Superlow Friction and Wear Properties," *Journal of Vacuum Science Technology A*, vol. 18, no. 4, pp. 1987-1992, 2000.

21. Heimberg, J.A., Wahl, K.J., and Singer, I.L., Erdemir, A., "Superlow Friction Behavior of Diamond-Like Carbon Coatings: Time and Speed Effects," *Applied Physics Letters*, vol. 78, no. 17, pp. 2449-2451, 2001.

22. Bienk, E.J., Reitz, H., and Mikkelsen, N.J., "Wear and Friction Properties of Hard PVD Coatings," *Surface Coatings and Technology*, vol. 76-77, pp. 475-480, 1995.

23. Sugimoto, I. and Miyake, S., "Oriented Hydrocarbons Transferred from a High Performance Lubricative Amorphous C:H:Si Film During Sliding in a Vacuum," *Applied Physics Letters*, vol. 56, no, 19, pp. 1868-1870, 1990.

24. Liu, Y., Erdemir, A., and Meletis, E.I., "An Investigation of the Relationship Between Graphitization and Frictional Behavior of DLC Coatings," *Surface and Coatings Technology*, vol. 86-87, pp. 564-568, 1996.

25. Donnet, C., Fontaine, J., Grill, A., and LeMogne, T., "The Role of Hydrogen on the Friction Mechanism of Diamond-Like Carbon Films," *Tribology Letters*, vol. 9, no. 3-4, pp. 137-142, 2000.

26. Bernal, J.D., "The Structure of Liquids," *Proceedings of the Royal Society A*, vol. 280, pp. 299-322, 1964.

27. Spaepen, F., "A Microscopic Mechanism for Steady State Inhomogeneous Flow in Metallic Glasses," *Acta Metallurgica*, vol. 25, pp. 407-415, 1977.

28. Argon, A.S., "Plastic Deformation in Metallic Glasses," *Acta Metallurgica*, vol. 27, pp. 47-58, 1979.

29. Argon, A.S. and Shi, L.T., "Development of Visco-Plastic Deformation in Metallic Glasses," *Acta Metallurgica*, vol. 31, no. 4, pp. 499-507, 1983.

30. Argon, A.S. and Shi, L.T., "Analysis of Plastic Flow in an Amorphous Soap Bubble Raft by the Use of an Inter-Bubble Potential," *Acta Metallurgica*, vol. 46, no. 2, pp. 275-294, 1982.

31. Maeda, K. and Takeuchi, S., "Atomistic Process of Plastic Deformation in a Model Amorphous Metal," *Philosophical Magazine A*, vol. 44, no. 3, pp. 643-656, 1981.

32. Srolovitz, D., Vitek, V., and Egami, T., "An Atomistic Study of Deformation of Amorphous Metals," *Acta Metallurgica*, vol. 31, no. 2, pp. 335-352, 1983.

33. Deng, D., Argon, A.S., and Yip, S., "A Molecular Dynamics Model of Melting and Glass Transition in an Idealized Two-Dimensional Material I", *Philosophical Transactions of the Royal Society of London A*, vol 329, pp. 549-573, 1989.

34. Deng, D., Argon, A.S., and Yip, S., "Topological Features of Structural Relaxations in a Two-Dimensional Model Atomic Glass II", *Philosophical Transactions of the Royal Society of London A*, vol 329, pp. 575-593, 1989.

35. Deng, D., Argon, A.S., and Yip, S., "Kinetics of Structural Relaxations in a Two-Dimensional Model Atomic Glass III", *Philosophical Transactions of the Royal Society of London A*, vol 329, pp. 595-612, 1989.

36. Deng, D., Argon, A.S., and Yip, S., "Simulation of Plastic Deformation in a Two-Dimensional Atomic Glass by Molecular Dynamics IV", *Philosophical Transactions of the Royal Society of London A*, vol 329, pp. 613-640, 1989.

37. Brostow, W. and Dussault, J-P, "Construction of Voronoi Polyhedra," *Journal of Computational Physics*, vol. 29, pp. 81-92, 1978.

38. Finney, J.L., "A Procedure for the Construction of Voronoi Polyhedra," *Journal of Computational Physics*, vol. 32, pp. 137-143, 1979.

39. Finney, J.L., "Random Packings and the Structure of Simplae Liquids I. The Geometry of Random Close Packing," *Proceedings of the Royal Society of London A*, vol. 319, pp. 479-493, 1970.

40. Finney, J.L., "Random Packings and the Structure of Simplae Liquids II. The Molecular Geometry of Simple Liquids," *Proceedings of the Royal Society of London A*, vol. 319, pp. 495-507, 1970.

41. Tanaka, M., "Statistics of Voronoi Polyhedra in Rapidly Quenched Monatomic Liquids. II. Comparison Between Argon and Rubidium," *Journal of the Physical Society of Japan*, vol. 55, no. 10, pp. 3428-3436, 1986.

42. Michalski, J., "Thermal Conductivity of Amorphous Solids Above the Plateau: Molecular Dynamics Study," *Physical Review B*, vol. 45, no. 13, pp. 7054-7065, 1992.

43. Nakatani, K., Nakatani, A., Sugiyama, Y., and Kitagawa, H., "Molecular Dynamics Study on Mechanical Properties and Fracture in Amorphous Metal," *AIAA Journal*, vol. 38, no. 4, pp. 695-701, 2000.

44. Sinnott, S.B., Colton, R.J., White, C.T., Shenderova, O.A., Brenner, D.W., and Harrison, J.A., "Atomistic Simulations of the Nanometer-scale Indentation of Amorphous-carbon Thin Films," *Journal of Vacuum Science Technology A*, vol. 15, no. 3, pp. 936-940, 1997.

45. Kaukonen, M. and Nieminen, R.M., "Atomic-scale Modeling of the Ion-beam-induced Growth of Amorphous Carbon," *Physical Review B*, vol. 61, no. 4, pp. 2806-2811, 2000.

46. Plaisted, T.A., Ni, B., Zahrt, J.D., Sinnott, S.B., "Comparison of Growth of Hydrocarbon Thin Films by Molecular-beam and Cluster-beam Deposition: Atomistic Simulations," *Thin Solid Films*, vol. 381, pp. 73-83, 2001.

47. Stoneham, A.M., Godwin, P.D., Sutton, A.P., Bull, S.J., "Elastic and Plastic Deformation of Diamondlike Carbons," *Applied Physics Letters*, vol. 72, no. 24, pp. 3142-3144, 1998.

48. Haerle, R., Galli, G., Baldereschi, A., "Structural Models of Amorphous Carbon Surfaces," *Applied Physics Letters*, vol. 75, no. 12, pp. 1718-1720, 1999.

49. Bilek, M.M.M., McKenzie, D.R., McCulloch, D.G., and Goringe, C.M., "Ab initio Simulation of Structure in Amorphous Hydrogenated Carbon," *Physical Review B*, vol. 62, no. 5, pp. 3071-3077, 2000.

50. Zhen, S. and Davies, G.J., "Calculation of the Lennard-Jones n-m Potential Energy Parameters for Metals," *Physica Status Solidi A*, Vol. 78, pp. 595-605, 1983.

51. Parrinello, M. and Rahman, A., "Polymorphic Transitions in Single Crystals: A New Molecular Dynamics Method," *Journal of Applied Physics*, vol. 52, no. 12, pp. 7182-7190, 1981.

52. Phillpot, S.R., Yip, S., and Wolf, D., "How Do Crystals Melt?" *Computers in Physics*, Nov/Dec, pp. 20-31, 1989.

53. Kristensen, W.D., "Computer Simulated Amorphous Structures (I). Quenching of a Lennard-Jones Model System," *Journal of Non-Crystalline Solids*, vol. 21, pp. 303-318, 1976.

54. Gilman, J.J., "Mechanical Behavior of Metallic Glasses," *Journal of Applied Physics*, vol. 46, no. 4, pp. 1625-1633, 1975.

55. Chen, H., He, Y., Shiflet, G.J., and Poon, S.J., "Deformation-Induced Nanocrystal Formation in Shear Bands of Amorphous Alloys," *Nature*, vol. 367, pp. 541-543, 1994.

56. Ogura, A., Tarumi, R., Shimojo, M., Takashima, K., and Higo, Y., "Control of Nanocrystalline Orientation Using the Application of a Stress Field in an Amorphous Alloy," *Applied Physics Letters*, vol. 79, no. 7, pp. 1042-1044, 2001.

57. Kim, J.-J., Choi, Y., Suresh, S., and Argon, A.S., "Nanocrystallization During Nanoindentation of a Bulk Amorphous Metal Alloy at Room Temperature," *Science*, vol. 295, pp. 654-657, 2002.

58. Tarumi, R., Ogura, A., Shimojo, M., Takashima, K., and Higo, Y., "Molecular Dynamics Simulation of Crystallization in an Amorphous Metal During Shear Deformation," *Japanese Journal of Applied Physics*, vol. 39, pp. L611-L613, 2000.

59. Cape, J.N., Finney, J.L., and Woodcock, L.V., "An Analysis of Crystallization by Homogeneous Nucleation in a 400-Atom Soft-Sphere Model," *Journal of Chemical Physics*, vol. 75, no. 5., pp. 2366-2373.

60. Tanemura, M., Hiwatari, Y., Matsuda, H., Ogawa, T., Ogita, N., and Ueda, A., "Geometrical Analysis of Crystallization of the Soft-Core Model," *Progress of Theoretical Physics*, vol. 58, no. 4, pp. 1079-1095, 1977.

61. Humphrey, W., Dalke, A., and Schulten, K., "VMD - Visual Molecular Dynamics," *Journal of Molecular Graphics*, vol. 14, no. 1, pp. 33-38, 1996.

CHAPTER 5

Experimental Measurement of Friction in Thin Film Systems

5.1 Introduction

Thin, hard films are attractive solutions to the problem of designing low-friction systems without the use of lubricants, an issue of vital importance in industries providing protective coatings for cutting tools, for example. Ceramics are usually the preferred coating material due to their exceptional hardness, wear resistance, chemical inertness, and high temperature tolerance [1–3], although lately diamond-like carbon (DLC) has been receiving much attention because of its intriguing mechanical and chemical properties [4–8]. The main purpose of most hard coatings is to protect the substrate and resist wear, thereby prolonging the life of the component, and to that end they have proven to be quite successful. For example, TiN and TiC coatings have been shown to improve the life of high-speed cutting tools by a factor of 2–4 [9]. The coatings also offer the additional benefit of low friction [10], which is the consequence of their superb wear resistance.

Thin films with low friction and wear properties are also appealing possibilities for miniature systems such as micro-electromechanical systems (MEMS) and magnetic recording systems, which have extremely low tolerance for friction due to their unusually small size, yet their functional requirements are as demanding as their macroscopic counterparts. For example, micromotors that are only about 100 μm in overall diameter have a rated speed up to 100,000 rpm [11]. Before hard coatings can be used effectively in such environments, they must be designed for even lower friction than the current standard (the friction coefficient of typical hard coatings is of the order of 0.1 in air [1–3]). In order to properly design coatings for low friction, the governing mechanisms of friction in hard coatings, which may be fundamentally different from such classical models as plowing and asperity deformation [12,13], must be better understood. In the classical models, friction is directly related to plastic deformation of the surfaces, but the hardness and smoothness of most vapor-deposited films, in conjunction with a low normal load, can greatly reduce the occurrence of plowing and surface deformation. In such a case, friction would most likely be governed by the intermolecular forces at the sliding interface, and substantially high friction forces can result from strong adhesion between the sliding surfaces even in the absence of

excessive wear. It may even be suggested that tribology of hard coating systems may be better understood in the context of nanotribology [14], where frictional behavior is interpreted at the nano- or even atomic scale.

If friction indeed predominantly depends on the interfacial adhesion, the ideal strategy for the design of low-friction surfaces is to discourage strong intermolecular bonding at the contact, which may be achieved simply by selecting a metallurgically incompatible pair of coating materials, for example. In addition, friction may also be sensitive to the environment if the atmospheric gases significantly react with the surfaces, thereby modifying their chemical and energetic state. The resolution of these issues is an important task, not only for the improvement in the understanding of the frictional properties and behavior of the thin film systems, but also to the general area of tribology. In particular, the relationship between friction and adhesion is currently not understood very well (besides the abstract notion that high adhesion leads to high friction), and it may be clarified through an investigation of the friction in hard films, where adhesion most likely governs friction. Accordingly, the objective of the present work is to experimentally study the tribological properties of hard, thin films through measurements of friction. The emphasis of the research is placed on the sensitivity of friction to various material combinations, the effect of the atmosphere on friction, and the relationship between adhesion and friction.

5.2 Experimental Apparatus

5.2.1 Pin-on-Disk System

Figure 5–1 shows the standard pin-on-disk tribotester used to obtain friction measurements. The apparatus features a strain ring with four strain gages connected into the full Wheatstone bridge circuit, which is fed into an analog chart recorder. A signal amplifier with a variable gain up to 5000 is also implemented in order to facilitate the measurement of low friction. Still, this system has limited resolution of about 10 mN due to noise, and it was accordingly used only to measure relatively high friction. The normal load P is applied by placing dead weights of known mass directly on top of the slider. As the disk rotates at 10 rpm, the friction force F is continuously recorded, and the friction coefficient μ is obtained by $\mu = F/P$.

Three type of sliders are used in the testing. The first is a standard Rockwell C hardness indenter, which has a conical tip with an included angle of 120°. At the tip of the indenter is a well-polished diamond insert with a tip radius of 200 μm. The second slider is a 6.4 mm

(1/4") diameter silicon nitride ball, and the third is a 6.4 mm diameter sapphire ball, polished to optical grade smoothness. Relevant properties of the sliders are summarized in Table 5–1.

Table 5–1: Geometry and mechanical properties of sliders.

Slider	Radius (mm)	Young's Modulus (GPa)	Poisson's Ratio	Hardness (GPa)
Diamond tip	0.2	1000	0.17	85
Sapphire ball	3.175	386	0.22	15
Si_3N_4 ball	3.175	310	0.25	18

Properties of diamond obtained from [6], properties of sapphire and silicon nitride obtained from [15].

5.2.2 Cantilever Apparatus

In addition to the pin-on-disk setup, a cantilever-based device, shown in Figure 5–2, is also employed to measure extremely low friction (i.e., below 10 mN). The lateral deflection of the cantilever beam is measured by four strain gages mounted on both sides of the beam near its base (two on each side). The gages are connected into the Wheatstone full bridge circuit, which is connected directly to the analog chart recorder. A signal amplifier is not necessary in this apparatus due to its excellent sensitivity, featuring a resolution of 0.1 mN. The steel beam is 122 mm long, 12.7 mm wide, and 0.18 mm thick, with a specimen holder at the end where various sliders can be secured. The normal load is applied by placing dead weights directly on top of the specimen holder. The sliders listed in Table 5–1 are also used in this apparatus. The disk is placed on round platform, the height of which is adjusted so that the beam is level when the slider is in contact with the surface of the disk.

The technique of measuring friction with this device involves a *vibrational* method, where the disk remains stationary (the surface does not rotate as in a standard pin-on-disk setup). With the slider secured in the specimen holder and the load in place, the test is initiated by manually deflecting the beam in one direction by an arbitrary distance, and then suddenly letting go. The outcome is vibrational response with damping due to frictional

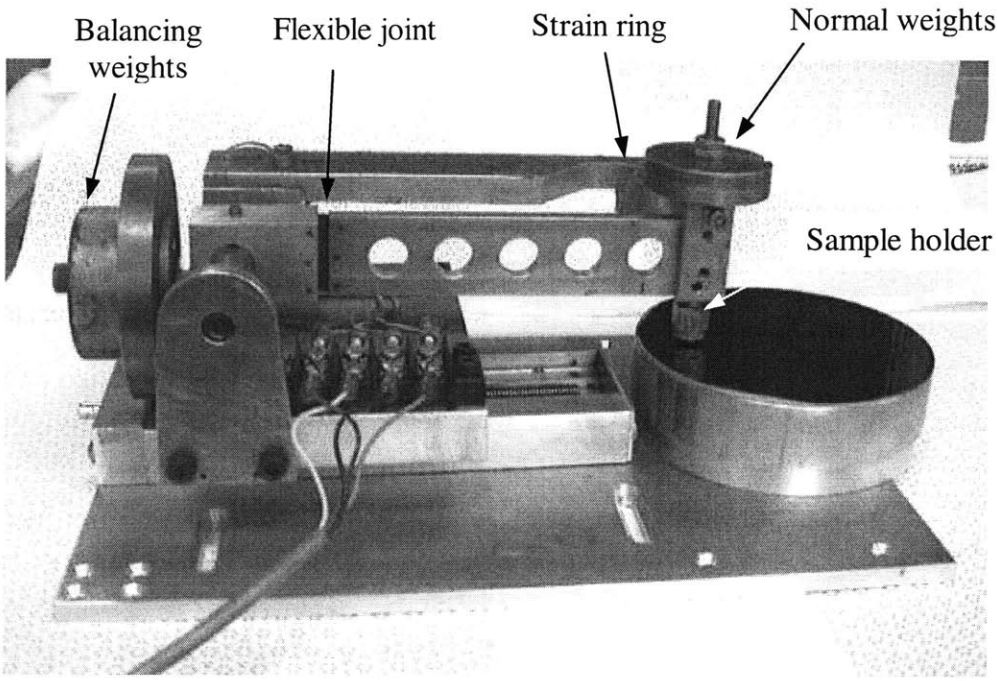

Figure 5–1: Pin-on-disk testing apparatus.

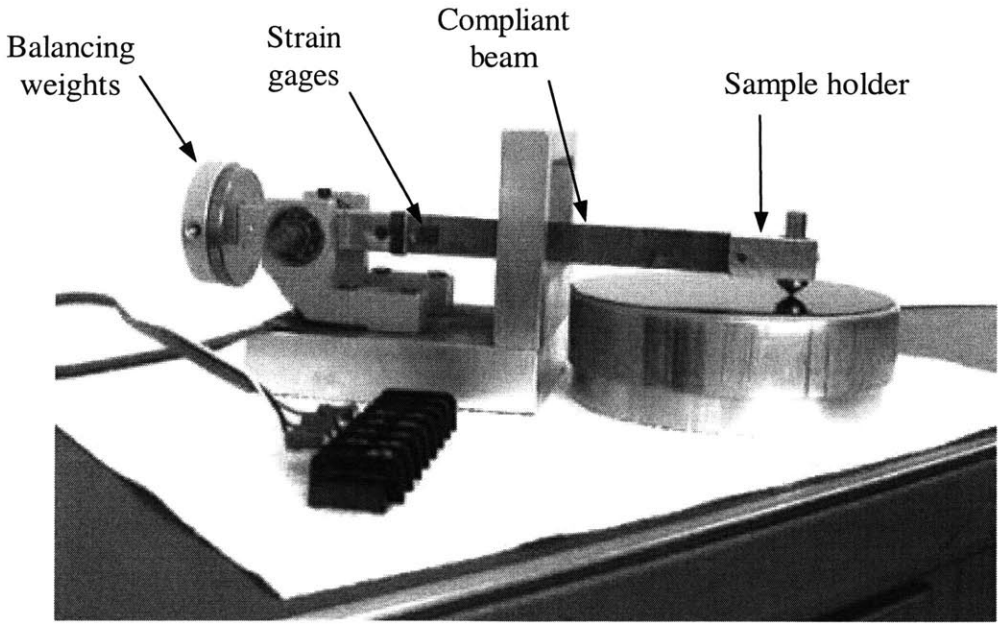

Figure 5–2: Cantilever testing apparatus.

dissipation, during which the slider slides back and force across the surface with a decaying amplitude and eventually comes to a full stop. The rate of amplitude decay (i.e., amplitude decrease per oscillation) depends on the friction between the slider and the surface, a correlation which can be used to obtain a convenient expression for friction. To simplify the analysis leading to this expression for friction, the following assumptions may be made. First, it may be assumed that the friction between the slider and the surface obeys Coulomb's law, which states that friction is independent of the speed. Second, the effect of possible variations of the surface topology can be ignored, particularly in light of the superb smoothness and uniformity of the films used here. Furthermore, the path of travel of the slider is assumed to be a line perpendicular to the undeformed beam, even though it is, in actuality, an arc. This assumption is valid when the ratio of the deflection to the length of the beam is sufficiently low. The beam is also assumed to behave according to linear elasticity and the small deflection theory, the latter of which is valid up to a deflection of 20% of the beam length.

Under the foregoing assumptions, the rate of decay of the amplitude is linear, which allows for a simple energy-based derivation leading to a convenient expression for the friction coefficient. Referring to the schematic of one oscillation (from state 1–2–3) in Figure 5–3, the deflection amplitudes (i.e., the maximum deflections when the slider has momentarily reached zero velocity and is about to change direction) are denoted by δ_1, δ_2, and δ_3, and it may be noted that all δ's are defined to be positive-valued. The total energy E_1 at state 1 is equal to the strain energy of the beam, which is given by

$$E_1 = \frac{1}{2} k \delta_1^2, \tag{5.1}$$

where k is the bending stiffness of the beam. Likewise, $E_2 = k\delta_2^{\,2}/2$ and $E_3 = k\delta_3^{\,2}/2$. The energy consumed by friction as the slider slides from 1 to 2 is equal to the difference in the strain energy,

$$F(\delta_1 + \delta_2) = E_1 - E_2, \tag{5.2}$$

where F is the friction force, assumed to be constant. Inserting Eqn. (5.1) and the related expression for E_2 into Eqn. (5.2) and substituting $\delta_1 = f_1/k$ and $\delta_2 = f_2/k$ (f_1 and f_2 are the *magnitudes* of the elastic force exerted by the beam at states 1 and 2),

$$F = \frac{f_1^2 - f_2^2}{2(f_1 + f_2)}. \tag{5.3}$$

The numerator in Eqn. (5.3) can be factored, so that $F = \Delta f_{12}/2$, where $\Delta f_{12} = f_1 - f_2$. With the decay assumed to be linear, it follows that $\Delta f_{12} = \Delta f_{23}$, and it can further be shown that $F = \Delta f_{13}/4$. This last step has practical value in that the 1–2 process is only a half-oscillation, and it is preferable to compute friction based on a full oscillation, mainly because Δf_{13} does not depend on the zero-deflection reference line on the chart recorder, whereas Δf_{12} does require confidence in the reference, which is sometimes undependable due to problems with reference drift. The expression for the friction coefficient for the general case of many oscillations is then

$$\mu = \frac{\Delta f}{4nP}, \tag{5.4}$$

where Δf is the total change in the amplitude (measured in force) over n number of oscillations, and P is the normal load. Figure 5–4 illustrates an example of the output from an experiment conducted with the cantilever apparatus. In the example, $n = 5$. (It is good practice to start counting at the first "free" peak, and not from the point of release, because there might have been some friction between the slider and the finger during the release, for example. It is also important to stop counting at the last "free" peak, *before* the slider comes to a full stop.) It is statistically favorable to compute the friction over as many oscillations as possible because friction can actually vary during the test due to a number of reasons, such as topological variations of the surface or a slight dependence of friction on the sliding speed.

5.2.3 Vacuum System

At times, the testing was conducted under a controlled environment inside a vacuum chamber, shown in Figure 5–5. The pin-on-disk and cantilever systems both fit inside the chamber, and a sealed feed-through mechanism was used to rotate the disk for the pin-on-disk setup or execute the initial deflection and release for the cantilever setup. The vacuum is generated by a mechanical pump, and a minimum chamber pressure of 50 μm Hg is possible. In addition to vacuum, testing was also done in hydrogen and argon atmospheres by initially creating a vacuum, and then filling the chamber with the desired gas.

5.2.4 Atomic Force Microscope

In addition to standard tribotesting, microscale friction testing was conducted using an atomic force microscope (AFM), which was equipped to measure the vertical (i.e., normal) force as well as the lateral (i.e., friction) force. The Nanoscope IIIa apparatus was used in the

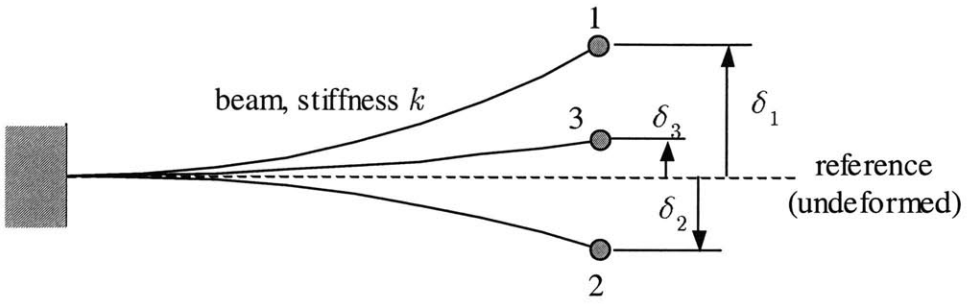

Figure 5–3: Schematic of cantilever testing procedure.

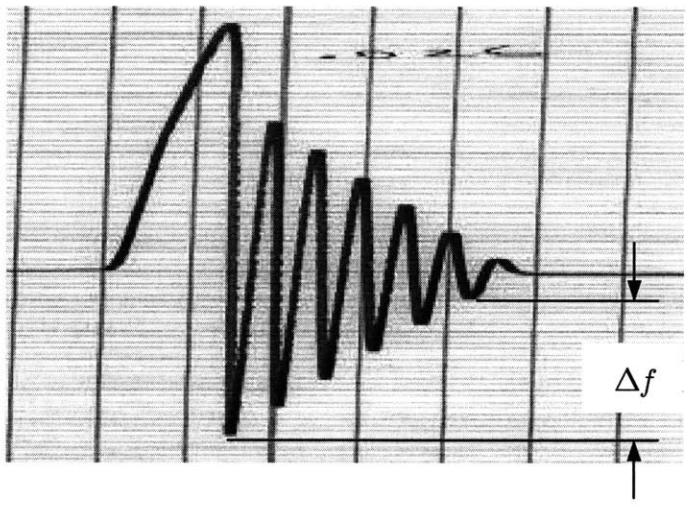

Figure 5–4: Friction measurement from cantilever apparatus.

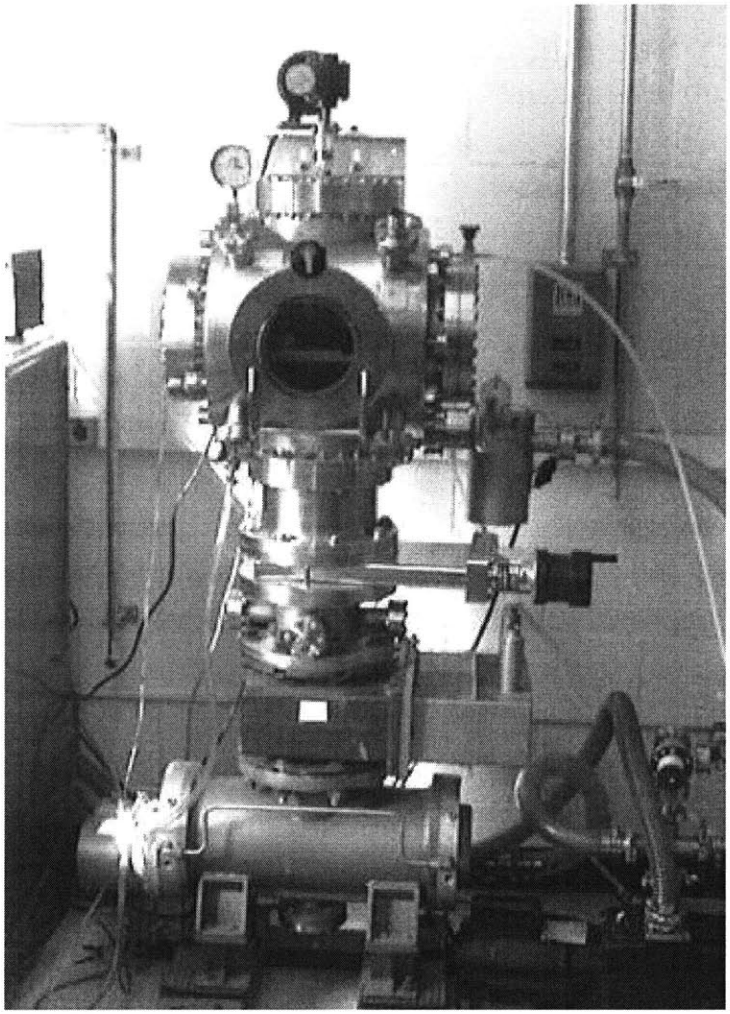

Figure 5–5: Vacuum apparatus.

"contact mode". The tip was a triangular Si_3N_4 cantilever, 100 μm long, with a sharp point mounted above the surface with a slight tilt from horizontal. The tip was mounted on a piezoelectric tube, which was used for controlling fine-scale motion. The tube assembly was mounted on a vertical slide attached to a stepper motor that controls coarse motion. The normal force was measured by the downward deflection of the cantilever, whose nominal bending stiffness is 0.38 N/m. The friction, measured by torsion of the cantilever, was recorded in units of volts. A optical microscope is integrated into the AFM setup in order to facilitate the tip location and calibration. The AFM stage was suspended on an pneumatic isolation table in order to minimize noise in the data. The apparatus was also secured under a hood during its operation.

The AFM was used for two purposes. The first is to measure the adhesion between the tip and various surfaces by reciprocating the tip vertically (i.e., normal to the surface), such that the tip comes into contact with the surface, or technically, enters the repulsive field of the surface. Upon the retraction, the "pull-off" force, or the maximum attractive force before the tip fully disengages, is recorded for each cycle. The pull-off force is a direct measure of the adhesion. The second purpose of the AFM is to measure friction by scanning the sample laterally (i.e., parallel to the surface) while in repulsive contact with the surface. The normal deflection of the tip measures the normal force simultaneously as the torsion of the tip measures the friction force. The piezo actuator continuously adjusts the height during scanning so that the tip deflection, or the normal load, is maintained at a constant value. During the friction testing, the slow scan axis is disabled, meaning that the tip repeatedly scans over the same sliding path instead of scanning a square area, as is typically done for topography measurement, for example. All AFM testing was done in air.

Table 5–2: Material properties of films.

Surface	Young's Modulus (GPa)	Poisson's Ratio	Hardness (GPa)
Si (substrate)	130	0.28	10
TiN	440	0.25	22
Si_3N_4	310	0.25	18
DLC	141	0.20	15
DLC:H	30	0.20	6

Properties of silicon obtained from [16], TiN from [17] and [1] silicon nitride from [15]. DLC and DLC:H are from [5,18]

5.3 Characterization of Films

The disk was a 4" diameter Si wafer coated with 100 nm of TiN, DLC (diamond-like carbon, without any hydrogen), and Si_3N_4. These coatings were applied by the physical vapor deposition (PVD) process of sputtering from an outside source. In addition, a 1 μm

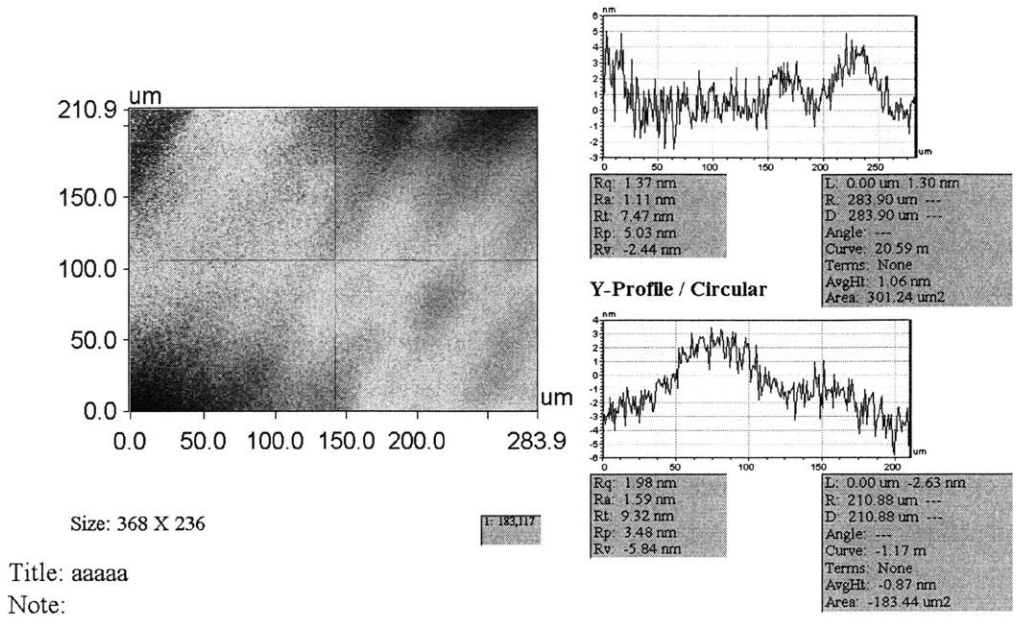

(a) TiN

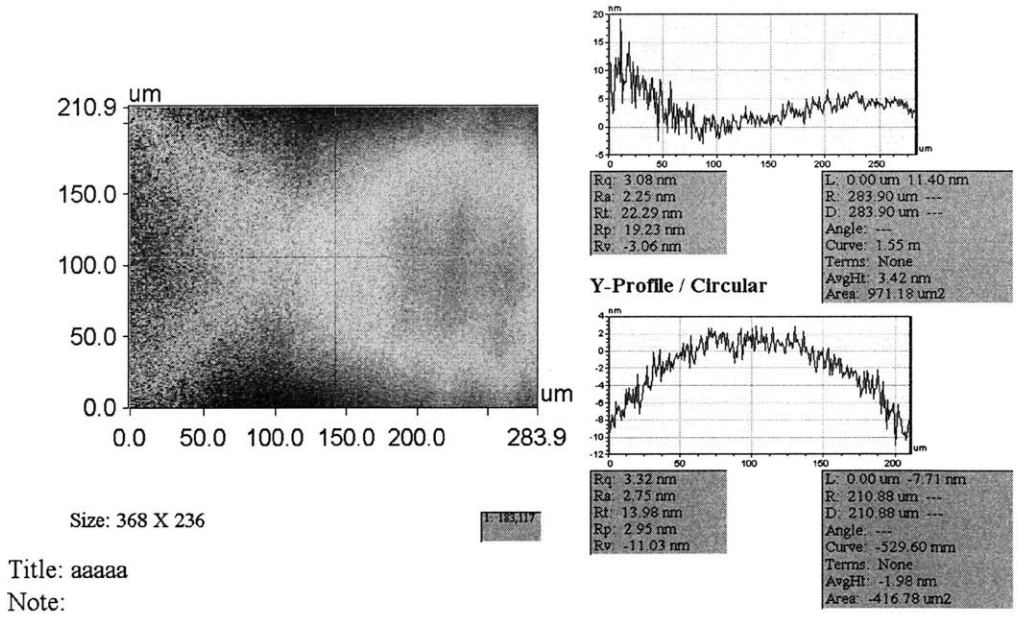

(b) DLC

Figure 5–6: Surface topography of TiN and DLC films using optical profilometry. (a) The average roughness of TiN over a 284 μm × 211 μm scan area is 1.4 nm. (b) The average roughness of DLC over a 284 μm × 211 μm is 2.5 nm.

thick DLC:H (diamond-like carbon with hydrogen) coated by a chemical vapor deposition (CVD) process (from a different source than the PVD lot) was used. An estimated 30% (atomic) of hydrogen is said to be contained in the DLC:H film. The surface topography of the films was measured using a Wyco optical profilometer, the results of which are given in Figure 5–6 for TiN and DLC. The surface measurements show that the film surfaces are extremely smooth (roughness less than 5 nm), which is characteristic of PVD and CVD processes. The Si_3N_4 and DLC:H films are measured by the AFM, and their roughness is comparable to that of the TiN and DLC films. The smoothness of the surfaces is a good indication that the asperity tips will not be excessively abrasive during sliding. The mechanical properties of the films obtained from literature are listed in Table 5–2.

5.4 Contact Mechanics

The size of an elastic contact between two surfaces can be estimated with the Hertzian analysis [19], which states that two spheres with radii R_1 and R_2 , elastic moduli E_1 and E_2 , and Poisson's ratios ν_1 and ν_2 pressed together by a normal load P produces a circular contact of radius a given by

$$a = \left(\frac{3PR}{4E}\right)^{1/3}, \tag{5.5}$$

where

$$\begin{aligned} \frac{1}{R} &= \frac{1}{R_1} + \frac{1}{R_2} \\ \frac{1}{E} &= \left[\frac{1-\nu_1^2}{E_1} + \frac{1-\nu_2^2}{E_2}\right] \end{aligned} \tag{5.6}$$

are the effective curvature and effective Young's modulus, respectively. The radii R_1 and R_2 can represent either the nominal geometry of the bodies or the local geometry of the asperities in contact, depending on the desired topological scale. The present analysis considers only the former. The pressure distribution over the contact area is semi-elliptical, where the peak pressure p_o is given by

$$p_o = \frac{3P}{2\pi a^2}. \tag{5.7}$$

A maximum shear stress of

$$\tau_{\max} = 0.31 p_o, \tag{5.8}$$

occurs at a distance of $0.48a$ directly below (and above) the center of the contact circle. As an approximation, a yielding criterion can be established as the point when the peak shear stress equals the shear strength of the material (which is estimated to be 1/6 of the hardness),

$$\tau_{\max} = \frac{1}{6}H, \tag{5.9}$$

where H is the hardness of the softer of the two surfaces. Combining Eqns. (5.5)–(5.9) leads to the following expression for the critical load P_c that satisfies the yielding criterion,

$$P_c = .026\frac{\pi^3 R^2 H^3}{E^2}. \tag{5.10}$$

All of the equations are based on the assumption that there is only one contact junction, and the consideration of multiple junctions (which may be applicable at the asperity level, for example) requires a more complex treatment, which is not done in this work because a single asperity model is deemed sufficient to capture all of the key elements of the contact mechanics in the present case.

Using the material and geometric properties of the sliders and surfaces listed in Tables 5–1 and 5–2, the critical load given by Eqn. (5.10) is computed for all slider/surface combinations. The results are presented in Table 5–3 along with the contact diameter at the critical load. In regard to the thin-film systems, it may be noted that the contact diameters are 2–3 orders of magnitude greater than the film thickness, in which case the elastic properties of the substrate, and not those of the coating, may be expected to govern the contact mechanics. Additionally, the peak shear stress will likely occur in the substrate rather than the film itself, so that it is more appropriate to use the hardness of the substrate in Eqn. (5.10) to obtain the critical load. Accordingly, the Hertzian analysis is also done for each slider against silicon, and the results are given in Table 5–3.

Using P_c as the limit, the load applied in the friction testing may be determined deliberately with the intention of avoiding excessive indentation, plowing, and deformation of the surface. Even if the load is kept below the critical value, however, there is never a guarantee that surface deformation will not occur because sharp micro-asperities, which have not been considered in the foregoing Hertzian analysis, can initiate local yielding at subcritical loads. Still, the use of subcritical loads should eliminate much of the deformation and plowing, especially with such smooth film surfaces. The friction tests were conducted using the following loads: 40 mN and 200 mN, which are both well below the critical loads.

The Hertzian contact radii (Eqn. (5.5)) under these loads are given in Table 5–4 for each of the sliders. It may be noted that the elastic properties of Si, and not the films, were used to compute the contact radii in Table 5–4, because the contact radius is always much greater than the film thickness. An immediate observation that may be made is that the contact radii with the diamond tip slider is consistently about a factor of 2.6 smaller that of the ball sliders.

Table 5–3: Critical load for various slider/surface combinations. The contact radius corresponding to the critical load is given in parentheses.

	P_c in N (a in μm)		
	Diamond tip	Sapphire ball	Si_3N_4 ball
TiN coating	3.3 (11.5)	801 (206)	1250 (248)
Si_3N_4 coating	3.0 (12.2)	828 (221)	1740 (293)
DLC coating	6.5 (12.2)	2350 (373)	2640 (395)
DLC:H coating	7.7 (33.8)	2087 (555)	2087 (555)
Si (substrate)	2.1 (13.6)	737 (256)	829 (271)

Table 5–4: Hertzian contact radii of various sliders against Si surface.

	a (μm)		
Load (mN)	Diamond tip	Sapphire ball	Si_3N_4 ball
40	3.6	9.7	9.9
200	6.2	16.6	16.9

5.5 Results and Discussion

5.5.1 Effect of Material Combinations

The first set of results addresses the question of whether the selection of the material combination has a significant effect on the friction, a topic closely linked to the relationship between friction and adhesion. Figure 5–7 displays the friction coefficient measurements in air for the various material combinations using the pin-on-disk setup and the cantilever setup. The sapphire and Si_3N_4 balls have mostly been tested in the pin-on-disk setup under a normal load of 200 mN, while the diamond tip is always tested in the cantilever setup under 40 mN. This has been done because the friction with the ball sliders is consistently too high (μ = 0.25–0.32) to measure in the cantilever unit (if the friction is too high, the test does not produce even a half-oscillation, and the friction cannot be determined), regardless of the surface material. On the other hand, the friction with the diamond tip is consistently too low (μ = 0.027–0.041) to be measured with the pin-on-disk setup. The lowest friction coefficient of 0.027 is with the diamond tip on the DLC surface, followed by the diamond tip on TiN, which produces a friction coefficient of 0.041. The diamond-DLC:H combination produces a friction coefficient of 0.09, which is over 3 times as much as diamond-DLC, and the higher friction may be ascribed to the chemical attributes of hydrogen, as one possibility. It may be speculated, for example, that hydrogen has the effect of strengthening the contact junction between the tip and the surface, perhaps by forming covalent bonds with the carbon atoms of the tip, or by participating in complex bonding schemes involving such atmospheric species as oxygen and water vapor, for example. Another possibility is that the hardness of DLC:H is substantially lower than that of DLC, so that DLC:H is more vulnerable to deformation and micro-plowing, which results in higher sliding friction. After the tests using the diamond tip, the tip of the diamond slider and the film surfaces were viewed under an optical microscope to check for wear grooves and surface damage, but no evidence of damage was detected in the tip, DLC, and DLC:H surfaces. Consequently, it seems that the lower hardness of the DLC:H film is not a plausible explanation, although there is always the possibility that plowing and wear may have occurred at a scale undetectable by the optical microscope.

The testing with the Si_3N_4 ball yields very little variation among the different surfaces, and the friction coefficient range of 0.23–0.29 is too small to establish a valid trend. In testing with the sapphire ball, the lowest friction is from the DLC:H surface ($\mu = 0.19$) while the highest friction is from the DLC surface ($\mu = 0.32$), which directly contrasts the trend observed with the diamond tip, where DLC was seen to give the lower friction. There may be several reasons for the difference in this particular trend. One suggestion may be that the

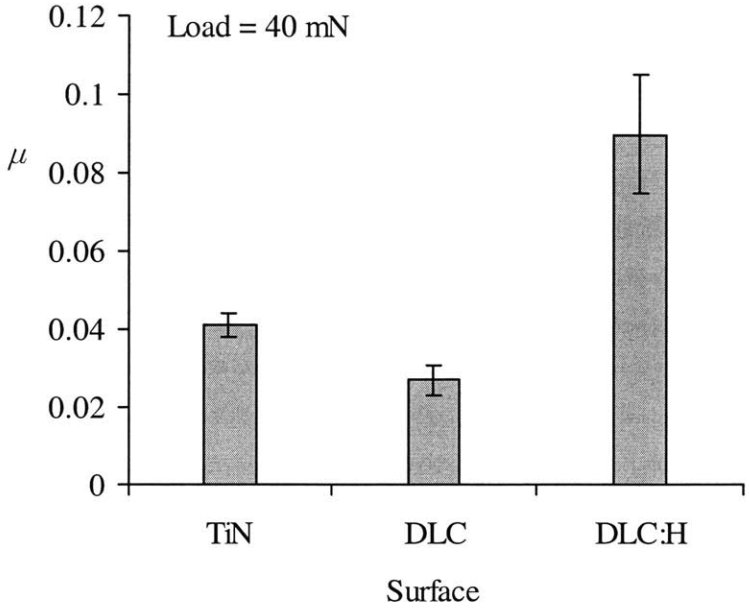

(a)

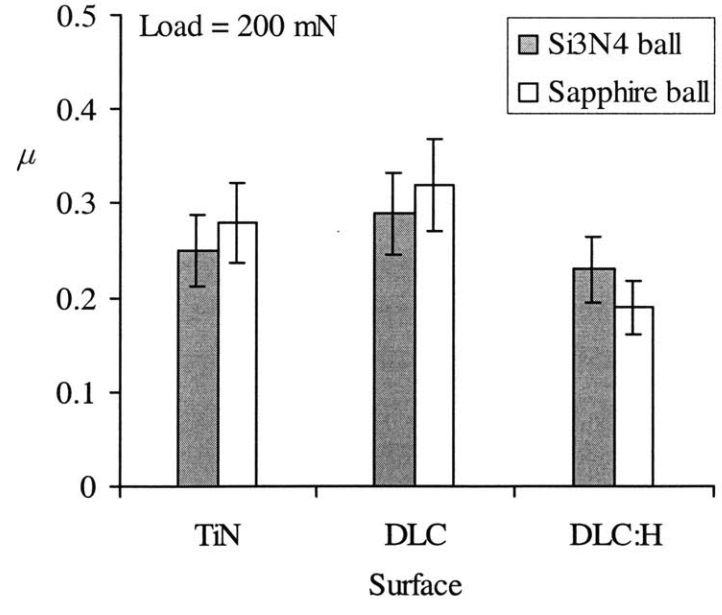

(b)

Figure 5–7: Friction coefficient of various slider/surface combinations in air. (a) Diamond slider, with cantilever apparatus. (b) Ball sliders, with pin-on-disk apparatus.

friction-raising effect that hydrogen has with diamond as the slider may have the opposite effect with sapphire, solely based on differences in the nature of the interatomic interactions between the surfaces. For example, although hydrogen atoms in the film may interact strongly with carbon atoms of the diamond slider, hydrogen is not known to form very strong bonds with aluminum atoms. In fact, the presence of hydrogen atoms may even weaken the interfacial junction with sapphire because H–X bonds (where X is a generic element) are generally weaker than C–X bonds. This argument may even be extended to the results of the silicon nitride ball. (See Table 5–5, for a list of bond energies relevant to this discussion.)

Table 5–5: Bond enthalpies for diatomic species [20].

Bond	Enthalpy (kJ/mol)	Bond	Enthalpy (kJ/mol)
C–C	607	H–C	338
		H–Al	285
C–Si	452	H–Si	299
C–N	754	H–N	339
C–O	1077	H–O	428

Data are for gaseous species at room temperature. The C–C and C–H bond enthalpies do not represent intramolecular bonds in hydrocarbons.

5.5.2 Effect of Slider Geometry

It is quite evident in Figure 5–7 that the friction coefficient is significantly higher with the ball sliders than the diamond slider. An incontrovertible resolution of this trend is not yet available, but a number of rational suggestions may be examined. For example, the Hertzian contact area is about 6 to 7 times larger when a ball is used instead of the diamond slider (see Table 5–4). Since the friction coefficient depends on the contact area in the elastic contact regime, the friction in the smaller contact would be lower even if the shear strength (per unit area) of the interface is nearly identical for the two cases. This particular theory can be tested by converting the data points in Figure 5–7 into the absolute friction normalized by the Hertzian contact area. The results shown in Figure 5–8 clearly demonstrate that the friction

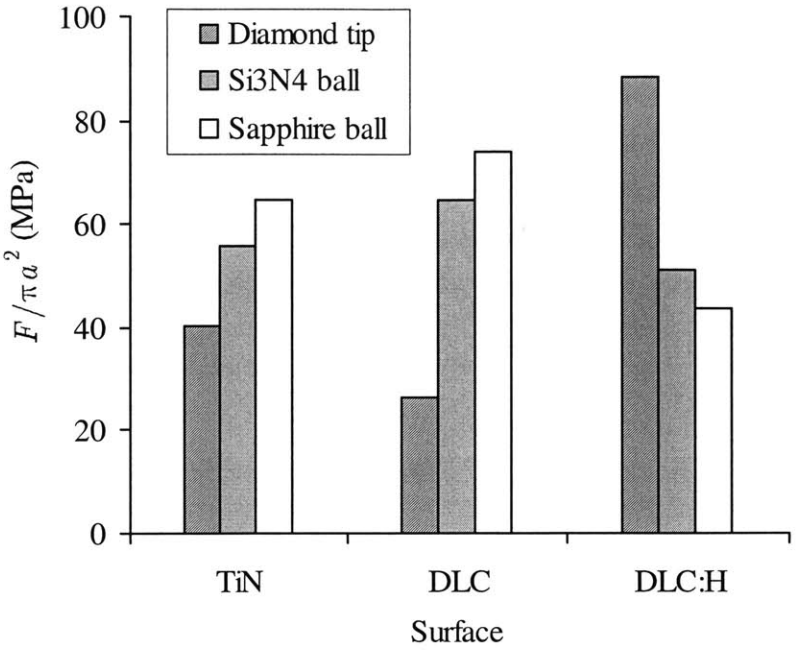

Figure 5–8: Friction normalized by Hertzian contact area for various slider/surface combinations.

per unit area of contact is still significantly less with the diamond slider, although the difference is not as much as before. So while the effects of the contact area cannot fully account for why the diamond slider produces so much less friction, it may be a partially satisfactory explanation.

A second possibility is that some deformation and wear still takes place despite the use of low normal loads, and moreover, the ball sliders may be more susceptible to wear than the diamond slider. There is evidence of this in Figure 5–9, where the optical microscope views show considerable amount of wear debris on both the sapphire ball and DLC surface after the test. Still, visible signs of permanent wear tracks and grooves could not be found either on the ball or the film, ruling out the possibility that plowing has occurred. The debris on the ball and the surface appear to be powder-like, and it is completely wiped away when cleaned with alcohol. It is not clear whether the debris comes from the ball or the surface, so the general conclusion may be made that it comes from both, since sapphire and DLC have similar hardness. The mechanism by which the wear debris is generated may be that of the fracture of the tips of microasperities. The wear debris is not detected in the tests done with

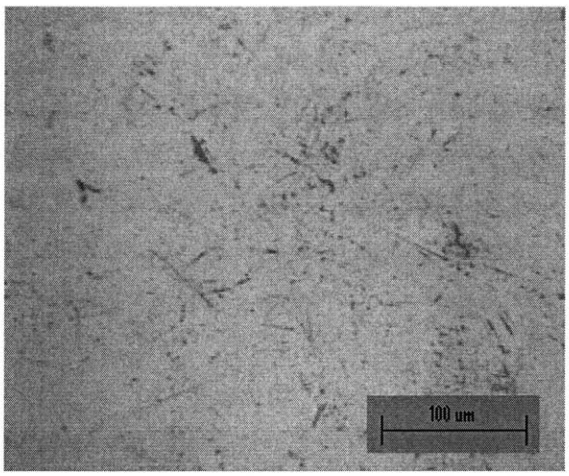

(a)

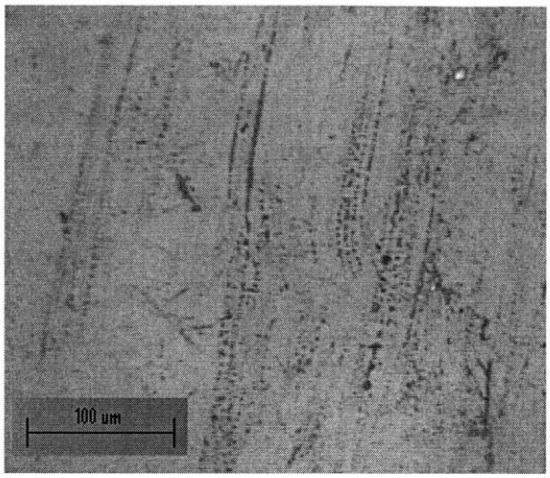

(b)

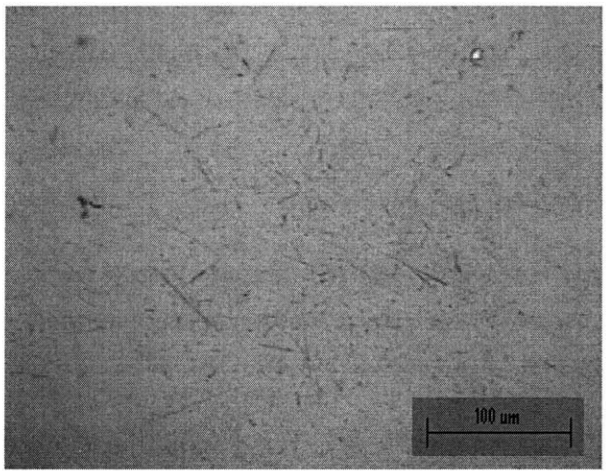

(c)

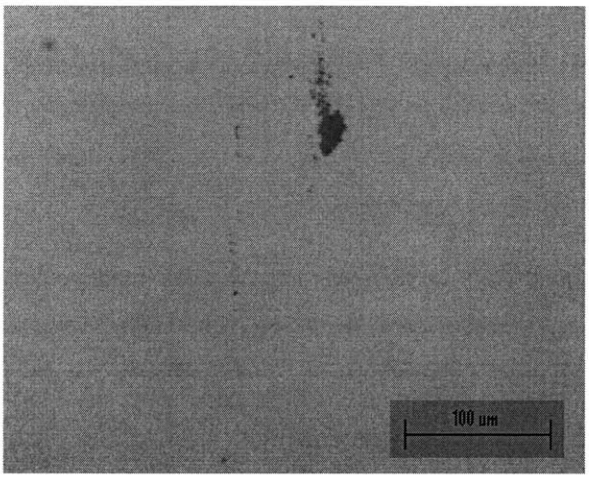

(d)

Figure 5–9: Surfaces after testing sapphire ball on DLC surface. Testing done with 200 mN load in air with pin-on-disk apparatus. (a) Sapphire ball surface before testing, (b) after testing but prior to cleaning, and (c) after cleaning with alcohol. (d) DLC surface after testing, uncleaned. Cleaning with alcohol removes the debris completely.

the diamond tip, which may be due to the fact that the smaller loads are used, leading to less chance for wear. Another reason may be that the area of contact is much smaller, and there is less chance of wear particles becoming trapped in the contact junction and taking part in further surface damage.

Another suggested explanation for the correlation between friction and the slider type is a material-based argument rather than a geometry-based argument. Diamond, compared to sapphire or Si_3N_4, may have weaker interaction with the film materials (except for DLC and DLC:H), resulting in a lower interfacial strength and adhesion. This is a difficult hypothesis to prove because the adhesion is not an easy property to measure. Experimentally obtained bond energies can provide some indication of the adhesion between two surfaces, but such information is not readily available for many of the relevant material pairs. However, it may be possible to reach a satisfactory resolution based on the following reasoning. If it is true that the diamond slider produces low friction strictly because of the chemical attributes of carbon, then the DLC surface should also give low friction regardless of the slider material, which is clearly not the case here. Therefore, the chemical attributes of carbon does not fully account for the low friction of the diamond tip in the present case.

5.5.3 Effect of Atmosphere

The effect of the atmosphere on friction was next investigated by conducting tests in the vacuum chamber. The cantilever apparatus with the diamond tip slider was used for this experiment. Figure 5–10 shows the results on the TiN, DLC, and DLC:H surfaces in vacuum, hydrogen, and argon atmospheres. The DLC film exhibits absolutely no sensitivity to the atmosphere, while TiN shows some variation, but nothing suggestive of a dramatic effect. The DLC:H shows a significant decrease of the friction coefficient in any atmosphere other than air. This suggests that oxygen gas or water molecules may play a big role in the relatively high friction of DLC:H in air, and this line of reasoning can further be extended by suggesting that the hydrogen atoms contribute chemically somehow, which explains why the DLC film does not exhibit any variation in friction in different environments. However, a more focused study of only the atmospheric effect needs to be done in order to obtain a more conclusive explanation.

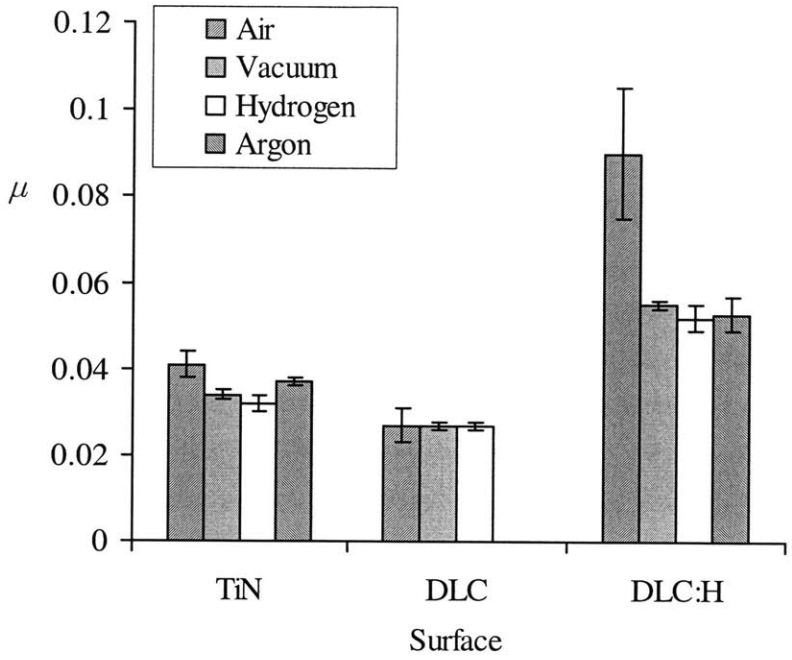

Figure 5–10: Friction coefficient in various atmospheres. Testing is done with cantilever apparatus inside vacuum chamber using diamond tip slider under 40 mN normal load. Vacuum data collected at 60 μm Hg pressure.

5.5.4 Effect of Adhesion

The relationship between the adhesion between two surfaces and the resulting friction was next examined using the atomic force microscope (AFM). The adhesion between the AFM tip (made of Si_3N_4) and three surfaces, DLC, TiN, and Si_3N_4, was measured by monitoring the "pull-off force", or the force at which the tip fully disengages from the surface. The pull-off forces are easily obtained from the force-distance curves shown in Figure 5–11, where the abscissa (i.e., "z position") refers to the vertical distance between the surface and the *base* of the tip, which is mounted on the piezo actuator, and the ordinate is the deflection of the AFM cantilever tip, which is related to the force between the tip and the surface. The zero deflection reference coincides with the flat part of the force-distance curve far to the right (note that "setpoint" does not refer to zero deflection). Below the reference is the attractive region and above the reference is the repulsive region. Note that the tip does not feel any attraction to the surface during the approach, but once it contacts the surface (i.e., enters into its repulsive field), it adheres to it and feels significant attraction during the retraction from

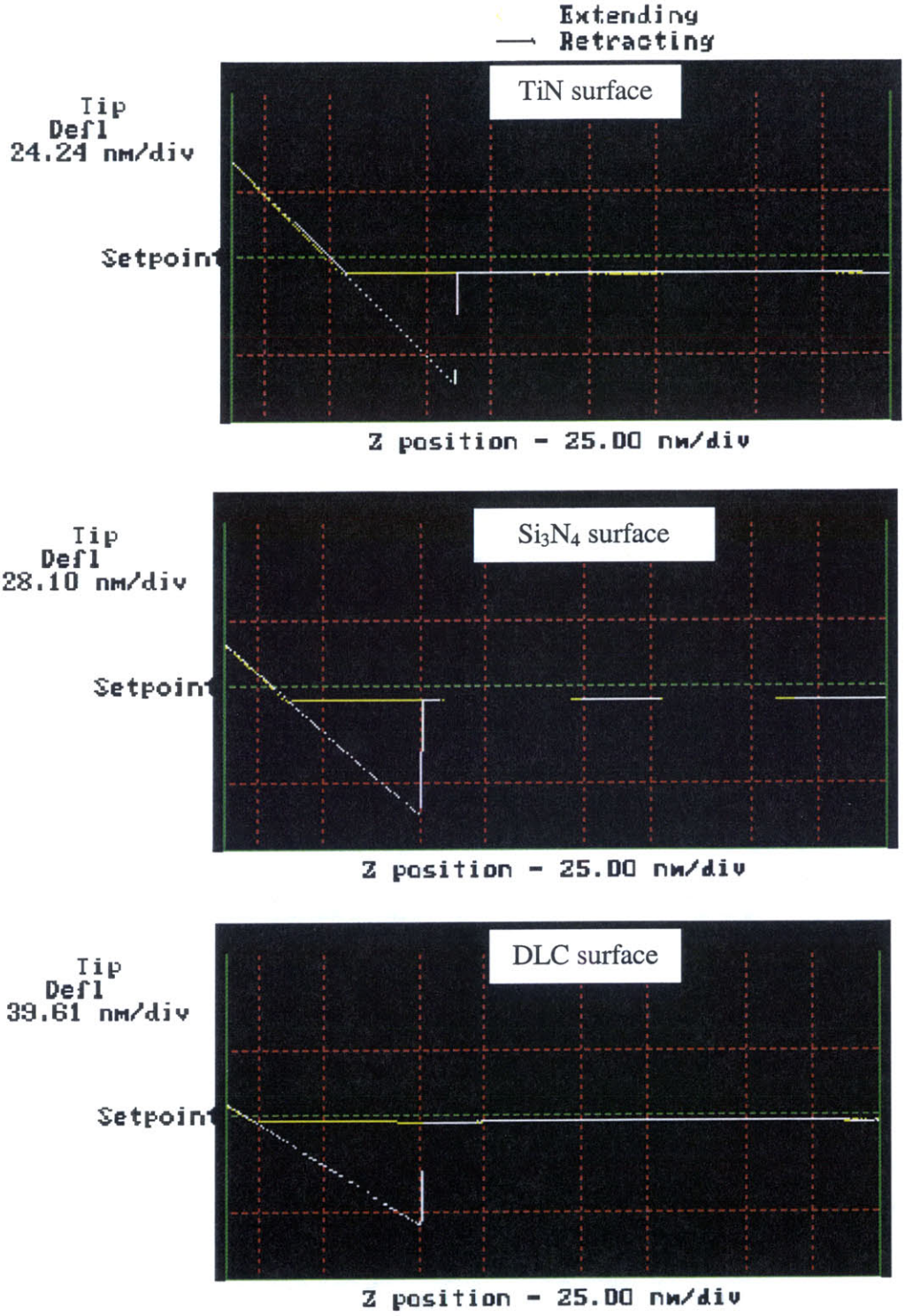

Figure 5–11: Adhesion measurements by AFM.

the surface. At some point during the retraction, the tip disengages the surface almost instantaneously, and the peak attraction just before the disconnection is the pull-off force, which is a direct measure of the adhesion between the tip and the surface. Table 5–6 lists the pull-off force for the three surfaces, which are all measured consecutively using the same tip. The surprising result is that the DLC surface, not Si_3N_4, is the most adhesive. This could be the effect of adsorbed gases or some other type of surface contamination.

Table 5–6: Pull-off force (F_{ad}) between Si_3N_4 AFM tip and various surfaces. The normal loads for the AFM friction measurements are also given.

Surface	F_{ad} (nN)	Normal Load (nN)
TiN	31	4.6
Si_3N_4	38	4.3
DLC	48	3

In addition to the pull-off force, the nanoscale friction between the tip and the surface was measured with the AFM. The results of the friction tests are shown in Figure 5–12, where the friction is given in units of volts, which is the raw output from the AFM. In order to convert this into the customary units of force, the volts must be converted into the amount of torsion of the tip (while the normal force is measured by the tip deflection, the friction force is measured by the tip torsion), which, in turn, must be converted into force. Neither the volts-to-torsion nor the torsional stiffness of the tip are currently available, so the conversion to units of force is impossible at this point, but the friction among the tests can at least be compared to each other, since the same tip is used on all three surfaces. The normal load during each test can be obtained from the adhesion measurement curves (Figure 5–11). In those graphs, the normal load is exactly the distance between the setpoint and the zero deflection reference, multiplied by the bending stiffness of the cantilever. The normal loads for each of the coatings tested are given in Table 5–6.

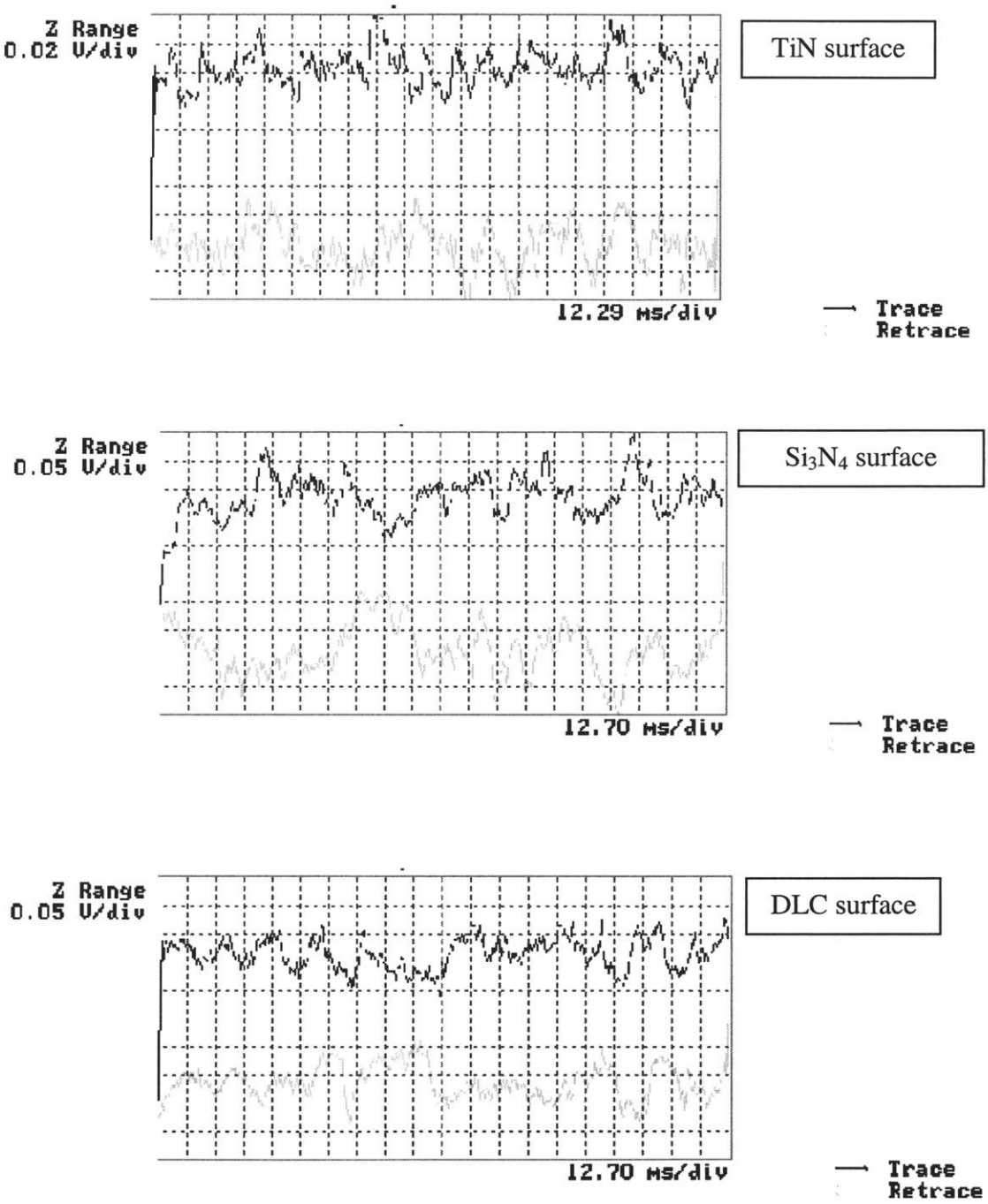

Figure 5–12: Friction measurements by AFM.

Figure 5–13 displays friction (in volts) plotted against adhesion. (Friction is taken to be the mean of the results shown in Figure 5–12.) It may be noted that the three tests are conducted at different normal loads, which is often necessitated by the need for an adequate output signal in AFM experiments. In order to compare the results evenly, the friction measurements in Figure 5–13 have been normalized by the respective normal loads. (This data manipulation is only sensible if the friction is proportional to the load. Past AFM experiments have shown that the proportionality is valid [21,22].) Figure 5–13 shows that while the lowest friction corresponds to the least adhesive surface (TiN), the most adhesive surface does not necessarily produce the highest friction. In fact, the friction of the DLC and Si_3N_4 surfaces are very similar, despite the fact that the DLC is 26% more adhesive. A generalization can hardly be made from just the three data points shown here, and more rigorous set of experiments are needed to reach a full conclusion, but the preliminary results seem to indicate that the relationship between friction and adhesion resembles the results of the MD simulations of the amorphous interface, where friction increases with adhesion only up to a point, beyond which friction becomes insensitive to adhesion (Chapter 4). The results of the simulations were interpreted by noting that as the adhesion is increased, the sliding at the interface becomes accompanied by more and more bulk deformation, such that beyond a certain limit, further increase of adhesion does not necessarily yield higher friction due to the fact that sliding is dominated by bulk deformation. The same mechanism may be applicable to the AFM friction tests. Although the materials are not amorphous (with the exception of DLC), there may be defects in the tip or the film that make the materials susceptible to deformation above a threshold shear stress, such that beyond a certain degree of adhesion, the sliding response mostly involves deformation, which means that the measured friction is no longer reflective of the sliding at the tip-surface interface.

Figure 5–14 is a plot of the friction coefficient measured with the cantilever testing apparatus against the adhesion force obtained from the AFM, in an attempt to compare the nanoscale and the macroscale experimental results. The friction tests were conducted between a Si_3N_4 ball and the DLC, TiN, and Si_3N_4 coatings under a 23 mN normal load. The correlation between the AFM friction measurements and the macroscopic friction tests is not very good. But there are several possible causes for the discrepancy. First, the silicon nitride ball and the AFM tip, even though they are made of the same material, has many differences in their properties that contribute to the friction discrepancy, such as the tip radius (the AFM tip is considerably sharper), surface roughness, surface contamination, hardness, and elastic modulus. Second, the AFM test is done over a 1 μm length, while the testing on the cantilever apparatus is done over several millimeters, so there is a vast difference in scale. It

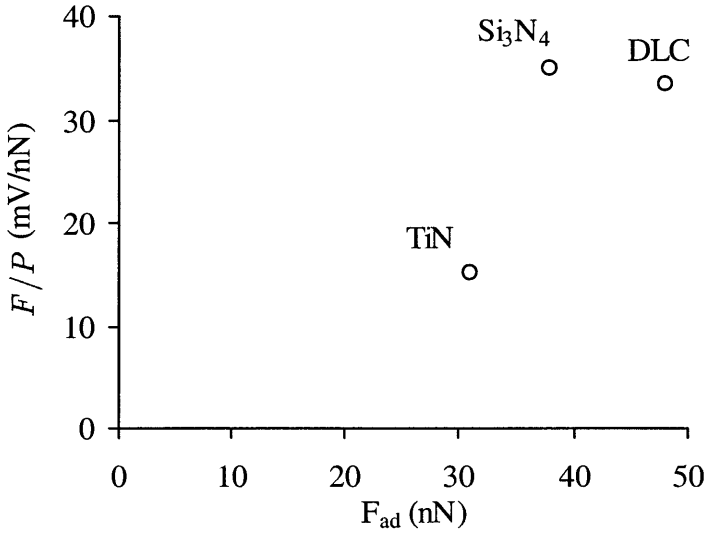

Figure 5–13: Friction measured by AFM vs. adhesion measured by AFM. Friction, in millivolts, has been normalized by the normal load.

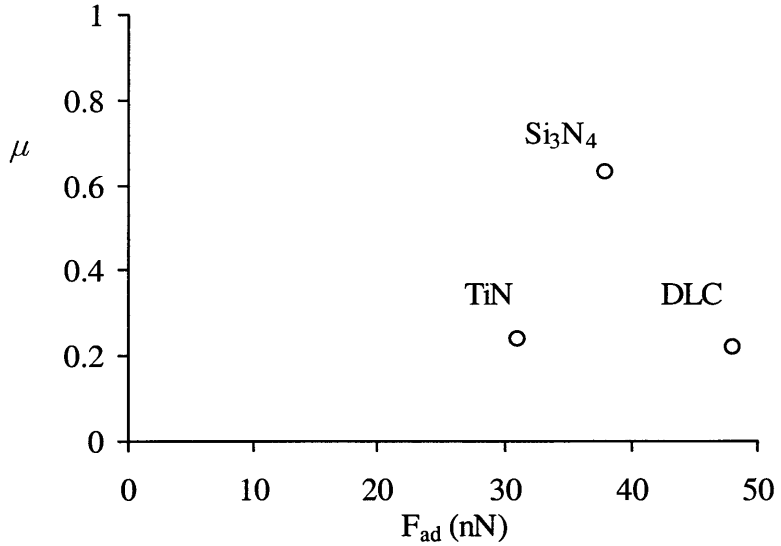

Figure 5–14: Friction measured by cantilever apparatus vs. adhesion measured by AFM. Friction testing is done with Si_3N_4 ball at 23 mN normal load in air

is possible, for instance, that the AFM friction measurement took place at a local anomaly, giving misleading results. Third, the same tip was used over and over, so by the last set of experiments (the testing order was TiN – Si_3N_4 – DLC), the tip may have accumulated debris and particles from the previous films.

5.6 Conclusions

With the aim of exploring the possibilities of achieving low friction through the use of thin, hard coatings, experiments were carried out using various coatings (100 nm thick DLC, 100 nm thick TiN, 100 nm thick Si_3N_4, and 1 μm thick DLC:H) and three types of sliders (diamond indenter, sapphire ball, and Si_3N_4 ball). The normal load was selected to be well below the critical load for the onset of yielding, as predicted by the Hertzian analysis, so that excessive plastic deformation could be avoided. Testing was also conducted in controlled atmospheres in order to study the effect of the environment on friction. In addition, testing was done on the atomic force microscope (AFM) to measure the adhesion between a Si_3N_4 tip and the coating surfaces. The following are the key results from this work.

- Comparing the sliders, the diamond indenter consistently gave the lowest friction coefficient by a full order of magnitude, regardless of the coating material, which may be ascribed to the observation of wear in the form of powder-like debris on the surfaces of the ball sliders and the films. Since permanent wear grooves and surface damage were not evident on either the ball or the film surfaces, the wear debris may have come from the fracture of particularly vulnerable asperity tips on either surface. Also, the Hertzian contact area is about 7 times greater with the ball sliders than the diamond tip slider, and the larger contact area may be associated with increased likelihood of trapped wear particles inflicting further surface damage.
- The DLC film shows much less friction ($\mu = 0.027$) than the DLC:H film ($\mu = 0.09$) when tested with the diamond tip in air, which may be due to the chemical properties of the hydrogen atoms in DLC:H. For example, the hydrogen may be involved in the formation of strong covalent bonds with the diamond slider. Against the ball sliders (the sapphire ball, in particular), the DLC:H film gives lower friction than DLC, which may be due to the fact that hydrogen forms weak bonds with the non-carbon slider materials.
- The measured friction coefficient vary in value from 0.027 to 0.09 for the diamond tip slider and 0.19 to 0.32 for the ball sliders among the various coating materials. Based on these results, it appears that a factor of 2–3 reduction in friction is practically attainable by choosing proper coating materials.

- The effect of the atmosphere on friction is marginal for most of the coatings with the exception of the DLC:H film, which exhibits a 39% reduction in the friction coefficient in controlled environments (Ar, H_2, vacuum). The reaction of hydrogen with oxygen or water molecules may be involved in the higher friction in air, although this is not known for sure at this time.
- The AFM testing shows that a correlation exists between the adhesion and friction at the microscale. The friction increases with the adhesion in the relatively low adhesion regime, but levels off in the higher adhesion regime. This behavior is consistent with the MD simulations of amorphous interfaces, which suggests that the sliding may be dominated by deformation of the tip or the surface at higher adhesion.

5.7 References

1. Bienk, E.J., Reitz, H., and Mikkelsen, N.J., "Wear and Friction Properties of Hard PVD Coatings," *Surface Coatings and Technology*, vol. 76-77, pp. 475-480, 1995.
2. Wiklund, U., Wänstrand, O., Larsson, M., and Hogmark, S., "Evaluation of New Multilayered Physical Vapour Deposition Coatings in Sliding Contact," *Wear*, vol. 236, pp. 88-95, 1999.
3. Hogmark, S., Jacobson, S., and Larsson, M., "Design and Evaluation of Tribological Coatings," Wear, vol. 246, pp. 20-33, 2000.
4. Enke, K., Dimigen, H., and Hübsch, H., "Frictional Properties of Diamondlike Carbon Layers," *Applied Physics Letters*, vol. 36, no. 4, pp. 291-292, 1980.
5. Bull, S.J., "Tribology of Carbon Coatings: DLC, Diamond, and Beyond," *Diamond and Related Materials*, vol. 4, pp. 827-836, 1995.
6. Habig, K-H., "Fundamentals of the Tribological Behaviour of Diamond, Diamond-like Carbon, and Cubic Boron Nitride Coatings," *Surface Coatings and Technology*, vol. 76-77, pp. 540-547, 1995.
7. McKenzie, D.R., "Tetrahedral Bonding in Amorphous Carbon," *Reports on Progress in Physics*, vol. 59, pp. 1611-1664, 1996.
8. Erdemir, A., Eryilmaz, O.L., and Fenske, G., "Synthesis of Diamondlike Carbon Films with Superlow Friction and Wear Properties," *Journal of Vacuum Science Technology A*, vol. 18, no. 4, pp. 1987-1992, 2000.
9. Su, K.-Y. and Cook, N.H., "Enhancement of High Speed Tool Life by Titanium Nitride Sputter Coating," *Proc. Fifth N. Am. Metalworking Research Conference*, Univ. of Massachusetts, Amherst, MA, May 23-25, SME, pp. 297-302, 1977.

10. Jamal, T., Nimmagadda, R., and Bunshah, R.F., "Friction and Adhesive Wear of Titanium Carbide and Titanium Nitride Overlay Coatings," *Thin Solid Films*, vol. 73, pp. 245-254, 1980.

11. Tai, Y.C., Fan, L.S., and Muller, R.S., "IC-processed Micro-motors: Design, Technology, and Testing," *Proc. IEEE Micro Electro Mechanical Systems*, 1-6, 1989.

12. Rabinowicz, E., **Friction and Wear of Materials**, John Wiley & Sons, Inc., New York, 1995.

13. Suh, N.P., **Tribophysics**, Prentice Hall, New Jersey, 1986.

14. Bhushan, B., Israelachvili, J.N., and Landman, U., "Nanotribology: Friction, Wear and Lubrication at the Atomic Scale," *Nature*, vol. 374, pp. 607-616, 1995.

15. **ASM Engineered Materials Reference Book**, ASM International, Metals Park, OH, 1989.

16. **Properties of Silicon**, EMIS Datareviews Series No. 4, INSPEC, The Institution of Electrical Engineers, New York, 1988.

17. **Handbook of Hard Coatings: Deposition Technologies, Properties, and Applications**, Ed. Bunshah, R.F., Noyes Publications, Park Ridge, N.J., 2001.

18. Cho, N-H., Krishnan, K.M., Veirs, D.K., Rubin, M.D., Hopper, C.B., Bhushan, B., "Chemical Structure and Physical Properties of Diamond-like Amorphous Carbon Films Prepared by Magnetron Sputtering," *Journal of Materials Research*, vol. 5, no. 11, pp. 2543-2554, 1990.

19. Johnson, K.L., **Contact Mechanics**, Cambridge University Press, Cambridge, UK, 1985.

20. **CRC Handbook of Chemistry and Physics 1999-2000: A Ready Reference Book of Chemical and Physical Data**, 81st Edition, Ed. Lide, D.R., CRC Press, Boca Raton, FL, 2000.

21. Mate, C.M., McClelland, G.M., Erlandsson, R., and Chiang, S., "Atomic-Scale Friction of a Tungsten Tip on a Graphite Surface," *Physical Review Letters*, vol. 59, no. 17, pp. 1942-1945, 1987.

22. Erlandsson, R., Hadziioannou, G., Mate, C.M., McClelland, G.M., and Chiang, S., "Atomic Scale Friction Between the Muscovite Mica Cleavage Plane and a Tungsten Tip," *Journal of Chemical Physics*, vol. 89, no. 8, pp. 5190-5193, 1988.

CHAPTER 6

Summary and Future Direction

6.1 Summary

The atomic-scale phenomena at the interface of sliding surfaces has been investigated by Molecular Dynamics (MD) simulations with the intent of elucidating the fundamental processes leading to friction. The system was modeled as ideal Lennard-Jones (L-J) surfaces, and finite-border boundary conditions, with a novel expression for the internal stress, were implemented for conducting the simulations under constant stress. In the interest of investigating critical parameters that determine friction of atomic-scale systems, the simulations have focused on the effect of interfacial structure and adhesion on the sliding behavior. The adhesion between the sliding surfaces was quantified in terms of the L-J parameters, and a parametric study was done to determine the theoretical reduction in friction that is possible for a unit reduction of adhesion. The effect of the interfacial structure was explored by simulating a variety of configurations, including the defect-free commensurate crystalline interface, tilt and twist grain boundaries, and an amorphous interface. In addition to the simulation study, friction testing of thin, hard films were conducted to supplement the theoretical study with relevant experimental data. An atomic force microscope (AFM) was also used to measure the adhesion of the coating surfaces against a silicon nitride tip, as well as the nano-scale friction of a single asperity contact.

The parametric study centered on the effect of the adhesion parameter ($\varepsilon_{AB}/\varepsilon_{AA}$) revealed rather surprising results. In addition to having an effect on the computed value of friction, the variation of the adhesion results in unique sliding regimes characterized by very different physical responses. In the commensurate crystalline interface, for example, adhesion determines whether sliding occurs in the frictional or frictionless regime, the former being associated with greater adhesion. The frictionless regime is characterized by the absence of jump phenomena, and sliding is consequently smooth and reversible, such that all work done on the system in pushing the finite border over the energy barrier is fully recovered within the sliding period through the process of being pulled by the border as it falls into an energy valley. In the frictional regime, friction occurs as a result of the jump phenomena and increases as the surfaces become more adhesive, such that the computed value of friction is

approximately linear to the ratio $\varepsilon_{AB}/\varepsilon_{AA}$. There is a distinct transition from the frictionless to the frictional regime marked by the onset of jump phenomena.

The simulations of the Σ5[100](310) symmetric tilt grain boundary (36.9° misorientation angle) exhibit three distinct sliding regimes based on the adhesion between the sliding crystals. At low levels of adhesion, jump phenomena do not occur and the sliding is frictionless. As the surfaces become more adhesive, jump phenomena occur and frictional sliding results, just as in the commensurate system. A uniqueness of the tilt grain boundary (GB) system is that as $\varepsilon_{AB}/\varepsilon_{AA}$ approaches unity (i.e., the interface approaches "perfect" adhesion), GB migration starts to take effect. GB migration, in which sliding is coupled by a motion of the GB in the direction normal to the boundary itself, is not accompanied by jump phenomena despite a substantially high peak sliding resistance. As a result, GB migration is frictionless.

The amorphous system exhibits frictional sliding in the entire range of adhesion simulated in this work ($\varepsilon_{AB}/\varepsilon_{AA} = 0.1$ to 1.0), but the elementary sources of the friction and the mechanism of sliding are very different from the cases of the crystalline and grain boundary systems. In the low adhesion range, sliding is essentially the accumulation of a series of local slips involving only a few atoms at randomly activated sites on the sliding interface. The local slips are also identified as local jump phenomena, which results in friction. As adhesion increases, sliding at the interface is accompanied by increasing degrees of deformation of the bulk regions. Eventually, the deformation results in the nucleation of a shear-induced crystallization process followed by an extremely rapid propagation of the crystalline zone.

The effect of the interfacial structure on friction may be summarized by the plot shown in Figure 6–1, where the computed friction for the commensurate, tilt and twist GB's, and amorphous systems are all shown on the same graph. As expected, the defect-free structure of the commensurate crystalline interface yields the highest friction overall, except in the low adhesion regime ($\varepsilon_{AB}/\varepsilon_{AA} = 0.1$ and 0.2), where the amorphous system has higher friction on account of the local jump phenomena. In contrast, the commensurate system, as well as the GB system, does not experience any jump phenomena because the ordered surface structure stipulates that any jump phenomena must involve the uniform slip of the entire plane, unlike the disordered structure of the amorphous interface, which allows for substantial individual motion. However, as the jump phenomena take full effect in the commensurate system, its friction is significantly higher than the amorphous friction. The friction of the amorphous system flattens out after $\varepsilon_{AB}/\varepsilon_{AA} = 0.4$ or so due to the fact that bulk deformation becomes prevalent, so that further increase of the interfacial strength has

very little effect on friction. Beyond $\varepsilon_{AB}/\varepsilon_{AA} = 0.4$, the sliding is best interpreted as bulk shear deformation of the amorphous materials. The tilt GB system exhibits the lowest friction of all (not counting the twist GB, which always has zero friction), suggesting that the most effortless sliding is associated with a structure that is somewhere between complete order (i.e., commensurate) and complete disorder (i.e., amorphous). The advantage of the GB system is that it has an intrinsic defect at the sliding interface, which yields a lower sliding resistance than the commensurate interface. In addition, the GB does not have any structural defects away from the interface, giving it superior resistance to bulk deformation in comparison to the amorphous system. The GB is the ideal low friction system, in that a low sliding resistance can be attained without the risk of subsurface deformation. However, it may be suggested that most practical systems behave more like the amorphous simulation, which undergoes deformation if the adhesion between the sliding surfaces become sufficiently high. In such cases, the importance of reducing the strength of the interatomic interaction at the interface is critical, as shown by the factor of 6 difference in friction between $\varepsilon_{AB}/\varepsilon_{AA} = 0.1$ and 1.0. However, it may also be noted that a factor of 10 reduction in $\varepsilon_{AB}/\varepsilon_{AA}$ only results in a factor of 6 reduction in friction, which indicates that the manipulation of the surface for adhesion has limited potential for low friction.

The validation of the simulation results by experimental data has been a challenging task, mostly due to the difficulty in measuring the adhesion between the sliding surfaces. The diamond tip slider seems to be ideal for friction testing under minimal surface deformation and grooving. The most insightful results have been of the diamond-like carbon (DLC) films containing hydrogen, which exhibited substantial sensitivity to the environment. AFM measurements of the adhesion and nanoscale friction revealed that the friction-adhesion relationship most closely resembles the simulation of the amorphous system, in that friction as a function of adhesion seems to increase only up to a certain asymptotic limit. This behavior can be justified by noting that the higher adhesion between the AFM tip and the surface may result in some microscopic deformation of the tip or the surface, which is best modeled by the amorphous system, since the commensurate and the GB systems are not capable of bulk deformation due to the absence of structural defects.

The main conclusion of the overall effort presented in this thesis is that friction at the atomic scale is, indeed, very sensitive to such parameters as the interfacial structure and adhesion, which are not critical at the macroscale. Therefore, the treatment of tribological problems in microsystems or thin, hard coatings must account for these factors. The simulations suggest that the strategy of designing for weakly adhering surfaces is promising

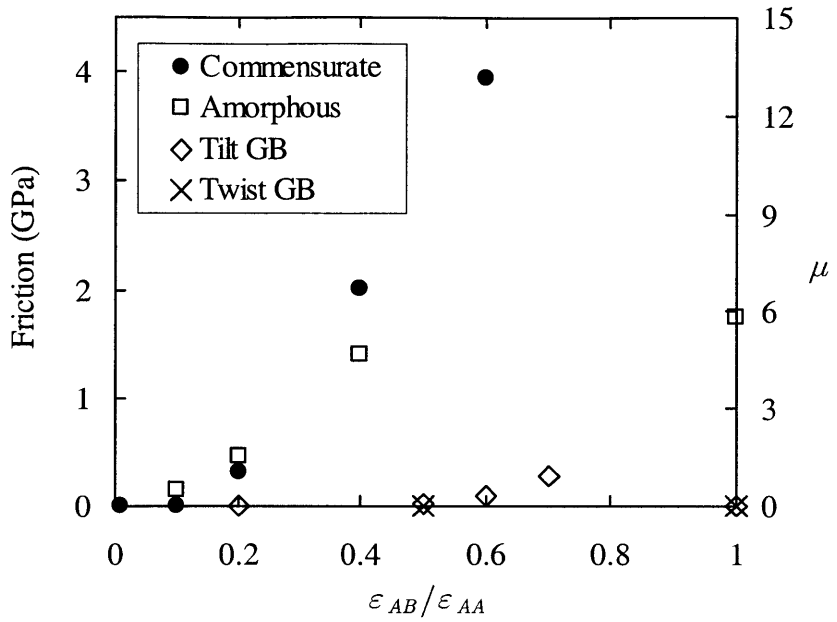

Figure 6–1: Friction from MD simulations of various interface structures. μ refers to the friction coefficient, defined as friction divided by the normal load of 300 MPa.

in terms of delivering low friction, but the reduction in friction for a unit reduction of adhesion may be less than one-to-one, and other schemes for low friction may need to be consulted in order to bring the friction down to ultra-low levels. The experiments suggest that the role of hydrogen is perhaps the most interesting in terms of the effect on tribological behavior, and the chemical properties and mechanistic functions of hydrogen in the sliding interface deserves much more attention in future endeavors.

6.2 Future Research

This thesis has been a small contribution to the improved understanding of the atomic-scale behavior of sliding systems, but it is hoped that future work based on the fundamental concepts explored here will reveal additional insights into the area of nanotribology. The following lists a number of topics that may be explored further.

- **Continue the investigation into the effect of interface geometry on friction.** In particular, the grain boundary study can be extended by simulating different misfit angles for both the tilt and twist GB's. This is a particularly intriguing area of research because

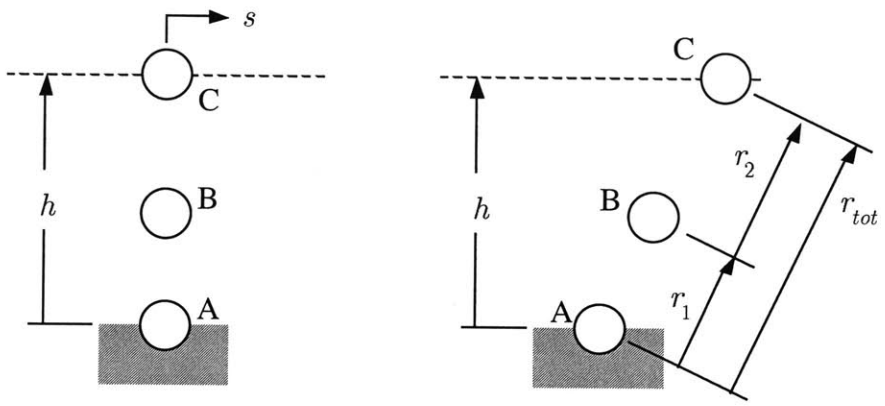

Figure A–1: Schematic of Tomlinson's model.

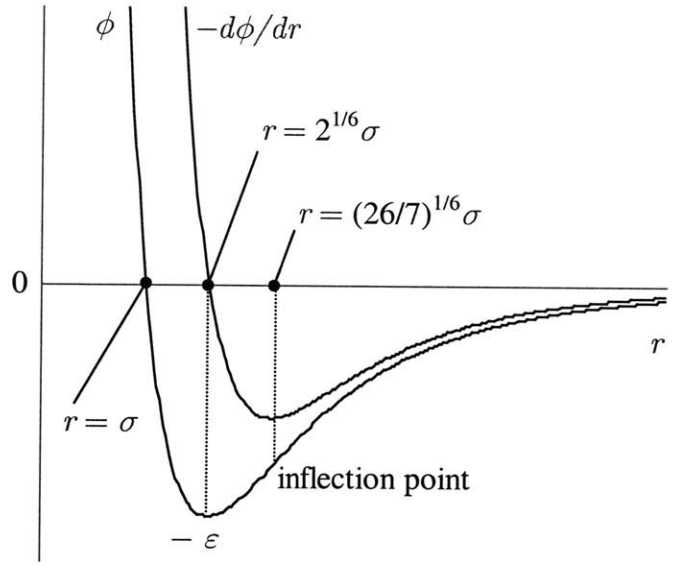

Figure A–2: Lennard-Jones 12–6 potential function and the interatomic force curve (the negative derivative of the potential function). Positve force indicates repuslion.

the results of this thesis indicate that the GB's yield the lowest friction. Consequently, a comprehensive understanding of the frictional properties of GB's may be instrumental in the development of ultra low friction surfaces.

- **Conduct more AFM friction experiments for the validation of the trends predicted by the MD simulations.** This is important because the simulation results are in need of some experimental confirmation. Such validation also provides a connection between theory and experiment, and establishes the proper perspective with which to view the role of simulations in the search for low friction systems. The AFM experiments conducted in this thesis (Chapter 5) indicate that it is possible to obtain measurements of friction at a single asperity, and the preliminary results agree well with the trend suggested by the simulations. In order to solidify the connection between the experimental data and the simulation results, a more careful study needs to be dedicated to the experimental part.
- **Investigate the role of the simulation cell size on the friction computation.** The simulation cell size dependence was mostly ignored in this thesis, but this neglect was partly made benign by conducting all of the simulations using similar cell sizes, thus preserving the validity of the comparisons drawn between the various systems which were simulated. However, the scaling law of Chapter 2 suggests that the cell height, in particular, is an essential element which directly factors into the friction. Therefore, it is important to further investigate this matter until a satisfactory understanding can be reached regarding the size effect. Most importantly, this investigation should be focused on the determination of any artifacts which may arise only from the simulation size effect, but have no actual physical significance.
- **Simulate the sliding of amorphous alloys.** The simulations of the amorphous system in Chapter 4 yielded many interesting results, such as the local jump phenomena and the shear-induced crystallization process. These effects may a product of the fact that the amorphous material consisted only of a single component, and the presence of a second phase alloy may drastically alter the sliding behavior. This may be especially true in the case of the crystallization, for it is well known that an inhomogeneous system is much less prone to transformation into the ordered structure. In addition, the presence of the alloy material may bring about significant changes to the friction, and certain properties of the alloy may be linked to reduction in friction. Although these are only speculations at present, they are intriguing possibilities that merit further research.
- **Simulate the friction of realistic materials, such as amorphous carbon and silicon.** This thesis was dedicated to a parametric study for the elucidation of generic trends and

the establishment of valid theoretical concepts in support of the simulated trends. The next step is the simulation of actual materials. Amorphous carbon (or diamond-like carbon, DLC) is perhaps the most suitable candidate for this investigation for two reasons. First, DLC is currently the focus of exciting experimental research, and it has shown remarkable tribological properties superior to any other coating material. This also means that plenty of experimental data are available for comparing to the simulation results. Secondly, proven potential functions for carbon are available in the literature, and these are capable of modeling the material in both the crystalline (diamond or graphite) and amorphous (DLC) states. There are many possible questions that can be addressed through the simulation of DLC, and among them is the mechanism of low friction in DLC films. For instance, the simulations can be used to confirm or refute the popular notion that the low friction comes from the graphitization of the carbon at the sliding interface. Another possible research direction is the incorporation of hydrogen into the simulation of DLC. This allows the exploration of the theory that the hydrogen acts as a lubricant to significantly lower friction.

APPENDIX A

Tomlinson's Theory of Atomic Friction

A.1 Theory of Tomlinson

Tomlinson was the first to propose a theory of atomic friction in 1929 [1], and he used a model of three atoms (or molecules), as illustrated in Figure A–1. As atom 'A' is held fixed in place, atom 'C' moves along the dashed horizontal line. Atom 'B' is the only unconstrained atom, and it responds to forces from both 'A' and 'C'. Tomlinson did not specify the interatomic potential function except to say that the atoms possess both repulsive and attractive fields, similar to the Lennard-Jones potential function, for example. Also, the analysis is quasistatic in that dynamics of 'B' is not considered, and the theory is based on the equilibrium positions of 'B' as a function of s. The theory goes on to say that the height h plays a key role in determining the system response. At relatively high h, atom 'B' never enters the repulsive field of 'A' nor 'C', and the entire sliding sequence occurs reversibly. At low h, atom 'B' feels repulsion from both 'A' and 'C' when 'C' has approached close enough. Then as 'C' eventually passes through and starts to move away, the system encounters an unstable equilibrium configuration, where a perturbation causes 'B' to suddenly "fly" back to a stable configuration. This process, called a *jump phenomenon* in this work, ends with 'B' reaching a stable position with appreciable kinetic energy, which can be interpreted as thermal energy. Therefore, the mechanism describes a way by which potential energy is converted into heat, which is assumed to then dissipate away by known modes of heat transfer.

A.2 Tomlinson's Model with Lennard-Jones Potential Function

A.2.1 Repulsive Mode

Tomlinson's plucking model is an impressive contribution considering that the analysis was done without the use of a computer. At the same time, his theory has never been tested analytically using realistic potential functions. The purpose of the present section is to examine the plucking model using the three-atom system (Figure A–1) and applying the Lennard-Jones (12-6) potential function,

$$\phi(r) = 4\varepsilon\left[(\sigma/r)^{12} - (\sigma/r)^{6}\right]. \tag{A.1}$$

The L–J function, plotted in Figure A–2, defines the potential energy between a pair of atoms as a function of the separation distance r. The parameter ε is the potential well depth and σ is related to the atomic diameter. The minimum of ϕ occurs at $r = 2^{1/6}\sigma$, this being the equilibrium separation distance for an isolated pair of atoms. The interatomic force, also shown in the same figure, is the negative derivative of the potential function. It can be seen that extreme repulsion quickly results when atoms are brought closer than the equilibrium separation. The maximum attraction occurs at $r = (26/7)^{1/6}\sigma$, which coincides with the inflection point on the potential energy curve. The total system energy Φ is the sum of two contributions,

$$\Phi = \phi(r_1) + \phi(r_2). \tag{A.2}$$

Strictly speaking, this problem is two-dimensional, but due to the central force assumption associated with all pair potentials, atom 'B' is in equilibrium only along the line segment connecting 'A' and 'C'. Therefore, there exists only one degree of freedom, which can be expressed by the ratio r_1/r_{tot}. This ratio, along with the position of 'C', fully specifies the system configuration at any time.

The equilibrium position of 'B' as a function of s are plotted in Figure A–3 for the case when $h = 2\sigma$. At this separation, the atoms feel repulsion at some point during sliding. The stability criteria for the equilibrium positions are:

$$\begin{aligned} \frac{\partial^2\Phi}{\partial r_1^2} &> 0 \quad \text{stable} \\ \frac{\partial^2\Phi}{\partial r_1^2} &< 0 \quad \text{unstable} \end{aligned} \tag{A.3}$$

Each equilibrium position in Figure A–3 has been tested against the stability criterion, and the stable configurations are shown in blue and the unstable ones in red. The symmetric configuration, $r_1/r_{tot} = 1/2$ (where 'B' is exactly halfway between 'A' and 'C'), is always an equilibrium configuration but not always stable. Near the repulsive region (between the dotted lines in Figure A–3), there exists only one equilibrium curve, but in most of the attractive regions, the equilibrium curve is multi-valued.

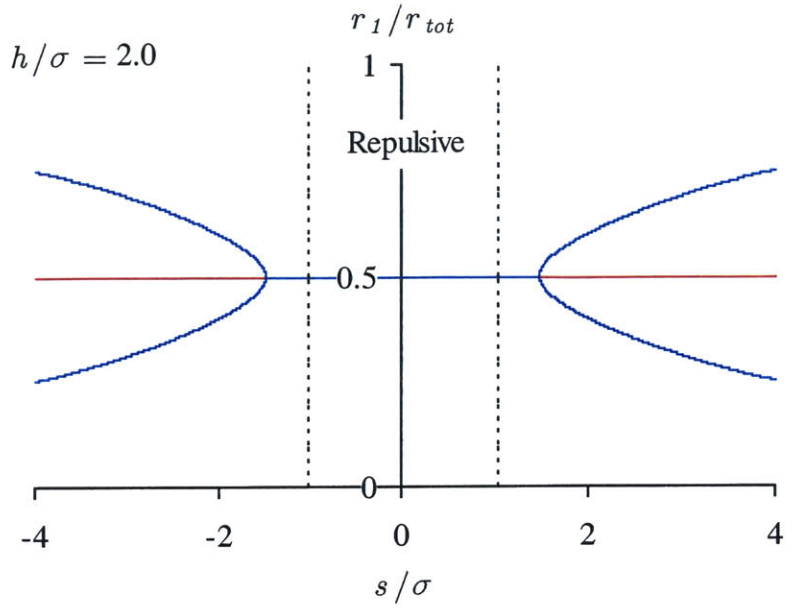

Figure A–3: Equilibrium configurations during repulsive sliding according to Tomlinson's model with Lennard-Jones potential. Blue lines are stable configurations. Red lines are unstable configurations. Arrows indicate path followed by system during quasistatic sliding.

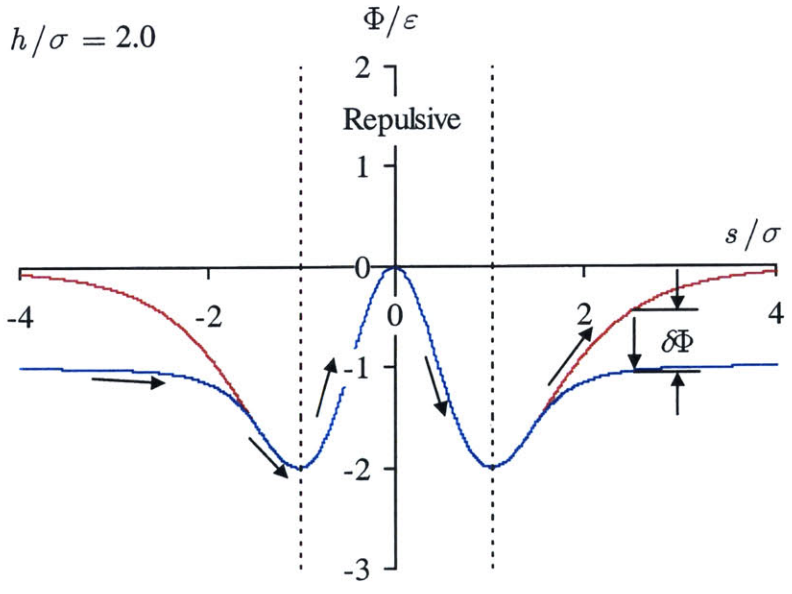

Figure A–4: Potential energy corresponding to equilibrium configurations in Figure A–3.

The history of the position of atom 'B' as 'C' slides by can be constructed by tracing a path of stable equilibria in Figure A–3 (follow arrows in the figure). At the left end of the graph where $s/\sigma \ll 0$ and atom 'C' is far away, there is one unstable equilibrium position at 'b' and two stable equilibrium positions at 'a' and 'c', but 'a' and 'c' are essentially equivalent due to symmetry ('a' becomes 'c' if the system in Figure A–1 is rotated upside-down). Therefore, 'c' will be ignored from here on, and since 'a' is the only stable position, it is reasonable to assume that atom 'B' starts there. (In the limit as $s \to -\infty$, it can be deduced that $r_1 \to 2^{1/6}\sigma$ since atom 'C' is outside the region of influence.) As 'C' approaches and r_{tot} decreases, 'B' continuously drifts toward 'C' due to the increase in the attractive force from 'C', but 'B' still remains closer to 'A'. At exactly $s/\sigma = -1.48$, atom 'B' reaches the midpoint between 'A' and 'C', and $r_1 = r_2 = (26/7)^{1/6}\sigma$, which is exactly the inflection point on the L–J potential function as well as the point of maximum attraction (see Figure A–2). During $-1.48 < s/\sigma < 1.48$, the system maintains the symmetric configuration ($r_1 = r_2$) as it passes into then out of the repulsive region. At $s/\sigma = 1.48$, the system encounters a bifurcation point branching out to a stable and unstable path. In the stable path, 'B' retreats back toward 'A', while in the unstable path, 'B' stays in the symmetric position. (Recall that the two stable paths are equivalent by symmetry, so the upper path is ignored.) Tomlinson states that at this critical junction, atom 'B' sometimes follows the unstable path for a finite distance δ until a perturbation causes 'B' to undergo the jump transition to the stable branch (see Figure A–3). How frequently the system chooses the unstable path and how long it stays on the unstable path are both determined by a probability factor. The potential energy curves corresponding to the unstable and stable paths are shown in Figure A–4. The potential energy drop during the jump phenoenon is denoted as $\delta\Phi$. Recall that this drop of the potential energy gets converted into kinetic energy in Tomlinson's model.

The problem with this model is that a dynamic system possessing kinetic energy prior to the plucking event never follows the unstable path. Therefore, plucking is possible only in the quasistatic limit, and it does not apply to finite temperature systems where atoms exhibit vibrational motion. Nevertheless, the essence of Tomlinson's theory is logically appealing and effective in explaining how work is converted into heat during frctional sliding.

A.2.2 Attractive Mode

Figures A–5 and A–6 show the equilibrium configuration and the potential energy curves for the attractive sliding case when $h = 2.7\sigma$. The symmetric configuration ($r_1/r_{tot} = 1/2$) is now always an unstable equilibrium. On the other hand, the configurations in which 'B' is

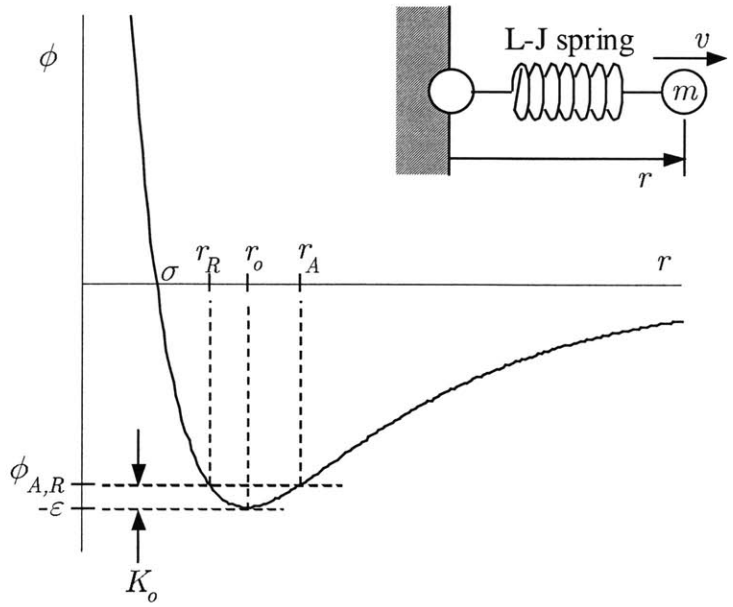

Figure B–1: Lennard-Jones 12-6 potential function.

In an anharmonic system, the vibrational period depends on the initial conditions as well as the potential function, and so it is necessary to define the initial position and velocity. At static equilibrium, $r = r_o = 2^{1/6}\sigma$, as this is the minimum energy separation of the L–J potential function. If the free atom initially at r_o is given an initial velocity v_o, it assumes an anharmonic vibration about r_o , provided that v_o is low enough for the atom to stay in the stable region of the potential well. During the vibration, there is constant exchange between the potential and kinetic energy, such that at $r = r_o$, the potential energy is at the minimum while the kinetic energy is at the maximum. Conversely, at the extremes of the oscillation ($r = r_A$, $r = r_R$), the potential energy is at the maximum while kinetic energy is zero. The maximum kinetic energy K_o is given by

$$K_o = \frac{1}{2} m v_o^2 . \tag{B.2}$$

At $r = r_A$ and $r = r_R$, all kinetic energy is converted into potential energy, so that

$$\phi|_{r=r_A} = \phi|_{r=r_R} \equiv \phi_{A,R} \ , \tag{B.3}$$

where

$$\phi_{A,R} = -\varepsilon + K_o . \tag{B.4}$$

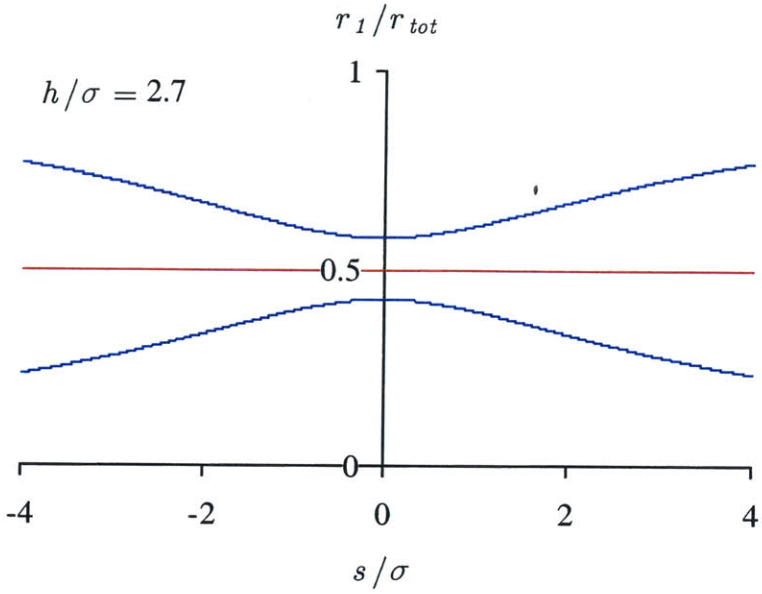

Figure A–5: Same as A–3, but for attractive sliding.

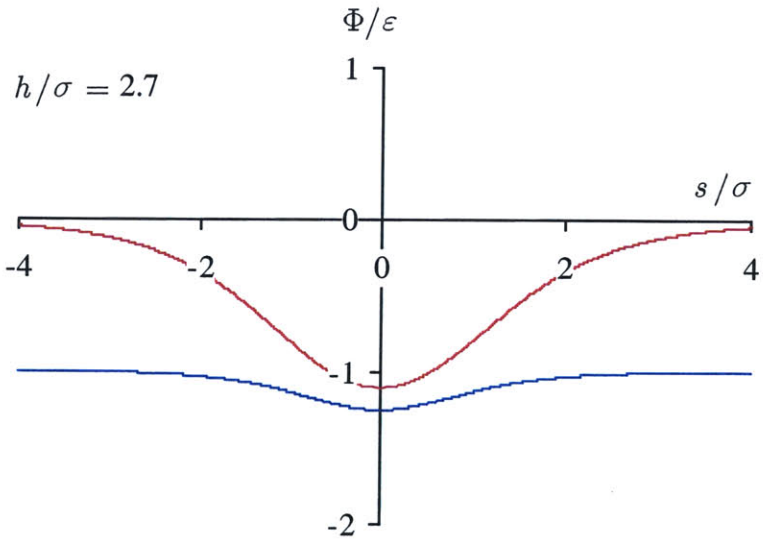

Figure A–6: Same as A–4, but for attractive sliding.

biased toward 'A' or 'C' are always stable. In contrast to the repulsive mode, the unstable and stable curves never cross paths, so the system only follows the stable path from beginning to end. This result supports Tomlinson's assertion that the sliding in the attractive mode is frictionless because jump phenomena do not occur at any time, which is consistent with intuitive expectations that kinetic friction only results in the presence of a normal load.

A.3 Reference

1. Tomlinson, G.A., "A Molecular Theory of Friction," *Philosophical Magazine*, Ser. 7, Vol. 7, No. 46, pp. 905-939, 1929.

APPENDIX B

Time Steps and Sliding Increments

B.1 Characteristic Time

The purpose of molecular dynamics (MD) simulations is to predict the phase trajectory of the non-linear many-body system as a function of time, and the size of the numerical time step used for the discrete integration of Newton's equation of motion is a central computational issue. The time step size must be small enough to capture the highest frequency phenomena present in the system, so the step size is system-dependent and it becomes necessary to identify the characteristic time of the given system. Most phenomena in the simulations performed here can be divided into two basic time scales. The coarse time scale is relevant to the macroscopic processes introduced to the system by external perturbations, namely the sliding of the border for friction simulation. The characteristic time for this process could be the time needed to slide the border by one lattice period, for example, which is of the order of 10^{-9} seconds for a realistic sliding speed. There is also a finer time scale for solid systems associated with the vibrations of atoms as they oscillate about equilibrium sites, whose characteristic time is the period of oscillation, and since this is the smaller of the two characteristic times, it is the important one.

In what follows, the vibrational period of an anharmonic system is calculated for a simple system consisting of two atoms interacting by the Lennard-Jones 12–6 potential function,

$$\phi(r) = 4\varepsilon\left[(\sigma/r)^{12} - (\sigma/r)^{6}\right], \tag{B.1}$$

where ε is a energy parameter defining the potential well depth and σ is a length parameter which is close to the atomic diameter in the hard-sphere approximation. Figure B–1 contains the plot of this function with respect to r, the separation. Also included in Figure B–1 is the schematic of the single degree-of-freedom system, which consists of a fixed atom linked to a free atom of mass m by a non-linear spring as defined by the L–J potential. Granted, this simple system cannot perfectly represent all of the characteristic frequencies in a many-body system, but it still captures enough of the essential dynamics to provide a good order-of-magnitude approximation.

Rearranging Eqn. (B.1),

$$(\sigma/r)^6 = \frac{1 \pm \sqrt{1+4\beta}}{2}, \tag{B.5}$$

where $\beta \equiv \phi/4\varepsilon$. Combining Eqns. (B.3)–(B.5) yields the following solutions for r_A and r_R in terms of K_o,

$$\begin{aligned} \frac{r_A}{\sigma} &= \left[\frac{2}{\left[1-\sqrt{K_o/\varepsilon}\right]}\right]^{1/6} \\ \frac{r_R}{\sigma} &= \left[\frac{2}{\left[1+\sqrt{K_o/\varepsilon}\right]}\right]^{1/6} \end{aligned}, \tag{B.6}$$

or

$$\frac{\Delta r}{\sigma} = \left[\frac{2}{\left[1-\sqrt{K_o/\varepsilon}\right]}\right]^{1/6} - \left[\frac{2}{\left[1+\sqrt{K_o/\varepsilon}\right]}\right]^{1/6}. \tag{B.7}$$

So far, the analysis is exact and Eqn. (B.7) is free of assumptions, but the first assumption is introduced here to relate K_o to the "temperature". The average kinetic energy $\bar{K}$ is related to system temperature T by the equipartition theorem,

$$2\bar{K} = n_{DOF} k_B T, \tag{B.8}$$

where n_{DOF} is the number of degrees of freedom and k_B is Boltzmann's constant. Admittedly, the statistical mechanical relationship of Eqn. (B.8) is intended for large system with several degrees of freedom, but it is applied to this simple system in the spirit of approximation. For a single degree of freedom system, Eqn. (B.8) becomes

$$\bar{K} = \frac{1}{2} k_B T. \tag{B.9}$$

The relationship between K_o and $\bar{K}$ is nontrivial for a nonlinear system, but assuming that the harmonic relationship is a valid approximation, v_o and the average velocity $\bar{v}$ are related by

$$\bar{v} = \frac{v_o}{(\pi/2)}, \tag{B.10}$$

which leads to

$$\bar{K} = \frac{K_o}{(\pi/2)^2}, \tag{B.11}$$

given that $\bar{K} = (1/2)m\bar{v}^2$. Combining Eqns. (B.9) and (B.11) results in

$$K_o = \frac{\pi^2}{8} k_B T \simeq k_B T, \tag{B.12}$$

where the last approximation was made for the sake of simplicity. Substituting the far right expression in (B.12) into (B.7) gives

$$\frac{\Delta r}{\sigma} \simeq \left[\frac{2}{\left[1-\sqrt{k_B T/\varepsilon}\right]}\right]^{1/6} - \left[\frac{2}{\left[1+\sqrt{k_B T/\varepsilon}\right]}\right]^{1/6}. \tag{B.13}$$

Finally, the average velocity is related to the temperature through Eqn. (B.9) in the following way,

$$\bar{v} = \sqrt{k_B T/m}. \tag{B.14}$$

Then period of atomic vibration is simply given as $\Pi = 2\Delta r/\bar{v}$, or

$$\frac{\Pi}{\sigma\sqrt{m/\varepsilon}} = \frac{2(\Delta r/\sigma)}{\sqrt{k_B T/\varepsilon}}. \tag{B.15}$$

In Eqn. (B.15), the normalization factor $\sigma\sqrt{m/\varepsilon}$ is the conventional L–J unit of time. In conclusion, Eqns. (B.13) and (B.15) provide approximations for the atomic vibration amplitude and period for a L–J system at a given temperature. Table B–1 contains the computed values of the characteristic parameters for copper near room temperature.

B.2 Computational Time Step Size

The absolute minimum computational time step is 1/4 the period of oscillation of an atom (Π), but it is obviously preferable to have as small a time step as practically possible. In this thesis, a time step of 1×10^{-15} seconds is used for all simulations, which is equivalent to $\Pi/226$. This step size should be plenty small to sample the entire vibrational trajectory of every atom. In conventional MD simulations the standard L–J time step is $.01\sigma\sqrt{m/\varepsilon}$,

which is about 3×10^{-15} seconds with the inputs from Table B–1. This simply means that the step size used here is of the same order of magnitude as what most MD simulations use.

Table B–1: Characteristic parameters for L–J copper.

Input	Characteristic parameters
$\varepsilon = 65.322 \times 10^{-21}$ J	$\sigma\sqrt{m/\varepsilon} = 2.95 \times 10^{-13}$ s
$\sigma = .23127 \times 10^{-9}$ m	$k_B T/\varepsilon = 0.061$
$m = 1.06 \times 10^{-25}$ kg	$\Delta r/\sigma = .094$
$T = 291$ K	$\Pi = 2.26 \times 10^{-13}$ s

B.3 Sliding Increment Size

Sliding is modeled by incrementally moving the upper border by a finite distance in these MD simulations (see Figure B–2). The length of the sliding increment should preferably be as small as possible in order to create smooth sliding, but too small of an increment results in an excessive amount of computation time. A sensible upper limit for the sliding increment is that it must be much smaller than the amplitude of atomic vibration, so that an execution of a sliding step will not overly disturb the atoms near the moving border. According to Table B–1, the amplitude of vibration for a L–J copper is $.094\sigma$, or .22 Å. The sliding increment used must be at least an order of magnitude smaller, and so the increments used in this work are never greater than .025 Å.

B.4 Relaxation time

Every time the sliding border is displaced by an increment, a step perturbation is essentially introduced into the system. The relaxation time following a sliding increment must be long enough to allow the system to settle into a new equilibrium configuration prior to the next increment. The required relaxation time depends on the degree of the perturbation, the size of the system, and material properties related to diffusion and pressure wave propagation, among other things. One possible approximation of the minimum

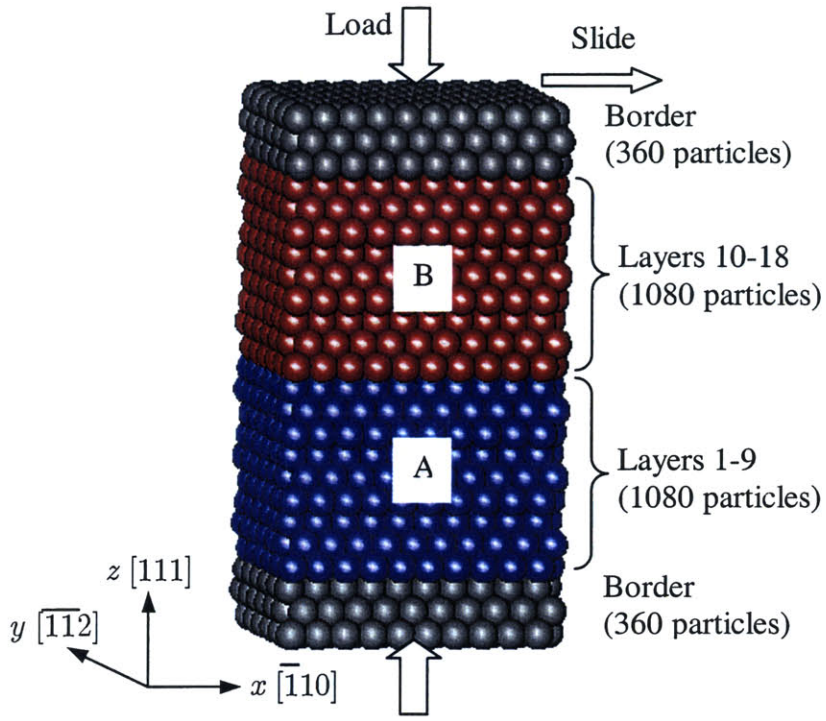

Figure B–2: Typical MD simulation system consisting of 2160 total dynamic atoms and 720 total boundary atoms. The upper border atoms are moved for sliding.

relaxation time is the time it takes for sound (i.e., a pressure wave) to fully traverse the length of the simulation cell. The speed of sound (v_s) in a medium is given by

$$v_s = \sqrt{B/\rho}\,, \tag{B.16}$$

where B is the bulk modulus and ρ is the material density. The bulk modulus for an isotropic solid is related to the Young's Modulus and Poisson's ratio by

$$B = \frac{E}{3(1-2\nu)}. \tag{B.17}$$

Using tabulated experimental values for copper ($E = 120.7$ GPa, $\nu = 0.35$, and $\rho = 8900$ kg/m^3), the velocity of sound according to Eqns. (B.16) and (B.17) is $v_s = 3882$ m/s. For a typical simulation cell with a height of 5 nm or so, it takes a sound wave 1.3×10^{-12} s to travel the full height, or 1300 computational time steps if a step is 1×10^{-15} s long. In this thesis, a relaxation time of 5000 steps is used.

APPENDIX C

Stress in MD Systems with Finite Borders

C.1 Virial Stress

The classic definition of stress is based on a macroscopic volume element containing enough material that the system behaves according to continuum laws of elasticity. Molecular dynamics (MD) systems only contain up to 10 million or so particles due to computational limits, falling well short of the continuum requirement which is, to a rough approximation, about 10^{23} atoms. Consequently, MD systems must be treated as discrete systems in regards to the definition of stress or pressure. The virial theorem of Clausius is the most recognized formulation of pressure for a system of dynamic particles, and the theory is discussed in detail in other excellent sources [1]. The present discussion will start with the generalized tensor form of the virial theorem,

$$\overline{\sum_i m_i \mathbf{v}_i \mathbf{v}_i'} = \overline{-\sum_i \mathbf{r}_i \mathbf{F}_i'}, \tag{C.1}$$

where m_i is the mass and $\mathbf{v}_i$ (u_i , v_i , w_i), $\mathbf{r}_i$ (x_i , y_i , z_i), $\mathbf{F}_i$ are the velocity, position, and force vectors of particle i. The vectors are in column form and the prime denotes the transpose so that both sides of Eqn. (C.1) yield 3×3 matrices. The summations are performed over all of the particles in the system. The overhead bar denotes an average over a sufficiently long time such that the system can be considered to be in equilibrium. The original virial theorem can be recovered by taking the trace of both sides of Eqn. (C.1).

The net force $\mathbf{F}_i$ on particle i has of two contributions. The *internal component* is the sum of all forces exerted by neighboring particles interacting with i by interatomic potential functions. The *external component* usually comes from the traction on the boundary of the system and affects only the particles that are near the boundary. However, the system boundary in the virial analysis is not well defined, and it may simply be assumed that an imaginary boundary enclosing all of the particles in the system does exist far away. Furthermore, the exact nature of the interaction between this boundary and nearby particles is not specified, and the manner in which the system particles feel the traction is also not addressed. The virial theorem essentially works around the need for such surface

information by converting the surface integral of the traction into a volume integral using the divergence theorem, as it will be shown shortly. There may be a concern about the validity of applying the divergence theorem to a discrete system, which can be justified by assuming that the boundary is very large in comparison to atomic dimensions, such that all relevant spatial properties can be approximated to be continuous at the length scale associated with the boundary.

The derivation of the stress tensor from Eqn. (C.1) for a *pairwise* interacting system is straightforward. The right hand side of (C.1) can be decomposed into internal and external contributions so that the equation can be rewritten as

$$\overline{\sum_i m_i \mathbf{v}_i \mathbf{v}_i'} = \overline{-\sum_i \sum_{j \neq i} \mathbf{r}_i \mathbf{f}_{ij}'} - \int_\Gamma \mathbf{r}\mathbf{n}'\mathbf{S} d\Gamma , \tag{C.2}$$

where $\mathbf{f}_{ij}$ is the force imparted on particle i by j, $\mathbf{S}$ is the constant external stress acting on the arbitrary system boundary Γ, and $\mathbf{n}$ is the outward normal vector of the boundary. The overhead bar is omitted from the last term because it is time invariant for a system contained by an undeforming boundary subject to constant external stress. Using the divergence theorem, it follows that

$$\mathbf{S} = \overline{\boldsymbol{\tau}} , \tag{C.3}$$

where

$$\boldsymbol{\tau} = -\frac{1}{V}\left[\sum_i m_i \mathbf{v}_i \mathbf{v}_i' + \sum_i \sum_{j>i} \mathbf{r}_{ij} \mathbf{f}_{ij}'\right], \tag{C.4}$$

where V is the system volume, $\mathbf{r}_{ij} = \mathbf{r}_i - \mathbf{r}_j$, and the familiar $j>i$ notation avoids double counting. The tensor $\boldsymbol{\tau}$ is the so-called *virial stress tensor*, a fluctuating quantity whose equilibrium time average is equal to the external stress $\mathbf{S}$, a constant boundary condition. The virial stress consists of two parts, the first being a kinetic term and the second a potential term. The kinetic term relates to the spatial average of the momentum flux throughout the system, and its role can be understood by noting that in the absence of interatomic forces, the kinetic term yields the ideal gas relation. The potential term is the measure of the contribution from interatomic forces throughout the system, which makes this expression valid for liquids and solids in addition to gases.

C.2 Mechanical Stress

This section presents an alternative, mechanical derivation of the stress tensor for a system of interacting particles under periodic boundary conditions. The purpose of this derivation is to show that the mechanical approach yields a stress tensor which is equivalent to the virial stress tensor, thus providing confidence in the following section to apply the mechanical approach to finite border systems where the virial approach is not valid.

Figure C–1a shows a 2–D projection of a fully periodic MD simulation cell. The dotted line represents an imaginary horizontal plane of area A located at an arbitrary distance z above the lower face of the cell, or it could alternatively be interpreted as an imaginary cut dividing the system into two free bodies. Considering only the z–x shear component for now, the mechanical stress τ_{zx}^{m*} is defined as:

$$\tau_{zx}^{m*}(z) = -\frac{1}{A}\sum_{c} m_a u_c w_c + \frac{1}{A}\sum_{a}\sum_{b} f_{x,ab}\,. \tag{C.5}$$

The first term is the momentum flux of any particles which happen to be passing through the plane, and accordingly the index c represents only those particles whose z-coordinate is level with the plane, i.e. $z_i = z$. The second term is the sum of all interparticle forces acting *across* the plane, so that index a loops over only the particles below the plane while b covers the particles above the plane, and $f_{x,ab}$ is the x-component of the force imparted on particle a by particle b. Note that the sign convention is consistent with the classical definition of stress. It may further be noted that periodic boundary conditions are in effect, so the summations in the second term must include the image particles in the neighboring cells. The * superscript is meant to denote that Eqn. (C.5) is valid only for a plane located at position z, and the volume average of the mechanical stress is:

$$\tau_{zx}^{m} = \frac{1}{L}\int_0^L \tau_{zx}^{m*}(z)\,dz = \frac{1}{V}\int_0^L \left[-\sum_{c} m_c u_c w_c + \sum_{a}\sum_{b} f_{x,ab}\right] dz\,, \tag{C.6}$$

where L is the height of the cell. Recall the special definitions of the indices in that c only counts particles if $z_i = z$, and the domains of a and b vary with z. The special indices can be converted into general indices i and j by introducing the parameters δ and λ and rewriting Eqn. (C.6) as

$$\tau_{zx}^{m} = \frac{1}{V}\left[-\sum_{i}\int_0^L m_i u_i w_i \delta\, dz + \sum_{i}\sum_{j>i}\int_0^L f_{x,ij}\lambda\, dz\right], \tag{C.7}$$

where the new parameters have properties similar to the delta function:

$$\delta = \begin{cases} 1 & z = z_i \\ 0 & \text{all other } z \end{cases} \tag{C.8}$$

and

$$\lambda = \begin{cases} 1 & z_i < z < z_j \\ -1 & z_j < z < z_i \\ 0 & \text{all other } z \end{cases}, \tag{C.9}$$

in which z_i and z_j are the z-coordinates of particle i and j, respectively. The purpose of the top two conditions in (C.9) is to maintain the correct sign convention even when particle i is above particle j, and the last condition ensures that the integrand vanishes unless the imaginary plane lies between the particles. In Eqn. (C.7) it was possible to bring all summations outside of the integrals because the general indices i and j loop unconditionally over all particles without regard to the position z of the imaginary plane. The force $f_{x,ij}$ is also independent of z, and so the integration yields

$$\tau_{zx}^{m} = -\frac{1}{V}\left[\sum_i m_i u_i w_i + \sum_i \sum_{j>i} \left(z_i - z_j\right) f_{x,ij}\right]. \tag{C.10}$$

Repeating the analysis for the other components of stress leads to the tensor form

$$\boldsymbol{\tau}^{m} = -\frac{1}{V}\left[\sum_i m_i \mathbf{v}_i \mathbf{v}_i' + \sum_i \sum_{j>i} \mathbf{r}_{ij} \mathbf{f}_{ij}'\right], \tag{C.11}$$

which is equivalent to Eqn. (C.4), the virial stress tensor.

In the preceding mechanical analysis, the interaction of particles near the cell walls was not dealt with in detail, but the following proves that the contribution to the mechanical stress by a pair interaction across the cell boundary is no different from an interaction in the middle of the cell. Referring to Figure C–1b, suppose that particle i is near the lower cell wall while particle j is located near the top wall. According to the minimum image criterion [2], i does not interact directly with j, but interacts instead with j*, the periodic image of j. Likewise, j interacts with i*, the periodic image of i. These interactions must be included in the computation of the mechanical stress only when the imaginary plane is below particle i or above particle j. Since the integration in Eqn. (C.7) starts at zero and ends at L, the i–j* and

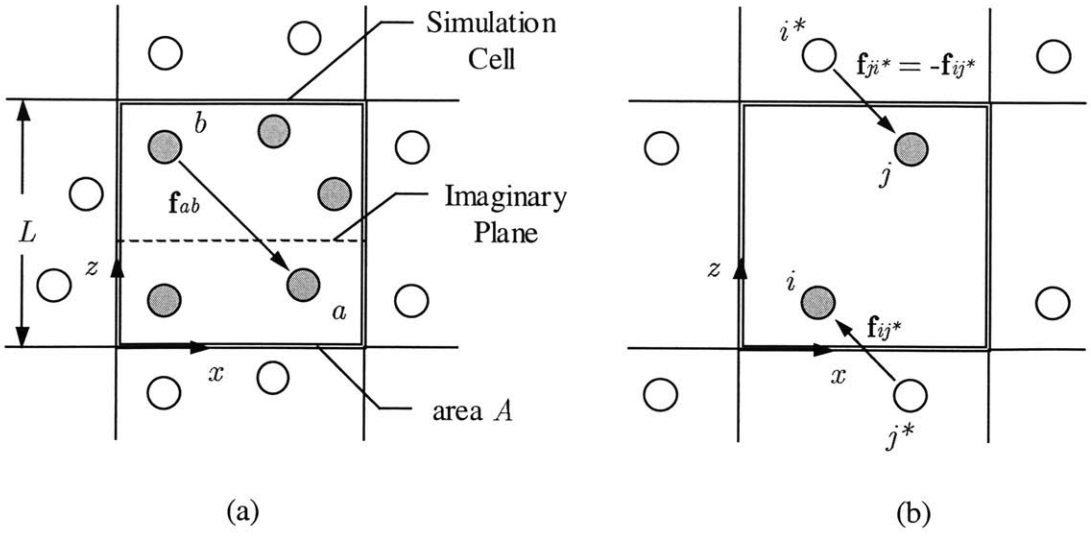

Figure C–1: (a) Schematic of a periodic MD system. Filled circles represent system atoms, open circles are periodic images. (b) Schematic of interaction of system atoms and image atoms.

j–i^* interactions make contributions of $f_{x,ij^*}z_i$ and $f_{x,ji^*}(L - z_j)$, respectively, whose sum is equal to $f_{x,ij^*}(z_i - z_{j^*})$ due to the relations $f_{x,ji^*} = -f_{x,ij^*}$ and $z_{j^*} = z_j - L$. The point is that Eqn. (C.11) is valid, even with periodic boundary conditions.

C.3 Stress Tensor For Finite Border Boundary Conditions

The virial stress is good for fully periodic systems (i.e., with periodic boundary conditions applied in all directions), but it fail when the system contains even one non-periodic boundary. An example of a non-periodic boundary is the finite border boundary conditions illustrated in Figure C–2, where the periodic boundary conditions are removed in the z direction and replaced by finite borders in the form of particles fixed in place. Periodic boundary conditions are still in effect in the x direction (and also the y direction, if the system is 3-dimensional). Note that the fixed particles are not considered a part of the system, and they are constrained from free motion. Tsai [3] was the first to suggest that the virial stress in inappropriate for finite border systems, incurring and error associated with the interaction of the border particles and nearby system particles. He concluded that the error decreases with the system size, but he did not propose any type of correction for finite border systems. Cheung and Yip [4] have also confirmed that the virial stress tensor is not generally valid for

heterogeneous systems by demonstrating that the calculation of the virial stress at free surfaces produces erroneous results of significant magnitude. It has not been made clear exactly why the virial stress tensor fails in the absence of fully periodic boundaries, but it may have something to do with the fact that actual boundaries are not considered in its derivation.

While the virial stress tensor is invalid in the presence of finite borders, the mechanical stress tensor is good for any arbitrary boundary conditions, and the following analysis applies the mechanical method to obtain a valid expression for the stress tensor of a system with finite borders. The interaction of the border particles with the system particles is defined by potential functions, as usual. Following the procedure described in Section C.2, the *volume average* of the mechanical stress for a finite border system can be expressed as

$$\tau_{zx}^{m} = \frac{1}{V}\Bigg[-\sum_{i}\int_{0}^{L} m_i u_i w_i \delta dz + \sum_{i}\sum_{j>i}\int_{0}^{L} f_{x,ij}\lambda dz + \sum_{i}\sum_{k}\int_{0}^{L} f_{x,ki}\gamma dz + \sum_{i}\sum_{n}\int_{0}^{L} f_{x,in}\nu dz\Bigg], \tag{C.12}$$

where the indices i and j loop over only the system particles, while the indices k and n loop over only the bottom and top border particles, respectively. Equation (C.12) is similar to Eqn. (C.6), except for the additional terms which account for the border particles. The definitions of δ and λ are given in Eqns. (C.8) and (C.9), and the parameters γ and ν are similarly defined as

$$\gamma = \begin{cases} 1 & z < z_i \\ 0 & \text{all other } z \end{cases}, \qquad \nu = \begin{cases} 1 & z > z_i \\ 0 & \text{all other } z \end{cases}, \tag{C.13}$$

which reduces Equation (C.12) to

$$\tau_{zx}^{m} = -\frac{1}{V}\Bigg[\sum_{i} m_i u_i w_i + \sum_{i}\sum_{j>i}\big(z_i - z_j\big) f_{x,ij} + \sum_{i}\sum_{k} z_i f_{x,ik} + \sum_{i}\sum_{n}\big(z_i - L\big) f_{x,in}\Bigg]. \tag{C.14}$$

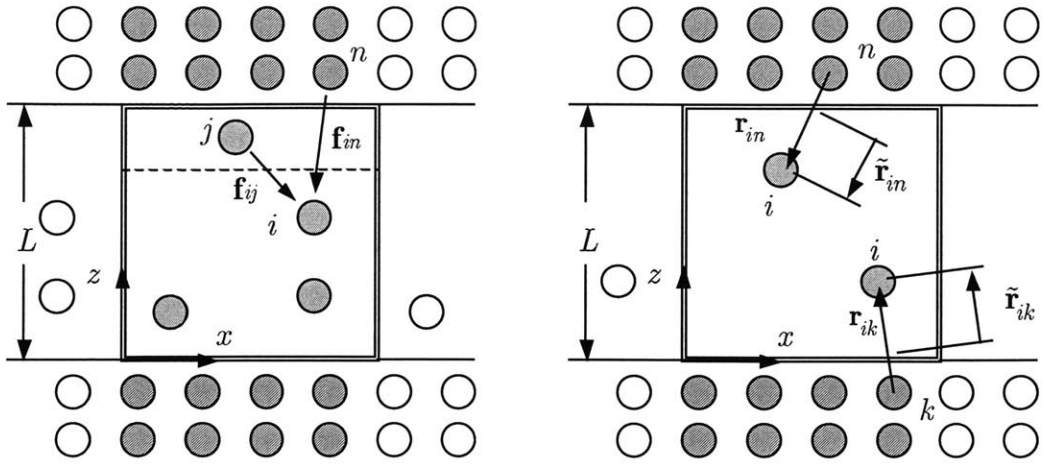

Figure C–2: (a) Schematic of finite border MD system. Filled circles are system atoms and hatched circles are border atoms. Open circles represent periodic images. (b) Schematic of system atoms interacting with border atoms.

The remaining components of stress can be analyzed in the same way, resulting in the tensor expression,

$$\boldsymbol{\tau}^m = -\frac{1}{V}\left[\sum_i m_i \mathbf{v}_i \mathbf{v}_i' + \sum_i \sum_{j>i} \mathbf{r}_{ij}\mathbf{f}_{ij}' + \sum_i \sum_k \tilde{\mathbf{r}}_{ik}\mathbf{f}_{ik}'\right], \tag{C.15}$$

where k now represents all border atoms (upper and lower), and the vector $\tilde{\mathbf{r}}_{ik}$ denotes the interior portion of the interatomic vector $\mathbf{r}_{ik}$ (see Figure C–2b). Equation. (C.15) is a valid expression for the stress of a system of discrete particles under the finite border boundary conditions.

C.4 Constant Stress Method for Finite Border Systems

Most commonly, finite border boundary conditions are used in conjunction with fixed cell dimensions, which has a major drawback in that the stress cannot be controlled during the simulation. The Parrinello-Rahman (P–R) method [5] allows the cell to dynamically vary its size and shape to meet the desired state of stress, but while it is effective for a fully periodic system, it cannot be applied to a finite border system. The biggest reason for this is

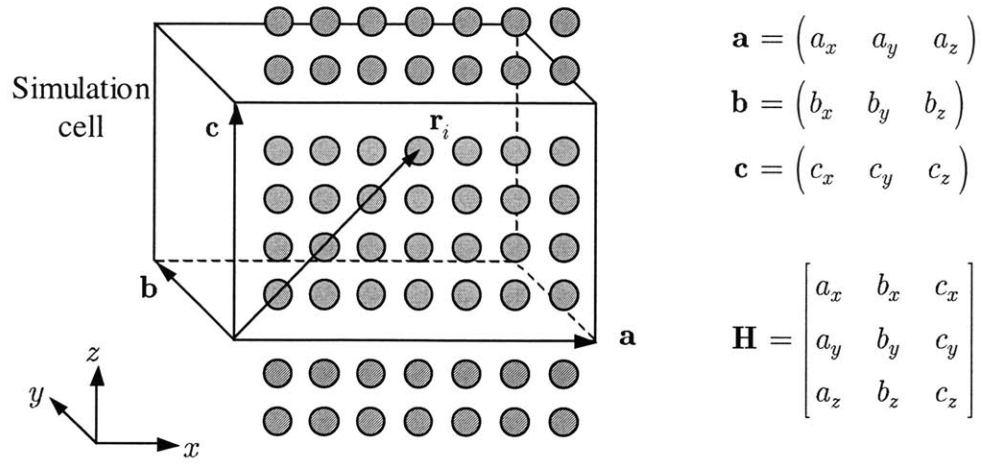

Figure C–3: Schematic of MD cell with finite borders. Filled circles are system atoms and hatched circles are border atoms.

that the most important driving term in the P–R scheme is the virial stress tensor, which is not appropriate for finite border systems. However, the mechanical stress tensor developed in Section C.3 is valid, and it can be implemented in a scheme similar to the P–R method for conducting constant stress simulations with finite border systems. This is done by treating the simulation cell walls as dynamic elements by assigning them fictitious masses and allowing them to move during the simulation.

Following the convention established by P–R, the dimensions of the simulation cell are stored in a 3×3 matrix called $\mathbf{H}$ (see Figure C–3). The position vector for particle i is expressed as $\mathbf{r}_i = \mathbf{H}\mathbf{s}_i$, where $\mathbf{s}_i$ is a dimensionless coordinate vector. For the system particles inside the cell, all components of $\mathbf{s}$ fall between 0 and 1. For the border particles outside the cell, the z-component of $\mathbf{s}$ is greater than 1 for particles in the upper border, and less than 1 for particles in the lower border. Newton's second law for particle i inside the cell can be expressed in terms of $\mathbf{s}_i$ and $\mathbf{H}$,

$$\ddot{\mathbf{s}}_i = \frac{1}{m_i}\mathbf{H}^{-1}\sum_{j,k,n}\mathbf{f}_{ij,ik,in} - 2\mathbf{H}^{-1}\dot{\mathbf{H}}\dot{\mathbf{s}} - \mathbf{H}^{-1}\ddot{\mathbf{H}}\mathbf{s}\,, \tag{C.16}$$

where the summation is taken over all system (index j) and border (indices k and n) particles, excluding particle i.

The **s** vectors of the border particles remain invariant, but as **H** varies the real coordinates of the border particles change proportionately with the cell. This means that the finite borders undergo strains equal to the simulation cell. The motion of the cell walls is governed by a simple dynamic equation,

$$W\ddot{\mathbf{H}} = (\mathbf{S} - \boldsymbol{\tau})\mathbf{A}\,. \tag{C.17}$$

where **S** is the constant external stress tensor prescribed as a boundary condition and $\boldsymbol{\tau}$ is the mechanical stress from Eqn. (C.15) (superscript m has been dropped). The scalar parameter W, called the wall mass, is the fictitious mass assigned to each cell wall in order to give them dynamic character. For simplicity, each of the six walls are assigned the same mass, whose magnitude can be adjusted to achieve the desired response frequency. **A** is an area tensor containing information about the size and orientation of the cell walls, given by

$$\mathbf{A} = V\left(\mathbf{H}^{-1}\right)' \tag{C.18}$$

(See [5] for full details). Equation (C.17) is simply a set of linear equations for an undamped forced system, with the main purpose of achieving a simulation cell shape and size such that $\bar{\boldsymbol{\tau}} = \mathbf{S}$ (i.e., the equilibrium time average of the mechanical stress is equal to the prescribed stress). It is noted that unlike the original P–R method, the above does not follow a formal Lagrangian derivation with a known Hamiltonian and, consequently, the system cannot be identified with a valid statistical ensemble. But for the purposes of this study, (C.16) and (C.17) are governing equations which functionally satisfy the constant stress condition.

C.5 References

1. Hirschfelder, J.O., Curtiss, C.F., and Bird, R.B, **Molecular Theory of Gases and Liquids**, John Wiley & Sons, Inc., 1954.
2. Allen, M.P. and Tildesley, D.J., **Computer Simulation of Liquids**, Clarendon Press, Oxford, 1987.
3. Tsai, D.H., "The Virial Theorem and Stress Calculation in Molecular Dynamics," *Journal of Chemical Physics*, vol. 70, no. 3, pp. 1375-1382, 1979.
4. Cheung, K.S. and Yip, S., "Atomic-Level Stress in an Inhomogeneous System," *Journal of Applied Physics*, vol. 70, no. 10, pp. 5688-5690, 1991.
5. Parrinello, M. and Rahman, A., "Polymorphic Transitions in Single Crystals: A New Molecular Dynamics Method," *Journal of Applied Physics*, vol. 52, no. 12, pp. 7182-7190, 1981.

APPENDIX D

Surface Energy and Interface Energy Analysis

D.1 Surface Energy

The purpose of the present analysis is to obtain an analytical expression for the energy of the FCC (111) free surface. The system under analysis consists of several (111) layers (the exact number of layers is not crucial). The interatomic spacing is obtained from the hard-sphere approximation, where D denotes the diameter of a sphere. Every bulk atom has 12 nearest neighbors, each located a distance of D away, in addition to 6 second nearest neighbors, each located $\sqrt{2}D$ away. In comparison, a surface atom only has 9 nearest and 3 second nearest neighbors, which accounts for its state of higher energy. It is noted that the longer range effects (3rd neighbors and beyond) also influence the surface energy, but their effect is marginal in comparison to the close range interactions, and so this analysis considers only up to the second neighbor shell for the sake of simplicity. It is emphasized that in accordance with the hard-sphere approximation, the interatomic spacing at the surface is the same as that in the bulk, meaning that surface relaxations not considered.

There is a periodicity in the plane of the surface defined by a unit cell containing two atoms, as illustrated in Figure D–1. The area A of the unit cell is, in terms of the sphere diameter,

$$A = \sqrt{3}D^2 . \tag{D.1}$$

By definition, the surface energy γ is 1/2 of the energy required to create a unit area of the surface. Assuming *pairwise* interacting atoms, the surface energy can be computed by summing up the excess energy of the surface atoms in a unit area, where the excess energy defined to be the amount exceeding the bulk energy per atom. Each surface atom is missing 3 nearest neighbor bonds, and each missing bond contributes $\phi_1/2$ to the atom's excess energy, where ϕ_1 is the bond energy and the factor of 1/2 is necessary on account of the pairwise assumption. In addition, a surface atom is missing 3 second nearest neighbors, and each of those bonds contribute $\phi_2/2$ to the excess energy. Since each unit cell has 2 surface atoms, the surface energy per unit cell is given by

$$\gamma = \frac{3\phi_1 + 3\phi_2}{A}. \tag{D.2}$$

The bond energies ϕ_1 and ϕ_2 can be approximated using the Lennard-Jones (L–J) potential function,

$$\phi_{LJ} = 4\varepsilon\left[(\sigma/r)^{12} - (\sigma/r)^{6}\right], \tag{D.3}$$

where the constants ε and σ are material-defining parameters related to the interatomic bond energy and the atomic diameter, respectively. These parameters will be maintained as variables throughout the derivation of the surface energy, so that a general expression can be obtained in terms of ε and σ. The L–J potential function has one minimum at $r = 2^{1/6}\sigma$, this being the separation distance of a pair of isolated atoms in mechanical equilibrium. Thus, it is reasonable to establish the following relationship between the hard-sphere diameter and σ,

$$D = 2^{1/6}\sigma, \tag{D.4}$$

which leads to

$$\begin{aligned} \phi_1 &= -\phi_{LJ}\left(2^{1/6}\sigma\right) = \varepsilon \\ \phi_2 &= -\phi_{LJ}\left(2^{2/3}\sigma\right) = \frac{15}{64}\varepsilon \end{aligned} \tag{D.5}$$

The minus signs in Eqns. (D.4) and (D.5) are necessary because the L–J function has a negative value at the bottom of the potential well. The unit cell area can also be expressed in terms of σ by combining Eqns. (D.1) and (D.4), so that

$$A = 2^{1/3}3^{1/2}\sigma^2. \tag{D.6}$$

Finally, combining Eqns. (D.2), (D.5), and (D.6) yields the following expression for the surface energy:

$$\frac{\gamma}{\left(\varepsilon/\sigma^2\right)} = \frac{79\sqrt{3}}{64\sqrt[3]{2}} \simeq 1.7. \tag{D.7}$$

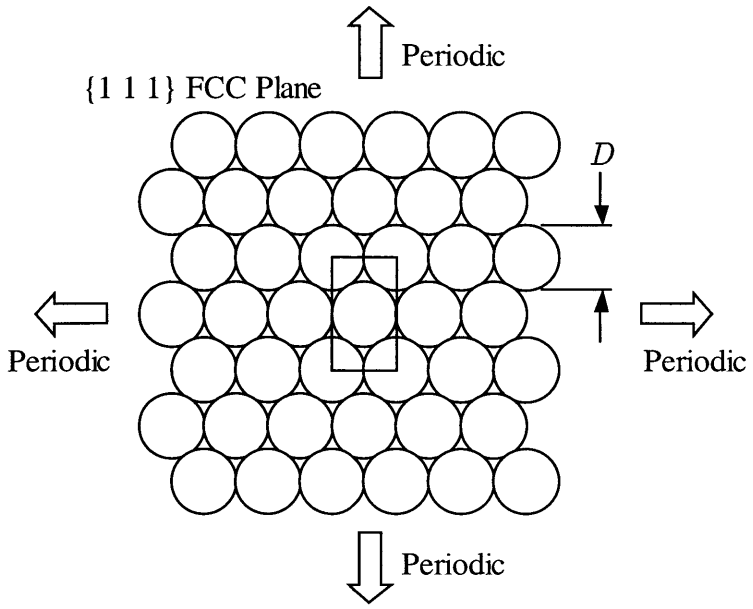

Figure D–1: Schematic of (111) FCC surface with hard sphere structure. The surface extends periodically in the plane. The unit cell of periodicity is outlined as the rectangle whose dimensions are $D \times \sqrt{3}D$.

D.2 Interface Energy

The formulation of the interface energy is similar to that of the surface energy, except for the presence of an A–B interface instead of the free surface, where A and B refer to the surfaces that form the interface. As with the free surface model, the atomic structure is obtained from the hard sphere approximation. It is further assumed that the sphere diameters of A and B are identical, and both are denoted as D. The interface is also assumed to be commensurate, which means that the lattices of A and B match perfectly, and such structural defects as dislocations, stacking faults, and grain boundaries are not present. The interface plane is the (111) FCC plane, and the interface is periodic with the unit cell shown in Figure D–1. Similar to the surface energy, the interface energy is defined as the excess energy per unit area of the interface, where the excess energy is the amount of energy exceeding the reference bulk value. Assuming pairwise interactions, the excess energy can be computed by summing the excess energy of all interfacial bonds. There are 3 nearest and 3 second nearest interfacial neighbors per interfacial atom, which means that a unit cell contains 6 nearest and 6 second nearest interfacial bonds. Thus, the interface energy γ_{AB} is given by

$$\gamma_{AB} = \frac{6\phi_1^i + 6\phi_2^i}{A}, \tag{D.8}$$

where ${\phi_1}^i$ and ${\phi_2}^i$ are the excess energies of interfacial bonds associated with the nearest and second nearest neighbors, respectively. These can be estimated with the L–J potential function in Eqn. (D.3). Three sets of L–J parameters are now required, one each for the A–A and B–B interactions and one for the A–B interaction, and these will be distinguished by subscript notation (ε_{AA}, σ_{BB}, ε_{AB}, and so on). In light of the previous assumption that the diameters of the A and B spheres are the same, it is reasonable to also assume that $\sigma_{AA} = \sigma_{BB} = \sigma_{AB}$, and the subscripts are dropped from σ from here on. It is further assumed that the bulk properties of materials A and B are similar, which leads to the simplification: $\varepsilon_{AA} = \varepsilon_{BB}$. On the other hand, $\varepsilon_{AB} \neq \varepsilon_{AA}$ is a necessary condition to have an inhomogeneity at the interface. Given these assumptions, the excess energies can be expressed as

$$\begin{aligned} \phi_1^i &= \phi_{LJ,AB}\left(2^{1/6}\sigma\right) - \phi_{LJ,AA}\left(2^{1/6}\sigma\right) = \varepsilon_{AA} - \varepsilon_{AB} \\ \phi_2^i &= \phi_{LJ,AB}\left(2^{2/3}\sigma\right) - \phi_{LJ,AA}\left(2^{2/3}\sigma\right) = \frac{15}{64}\left(\varepsilon_{AA} - \varepsilon_{AB}\right) \end{aligned} \tag{D.9}$$

Combining Eqns. (D.6), (D.8), and (D.9),

$$\frac{\gamma_{AB}}{\left(\varepsilon_{AA}/\sigma^2\right)} = \frac{79\sqrt{3}}{32\sqrt[3]{2}}\left(1 - \frac{\varepsilon_{AB}}{\varepsilon_{AA}}\right) \simeq 3.4\left(1 - \frac{\varepsilon_{AB}}{\varepsilon_{AA}}\right). \tag{D.10}$$

D.3 Work of Adhesion

The work of adhesion W_{ad} is defined as

$$W_{ad} = \gamma_A + \gamma_B - \gamma_{AB}, \tag{D.11}$$

where γ_A and γ_B are the surface energies of A and B. All of the terms on the RHS of Eqn. (D.11) are given in Eqns. (D.7) and (D.10), so the formula for W_{ad} is obtained easily:

$$\frac{W_{ad}}{\left(\varepsilon_{AA}/\sigma^2\right)} = \frac{79\sqrt{3}}{32\sqrt[3]{2}}\left(\frac{\varepsilon_{AB}}{\varepsilon_{AA}}\right) \simeq 3.4\frac{\varepsilon_{AB}}{\varepsilon_{AA}}. \tag{D.12}$$

D.4 Compatibility Factor

The so-called compatibility factor, c_m, is a familiar term in classical tribology which is used for the convenient expression of the degree of adhesion between two materials. It is defined as

$$c_m = \frac{W_{ad}}{\gamma_A + \gamma_B}. \tag{D.13}$$

Noting that $\gamma_A = \gamma_B$ in the present case and combining Eqns. (D.7) and (D.13) leads to the very convenient outcome that

$$c_m = \frac{\varepsilon_{AB}}{\varepsilon_{AA}}.$$